First study of fast variability in Markarian 421 with the MAGIC stereoscopic system

Dissertation

Physik-Department
Technische Universität München

Max-Planck-Institut für Physik
(Werner-Heisenberg-Institut)

vorgelegt von
Burkhard Steinke
im März 2012

TECHNISCHE UNIVERSITÄT
MÜNCHEN

Technische Universität München

Max-Planck-Institut für Physik
(Werner-Heisenberg-Institut)

First study of fast variability in Markarian 421 with the MAGIC stereoscopic system

Burkhard Friedrich Walter Steinke

Vollständiger Abdruck der von der Fakultät für Physik der Technischen Universität München zur Erlangung des akademischen Grades eines

Doktors der Naturwissenschaften

genehmigten Dissertation.

Vorsitzender:	Univ.-Prof. Dr. A. Ibarra
Prüfer der Dissertation:	1. Hon.-Prof. Dr. S. Bethke
	2. Univ.-Prof. Dr. L. Oberauer

Die Dissertation wurde am 14.03.2012 bei der Technischen Universität München eingereicht und durch die Fakultät für Physik am 16.04.2012 angenommen.

Abstract

Markarian 421 is the closest known and one of the best studied very high energy (VHE) γ-ray emitting blazars. Its spectral energy distribution (SED) shows a characteristic two component structure: The first component ranges from the radio over optical and UV to the X-ray band, the second emerges in the γ-ray regime. The two *Major Atmospheric Gamma-ray Imaging Cherenkov* (MAGIC) telescopes, measuring in the VHE γ-ray regime, perform regular observations since the end of 2009. In this work, the first stereoscopic observations of Markarian 421 during high source activity from January 2010 were analysed and studied with regard to flux and spectral variations.

Two distinct flares were observed on 14–15/01/2010 and 20/01/2010, reaching a flux level of 2.7 Crab units (c.u.) and 2.6 c.u. above 200 GeV, respectively. The observation periods immediately before and after the flares showed comparatively low flux levels ($0.5 - 1.5$ c.u.). The corresponding SEDs, obtained from hour-scale exposures and ranging from 80 GeV to 5 TeV and 8 TeV, respectively, exhibit a clear curvature in case of the flares and the position of the high-energy peak could be measured directly. Due to the low energy threshold and high sensitivity of the MAGIC stereoscopic system, this is the first time that the spectral evolution in a broad VHE γ-ray range could be resolved on these short timescales.

Embedded into a framework of simultaneous multiwavelength observations, the high-activity states found with MAGIC in the VHE γ-ray regime showed clear correlations with high emission activity in the X-ray regime. This suggests that both emissions are produced in the same region by (possibly) the same population of particles. Radio and optical/UV data did not show any correlated emission.

The multiwavelength results were described with two one-zone synchrotron self-Compton models. One model explains the X-ray and VHE γ-ray emission to originate from a common region and shows a correlation of the electron number density with source activity. It was found that the changes of this parameter can satisfactorily explain the main flux variations in both emission regimes. In this framework, an increased electron number density is responsible for a raised flux level. The other model also includes the optical/UV emission into the description. Here, four parameters show correlations with source activity, but it was found that these parameters alone can not be responsible for the flare emission.

The quality of the MAGIC results was crucial in imposing model constraints, since MAGIC was the only instrument covering the high-energy SED component in this analysis. With wide-range measurements obtained on short timescales, these results constitute a substantial improvement compared to preceding works.

Kurzfassung

Markarian 421 ist einer der am dichtesten zur Erde gelegenen und besterforschten Blazare. Seine spektrale Energieverteilung (SED) zeigt eine charakteristische Zweikomponentenstruktur: Die erste Komponente erstreckt sich aus dem Radio- über den optischen und UV- hin zum Röntgen-Wellenlängenbereich, die zweite Komponente verläuft im γ-Strahlungsbereich. Die zwei *Major Atmospheric Gamma-ray Imaging Cherenkov* (MAGIC) Teleskope, deren Messbereich im sehr hochenergetischen (VHE) γ-Strahlungsbereich liegt, führen seit Ende 2009 regelmäßige Observationen durch. In dieser Arbeit wurden die ersten stereoskopen Observationen von Markarian 421 während einer Phase erhöhter Quellaktivität analysiert und hinsichtlich Fluss- und Spektralschwankungen untersucht.

Am 14.–15.01.2010 und 20.01.2010 wurden zwei Strahlungsausbrüche (Flares) beobachtet, die einen Flussstand von 2.7 Crabeinheiten (c.u.) bzw. 2.6 c.u. über 200 GeV erreichten. Die Observationszeiträume unmittelbar vor und nach den Flares zeigten vergleichsweise niedrige Flussstände ($0.5 - 1.5$ c.u.). Die zugehörigen SEDs (80 GeV $- 5$ TeV bzw. 8 TeV), erstellt aus relativ kurzen Expositionen ($\approx 1 - 2$ h), weisen im Falle der Flares eine eindeutige kurvenförmige Struktur auf und der Scheitelpunkt der hochenergetischen SED-Komponente konnte direkt gemessen werden. Aufgrund der geringen Energieschwelle und der hohen Sensitivität der stereoskopen MAGIC-Teleskope ist dies das erste Mal, dass die spektrale Entwicklung in einem breiten Bereich der VHE γ-Strahlung auf diesen kurzen Zeitskalen aufgelöst werden konnte.

Kombiniert mit simultanen Multiwellenlängenbeobachtungen, zeigten die von MAGIC beobachteten Zustände hoher Aktivität im VHE γ-Strahlungsbereich klare Korrelationen mit Zuständen hoher Aktivität im Röntgenbereich. Dies deutet darauf hin, dass beide Emissionen in der gleichen Region von (möglicherweise) den gleichen Teilchen erzeugt werden. Radio- und optische/UV-Strahlung wiesen keine korrelierte Emission auf.

Die Multiwellenlängenergebnisse wurden mit zwei Einzonen-Synchrotron-Self-Compton-Modellen beschrieben. Eines der Modelle erklärt die Röntgen- und VHE γ-Strahlungsemission als aus einer gemeinsamen Region stammend und weist eine Korrelation der Elektronenzahldichte mit der Quellaktivität auf. Es zeigte sich, dass die Veränderungen dieses Parameters die Flussvariationen in beiden Emissionsbereichen generell erklären können. In diesem Rahmen ist eine erhöhte Elektronenzahldichte verantwortlich für erhöhte Flussstände. Das andere Modell bezieht auch die optische/UV-Emission in die Beschreibung mit ein. Hier zeigten vier Parameter Korrelationen mit der Quellaktivität, deren Veränderungen allein allerdings nicht ausreichen, um die Flussvariationen befriedigend zu beschreiben.

Die Qualität der MAGIC-Ergebnisse war entscheidend bei der Eingrenzung der Modellparameter, da MAGIC das einzige Instrument in dieser Analyse war, das die hochenergetische SED-Komponente abdeckte. Mit Messungen in einem breiten Energiebereich auf relativ kurzen Zeitskalen stellen diese Ergebnisse eine wesentliche Verbesserung im Vergleich zu vorhergehenden Arbeiten dar.

Contents

Abbreviations and acronyms

A_{eff}	Effective area
ADC	Analog-to-digital converter
AGN	Active Galactic Nuclei
AMC	Active mirror control
app.	Appendix
ASCII	American Standard Code for Information Interchange
Az	Azimuth
bgd	Background
BL Lac	BL Lacertae
c.u.	Crab unit ($2.19^{+0.15}_{-0.13}$ 10^{-10} cm^{-2} s^{-1})
CANGAROO	Collaboration between Australia and Nippon for a Gamma Ray Observatory in the Outback
CCD	Charge-coupled device
CGRO	Compton Gamma-Ray Observatory
CoG	Centre of gravity
CORSIKA	Cosmic Ray Simulations for Kascade
DAC	Digital-to-analog converter
DAQ	Data aquisition
DC	Direct current
DEC	Declination
DRS2	Domino Ring Sampler 2
EBL	Extragalactic background light
EGRET	CGRO Energetic Gamma-Ray Experiment Telescope
eq.	Equation
ESW	Electrostatic waves
eV	Electron Volt
FADC	Flash analog-to-digital converter
fig.	Figure
FSRQ	Flat Spectrum Radio Quasar
FWHM	Full width half maximum
GeV	Giga (10^9) eV
GUI	Graphical user interface
H.E.S.S.	High Energy Stereoscopic System

HBL	High-frequency BL Lac
HE	High energy
HEGRA	High Energy Gamma-Ray Astronomy
HV	High voltage
IACT	Imaging Atmospheric Cherenkov Telescope
IC	Inverse Compton
ICRC	International Cosmic Ray Conference
ID	Identification
IR	Infrared
LAT	Fermi Large Area Telescope
LBL	Low-frequency BL Lac
LE	Low energy
LED	Light-emitting diodes
LV	Low voltage
MAGIC	Major Atmospheric Gamma-ray Imaging Cherenkov
MARS	MAGIC Analysis and Reconstruction software
MC	Monte-Carlo
MeV	Mega (10^6) eV
MJD	Modified Julian Date
Mrk	Markarian
MWL	Multiwavelength
NDF	Number degrees of freedom
NN	Nextneighbour
NSB	Night sky background
OVRO	Owens Valley Radio Observatory
pc	parsec, $1\text{pc} = 30.8568 \cdot 10^{15}$ m
PC	Personal computer
PCI	Peripheral Component Interconnect bus
phe	photo electrons
PIC	Proton induced cascade
PMT	Photomultiplier tube
PSF	Point spread function
QE	Quantum efficiency
RA	Right ascension
RF	Random forest
SCCP	Slow control cluster processor
sec.	Section
SED	Spectral energy distribution
SS-PIC	Synchrotron-self proton induced cascade
SSC	Self synchrotron Compton
t_{obs}	Observation time
tab.	Table
TeV	Tera (10^{12}) eV
UMRAO	University of Michigan Radio Astronomy Observatory

UV	Ultraviolet
UVOT	Swift Ultraviolet/Optical Telescope
VCSEL	Vertical-cavity surface-emitting laser
VERITAS	Very Energetic Radiation Imaging Telescope Array System
VHE	Very high energy
VME	Versa Module Eurocard bus
XRT	Swift X-ray Telescope
ZA	Zenith angle
Zd	Zenith

Chapter 1

Introduction

Active Galactic Nuclei (AGN) are one of the most powerful phenomena in the non-thermal universe. The AGN subclass of blazars allows a deep and unique insight into the extreme acceleration and emission processes, since for this class one of the relativistic particle jets, which arise at the poles of the rotating system of central black hole and accretion disk, is directly pointing towards Earth. Here, we as observers can look down the jet and draw conclusions on the physical processes, because due to relativistic beaming the corresponding emission is not obscured from the AGN dusk torus as under other viewing angles.

With a distance of $\approx$ 500 million lightyears, Markarian (Mrk) 421 is the closest known and one of the best studied representatives of the blazar subclass. Its broadband spectral energy distribution (SED) of electromagnetic radiation shows the typical two-component structure of blazars: The first component extends from the radio to the X-ray waveband with a peak in the soft to medium X-ray range, the second component extends in the γ-ray waveband up to GeV and TeV energies with a peak around 100 GeV. Additionally, large and occasional flux variations up to one order of magnitude on short and long timescales have been observed for Mrk 421. While measurements in the radio, optical/UV and X-ray regime have already been performed with high sensitivity on short timescales in the past, measurements in the γ-ray regime required averaging of particularly long time periods to achieve acceptable precision for spectral studies. With the beginning of scientific operation of the MAGIC stereoscopic telescope system in late 2009, an improved quality in short time measurements also in the very high energy γ-ray regime could be achieved. In this thesis, the first MAGIC stereoscopic observations of Mrk 421 during high source activity are analysed and the resulting high precision day-to-day SEDs are presented.

Embedded into a multiwavelength framework, the measurements of MAGIC cover the second SED component and are able to put constraining datapoints below and above the corresponding peak. Due to the new sensitivity in this energy regime, comprehensive model sets can be fitted to the data and allow interpretations of the emission mechanisms. Here, open questions are: What produces the short term

activity of Mrk 421? Are changes in particular physical properties responsible for the flux variations? And what scenarios might generate such changes? This thesis tries to answer these questions and attempts to bring the knowledge regarding Mrk 421 forward to a deeper understanding and comprehension.

The text is organised as follows: In chapter 2, the basic foundations of very high energy γ-ray astrophysics are introduced. Focus is laid on AGN and the blazar subclass. The physical processes that are considered to take place inside the blazar jets are discussed in chapter 3. Chapter 4 addresses the basic principles of the Imaging Atmospheric Cherenkov Telescope observation technique, which is used by the MAGIC telescopes. The MAGIC telescopes themselves are introduced in chapter 5. Focus is laid on the camera of MAGIC-II and its control software, whose installation and maintenance was a relevant part of this thesis. In chapter 6, the analysis of MAGIC data is discussed and a detailed study of the influences of the stereoscopic trigger scheme on the observed γ-rate, particular in the Mrk 421 case, is presented in chapter 7. Chapter 8 is about the reference analysis of the Crab nebula, the "standard candle" for Imaging Atmospheric Cherenkov Telescopes. The analysis of the MAGIC Mrk 421 dataset from January 2010 is presented in chapter 9. Its embedding into a multiwavelength framework is presented in chapter 10: First, the instruments and wavebands offering simultaneous data with the particular MAGIC analysis periods and second, the SEDs resulting from the multiwavelength observations and their modelling within a one-zone synchrotron self-Compton scenario. Implications and interpretations of the obtained results are discussed in chapter 11. A summary and an outlook to future prospects are given in chapter 12. Supplementary information, such as an excursus on SED notation, details on used cut values, data point numbers of presented plots, observations details of the participating multiwavelength instruments and a dedicated verification of the the applied model code, is given in the appendix.

Chapter 2

Very high energy (VHE) γ-ray astrophysics

In this chapter, the basic foundations of very high energy (VHE) γ-ray astrophysics are introduced. Focus is laid on Active Galactic Nuclei (AGN) and the blazar subclass, whose representative Markarian (Mrk) 421 is subject of this thesis.

2.1 Cosmic rays

In 1912, the existence of ionizing particles continually bombarding the atmosphere of the earth was first noticed by Victor Hess [Hes12]. Today we know that these cosmic rays mainly consist of protons (of about 79 %) and α-particles (of about 15 %), as well as of heavier nuclei, anti protons, electrons and positrons in smaller fractions [Nak10]. Fig. 2.1 shows the cosmic ray spectrum of all particles at the top of the atmosphere. The spectrum spans over many decades and can be well described by a segmented power law:

$$\frac{\mathrm{d}N}{\mathrm{d}E} \propto E^{-\alpha} \tag{2.1}$$

with the spectral index

$$\alpha = \begin{cases} 2.7 & \text{for } 10^{10} < E < 10^{16} \text{ eV} \\ 3.0 & \text{for } 10^{16} < E < 10^{18} \text{ eV}. \end{cases} \tag{2.2}$$

The breaks in the spectrum are named as *knee* (around $10^{15} - 10^{16}$ eV) and *ankle* (around $10^{18} - 10^{19}$ eV). It is believed that the knee represents an upper limit of acceleration by galactic sources like supernovae, while the ankle is associated with the onset of an extragalactic population of cosmic particles. This extragalactic population is considered to be less intense but to have a harder spectrum, that dominates at high energies [Blu09]. Another possible effect to contribute to the spectral form at high energies is leakage of galactic particles: For particles with

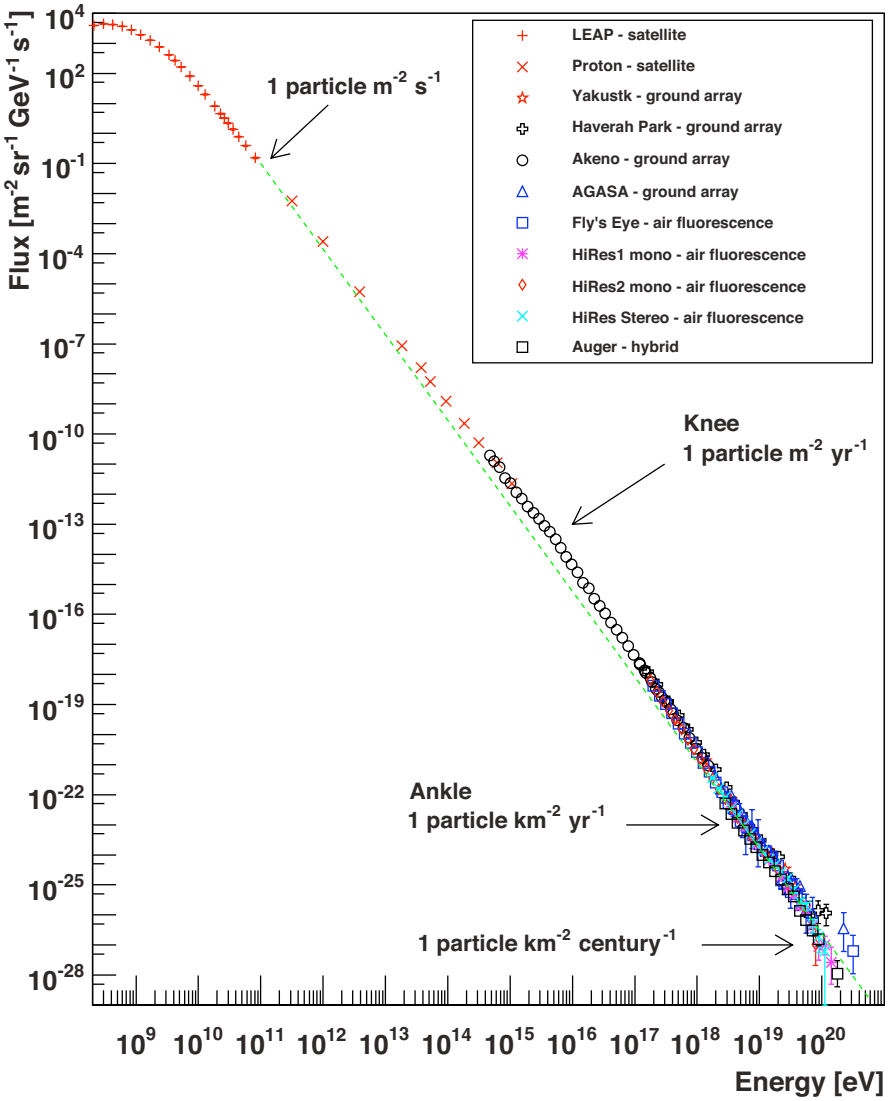

Figure 2.1: All particle cosmic ray spectrum, measured by the denoted instruments. Adapted from [Han11].

sufficiently high energies the Larmor radius exceeds the radius of the galaxy, which leads to an escape of these particles.

For cosmic rays with energies above 10^{20} eV, the universe becomes opaque. The resonant reaction with the 2.7 K microwave background

$$p + \gamma_{2.7\mathrm{K}} \rightarrow \Delta^{+} \rightarrow p + \pi^{0}, n + \pi^{+} \tag{2.3}$$

becomes energetically allowed and limits the free path of protons with $E \approx 10^{20}$ eV to ≈ 8 Mpc [Ber04]. This effect is known as Greisen Zatsepin Kuzmin (GZK) limit and characterises the upper edge of the cosmic ray spectrum.

The origin of cosmic rays and their propagation mechanisms are still subject of intense research. Particularly the question which processes accelerate particles to such high energies, is not sufficiently answered. The power-law formed spectrum indicates non-thermal processes for the acceleration. The mechanism proposed by Enrico Fermi in 1949, in which the particles are accelerated by stochastic scattering in magnetic turbulence structures [Fer49], lead to the currently accepted model of cosmic ray diffusive acceleration at magnetic shock fronts (first order Fermi acceleration). Here, the particles gain an amount of energy $\Delta E \propto E$ every time they pass the magnetic shock front. They may undergo complete cycles, passing from the region ahead the shock (upstream) to the region behind the shock (downstream) and back. There is a given probability at each cycle that a particle is lost downstream and does not return to the shock. Particles that have remained longer in the acceleration process will achieve higher energies [Blu09]. This process is explained in detail in sec. 3.2.1.

After a time t the maximum energy achieved is $E_{\mathrm{max}} \propto z\beta_{\mathrm{s}} B t v_{\mathrm{s}}$, with z the particle charge, v_{s} the shock velocity and $\beta_{\mathrm{s}} = v_{\mathrm{s}}/c$ and B the magnetic field strength. This results in an upper limit, assuming a minimal diffusion length equal to the Larmor radius of a particle in the magnetic field behind and ahead of the shock (Hillas criterion) [Blu09]. Fig. 2.2 shows this relation for various astrophysical objects. Among the few candidates to accelerate particles up to the observed high energies are Active Galactic Nuclei (AGN), for which a representative of the blazar subclass, Markarian (Mrk) 421, is studied in this thesis.

2.2 γ-ray astronomy

Due to the deflection in galactic and intergalactic magnetic fields, charged cosmic rays are generally isotropised. Thus, the direction of their arrival at Earth does not give information about the direction of their source. Cosmic γ-rays are not charged, and therefore they are not subject of deflections and point back to their origins. In consequence, cosmic γ-rays can be used as messengers of cosmic ray sources, in which they are considered to be produced related to the production and acceleration of the charged cosmic particles. Such γ-ray production processes are neutral pion decay or synchrotron radiation and inverse Compton upscattering, which will be discussed in detail in sec. 3.1.

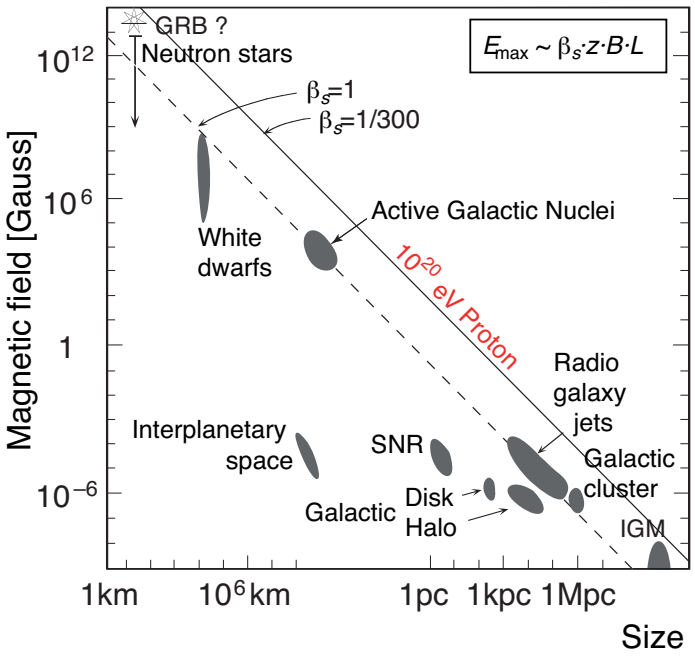

Figure 2.2: Astrophysical objects in which cosmic rays could be accelerated (Hillas plot). Assuming first order Fermi acceleration, the maximum reachable energy is determined by the shock velocity (β_s), the charge of the particle (z), the magnetic field strength (B) and the size of the acceleration region (L). Adapted from [Blu09].

Cosmic γ-ray radiation covers a huge energy band, ranging from 10^6 to 10^{20} eV. Therefore, it is convenient to introduce several sub-divisions, taking into account the specific astrophysical objectives and detection methods relevant to different energy bands. Generally, the observational γ-ray astronomy can be divided into 6 areas: *low* (LE: below 30 MeV), *high* (HE: from 30 MeV to 30 GeV), *very high* (VHE: from 30 GeV to 30 TeV), *ultra high* (UHE: from 30 TeV to 30 PeV) and finally *extremely high* (EHE: above 30 PeV) energies [Aha04a]. Since the atmosphere of the Earth effectively blocks all electromagnetic radiation of energies greater than 10 eV [Wee03], the first two energy bands are studied by satellite or balloon borne experiments, while the higher energies are covered by ground-based instruments using secondary interactions in the atmosphere as detection mechanism.

A major breakthrough in γ-ray astronomy was achieved with the Compton Gamma-Ray Observatory (CGRO) in 1991 [Ber04]. The four instruments on board this satellite, covering an energy range from 30 keV to 30 GeV, detected an unprecedented number of γ-ray sources. Particularly the Energetic Gamma-Ray Experiment Telescope (EGRET), operating in the energy range from 20 MeV to 30 GeV, discovered 217 sources (101 related to known astrophysical objects, 170 unidentified) [Har99]. The CGRO mission was followed in 2008 by the Fermi Gamma-ray Space Telescope. Its main instrument, the Large Area Telescope (LAT), covers an energy range from 30 MeV to 300 GeV. The first catalogue of LAT sources already comprised 1451 sources [Abd10a], giving an impression of the improved sensitivity and resolution of the instrument.

The steeply falling of the γ-ray spectrum limits the energies, for which satellite born instruments can detect sufficient numbers of γ-ray photons. In this VHE energy range, the ground-based Imaging Atmospheric Cherenkov Telescopes (IACT) are successfully operated. These telescopes use Cherenkov radiation induced by γ-ray initiated atmospheric air showers to detect the VHE photons (this method is introduced in detail in chapter 4). The Whipple[1] and HEGRA[2] telescopes, located at Mount Hopkins, USA and at the Roque de los Muchachos, Canary Island of La Palma respectively, were the first IACT delivering results with satisfactory sensitivity. In 1989, the first VHE γ-ray source, the Crab nebula, was hence detected by the Whipple collaboration [Wee89].

Today, the following IACT instruments are in operation: CANGAROO[3] (Australia), H.E.S.S.[4] (Namibia), VERITAS[5] (Mount Hopkins, USA) and MAGIC[6] (Roque de los Muchachos, Canary Island of La Palma). The MAGIC telescopes will be introduced in detail in chapter 5. These telescopes, using improved tech-

[1]Whipple: Here used for the 10 m reflector for γ-ray astronomy at the F. L. Whipple Observatory

[2]HEGRA: High Energy Gamma-Ray Astronomy

[3]CANGAROO: Collaboration between Australia and Nippon for a Gamma Ray Observatory in the Outback

[4]H.E.S.S.: High Energy Stereoscopic System

[5]VERITAS: Very Energetic Radiation Imaging Telescope Array System

[6]MAGIC: Major Atmospheric Gamma-ray Imaging Cherenkov

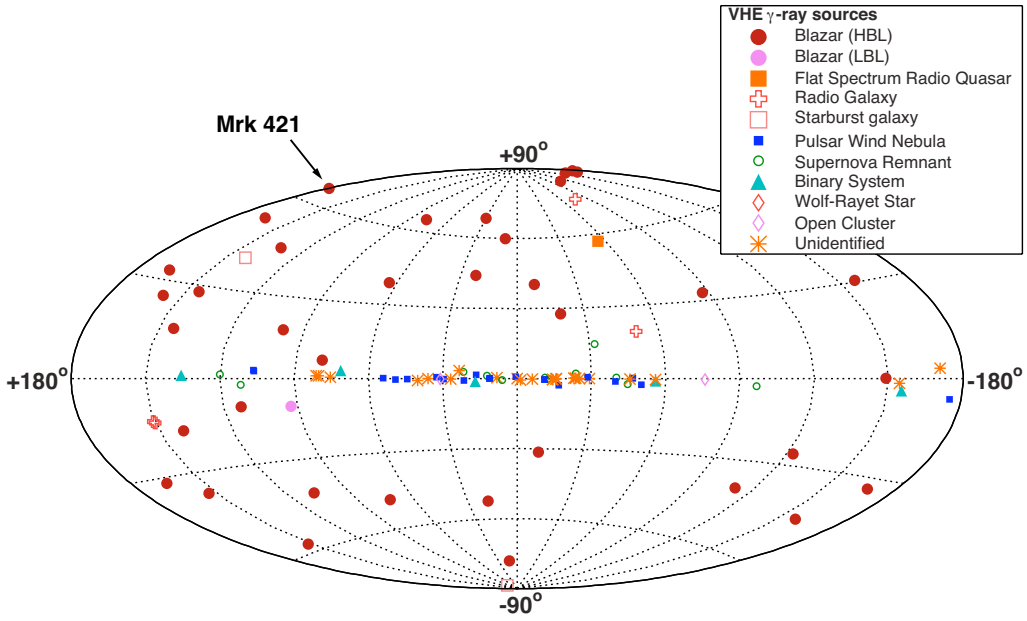

Figure 2.3: VHE γ-ray skymap for energies above 100 GeV. Shown are all currently detected VHE γ-ray sources in galactic coordinates. Markarian (Mrk) 421, studied in this thesis, is also shown. Adapted from [Wag11].

niques and multiple telescope systems, increased the number of detected VHE γ-ray sources to currently 107, shown schematically in fig. 2.3. 61 of them are considered to be located within the galaxy, 46 are thought to be extragalactic [Wag11].

2.3 Active Galactic Nuclei (AGN)

In the unified scheme [Ant93, Urr95], Active Galactic Nuclei (AGN) are comprised of a supermassive black hole, an accretion disk surrounding the black hole, a large dust torus in the same plane as the accretion disk, randomly distributed molecular clouds and two relativistic particle jets perpendicular to the accretion disk, terminating in large lobes. This general scheme is shown in fig 2.4.

In this model, the wide variety of AGN types, mainly classified by the variety of observational features, is a function of viewing angle [Urr95]: If the system is viewed edge-on, i.e. the jets and the line of sight form an angle of 90°, the thick dust torus is considered to obscure the emission from the core. In this case, the radio emission from the jets, particularly from the lobes, is clearly dominating and the AGN is seen as radio galaxy.

With decreasing angle between jet and line of sight, the radio and optical emission from the core become more apparent. In addition, broad emission lines from the gas clouds become visible. Since the radio emission from the lobes is

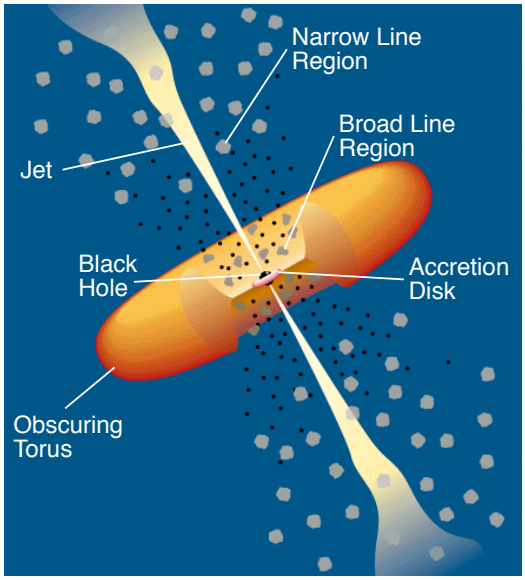

Figure 2.4: Scheme of AGN, showing the main components in the unified model. From [Urr95].

still dominating, the AGN is classified as lobe-dominated quasar. As the viewing angle decreases further, the core becomes more apparent and dominates the lobe emission, and the AGN is classified as core-dominated Quasar.

For little viewing angles, the synchrotron emission from the jets become the strongest emission. The AGN is now categorised as blazar. For a viewing angle of 0°, the observer is directly looking down the jet.

2.3.1 Central engine

The black hole in the centre of an AGN is generally seen as the source of energy of the whole system. While the formation of an accretion disk, responsible for the large X-ray emission, is understandable in terms of angular momentum conservation, the origin of the jets is less clear. They emerge from the vicinity of the black hole, point in directly opposite directions and remain collimated passing the surrounding of the black hole [Wee03].

Aligned to the rotational axis of the black hole, the jets might be fed by rotational energy, generated by angular momentum either from the time of origin of the black hole or from the accretion material. If the rotational axis coincide with the magnetic axis of the AGN, the formation of the jets and their collimation might be additionally connected to magnetic energy: For the black hole, it is impossible to accrete the magnetic flux carried in by the accretion material and therefore has to eject this magnetic flux along the magnetic axis.

The central engine seems to play an important role also in the formation of the jet density profile, leading to the observed emission. In the internal shock model, the central engine intermittently produces plasma shells of different mass

and energy, moving at different velocities along the jet. Faster but later shells can then catch up slower earlier ones, resulting in the development of relativistic shocks. The shocks heat the expanding plasma, generate or amplify a tangled magnetic field and accelerate a certain population of plasma particles to relativistic energies, causing the particles to radiate [Mim04, Ree94, Spa01] (for a detailed discussion of acceleration and radiation processes please see chapter 3).

2.3.2 Blazars

Blazars are the most extreme class of AGN known. They have been observed at all wavelengths, from radio to VHE γ-rays. The spectral energy distributions (SED, see app. A) of blazars are dominated by non-thermal and emission and show a characteristic two-component structure: The first component ranges from radio over optical and ultraviolet to the X-ray band, the second emerges in the γ-ray regime. If emission lines are apparent, the blazar is called Flat Spectrum Radio Quasar (FSRQ). If no emission lines are seen, the object is classified as BL Lacertae (BL Lac), named after the prototype source with these properties [Wee03, Urr95]. BL Lacs are additionally subdivided into low-frequency BL Lac (LBL) and high-frequency BL Lac (HBL), according to the peak frequency of their low-energy SED component: LBLs have their low-energy peak in the infrared-optical regime ($\lesssim 10^{15}$ Hz), while HBLs have their low-energy peak at X-ray energies ($\gtrsim 10^{15}$ Hz) [Abd10c, Boe10]. LBL blazars generally show higher luminosities than HBL blazars. Additionally, the high-energy peak frequency correlates with the low-energy peak frequency and the luminosity ratio between the high-energy and the low-energy component correlates with bolometric[7] luminosity [Fos98].

The emission of blazars is known to be variable at all wavelengths. In particular, the high-energy emission from blazars can vary by more than one order of magnitude between different observing epochs and is often accompanied with spectral changes [Boe10, Mon95, Muk97, Muk99]. High-energy variability is also observed at much shorter timescales, in some cases even down to just a few minutes [Aha07, Alb07e]. Typically, the flux variations show the largest amplitudes and shortest timescales at the high-frequency ends of the two SED components. In HBLs, this refers to the X-ray and VHE γ-ray regimes [Boe10].

The high bolometric luminosities, the rapid variability and the absence of $\gamma\gamma$ pair absorption features in the observed γ-ray spectra have motivated the concept of relativistic beamed emission, in which the non-thermal continuum emission of blazars is produced in $\lesssim 1$ light day sized emission regions, propagating with relativistic speed $\beta = v/c$ along the jet [Boe10, Bla78, Bla90, Der92a, Sch96a, Sch96b]. The resulting Doppler boosting is determined by the beaming (Doppler) factor $\delta = 1/[\Gamma(1 - \beta\cos\theta)]$, with Γ the bulk Lorentz factor of the emission region and θ the angle between the line of sight and the direction of the relativistic jet. The observed frequency ν is then related to the emitted frequency ν' through

[7] The measured total of all radiation at all wavelengths is called the bolometric magnitude.

$\nu = \delta\nu'/(1+z)$, with z the redshift of the source. The energy fluxes are connected through $F_\nu = \delta^3 F'_\nu$ and intrinsic variability on a timescale $t'_{\rm var}$ will be observed on a timescale $t_{\rm var} = t'_{\rm var}(1+z)/\delta$ [Boe10]. A consequence of the Doppler boosting is that observers are particularly sensitive to AGNs whose jets point towards them ($\theta \approx 0$, the blazar case), since the observed fluxes from these objects are boosted by a large factor (δ^3) compared to equally bright AGN with misaligned jet directions [Sch96a]. The basic acceleration and radiation processes, which are assumed to produce the intrinsic blazar emission, are discussed in the next chapter.

Chapter 3

Blazar jet physics

In this chapter, the physical processes that are considered to take place inside blazar jets are introduced: First, radiation and absorption processes that lead to the typical photon spectra of blazars, then the acceleration mechanisms that are considered to be responsible for the underlying particle spectra.

3.1 Photon production scenarios

Extensive multifrequency observations of blazars have been performed in the last years, revealing that the broadband continuum spectra of blazars consist of two components. In the leptonic photon production scenarios, these components are explained by synchrotron radiation of electrons (for the low energy component) and inverse Compton scattering of soft photons (for the high energy component). The one-zone synchrotron self-Compton (SSC) model is very successful in describing the observed multifrequency spectra: Here the synchrotron photons also act as seed photons for the inverse Compton scattering in one common emission region. This model has become the standard method for fitting the multiwavelength spectra of blazars.

In the following subsections, the basic assumptions of the SSC model are presented, giving emphasis on the physics of synchrotron emission and inverse Compton scattering. Other photon production scenarios are discussed afterwards.

3.1.1 Synchrotron radiation

A non-relativistic charge moving through a homogeneous magnetic field follows a helical path around the magnetic field lines. The motion consists of two components: one is parallel to the magnetic field lines, the other is rotation about them at the frequency of Larmor precision:

$$\nu_{\mathrm{L}} = \frac{1}{2\pi}\frac{eB}{m_e c}\sin\phi \tag{3.1}$$

with e the unit charge, B the magnetic field strength, ϕ the inclination angle between the direction of the magnetic field and the velocity vector of the charge and m_e the restmass of the charge. The charge radiates like a dipole with frequency ν_{L} in the charge rest frame [Wee03].

At relativistic energies, the radiation is more complex since the radiation is beamed into a cone of angle $\theta \approx m_e c^2/E$. Instead of occurring at a single frequency, the radiation shows a continuum spectrum distributed about the characteristic frequency ν_c, at which the maximum power is emitted [Wee03]:

$$\nu_c = \frac{3}{2}\nu_{\mathrm{L}}\gamma^2 = \frac{3}{4\pi}\frac{eB}{m_e c}\gamma^2 \sin\phi \tag{3.2}$$

with γ the Lorentz factor of the moving charge. For the characteristic energy follows:

$$E_c = h\nu_c = \frac{3h}{4\pi}\frac{eB}{m_e c}\gamma^2 \sin\phi. \tag{3.3}$$

3.1.2 Inverse Compton (IC) scattering

The scattering of a photon off an unbound electron is known as Compton scattering. The inverse Compton (IC) process, the collision of a high energy electron with a low energy photon, is physically the same as Compton scattering and can be described by a coordinate transformation to the rest frame of the electron [Wee03]. In this frame, the stationary electron scatters an energetic photon.

The cross section of this process is known as Klein-Nishina cross section [Lon11]:

$$\sigma_{\mathrm{KN}} = \pi r_e^2 \frac{1}{\alpha}\left(\left(1 - \frac{2\,(\alpha+1)}{\alpha^2}\right)\ln\left(2\alpha+1\right) + \frac{1}{2} + \frac{4}{\alpha} - \frac{1}{2\,(2\alpha+1)^2}\right) \tag{3.4}$$

with $r_e$the classical electron radius and $\alpha = E'_\gamma/m_e c^2$ (E'_γ: photon energy in the electron rest frame[1], m_e: electron restmass). In the classical limit ($E'_\gamma \ll m_e c^2$) this reduces to the Thomson cross section

$$\sigma_{\mathrm{T}} = \frac{8}{3}\pi r_e^2. \tag{3.5}$$

In the ultrarelativistic case ($E'_\gamma \gg m_e c^2$), the cross section can be expressed by the Klein-Nishina approximation

$$\sigma_{\mathrm{KN}} \approx \pi r_e^2 \frac{1}{\alpha}\left(\ln 2\alpha + \frac{1}{2}\right). \tag{3.6}$$

In the initial frame, the photon acquires considerable energy and this process can be seen as energy boosting for the photon. In the extreme relativistic case

[1]The photon energy in the electron rest frame transforms from the energy in the initial system E_γ according to the relativistic Doppler shift formula $E'_\gamma = \gamma E_\gamma\left(1 + (v/c)\cos\theta\right)$ with the Lorentz factor γ of the frame translation, the relative frame velocity v and the angle of incidence θ.

($\gamma \gg 1$, with γ the Lorentz factor of the frame translation (which is here the Lorentz factor of the electron in the initial frame)), the relativistic beaming is strong and most of the scattered photons are nearly parallel to the initial velocity vectors of the electrons. The maximum energy which the photon can acquire corresponds to a collision in which the photon is sent back along its original path (head-on) [Lon11]. In the Thomson limit, the maximum energy of the photon in the initial frame is then

$$E_{\gamma\,\mathrm{max\,T}} \approx 4\gamma^2 E_{\gamma\,0} \tag{3.7}$$

with $E_{\gamma\,0}$ the energy of the photon in the initial frame before the scattering. The energy change due to electron scattering in the Thomson limit can be viewed as the result of two successive Doppler boosts: one from the initial frame into the electron rest frame, and the other one back to the initial frame. In the Klein-Nishina limit the energy change is $\propto \gamma m_e$. This means that the electron gives all its energy to the photon in a single interaction [Kro99].

3.1.3 Synchrotron self-Compton (SSC) scenario

The photon production in the one-zone synchrotron self-Compton (SSC) scenario is based on synchrotron radiation of relativistic electrons and IC scattering of these soft synchrotron photons off the same population of electrons [Jon74, Mar85, Mar92]. Further assumptions and parameters of the model are:

- The emission region is one zone with the characteristic size R. Electrons and photons are isotropic in this region.
- The emission region is moving with relativistic velocity $\beta = v/c$.
- The magnetic field B in the emission region is homogeneous in the rest frame of the emission region.
- The injected electron spectrum basically is of a power law form:

  $$N_e^{\mathrm{inj}}(\gamma) = q_e\,\gamma^{-s} \quad \text{for} \quad \gamma_{\mathrm{min}} < \gamma < \gamma_{\mathrm{max}} \tag{3.8}$$

  with q_e the normalisation factor (often denoted as injection rate), γ the electron Lorentz factor, s the power law index and γ_{min} and γ_{max} the minimum and maximum Lorentz factor value respectively. The motivation for a power law form injection spectrum is stochastic escape from the acceleration process, see sec. 3.2.

  The time evolution of the electron distribution $N_e(\gamma, t)$ is then given by:

  $$\frac{\partial N_e(\gamma,t)}{\partial t} = N_e^{\mathrm{inj}}(\gamma) - \frac{\partial}{\partial\gamma}\left[\left(\frac{1}{t_{\mathrm{syn}}(\gamma)} + \frac{1}{t_{\mathrm{IC}}(\gamma)}\right) N_e(\gamma,t)\right] - \frac{N_e(\gamma,t)}{t_{\mathrm{esc}}} \tag{3.9}$$

  with t_{syn} and t_{IC} the characteristic timescale for the synchrotron and inverse Compton energy losses (cooling timescale) and t_{esc} the effective escape time

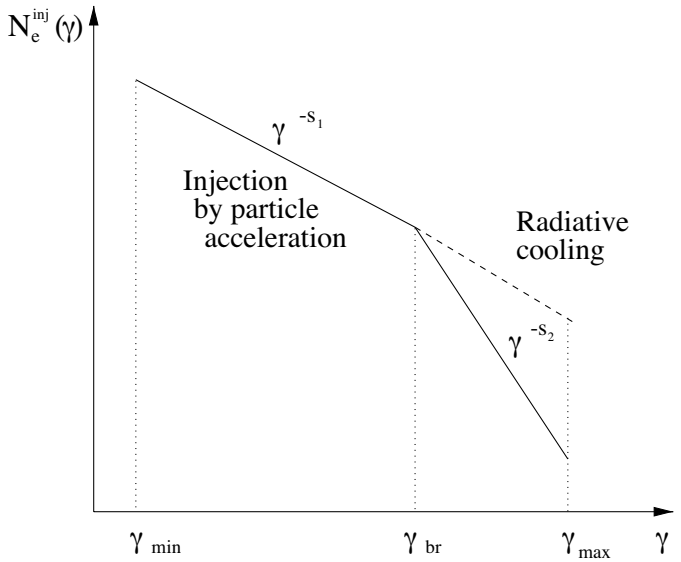

Figure 3.1: Scheme of the relativistic electron injection spectrum for an one-zone synchrotron self-Compton (SSC) model. The electron energy spectrum $N_e^{\mathrm{inj}}(\gamma)$ ranges from the minimum Lorentz factor γ_{min} to the maximum Lorentz factor γ_{max}. Additionally, a so-called break value γ_{br} is introduced: Here the spectral index of the power law spectrum changes due to radiative cooling, which decreases the number density of electrons. Adapted from [Kin02].

of the electrons (identified as the timescale of adiabatic expansion losses [Mas97]).

Modified SSC models use variations in the injection spectrum, for instance by applying the maximum Lorentz factor to the spectrum itself ($N_e^{\mathrm{inj}}(\gamma) = q_e\,\gamma^{-s}\,e^{-\gamma/\gamma_{\mathrm{max}}}$ [Kin02]), or by introducing one or more break values γ_{br}, for which the spectral index changes below and above these values (these break values are motivated by radiative losses for the injection spectrum). A scheme of a suchlike injection spectrum is shown in fig. 3.1.

- The beaming (Doppler) factor of the jet is given by $\delta = 1/[\Gamma(1 - \beta\cos\theta)]$, with Γ the bulk Lorentz factor of the emission region and θ the angle between the line of sight and the direction of the relativistic jet.

A scheme of the typical multifrequency spectrum produced by an one-zone SSC model is shown in fig. 3.2. Besides the two components arising from synchrotron emission and IC scattering, several features originating from the model parameters γ_{min}, γ_{max} and γ_{br} are shown. The influence of synchrotron self absorption is also indicated: If the intensity of synchrotron radiation becomes sufficiently high, re-absorption of the radiation by the synchrotron emitting electrons becomes important and modifies the spectrum. In the TeV regime, the Klein-Nishina suppression, related to the drastic decrease of the scattering cross section with increasing energy, is significantly reducing the photon flux.

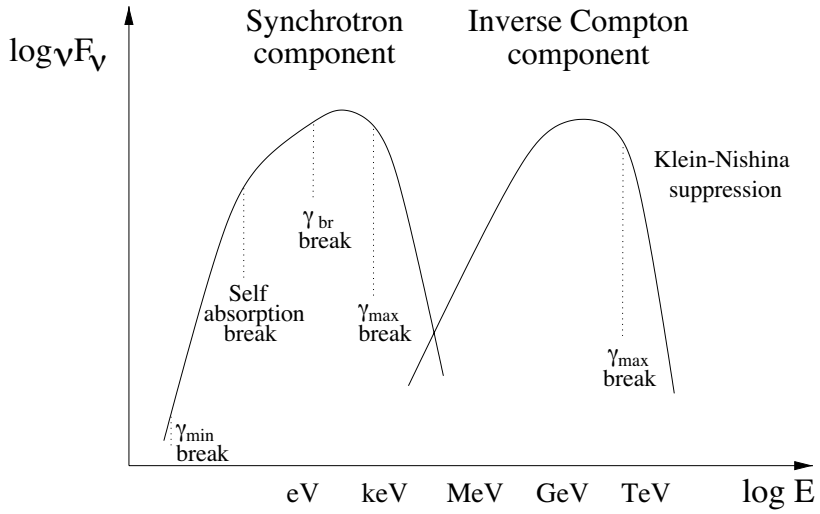

Figure 3.2: Scheme of the typical multifrequency spectrum produced by an one-zone SSC model. The multifrequency spectrum shows the two components of the synchrotron emission and the upscattered inverse Compton photons. The influences of $\gamma_{\rm min}$ and $\gamma_{\rm max}$ are also shown. Corresponding to the break in the electron spectrum ($\gamma_{\rm br}$), a break feature appears in the synchrotron spectrum. The effect of self-synchrotron absorption is also indicated. Around the TeV energy region, the Klein-Nishina effect (significant decreasing of the cross section) suppresses the flux compared to the Thomson regime. Adapted from [Kin02].

3.1.4 Other leptonic scenarios

In the leptonic scenarios, the low energy component of the blazar spectra originates from synchrotron emission of high relativistic electrons, while the high energy component is due to IC scattering of soft photons. In the SSC model, as introduced in detail above, the soft photons from the synchrotron emission act also as seed photons for the IC scattering.

In other models, the sources of these soft photons are external: In the ECD (External Comptonisation of direct Disk radiation) model, the ultraviolet to soft X-ray emission from the accretion disk is entering the jet directly [Der93], whereas in the ECC (External Comptonisation of radiation from Clouds) model the accretion disk photons are reprocessed in surrounding gas regions before they enter the jet [Sik94, Bla95].

3.1.5 Hadronic scenarios

Besides the above introduced leptonic scenarios, the photon spectra of blazars might also be produced in hadronic mechanisms. In the proton induced cascade (PIC) model, $p\gamma$ interactions with ambient photons lead to the production of secondary $e^{\pm}$ pairs or mesons like $\pi^{\pm}$ and π^0. The $\pi^{\pm}$ mesons eventually decay into $e^{\pm}$ and neutrinos, the π^0 mesons decay into photons and, up to a certain percentage, into photons and $e^{\pm}$. The $e^{\pm}$ from these processes can then produce

high energy photons by synchrotron emission and IC scattering. The resulting photons, together with the photons from the π^0 decay, might either escape from the jet or produce new pairs in $\gamma\gamma \rightarrow e^+e^-$ interactions, which radiate a new generation of photons [Man91, Man93, Rac00]. The efficiency of this model significantly increases with proton energy, therefore the postulation of extremely high energy (EHE, $E \geq 10^{19}$ eV) protons is required in the PIC scenario. In compact γ-ray production regions of the jet with characteristic sizes less than 10^{16} cm, protons are accelerated to such high energies only in the presence of large magnetic fields, $B \gg 1$ G [Aha00].

Another scenario is the proton-synchrotron model: Here, the high energy component of blazar spectra is due to synchrotron radiation of accelerated protons, while most of the low energy component is due to synchrotron radiation of co-accelerated electrons [Aha00, Mue00, Mue03]. As in the PIC scenario, this model requires extremely high proton energies ($E \geq 10^{19}$ eV) and highly magnetised ($B \approx 30 - 100$ G) emission regions [Aha00]. This can lead to an overlap of contributions from the PIC and from the proton-synchrotron scenario: High-energy radiation is then produced through photomeson production, proton and muon synchrotron radiation and subsequent synchrotron-pair cascading [Mue03].

Also *pp* interactions can contribute to the high-energy emission of blazars. In such scenarios, protons are accelerated and interact with protons either in collision zones of the jet with surrounding gas [Rac00] or – after beeing emitted from the acceleration region – in gas regions of the broad line region ("clouds", see fig. 2.4) near the line of sight [Dar97]. In the latter case, VHE γ-ray flux variations are produced when the clouds cross the line of sight close to the black hole.

3.1.6 Comparison of scenarios

In summary, various scenarios are able to explain the multifrequency spectra and variability of blazars. The most powerful and self-consistent scenario is the leptonic SSC model: It has much less free parameters than other scenarios, particularly hadronic scenarios. Pure hadronic models are also less successful in explaining the observed correlated variability of the X-ray and TeV regime due to their prediction of a rather constant spectral index in the γ-ray band. For these reasons, the one-zone SSC model is clearly favoured and also used for interpretations in this thesis.

A combination of hadronic and leptonic scenarios offers an interesting explanation for the observed strong variability due to intrinsic instabilities [Rac00]: Here, protons might be responsible for the injection of energetic electrons, which then produce the observed photon emission, for instance by the SSC mechanism [Kir92, Kaz92]. This indeed requires large densities of relativistic protons in the jet, but only moderate proton energies.

Another combination is the synchrotron-self proton induced cascade (SS-PIC) mechanism, in which high energy protons and electrons are co-accelerated in the same process. The protons then interact with synchrotron photons emitted by the

electrons, leading to γ-ray emission via the PIC scenario. As a consequence, the γ-ray emission due to the PIC process is in competition with the SSC emission of the electrons and its hard to distinguish the origin of the γ-ray photons [Rac00].

A clear evidence for hadronic processes would be the detection of neutrino emission from the corresponding source (neutrinos are also produced within the PIC cascade). But since the sensitivity of current neutrino telescopes is relatively low, this possible demonstration of evidence can not be expected in the near future.

3.2 Particle acceleration in the jet

Since the detection of non-thermal emission of jet-type astrophysical objects, it is conjectured upon its origin. Today, the acceleration of radiating particles by magnetised plasma is currently most favoured. Great importance is attached to the Fermi acceleration processes, wherein the charged particles obtain energy from the bulk motion of the plasma, i.e. kinetic energy of the plasma, via particle-wave interactions. In these processes, first denoted by [Fer49], the particles (with velocity v) are repeatedly reflected (magnetic scattering) in magnetic turbulence structures moving with velocity u. Under the assumption of energy conservation in the comoving scattering frame, the energy change of a particle due to reflection is given by:

$$\Delta E = E_2 - E_1 = 2\Gamma^2 \left(\frac{E_1 u^2}{c^2} - p_1 \cdot u \right) \tag{3.10}$$

with $\Gamma = (1 - u^2/c^2)^{-1/2}$ the Lorentz factor of the magnetic turbulence, $p = Ev/c^2$ the particle momentum and the indices 1 and 2 denoting the particle properties before and after scattering [Rie06]. An important property of Fermi acceleration is that the processes are collisionless in terms of interactions between particles, which would prevent acceleration because of collisional energy loss [Fer49, Gai90].

Depending on the particular process, one distinguishes between two types of Fermi acceleration: *First order*, taken place in astrophysical shock waves, and *second order Fermi acceleration*, taken place in the environment of magnetised molecular clouds. A special case is the acceleration due to shear flows in the magnetic structure, called *shear acceleration*. These acceleration types will be described in the following subsections. Then, the maximum achievable energy of the various processes and observational constraints are discussed.

3.2.1 First order Fermi acceleration or shock acceleration

A plasma of energetic particles ($v \approx c$) is disturbed by a non-relativistic shock front moving through it (e.g. caused by plasma shells of different velocities (internal shock model), see sec. 2.3.1). In the rest frame of the shock, the velocity ahead of the shock (upstream, u_u) is much higher than the velocity behind the shock (downstream, u_d). In the frame of the upstream plasma, the downstream plasma approaches with the resulting velocity $u = u_\mathrm{u} - u_\mathrm{d}$ and also in the frame of the

downstream plasma, the upstream plasma approaches with the same velocity u. The two regions can be regarded as two converging flows and in first order there is only head-on magnetic scattering for particles crossing the shock front [Rie06]. Crossing the shock, regardless from which side, always leads to a gain in energy for the crossing particles. The energy gain (eq. 3.10) becomes

$$\frac{\Delta E}{E_1} \propto \frac{u}{c} \tag{3.11}$$

and therefore first order in u/c [Rie06]. After crossing the shock, the momentum direction distribution of the accelerated particles isotropises in the upstream and downstream plasma, respectively, and the particles can undergo several shock crossings. This process is basically the same also in the case of relativistic shocks [Web87]. Due to stochastic escape from the acceleration region, this shock acceleration produces power law particle spectra:

$$N(E) \propto E^{-s} \tag{3.12}$$

with $s = (\rho + 2)/(\rho - 1)$ and $\rho = u_\mathrm{u}/u_\mathrm{d}$ the shock compression ratio. For strong shocks, a power law index of $s \approx 2$ is obtained [Dru83]. Non linear effects, for instance strong shock modification, lead to values $s < 2$ [Ber99], whereas a non-uniform magnetic field with non-static field lines leads to disturbance in the stochastic transport of the particles and therefore to values $s > 2$ up to $s = 2.5$ [Kir96].

The efficiency of the first order Fermi acceleration depends on the initial energy of the accelerated particles. To reach the observed values, the particles have to be pre-accelerated to considerably high energies. A possible solution for this *injection problem* gives [McC01]: Electrostatic waves (ESW), excited by streaming ion beams, carry the charged particles across a magnetic field. Here, the Lorentz force can principally accelerate the charged particles to ultrahigh energies. This process is called *ESW surfing acceleration*. Another solution – which might also take place in combination with the ESW surfing – is the acceleration due to the collapse of ESW [Die04].

3.2.2 Second order Fermi acceleration

In the case of a strong shock, the scattering of the charged particles is always head-on when crossing the shock front. This leads to first order Fermi acceleration, see above. In the absence of a shock front, the particles undergo head-on scattering as well as following (overtaking) scattering in the magnetic structure, for instance a magnetised molecular cloud. The particles gain and lose energy during these stochastic scattering processes. After many scatterings, the bulk motion of the particles corresponds to the bulk motion of the cloud. When the particles escape from the cloud, the gain in energy averaged over all momentum directions

is positive and second order in u/c [Fer49]:

$$\frac{\langle \Delta E \rangle}{E_1} \propto \left(\frac{u}{c}\right)^2 . \tag{3.13}$$

Second order Fermi acceleration leads to particle spectra $N(E) \propto E^{-s}$ with typical values of $s \leq 2$ [Vir05] and the energy gain is rather small compared to first order Fermi acceleration.

3.2.3 Shear acceleration

Shear acceleration is considered to take place in magnetic turbulence structures with regions of gradual shear flow. Particles crossing the shear undergo scattering in regions of different local velocities u_z, with u_z the characteristic region velocity in shear flow direction. The average energy gain per scattering becomes

$$\frac{\langle \Delta E \rangle}{E_1} \propto \left(\frac{\partial u_z}{\partial x}\right)^2 \tau^2 = \left(\frac{\tilde{u}}{c}\right)^2 \tag{3.14}$$

with $\tilde{u} = (\partial u_z/\partial x)\lambda$ the characteristic relative velocity of the scattering centres, $\lambda \simeq c\,\tau$ the particle mean free path and τ the mean scattering time [Jok90, Rie06]. Similar to second order Fermi acceleration, this process is second order in $\tilde{u}/c$. In general, the mean free path of electrons is much smaller than the mean free path of protons emitting at the same frequency. Therefore, shear acceleration is much more favourable for protons than for electrons [Rie04]. The resulting local particle spectra follows a power law $N(E) \propto E^{-s}$ with typical values of $s > 1$ [Ber81].

3.2.4 Maximum achievable energy

The maximum achievable particle energy depends on the acceleration timescale and the timescale, at which the particles lose their energy. Depending on the type of energy loss, this loosing timescale is denoted as escape timescale (where the particles leave the acceleration region) or cooling timescale (where the particles "cool" by radiative processes). Generally, acceleration timescale ($t_{\rm acc}$) and escape/cooling timescale ($t_{\rm esc/cool}$) are functions of the particle energy. The maximum energy of an acceleration process is reached for that energy, for which the escape/cooling timescale becomes larger than the acceleration timescale, i.e. for that energy, for which the acceleration is not sufficient anymore to compensate for the losses.

In the first order Fermi acceleration process, the acceleration timescale $t_{\rm acc}^{\rm 1st}$ depends on the residence times ahead (upstream) and behind (downstream) the non-relativistic shock [Dru83]. The assumptions of quasi-parallel shocks and quasi-linear magnetic fields ($|\delta B| \lesssim B$) lead to

$$t_{\rm acc}^{\rm 1st} \gtrsim 6 \frac{\gamma_e\, m\, c}{e\, B} \left(\frac{c}{u_{\rm s}}\right)^2 \tag{3.15}$$

with γ_e the particle Lorentz factor, m the particle mass and u_s the shock velocity measured in the upstream frame [Rie06]. For second order Fermi acceleration, one can derive the typical acceleration timescale by assuming the relativistic particles scattering off forward and reverse propagating Alfvén waves[2] [Rie06]:

$$t_\mathrm{acc}^\mathrm{2nd} \gtrsim \frac{3}{4}\left(\frac{c}{v_\mathrm{A}}\right)^2 \tau \tag{3.16}$$

with v_A the Alfvén speed (representing the motion of the magnetic turbulence) and τ the mean scattering time. Since $v_\mathrm{A} < u_\mathrm{s}$, second order Fermi acceleration is typically a factor of $(u_\mathrm{s}/v_\mathrm{A})^2$ slower than first order Fermi acceleration. For shear acceleration, the expression for the acceleration timescale is more complicated than for the first and second order Fermi acceleration, since geometrical information of the shear has to be included. But as important result one finds here that the acceleration timescale is inverse proportional to the particle Lorentz factor: $t_\mathrm{acc}^\mathrm{shear} \propto 1/\gamma_e$ [Rie06].

For the loosing timescale at blazar jets, radiative losses due to synchrotron radiation are the dominating constraints. The synchrotron cooling timescale is characterised by

$$t_\mathrm{cool}^\mathrm{sync} = \frac{9\,m^3\,c^5}{4\,\gamma_e\,e^4\,B^2}\,. \tag{3.17}$$

Equating $t_\mathrm{acc}^\mathrm{1st}$ and $t_\mathrm{cool}^\mathrm{sync}$ and taking into account the Hillas criterion (the gyro radius of the particle is smaller than the acceleration region) leads to the maximum Lorentz factor for diffusive shock acceleration (first order Fermi acceleration) inside a blazar jet:

$$\gamma_\mathrm{max}^\mathrm{1st} \simeq 5\cdot 10^6 \left(\frac{1\,\mathrm{G}}{B}\right)^{1/2}\left(\frac{m}{m_e}\right)\left(\frac{u_\mathrm{s}}{0.1\,c}\right) \tag{3.18}$$

with m_e the electron mass as normalisation [Rie06]. For second order Fermi acceleration, this gives (under the assumption that the mean scattering length is of the size of the gyro radius):

$$\gamma_\mathrm{max}^\mathrm{2nd}2 \simeq 1\cdot 10^5 \left(\frac{1\,\mathrm{G}}{B}\right)^{1/2}\left(\frac{m}{m_e}\right)\left(\frac{v_\mathrm{A}}{0.001\,c}\right). \tag{3.19}$$

For shear acceleration, the acceleration timescale scales with the particle Lorentz factor in the same way as the cooling timescale. This means that the synchrotron losses are not able to compensate the acceleration once it has started to work efficiently. This effect starts for sufficiently strong shears, i.e. for shears, that have a linear decreasing flow profile from relativistic to non-relativistic velocities of the size [Rie06]:

$$\Delta r \lesssim 3\cdot 10^{-8}\left(\frac{m}{m_e}\right)^2\left(\frac{1\,\mathrm{G}}{B}\right)^{3/2}\ \mathrm{pc}. \tag{3.20}$$

[2]The Alfvén wave is a concept of magnetohydrodynamics, considering the particle plasma as vibratory medium [Alf42]. The waves velocity is given by $v_\mathrm{A} = B/\sqrt{4\pi\rho}$ with ρ the plasma density.

3.2.5 Observational constraints

The observed synchrotron and IC emission properties of AGN jets require underlying particle spectra of the type $N(E) \propto E^{-s}$ with spectral indices $s \approx 2$. Here, first order Fermi acceleration naturally delivers these power law particle spectra and is an efficient and sufficiently fast mechanism. This interpretation is supported by the observational facts that structures inside the jets (knots) can be identified as regions of strong shock formation and that the detected fast variabilities (connected to t_{acc} and/or t_{cool}) can be explained self-consistently within the first order Fermi process [Kir98].

Although shock acceleration seems to be dominating, some features of AGN jets can not be explained by first order Fermi acceleration alone. High resolution observations show that for instance in the case of 3C 273[3] the variations of infrared to ultraviolet spectral indices are rather smooth along jet [Jes01, Jes05]. This implies that the physical conditions vary correspondingly smoothly all along the jet. This is contrary to the scenario of dedicated regions of shock acceleration (knots) and therefore suggesting additional continuous re-acceleration along the entire jet. Here, second order Fermi and/or shear acceleration are natural candidates to explain these observations [Rie06].

[3] 3C 273 is a so-called quasar (quasi-stellar radio source) in the constellation Virgo. It is the 273$^{\mathrm{rd}}$ object in the 3$^{\mathrm{rd}}$ Cambridge-Catalogue of Radio Sources. The jet inclination to the line of sight is estimated to be rather small, i.e. of the order $10^\circ - 30^\circ$ [Mik10, Sta04].

Chapter 4

The Imaging Atmospheric Cherenkov Telescope (IACT) technique

Many astrophysical objects are known to produce high energy γ-rays. For energies below ≈ 30 GeV, satellite or balloon borne instruments are used to detect the γ-ray emission directly. The collection area of these instruments is of the size of the detector (< 1 m^2). For higher energies, a much larger collection area is required, since the γ-ray flux is decreasing exponentially with increasing energy. Imaging Atmospheric Cherenkov Telescopes (IACT), using the atmosphere of the Earth as an intrinsic part of the detection technique, are achieving collections areas of $\approx 10^5$ m^2 [Nak10]. Therefore, IACT are well suited to observe γ-ray fluxes from ≈ 50 GeV to several tens of TeV. In this chapter, the basic principles and the underlying physics of the IACT observation technique are introduced.

4.1 Air showers

High energy cosmic rays incident on the atmosphere of the Earth induce a particle cascade, called air shower. Cherenkov radiation, generated by relativistic charged particles in the cascade (see sec. 4.2), is then used to detect, identify and trace the primary cosmic ray particle.

4.1.1 Photon and electron energy losses

Incident on the atmosphere, photons at low energies primarily lose energy by the photoelectric effect, although other processes (Compton scattering, Rayleigh scattering, photonuclear absorption) contribute. As the energy of the photon increases, pair production becomes the dominating process for photon energy losses. For electrons and positrons, ionisation dominates at low energies, although Møller scattering, Bhabha scattering and e^+ annihilation also contribute. While ionisation loss

rates rise logarithmically with energy, bremsstrahlung losses rise nearly linearly (fractional loss is nearly independent of energy) and dominates above a few tens of MeV in most media [Nak10].

In the pair production interaction, the incident γ-ray is completely annihilated with its energy transferred to an electron-positron pair which is created, given that the photon energy is greater than $2m_e c^2$. To hold the conservation laws of momentum and energy, this interaction takes place in the electric field of a nucleus[1]. Since the pair is strongly beamed forward in case of $E(\gamma) \gg 2m_e c^2$, the trajectory of the γ-ray can be inferred from the trajectories of the electron and positron [Wee03]. Together with generating high energy photons by bremsstrahlung, an electron-photon cascade (electromagnetic shower, see sec. 4.1.2) is started.

The mean distance that a γ-ray travels before it undergoes pair production is given by

$$\lambda_{pp} = \frac{9}{7} X_0 \tag{4.1}$$

with X_0 the radiation length (the characteristic distance in the traversed matter).

In the bremsstrahlung process, a charged particle is deflected in the electric field of a nucleus and emits electromagnetic radiation. In the classical treatment, the acceleration causing the deflection is proportional to Ze^2/m_e for a particle of charge e and mass m_e and a nucleus of charge Ze. The amplitude of the emitted radiation is proportional to this acceleration [Wee03].

The relativistic bremsstrahlung energy losses are of exponential form $-\,\mathrm{d}E/\,\mathrm{d}x \propto E$ and it is therefore possible to define the radiation length X_0 as the mean path, over which the charged particle loses a fraction $\left(1 - 1/e\right)$ of its energy:

$$\frac{-\,\mathrm{d}E}{\mathrm{d}x} = \frac{E}{X_0}\,. \tag{4.2}$$

4.1.2 Electromagnetic and hadronic air showers

Depending on the constitutes of the induced particle cascade, one distinguishes between electromagnetic and hadronic air showers.

An electromagnetic cascade is initiated when a high energy photon, electron or positron is incident on an absorber (here the atmosphere of the Earth). Bremsstrahlung and pair production exponentially generate more electrons, positrons and photons with lower energy (see left panels fig. 4.1). The shower consists exclusively of these particles and is therefore called electron-photon cascade or electromagnetic shower. The longitudinal development is lead by the high energy part of the cascade and therefore scales as the radiation length in the material [Nak10]. As the electron energies fall below the critical energy $E_\mathrm{c} \approx 83$ MeV for generating more shower particles, they will rather dissipate their energy by ionization and excitation. In addition, with decreasing energy, the production cross

[1] The interaction can also occur in the field of an electron but the cross section is much smaller and the energy threshold is higher.

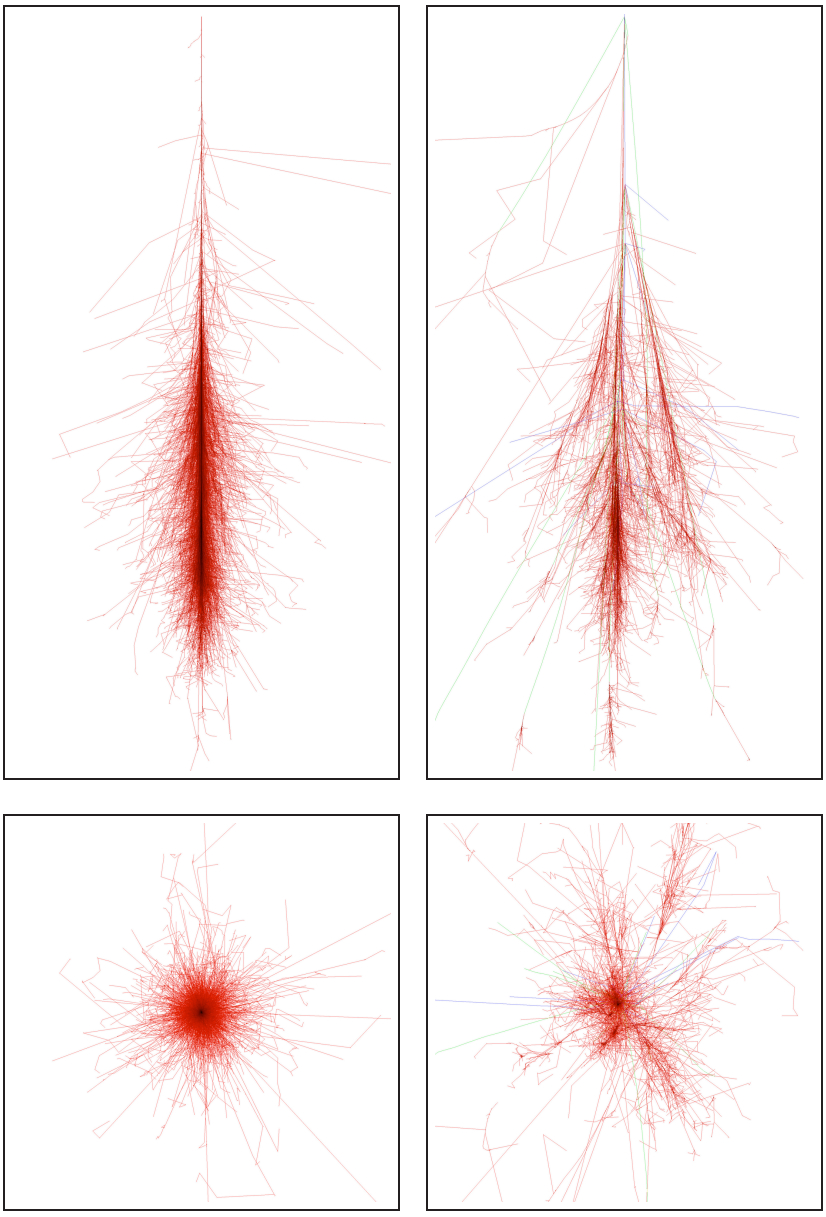

Figure 4.1: Simulation of a γ-ray (left side) and proton (right side) induced air shower. Both showers are simulated with a 100 GeV primary particle in CORSIKA. The upper panels show the vertical, the lower panels the lateral development (top view in the direction of the shower axis). Red colour represents positron, electron and γ-ray particle tracks, blue colour represents hadron particle tracks and green colour represents muon particle tracks. In general, hadronic showers show a much higher lateral spread due to the transverse momentum of pions, produced in strong interactions. From [Sch11].

section for e^+e^- pairs decreases until it becomes of the same order as that for Compton scattering and photoelectric absorption. Thus, the shower reaches its maximum development when the average energy of the cascade particles is about E_c. The maximum number of generated photons and particles is proportional to E_0, the energy of the initial particle. At larger depths, the number of particles falls off because of ionisation losses, which become dominant once the electrons become non relativistic [Lon11].

A hadronic cascade is produced by a high energy hadron such as a nucleon (e.g. proton), pion or atomic nucleus incident on an absorber. These particles interact with a nucleus of the absorber via the strong force and secondary hadronic particles are produced (see right panels fig. 4.1). Since some of the primary particles carry electric charge, parts of the hadronic showers are also electromagnetic. Hadronic cascade processes are characterized by relatively few high energy particles being produced (in contrast to electromagnetic cascades). In general, hadronic showers show much higher lateral spread due to the transverse momentum of pions, produced in strong interactions. The lost energy of the primary particle and the $\pi^0 \rightarrow \gamma\gamma$ fraction highly differ from event to event [Nak10].

In cases where the incident particle is relativistic, also the secondary particles of air showers (electromagnetic and hadronic) tend to travel with relativistic velocities. This means that the secondary particles exceed the speed of light in the absorber medium and Cherenkov radiation is produced. This effect is subject of the next section.

4.2 Cherenkov radiation

Cherenkov radiation occurs when a charged particle travels through a dielectric medium with a velocity greater than the velocity of light in the medium. The particle interacts electrically with the molecules in its immediate vicinity and disturbs their neutrality. The induced polarisation causes the molecules to radiate. A slow moving particle is inducing a symmetrical disturbance around and along the particle trajectory (see fig. 4.2 (left)). In this case there is no residual electric field and therefore no detectable radiation [Wee03]. For a particle moving at relativistic velocity, the radial symmetry is still preserved but a dipole field results along the trajectory, which produces detectable effects (see fig. 4.2 (right)). As the particle traverses the dielectric medium, each finite element radiates a short electromagnetic pulse. In the forward direction, the wavefront from each path element will interfere positively (see fig. 4.3) [Wee03]. The angle θ_C of the resulting Cherenkov radiation relative to the particles direction is

$$\cos\theta_C = \frac{1}{n\beta} \tag{4.3}$$

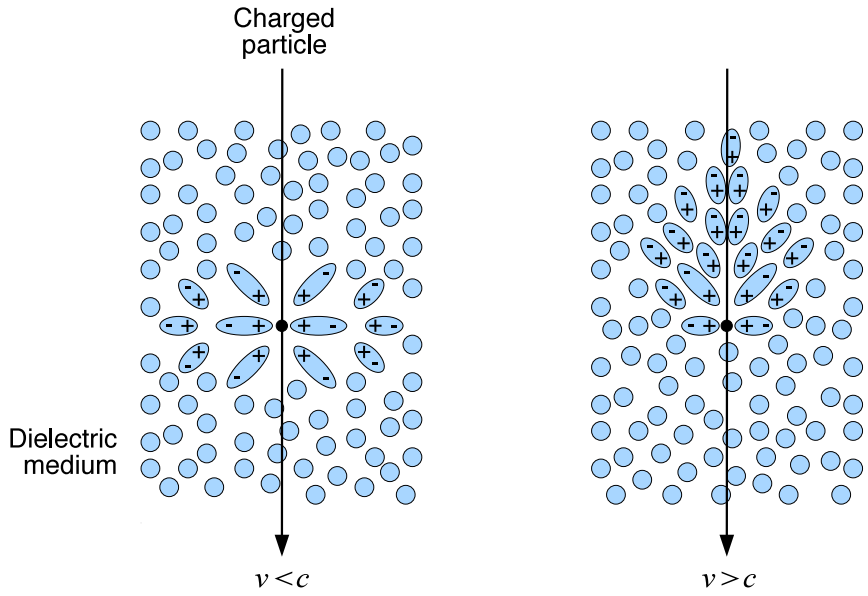

Figure 4.2: Sketch for the local polarisation in a dielectric medium during the passage of a slow moving charged particle (left) and a charged particle that exceeds the speed of light in the medium (right). The arrow represents the trajectory and the black dot the current location of the charged particle. The circles represent the molecules of the medium. For the slow moving particle the induced polarisation is symmetrical around and along the trajectory whereas it is resulting in a dipole field along the trajectory for the relativistic particle. Adapted from [Wee03].

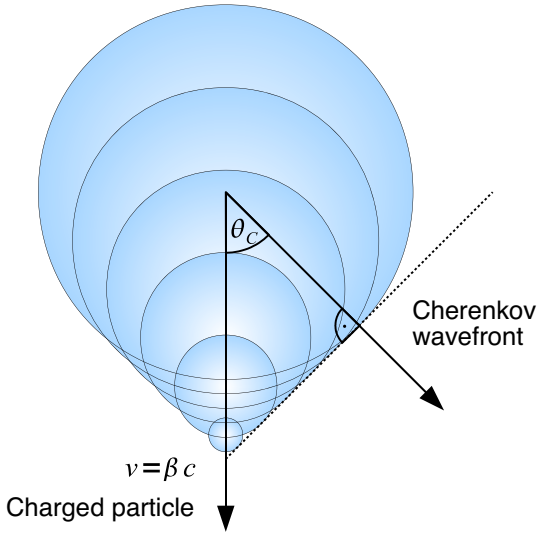

Figure 4.3: Sketch on the propagation of Cherenkov radiation. The shown spherical waves are caused by the electric field of a charged particle traversing a dielectric medium with a velocity exceeding the speed of light in the medium. For $v > c/n$ a wavefront is formed, that is propagating in the direction determined by the Cherenkov angle θ_C.

with n the refractive index of the medium and $\beta = v/c$ the particle velocity over the vacuum speed of light. The threshold velocity for Cherenkov radiation is therefore

$$\beta_{\mathrm{th}} = \frac{1}{n}\,. \tag{4.4}$$

From this follows that the radiation will only occur for particle velocities that exceed the speed of light in the medium ($v > c/n$) and for refractive indices $n > 1$ (which covers the optical region for most media). The maximum Cherenkov angle is given for $\beta = 1$:

$$\cos\theta_{\mathrm{C\,max}} = \frac{1}{n}\,. \tag{4.5}$$

4.3 Cherenkov radiation by air showers

The condition for Cherenkov light emission can be translated into a condition for the energy of the charged particle as a function of its rest mass m_0:

$$E_{\mathrm{th}} = \frac{m_0 c^2}{\sqrt{1 - n^{-2}}}\,. \tag{4.6}$$

From this equation follows that electrons and positrons with their comparatively small masses govern the Cherenkov light emission in air showers.

A γ-ray induced air shower starts roughly at the point of first interaction ($\approx 20 - 25$ km altitude) and extends down to several km. The cumulative Cherenkov light of the air shower electrons and positrons forms a thin disk traversing the atmosphere along the shower axis. Since the Cherenkov angle θ_{C} is a function of the refractive index n, the characteristic emission angle increases as the particles move deeper into the atmosphere (the refractive index n rises with decreasing altitude). At the shower maximum ($\approx$ 10 km altitude), the common characteristic Cherenkov angle is close to 1° [Hil96]. On ground level (a typical altitude of IACT locations is $\approx$ 2 km due to its proximity to the shower maximum), the Cherenkov light of all emitting regions of a shower superimposes to a nearly uniformly illuminated region, called *Cherenkov light pool*. The lateral distribution of the Cherenkov photon density is shown in fig. 4.4 for a 100 GeV γ-ray air shower. The characteristic hump at $\approx$ 120 m distance from the shower axis arises from the focussing effect of the increasing emission angle. Up to this distance, mainly shower core particles contribute to the Cherenkov light. For higher distances, mainly halo particles contribute to the light emission.

Fig. 4.5 shows the differential photon density inside the Cherenkov light pool at $\approx$ 10 km and $\approx$ 2 km altitude, resulting from γ-ray air showers of varying primary energy. The differential density $\mathrm{d}N/\mathrm{d}\lambda$ is increasing with smaller wavelengths of the Cherenkov light.

The total photon density inside the Cherenkov light pool is proportional to the energy of the primary cosmic ray, since nearly a constant fraction of the primary energy is converted into Cherenkov photons. This correlation is a key feature of

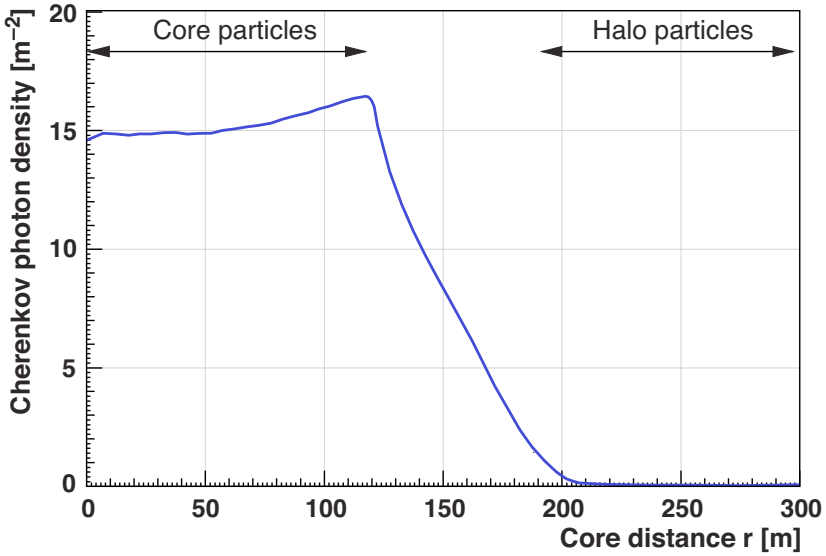

Figure 4.4: Lateral distribution of the Cherenkov photon density at ≈ 2 km altitude for a 100 GeV γ-ray air shower (0° inclination). The dependence of the emission angle on the refractive index and therewith on the altitude leads to an focussing effect (Cherenkov light pool), resulting in a characteristic hump at $r \approx 120$ m. Up to this distance, mainly shower core particles contribute to the Cherenkov light. For higher distances, mainly halo particles contribute to the light emission. Adapted from [Bar98, Wag06].

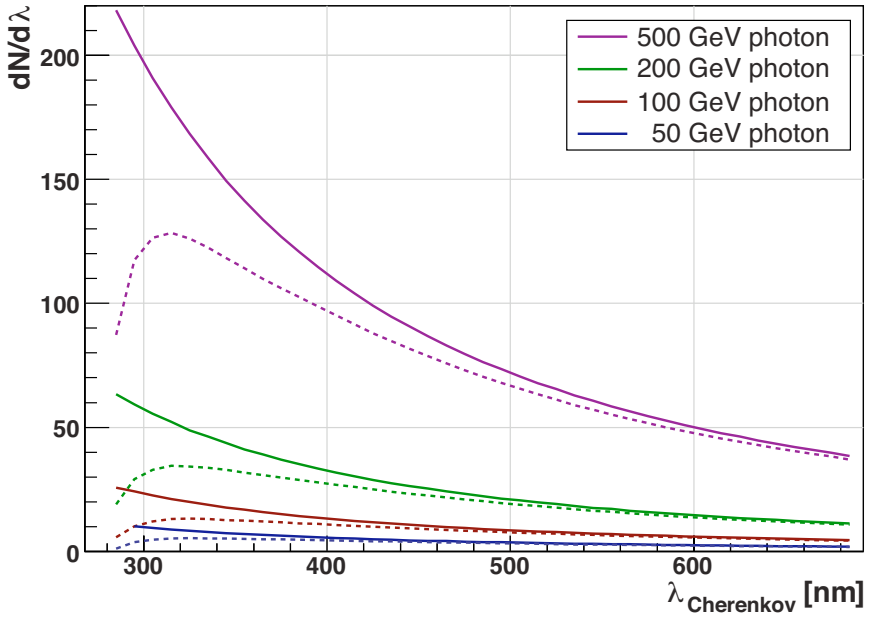

Figure 4.5: Spectra of Cherenkov light emission from air showers induced by γ-rays of varying energy (0° inclination). The solid lines represent the spectra at ≈ 10 km altitude, the dashed lines represent the corresponding spectra at ≈ 2 km altitude, affected by absorption processes. From [Wag06].

the IACT technique: It allows to determine the energy of the primary cosmic ray by measuring the Cherenkov light intensity of the corresponding air shower.

The Cherenkov light induced by cosmic ray air showers underlies several attenuation processes while travelling through the atmosphere. Dominantly, the Cherenkov light is affected by Rayleigh scattering, for which the photons scatter off air molecules ($d < \lambda$). Since the scattering cross section is proportional to λ^{-4}, mainly the high energy part (UV/blue) of the spectrum is significantly attenuated. Also Mie scattering off aerosols ($d \approx \lambda$) has an effect on the Cherenkov light spectrum. The cross section is proportional to $\lambda^{-(1-1.5)}$ and therefore Mie scattering is attenuating the whole Cherenkov photon spectrum. Additionally, light with $\lambda < 280$ nm (UV) is attenuated by absorption of O_3 (ozone) molecules and light with $\lambda > 800$ nm (infrared) is attenuated by absorption by H_2O (water) and CO_2 (carbon dioxide) molecules [Wag06]. All these effects lead to a total attenuation of the Cherenkov light at ground level (2200 m) as shown in fig. 4.5. The resulting spectra peak in the UV/blue wavelengths ($300 - 350$ nm).

The emitted Cherenkov light is very faint: it has a density from 100 to several 100 photons/m^2 for 1 TeV primary γ-ray photon, depending on the altitude [Aha04a]. For these reasons, Cherenkov telescopes must have a large optical reflector and the camera must be sensitive to the corresponding wavelength range. Since the Cherenkov light flash lasts only a few ns at ground level, the read-out system has to be sufficiently fast at the order of ≈ 10 ns.

4.4 Imaging technique

The general setup for stereoscopic IACT observations is shown in fig. 4.6. The imaging is based on a projection of the air shower to the telescope camera (see fig. 4.7). The image in the camera is of elliptical shape and light from the inception of the shower is projected to the head of the image, while light from the ending of the shower is projected to the tail. The image shape gives information on the type of the primary particle (discrimination of γ-ray induced events against background) and its orientation gives information on the arrival direction. The intensity of the shower image is a measure of the primary energy.

The concept of stereoscopic observations is based on simultaneous imaging of air showers in different projections by two IACT telescopes (see fig. 4.6). Compared with monoscopic observations, where the inclination of the shower is inconclusive in the shower-telescope-plane, the stereoscopic concept enables a full determination of the arrival direction with an accuracy of $\approx 0.1°$. In addition, the coincidence trigger of two telescopes and more precise determination of shower attributes enlarge significantly the discrimination power for γ-ray induced events against hadronic background and light of different origin (night sky background). This leads to an improved flux sensitivity compared to single telescope observations. And finally, the improved determination of the shower maximum and shower core position enables to reduce the energy resolution to $15 - 20$ %.

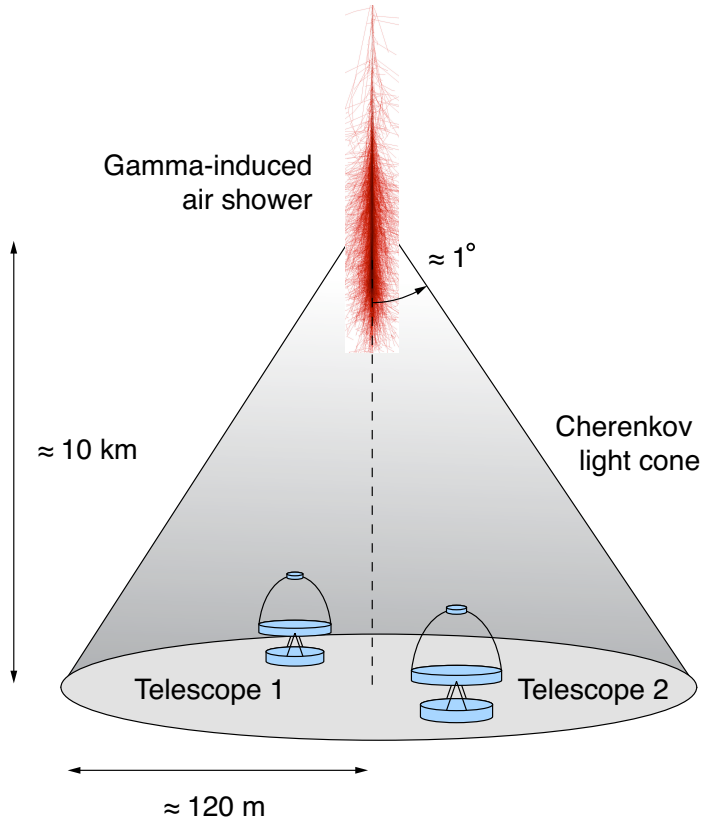

Figure 4.6: Scheme of IACT setup for stereoscopic observations (not to scale). A γ-ray induced air shower starts roughly at the point of first interaction ($\approx 20 - 25$ km altitude) and extends down to several km. At the shower maximum ($\approx$ 10 km altitude), the common characteristic Cherenkov angle is close to 1°. The Cherenkov light pool on the ground has a radius of $\approx$ 120 m at the typical altitude of IACT sites ($\approx$ 2 km).

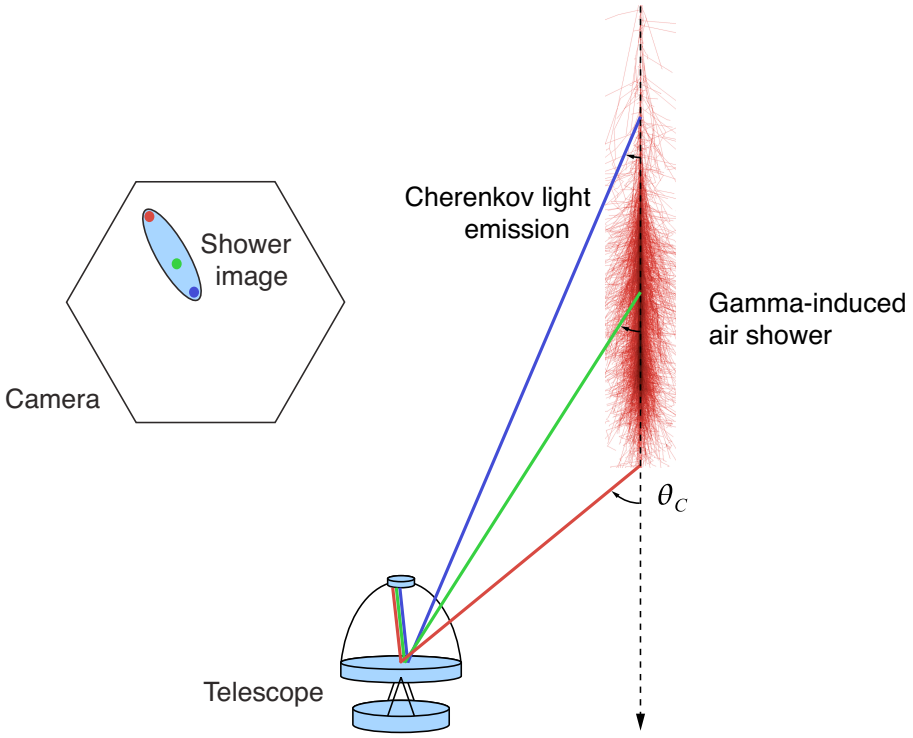

Figure 4.7: Scheme of air-shower projection to the camera of an IACT telescope (not to scale). The Cherenkov light is emitted under the altitude-dependent emission angle θ_C. The image in the camera is of elliptical shape and light from the inception of the shower is projected to the head of the image, while light from the ending of the shower is projected to the tail. Since the projection is not linear, the image is slightly deformed and light from the shower middle is not centred in the image but shifted to the head.

Chapter 5

The MAGIC telescopes

The *Major Atmospheric Gamma-ray Imaging Cherenkov* (MAGIC) telescopes (see fig. 5.1) are a system of two IACT, located at the Canary Island of La Palma at 2200 m a.s.l. The first telescope, MAGIC-I, is in operation since 2004, the second telescope, MAGIC-II, has been successfully commissioned in 2009. Since autumn 2009, regular stereoscopic observations with both telescopes are performed.

In this chapter, the main components of the two telescopes are introduced. Focus is laid on the camera of MAGIC-II and its control software, whose installation and maintenance was a relevant part of this thesis.

5.1 Reflectors

Both MAGIC telescopes, located at a distance of 85 m of each other, are built using a light-weight carbon-fibre structure to provide a mirror dish of 17 m diameter. Each MAGIC telescope has a total weight of 60 tons and a positioning time of only 20 s (180° turn). The camera of each telescope is placed in the focus of the parabolic reflector at a distance of 17 m from the mirror surface.

The reflector of each telescope provides a total mirror area of 236 m^2 (MAGIC-I) and 247 m^2 (MAGIC-II) respectively. The mirror elements have a curved shape to approximate a paraboloid for the total reflector [Dor08]. This parabolic shape preserves the time structure of the shower signal. Each reflector consists of 964 (MAGIC-I) and 247 (MAGIC-II) mirror elements respectively. For MAGIC-I, each element is consisting of a diamond-milled aluminium surface. The point spread function (PSF) of the adjusted MAGIC-I reflector is of $\approx$ 10 mm diameter in the focal plane. For MAGIC-II, two different mirror types are used: 143 mirror elements, placed in the centre of the reflector, consist of diamond-ground aluminium mirrors (as in MAGIC-I). The outer elements of the reflector (104 elements) are made of 2 mm glass plates, stabilised by an aluminium honeycomb structure in between. The reflecting surface itself is made of an aluminium layer. The adjusted reflector of MAGIC-II shows a PSF of $\approx$ 9 mm. The reflectivity of the all-aluminium mirrors is $\approx$ 80 % and for the glass-aluminium mirrors $\approx$ 85 %.

Figure 5.1: The MAGIC telescopes at the Roque de los Muchachos, Canary Island of La Palma. Picture credit: R. M. Wagner.

For both telescopes, an active mirror control (AMC) system compensates for dish formations by adjusting the mirror positions depending on the elevation angle [Bil07]. The focus of both reflectors is at distance of 10 km, where the maximum of γ-ray induced air showers is expected. The pointing position of the telescopes is tracked with a charge-coupled device (CCD) camera (starguider camera), installed at the centre of the mirror dish. With this system, a pointing accuracy of < 1.5 arcmin is achieved [Bre09].

5.2 Cameras

The MAGIC-I camera consists of 577 hexagonal shaped photomultiplier tube (PMT) pixel with an angular size (diameter) of 0.1° in the inner and 0.2° in the outer part of the camera, respectively. The MAGIC-II camera is equipped uniformly with 1039 pixels with an angular size of 0.1°. Both cameras are covering a total field of view of 3.5°.

The PMT of the MAGIC-I telescope are equipped with a wavelength shifter coating to increase the sensitivity in the UV waveband (in which the Cherenkov light of air showers is mainly emitted) and to enhance the quantum efficiency (QE) in the wavelength range $300 - 650$ nm [Geb04]. With this configuration, the MAGIC-I PMT show a QE value of ≈ 30 % at a wavelength of 350 nm (where the Cherenkov light of air showers has its highest intensity) [Bor09]. The MAGIC-II PMT are operated without coating and show a QE value of ≈ 32 %.

In order to observe also under moderate moonlight conditions, the used PMT

of both telescopes are of a six dynode configuration and are operated at a rather low gain (at the order of 10^4). Additionally, the PMT are equipped with hexagonal shaped light guides (*Winston cones* [Win70]) to minimise the dead area between the spherical PMT [Ost00].

The amplified electronic signal of the PMT is converted into an analogue optical signal by a vertical-cavity surface-emitting laser (VCSEL) diode. The light output is transmitted by optical fibres to the counting house, where it is converted back to analogue electronic signals.

In the following subsections, the control program of the MAGIC-II camera is introduced and explained. The implementation of the control program into the central control software of MAGIC and the addition of security routines (to fulfil work safety necessities and to protect the camera against accidental misuse) was an active constituent of this thesis.

5.2.1 MAGIC-II camera control

Each pixel of the MAGIC-II camera consists of a six dynode PMT, a Cockcroft-Walton high voltage (HV) supply, an capacitive (AC) coupled high bandwidth preamplifier to compensate the low gain of the PMT, a vertical-cavity surface-emitting laser (VCSEL) diode to convert the PMT signal into an optical signal to be transmitted by an optical fibre to the counting house, an anode current monitor, a pulse injector, temperature sensors and a monitor diode for the VCSEL light output. The camera electronics is powered by two 5 V power supplies mounted in two boxes placed on the lower part of the camera, outside of the housing. Every seven pixels are grouped in a hexagonal configuration to form one cluster.

The camera is controlled by a slow control cluster processor (SCCP). A SCCP board installed in each cluster controls the operations of the camera and reads several parameters. The HV of each pixel can be set individually and the PMT current, the HV and the temperature at the VCSEL can be continuously monitored. A test-pulse generator board installed in each PMT to test the electrical chain is also controlled at this stage. In addition, the camera control program operates the lids in front of the plexiglas window that protects the PMT and steers the power supplies of the camera.

The SCCP has a flash programmable processor with 12 bits resolution digital-to-analogue converter (DAC) in the voltage range $0 - 1.25$ V and 12 bits resolution analogue-to-digital converter (ADC) in the range $0 - 2.5$ V. Each SCCP board is connected to a VME[1] board in one of the two VME crates in the upper and lower part of the camera.

The VME crates are connected to the camera control PC in the counting house via an optical PCI[2]-to-VME link (see fig. 5.2).

[1] Versa Module Eurocard (VME) is a multi-user bus system widely used in process control applications. It is standardised by the International Electrotechnical Commission (IEC) as ANSI/IEEE 1014-1987.

[2] Peripheral Component Interconnect (PCI) is a bus standard used for attaching hardware

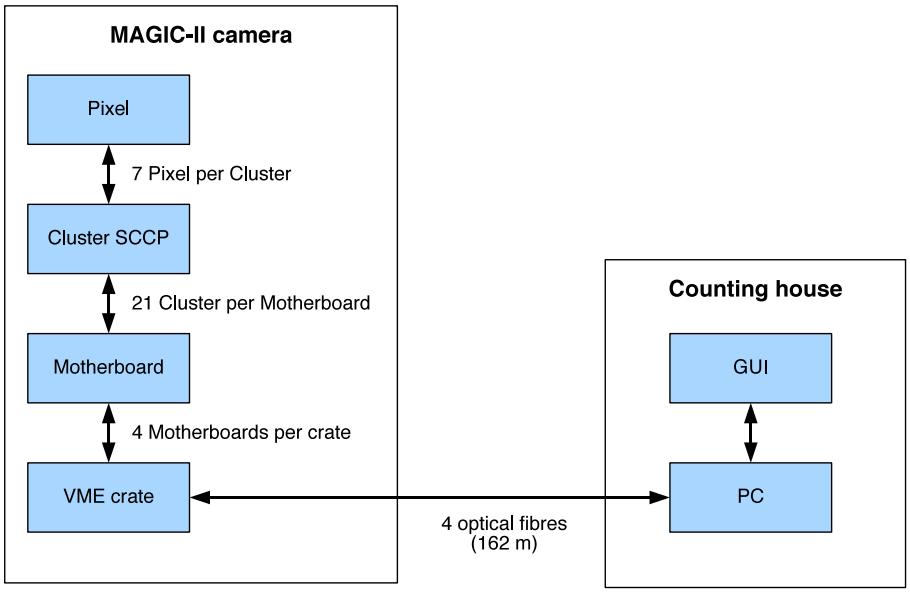

Figure 5.2: Scheme of the MAGIC-II camera control chain. 7 PMT (pixels) are controlled by one Cluster SCCP. 22 Cluster SCCP are connected to a motherboard, 4 motherboards at a time are adjunct to a VME interface crate. 4 optical fibres link the two used VME crates to the control PC.

The camera control program is written in the visual programming language LabVIEW by National Instruments. The main components of the program are the *Central Variables File* and the *Command Control Routine* (see fig. 5.3). User commands can be given either via the graphical user interface (GUI) itself or via the supervising central control program. In addition, the camera control program disposes a security control routine, which checks permanently external and internal parameter and reacts, when necessary, autonomously without any user interaction.

Central Variables File

All available read-out information of each pixel, such as HV, direct current (DC), VCSEL temperature and monitor diode current, and general read-out information about the camera, such as camera temperature and humidity, temperature and humidity of the low voltage (LV) power supply boxes, is written to the *Central Variables File* (see fig. 5.3). It also contains the desired values of the HV, VCSEL bias, attenuators and test pulse generators as given in the user settings together with the lid status and the active mirror control (AMC) and starguider light-emitting diodes (LED) intensity.

The Central Variables File provides the GUI display, the report routine to the supervising central control program and the logbook with the relevant information. Also the *Camera Security Control System* is provided by the Central Variables File.

devices in a computer.

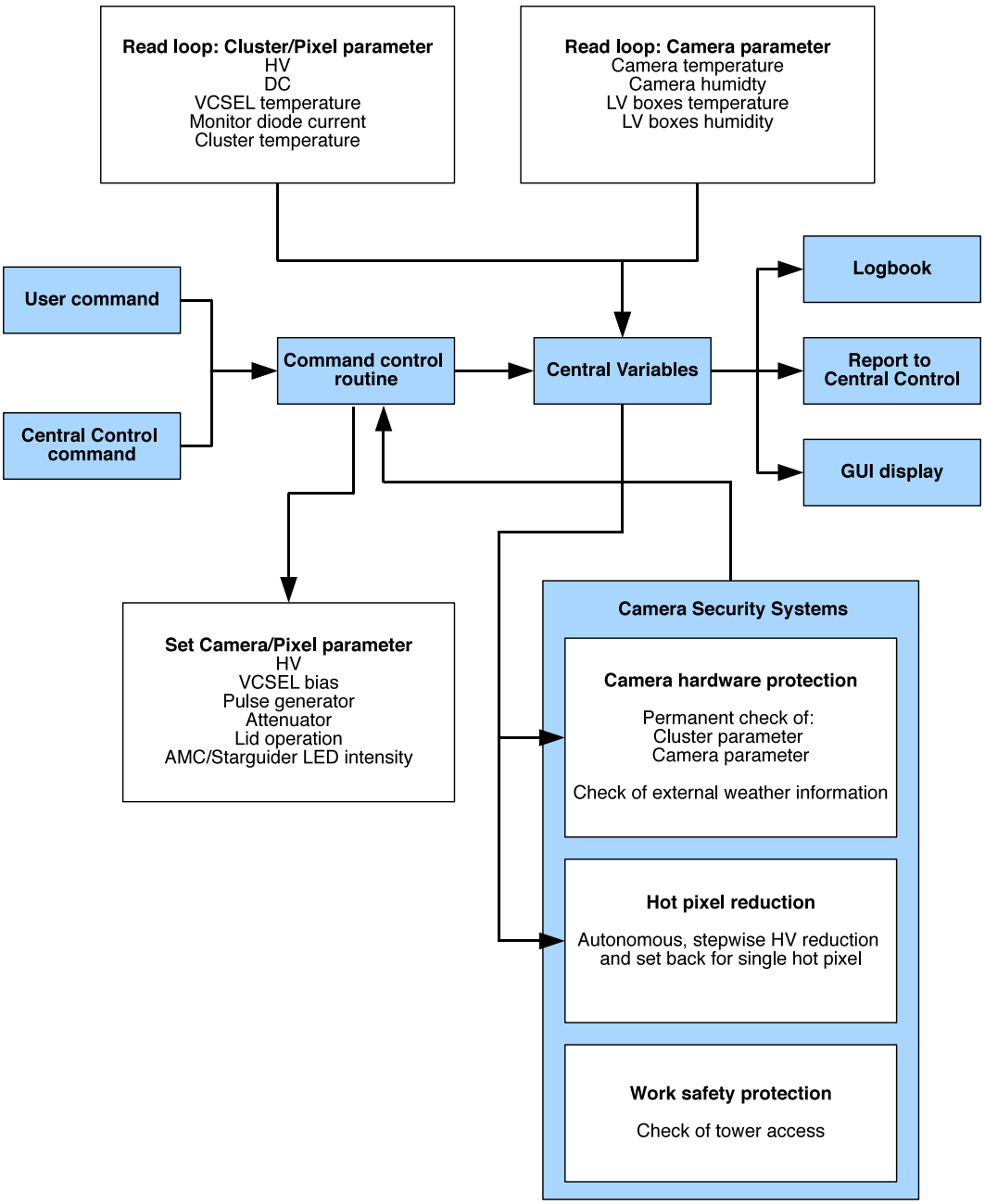

Figure 5.3: Scheme of the MAGIC-II camera control program.

Command Control Routine

The *Command Control Routine* permanently checks the user input and the Camera Security Control System. If any changes are given, the Command Control Routine sets the desired values, such as HV, VCSEL bias, pulse generator, attenuators, AMC or starguider LED intensity, or actions, such as lid operation or switching on/off the LV power supply (see fig. 5.3). In addition, the Command Control Routine writes the new information to the Central Variables File.

Camera Security Control System

The camera control program includes a safety routine, which shall protect the camera from misuse by accidental commands, from bad weather conditions and from hardware errors. This *Security Control System* is permanently checking the pixel and camera parameter and the external weather information, such as wind speed, temperature and humidity. If a parameter exceeds the predefined limits, the Security Control System reacts without any user interaction by sending the necessary commands to the Command Control Routine (see fig. 5.3). For instance, an exceeding windspeed leads to an automatically closing of the camera lids.

Single Hot Pixel Reduction

The *Single Hot Pixel Reduction* is a routine to protect the PMT from light irradiation of high intensity, originating from bright stars in the field of view. It reacts autonomous if the DC current limit (20 μA) is exceeded for a single pixel or a set of pixel for more than 10 s. In this case, an iterative reducing of the HV of the corresponding pixel(s) in steps of 50 V is started. This reducing stops when the DC current is below the limit. The time between the iteration steps is $15 - 25$ s.

Since the relevant stars move in the camera plane with elapsing time, the affected pixels change during the operation. To take this into account, the HV of the reduced pixel(s) will be set back automatically after 15 min (individual counting for each pixel) in iterative steps of 50 V. The set back will stop, when the DC current exceeds the limit again (in this case another waiting time of 15 min is started) or the HV reaches the former starting value (the value before the reduction started).

User input (from the central control program or directly from the camera control program) concerning the HV of the reduced pixel(s) has priority and is therefore overwriting the automatic set back of this/these pixel(s).

Any change of the position of the telescope (change to different wobble position or to another source) will lead to an automatic set back of the HV of the reduced pixel(s) to the former starting value (the value before the reduction started).

An ongoing single hot pixel reaction is stated at the GUI display and the affected pixels are shown on a special list (*HP list*). If necessary, the HV for all the reduced pixels can be set back to the former starting value (the value before the reduction started) by user intervention. Also the routine itself can be stopped

by the user in case of necessity. The alert reaction on the mean DC current is not affected by stopping the single hot pixel routine.

The Single Hot Pixel Reduction is an autonomous circuit protecting the camera hardware with a minimum of interference. The input/output is user-friendly, every step and action of the circuit is displayed. The operator can take over control at every stage of the routine, if necessary. Otherwise the routine will work autonomously without any user interaction.

Automatic working safety circuit

When the tower of MAGIC-II is in access position, the PC control of the camera is disabled automatically. This was introduced to enlarge the safety arrangements for works at the MAGIC-II camera, for instance maintenance works. In this way, accidental activating of the camera, for instance opening the camera lids, can not harm workers in the access tower.

Interaction with the central control program

The global control of the telescope is the supervising central control program. The camera control program is an independent subsystem of the global control chain. User commands given via the central control program are sent to camera control via ASCII[3] text string. This string is processed within the camera control program and leads to the same actions as if the commands were given directly via the camera control GUI interface.

Camera control permanently sends a report string to the central control program out of the Central Variables File. So central control gets all essential information about the camera and is able to sufficiently monitor the camera.

5.2.2 Monitoring of MAGIC-II camera parameters

The permanent reading of camera parameters as described above allows a consequent monitoring of important camera parameters. The PMT used in the MAGIC-II camera have to be operated in a small temperature range to give stable response to Cherenkov light signals. Therefore, the MAGIC-II camera is equipped with a cooling system, providing a constant temperature of 18° C. This cooling system is integrated into the mounting device of the pixels, the so-called *cooling plate*. Also, a too humid camera inside might cause damage due to the high voltage applied to the PMT. Thus, the monitoring of camera temperature and humidity gives vital information for regular operation. For that purpose, 6 temperature and 4 humidity sensors are installed in the MAGIC-II camera.

[3] American Standard Code for Information Interchange (ASCII) is a 7 bit character encoding-scheme used in computers and other communication devices.

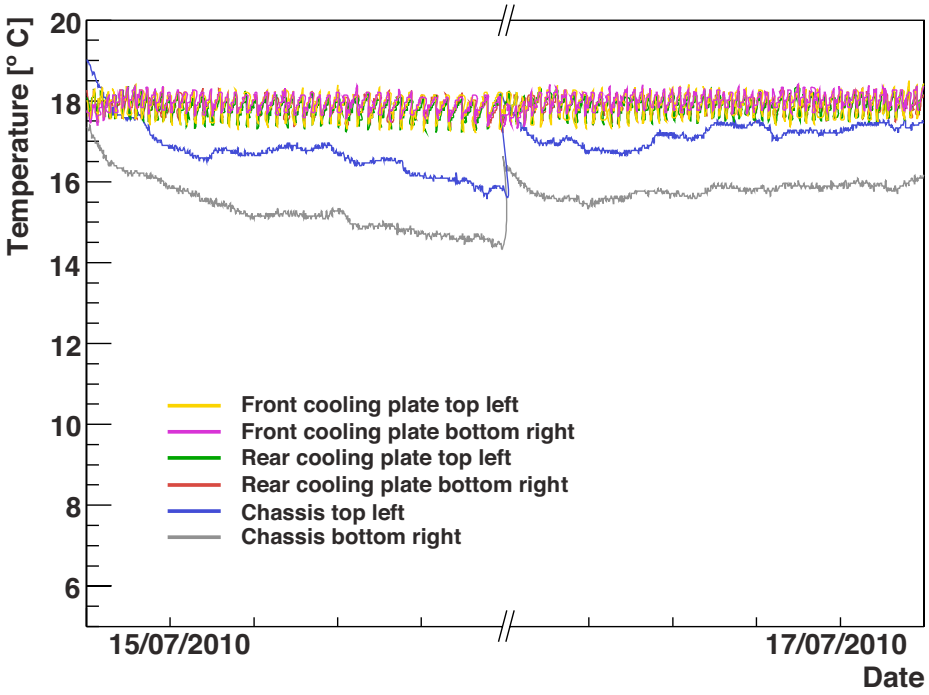

Figure 5.4: MAGIC-II camera temperatures during operation 15/07/2010 – 17/07/2010. These nights represent typical operation conditions during summer. The 4 temperature sensors close to the cooling plate show a stable temperature of $(18 \pm 0.5)^\circ$ C, which represents the nominal cooling temperature of 18° C. The switching on and off of the cooling system is indicated by the regular up and down of the values of these sensors (saw tooth structure). The sensors located at the rim of the camera chassis show higher temperature variations ($(14 - 18)^\circ$ C, blue and grey lines). These sensors are not close to the cooling plate and therefore the outside temperature has a bigger influence here, also due to thermal connection.

Temperature monitoring

Fig. 5.4 shows the values of the 6 MAGIC-II temperature sensors during operation 15/07/2010 – 17/07/2010. These exemplary nights represent typical operation conditions during summer. The 4 temperature sensors close to the cooling plate show a stable temperature of $(18 \pm 0.5)^\circ$ C, which represents the nominal cooling temperature of 18° C. The switching on and off of the cooling system is indicated by the regular up and down of the values of these sensors (saw tooth structure). The sensors located at the rim of the camera chassis show higher temperature variations ($(14 - 18)^\circ$ C). These sensors are not close to the cooling plate and therefore the outside temperature has a bigger influence here, also due to thermal connection.

Fig. 5.5 shows the MAGIC-II camera temperatures during operation 06/01/2011 – 08/01/2011. These nights represent typical operation conditions during winter. The temperature sensors close to the cooling plate show a stable temperature of $(17 \pm 0.5)^\circ$ C. Due to the reduced outside temperatures in winter,

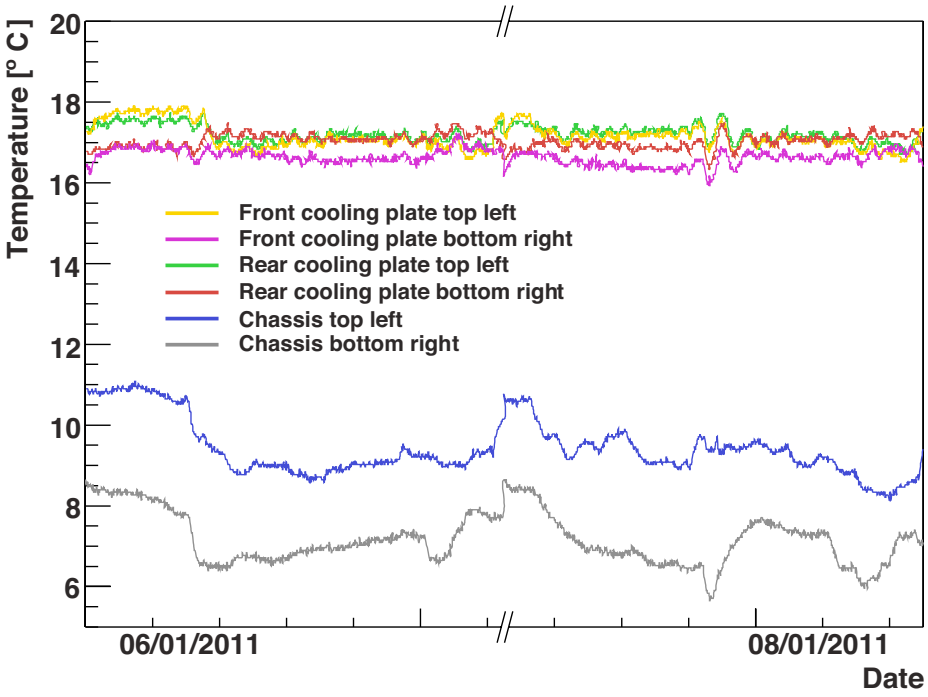

Figure 5.5: MAGIC-II camera temperatures during operation 06/01/2011 – 08/01/2011. These exemplary nights represent typical operation conditions during winter. The temperature sensors close to the cooling plate show a stable temperature of $(17 \pm 0.5)^\circ$ C. Due to the reduced outside temperatures in winter, this value is 1° C lower than the nominal cooling temperature. The low outside temperature is indicated by chassis sensors temperatures (thermal connection), ranging from 5.5° to 11° C.

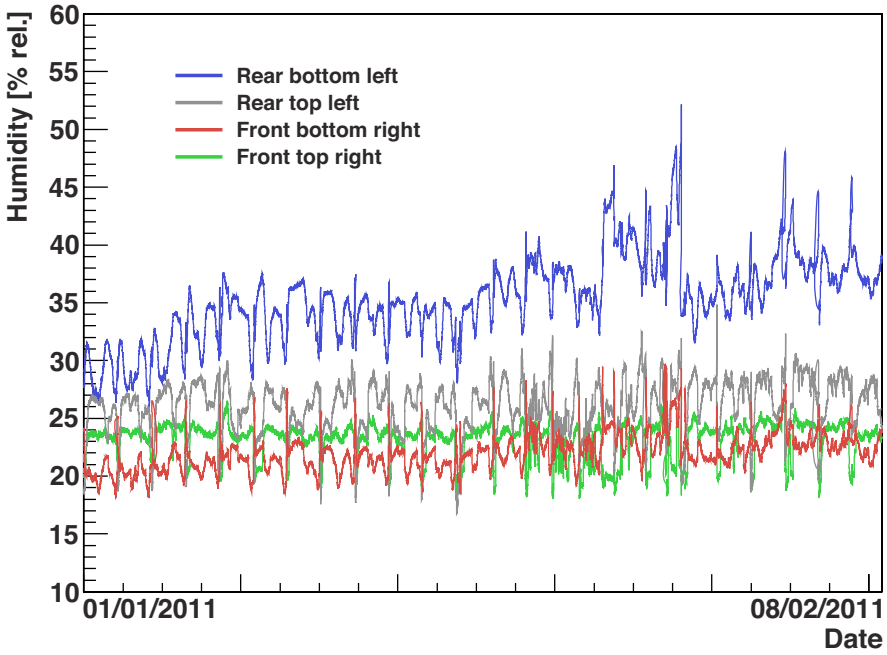

Figure 5.6: MAGIC-II camera humidities during operation nights 01/01/2011 – 08/02/2011. This period represents typical operation conditions during humid winter season. The humidity sensors in the front part and in the top part of the camera show stable values in the range $17 - 30$ % rel. The sensor located at the rear bottom left (blue line) has a higher value compared to the other sensors and shows an increasing humidity during the period. This position in the camera is more affected by low outside temperatures (thermal connection) and condensation water. For all sensors, the deviations originating from nightly switching on and off of the camera can clearly be identified (small-scale up and down behaviour).

this value is 1° C lower than the nominal cooling temperature. The low outside temperature is indicated by the temperatures of the chassis sensors, ranging from 5.5° to 11° C.

In summary, the temperature near the cooling plate and therefore near the technical important components of the PMT is stable in the demanded range of a few ° C around 18° C for both summer and winter conditions.

Humidity monitoring

Fig. 5.6 shows the values of the 4 MAGIC-II humidity sensors during operation 01/01/2011 – 08/02/2011. This exemplary period represents typical operation conditions during humid winter season. The humidity sensors in the front part and in the top part of the camera show stable values in the range $17 - 30$ % rel. The sensor located at the rear bottom left has a higher value compared to the other sensors and shows an increasing humidity during the period. This position in the camera is more affected by low outside temperatures (thermal connection) and condensation water. For all sensors, the deviations originating from nightly

switching on and off of the camera can clearly be identified (small-scale up and down behaviour).

One can conclude that the humidity of the camera is stable near the technical important components of the PMT (HV generation) and does not exceed the operation threshold of 50 % rel. also in humid winter season. Condition is a well closing camera and no brought-in humidity, for instance by opening the camera for maintenance during high outside humidity.

5.3 Trigger system

The trigger area of the MAGIC-I telescope covers an inner camera section of radius 0.95°, whereas the trigger area of MAGIC-II has a size of 1.25°. The trigger areas are consisting of a logical combination of 19 overlapping macro-cells, each containing 37 pixel. A different distribution of macro-cells leads to the increased trigger area size of MAGIC-II (factor 1.7) and results in an increased sensitivity. The configuration of the trigger cells are shown in fig. 5.7.

In the stereoscopic mode, only events triggering both telescopes are recorded. As trigger condition for the individual telescope serves the so-called 3NN trigger: Each telescope must have 3 pixels above a certain threshold (level-0 trigger) in a compact next-neighbour (NN) topology in order to become a telescope trigger (level-1 trigger). The stereo trigger makes a time coincidence between both telescopes with respect to the delay due to the relative position of the telescopes and their pointing direction. The individual telescope trigger rates are of the order of several kHz, the stereo trigger rate lies in the range of $150 - 200$ Hz with a few Hz being accidental triggers [Car11].

5.4 Data acquisition (DAQ) system

The data acquisition (DAQ) system of MAGIC-I is based on multiplexed flash analogue-to-digital converter (FADC). One FADC is successively digitising 16 read-out channels, for each of them the signals are delayed corresponding to their read-out order [Goe07]. For MAGIC-II, Domino Ring Sampler 2 (DRS2 [Rit04]) chips are used to store the analogue signals before digitisation. This multi-capacitor buffer is read out when positive trigger feedback is given and the signals are digitised by a 12-bit analogue-to-digital converter (ADC). The maximum rate of the data acquisition is ≈ 150 MByte/s, corresponding to an event rate of 1 kHz [Tes09].

5.5 Calibration

In order to convert the read-out values from the FADC (MAGIC-I) and DRS2 ADC (MAGIC-II) into number of photoelectrons (phe), corresponding conversion factors have to be obtained from dedicated calibration procedures: In MAGIC-I, three different colour light-emitting diodes (LED, emitting at 370 nm, 460 nm

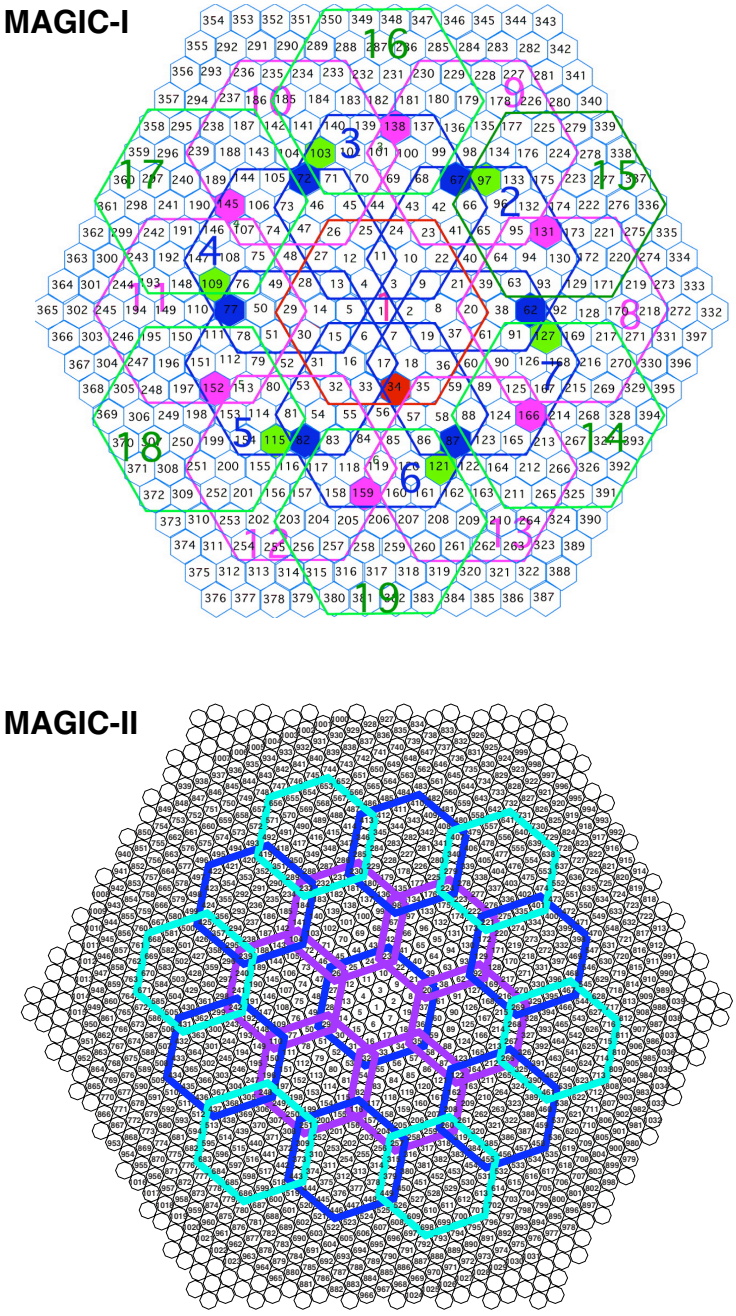

Figure 5.7: Trigger cells for the MAGIC-I (at top) and MAGIC-II (at bottom) telescope camera. The camera size is not to scale, since for MAGIC-I only the inner part including the 577 0.1° pixel (PMT) is shown, while for MAGIC-II the complete camera with its 1039 0.1° pixel (PMT) is depicted. The trigger areas are consisting of a logical combination of 19 overlapping macro-cells, each containing 37 pixel. The trigger area of MAGIC-I has a size 0.95°, the one of MAGIC-II has a size of 1.25°. A different distribution of macro-cells leads to the increased trigger area size of MAGIC-II (factor 1.7) and results in an increased sensitivity.

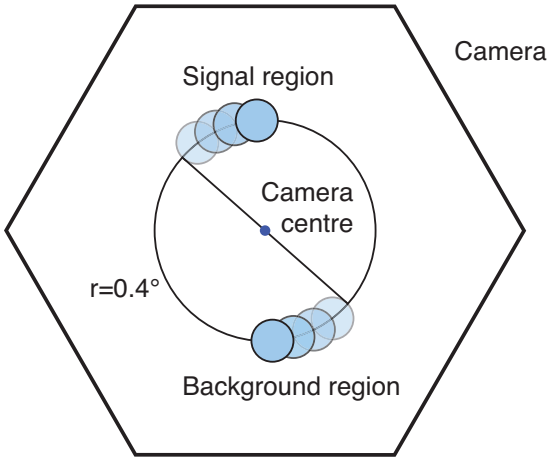

Figure 5.8: Sketch for the wobble observation mode. Two points 0.4° off the source and at opposite direction are tracked alternately with the camera centre for 20 min. The signal region is moving on a ring with radius $r = 0.4°$ from the camera centre. The corresponding background control region is rotated by 180°.

and 520 nm) are used to uniformly illuminate the camera with ultrafast pulses ($3-4$ ns FWHM) in different intensities. In MAGIC-II, a Nd-YAG laser[4] operated at 3$^{\text{rd}}$ harmonic (355 nm) in combination with several filters is used to produce fast pulses (700 ps), covering the full dynamic range of the PMT. An integrated Ulbricht sphere diffuses the laser emission to uniformly illuminate the camera. By measuring the deviations in the PMT signals from a Poisson distribution (the number of phe obtained from the LED pulses is expected to follow Poisson statistics), the number of phe corresponding to a certain signal amplitude can be estimated (*excess noise factor* or *F-factor* method). Details on the calibration, performed during dedicated time slots (calibration runs) as well as during regular data taking (interleaved calibration), can be found in [Gau05] and [Bor09].

5.6 Observation mode

The data taking for this thesis was performed in the so-called *false source* or *wobble* mode. In this observation mode, two points 0.4° off the source and at opposite direction are tracked alternately with the camera centre for 20 min [Fom94, Dau97]. The signal region is moving on a ring with radius $r = 0.4°$ from the camera centre (see fig. 5.8). The corresponding data for the background control analysis are taken from the same dataset, but 180° rotated with respect to the camera centre. The changing of the source position every 20 min, and therefore also the changing of the background position, compensates for possible camera inhomogeneities. The two wobble positions are denoted as *wobble 1* and *wobble 2*.

[4] A Nd-YAG laser is a solid-state laser using a neodymium-doped yttrium aluminium garnet ($Nd:Y_3Al_5O_{12}$) crystal as emitting medium.

Chapter 6

The MAGIC analysis chain

The standard analysis of MAGIC data uses a package of ROOT-based [Bru97] programs written in C++, called MARS (MAGIC Analysis and Reconstruction software). The analysis chain is divided into several steps, each of which is performed by an independent program which takes as input the output of one or more of the previous stages [Lom11, Mor09]. In this chapter, these analysis steps are introduced.

6.1 Signal extraction and calibration

For extracting the signal of each camera pixel, an integration around the peak of a cubic spline built from the raw digitized pulse is applied (after subtraction of pedestal offsets). Since the pixels show differences in gain, the signals are equalised in a flatfielding procedure. Additionally, the arrival time of the pulse is determined as the position of the rising edge of the spline at 50 % of the peak value. Relative offsets are introduced to correct for deviations. The corresponding correction numbers are calculated from dedicated pedestal and calibration events, obtained from calibration runs or during regular data taking (interleaved). To convert the signal amplitudes into a physical meaningful unit (number of photo electrons, phe), the F-factor method is applied for absolute calibration (see sec. 5.5) [Mor09].

6.2 Image cleaning

After the calibration, an image cleaning procedure is applied in order to select only that pixels, which contain Cherenkov light. In this procedure, the pixels of an image have to fulfil certain criteria: Firstly, their signal amplitude has to be above a lower threshold of 6 phe (MAGIC-I) and 9 phe (MAGIC-II) respectively. Secondly, these pixels have to have at least one next-neighbour pixel above the same threshold in a time coincidence of 1.5 ns. Pixels fulfilling these conditions are called shower core pixels. Additionally, adjacent pixels (so-called boundary pixels) are allowed to pass into further analysis if their signal amplitude is above

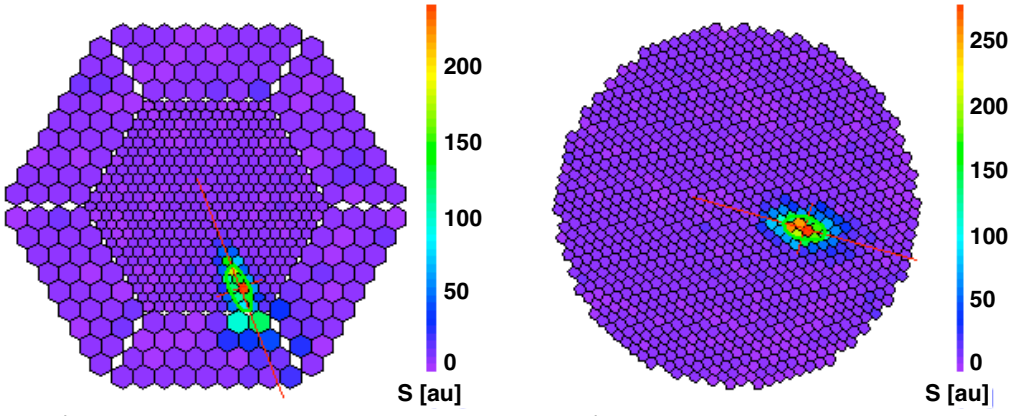

Figure 6.1: Typical stereo γ-ray shower image in MAGIC-I (left) and MAGIC-II (right) camera. The signal (S) is linearly colour coded in arbitrary units (au) and the shower main axes are indicated by red lines. The different sets of photomultiplier tubes are also represented (see sec. 5.2).

a lower threshold of 3 phe (MAGIC-I) and 4.5 phe (MAGIC-II) respectively. The arrival time of the boundary pixels must be within 4.5 ns of the mean arrival time of the core pixels [Lom11]. Fig. 6.1 shows a typical image of a γ-ray induced air shower, as obtained with the MAGIC-I and MAGIC-II cameras after image cleaning.

6.3 Parametrisation

The basis for the analysis and interpretation of shower images is the set of *Hillas* parameters calculated from the second moments of an image [Hil85]. These parameters, itemized below, are used for event discrimination and reconstruction. The reference frame for calculating the Hillas parameters is a two dimensional coordinate frame (x- and y-axis) in the camera plane with the nominal source position as origin.

The first moments of a shower image are defined as:

$$\overline{x} = \frac{\sum_i q_i \cdot x_i}{\sum_i q_i} \tag{6.1}$$

with q_i the charge of the pixel i and x_i its x-coordinate in the camera frame. With analogue denomination:

$$\overline{y} = \frac{\sum_i q_i \cdot y_i}{\sum_i q_i} \tag{6.2}$$

$$\overline{x^2} = \frac{\sum_i q_i \cdot x_i^2}{\sum_i q_i} \tag{6.3}$$

$$\overline{y^2} = \frac{\sum_i q_i \cdot y_i^2}{\sum_i q_i} \tag{6.4}$$

$$\overline{xy} = \frac{\sum_i q_i \cdot x_i \cdot y_i}{\sum_i q_i} \,. \tag{6.5}$$

The pair $(\overline{x}, \overline{y})$ is called centre of gravity (CoG) of the shower image. It corresponds to the position of the weighted mean signal along the x-axis and y-axis of the camera frame, respectively. For the variances (second moments) holds:

$$\sigma_x^2 = \overline{(x - \overline{x})^2} = \overline{x^2} - \overline{x}^2 \tag{6.6}$$

$$\sigma_y^2 = \overline{(y - \overline{y})^2} = \overline{y^2} - \overline{y}^2 \tag{6.7}$$

$$\sigma_{xy} = \overline{(x - \overline{x})\,(y - \overline{y})^2} = \overline{xy} - \overline{x} \cdot \overline{y} \,. \tag{6.8}$$

The Hillas parameters are now given by:

- *Size:* Total charge contained in the image, defined as

$$Size = \sum_i q_i \,. \tag{6.9}$$

  The *Size* is roughly proportional to the primary particle energy for a given impact parameter.

- *Length:* RMS value of the photon distribution along the major image axis, defined as

$$Length = \sqrt{\frac{\sigma_x^2 + \sigma_y^2 + z}{2}} \tag{6.10}$$

  with $z = ((\sigma_y^2 - \sigma_x^2)^2 + 4\sigma_{xy})^{1/2}$. For a given *Size*, the *Length* is smaller (on average) for γ-ray images than for hadronic images and therefore provides strong discrimination power.

- *Width:* RMS value of the photon distribution along the minor image axis, defined as

$$Width = \sqrt{\frac{\sigma_x^2 + \sigma_y^2 - z}{2}} \,. \tag{6.11}$$

  Like the *Length*, the *Width* is on average smaller for γ-ray images than for hadronic images (for a given *Size*). This is due to the smaller average transverse momentum in the pure electromagnetic shower induced by γ-ray photons. Therefore, the discrimination power of the *Width* is also strong.

- *Conc(n):* Set of concentration parameters defined as ratio between the total charge of n pixels with the strongest signal and the total charge of the image (*Size*):

$$Conc(n) = \frac{\sum_{j=1}^{n} q_j}{\sum_i q_i} = \frac{\sum_{j=1}^{n} q_j}{Size} \tag{6.12}$$

with j indicating the n pixels with the strongest signal and i indicating all pixels of the image. This parameter is also used for discrimination, since γ-ray induced showers show a higher light concentration (higher *Conc(n)*) than hadronic showers.

- *Distance:* Angular distance between CoG of the image and nominal source position, defined as
$$Distance = \sqrt{\overline{x}^2 + \overline{y}^2}\,. \tag{6.13}$$
This parameter is a measure for the impact parameter of the shower event and is used for improving the energy estimation of the primary particle.

- *Leakage(n):* Ratio between the charge in the n outermost pixel rings of the camera and the total charge of the image (*Size*):
$$Leakage(n) = \frac{\sum_{j=1}^{k} q_j}{\sum_i q_i} = \frac{\sum_{j=1}^{k} q_j}{Size} \tag{6.14}$$
with j indicating the k pixels of the n outermost pixel rings and i indicating all pixels of the image. This parameter is used to reject events, for which significant parts of the image lie outside the camera. Particularly for large shower images (high energy events), this rejection improves the reliability of the energy estimation.

A scheme of the parameter definitions is shown in fig.6.2.

6.4 Data quality selection

Data runs to be used in the analysis have to fulfil several quality criteria. If one or more of these criteria are not fulfilled, the corresponding data are discarded. The main quality parameter is the stereo trigger rate, for which optimal values are in the range $150 - 200$ Hz (see sec. 5.3). The cut parameter for this work was the stereo trigger rate after a *Size*-cut of 100, denoted as $Rate_{100}$. Due to the *Size*-cut, the values of this parameter are reduced but more stable compared to the standard stereo trigger rate. Data subruns with $Rate_{100}$ values of $55 - 105$ Hz were generally accepted for this work (a subrun is the smallest unit within the data acquisition (DAQ) and refers to a few minutes observation time, according to the DAQ rate). Additionally, each accepted subrun has to show a $Rate_{100}$ value within a $\pm 15\%$ range around the mean value of the individual observation (exemplarily shown for the Markarian (Mrk) 421 observation 14/01/2010 in fig. 6.3). Lower trigger rates can be brought about by bad weather conditions or hardware problems of the detector. Reasons for a higher trigger rate can be bright stars in the field of view, moonlight or passing cars. The differences in the $Rate_{100}$ values between the telescopes originate from different image cleaning procedures (see sec. 6.2). This results in different *Size* distributions for the telescopes, leading to different event distributions above a certain *Size* value.

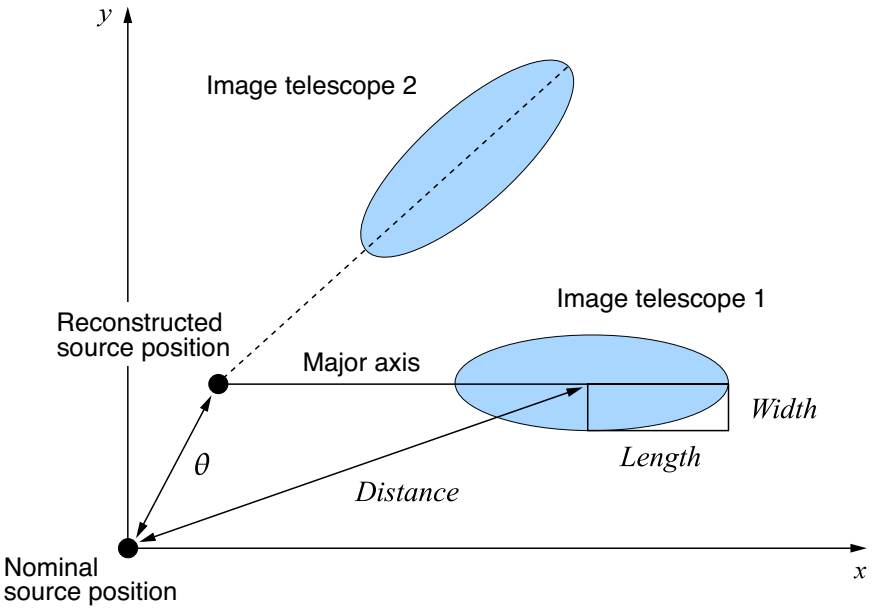

Figure 6.2: Definition of the basic Hillas parameters for a γ-ray image: *Width*, *Length*, *Distance*. Shown is also the image from the second telescope to illustrate the geometrical-based source position reconstruction. The angular distance of nominal and reconstructed position is called θ.

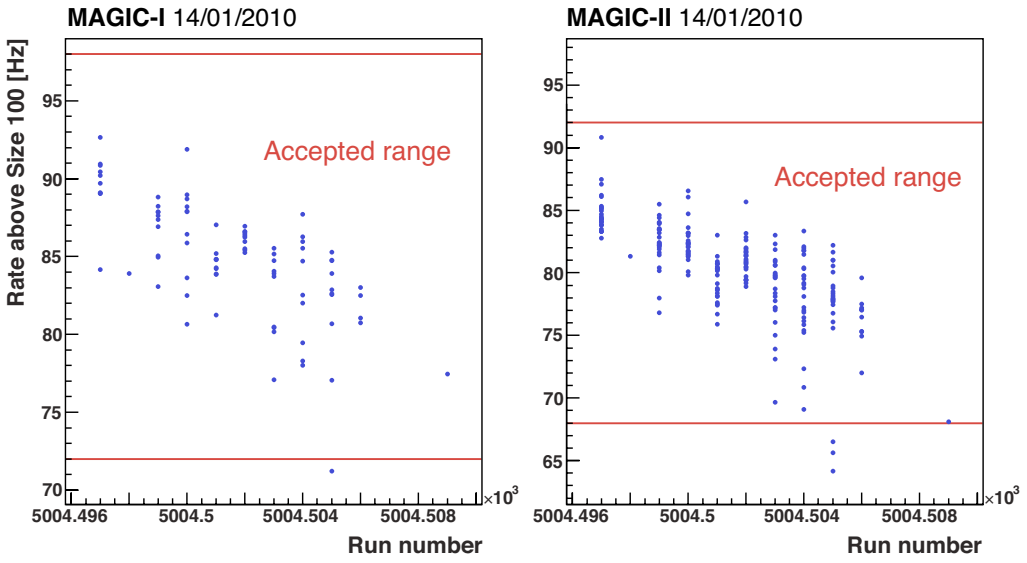

Figure 6.3: Application of $Rate_{100}$ cut (stereo trigger rate of each telescope above $Size$=100) exemplarily shown on Mrk 421 14/01/2010 observation. Each dot depicts the $Rate_{100}$ value of one subrun. The mean rate is (84.9 ± 0.4) Hz for MAGIC-I and (80.3 ± 0.3) Hz for MAGIC-II, resulting in an $Rate_{100}$ acceptance range of $72 - 98$ Hz (MAGIC-I) and $68 - 92$ Hz (MAGIC-II). The red lines depict the upper and lower limit. Differences in the $Rate_{100}$ values between the telescopes originate from different image cleaning procedures (see sec. 6.2). Note that different *Size* cuts are used for the signal analysis.

Additionally, a parameter describing the amount of clouds in the sky, called *Cloudiness*, is used for quality selection. It is defined as $Cloudiness = a\,T_{\mathrm{sky}} - P_6(\mathrm{ZA}) - b\,H - c\,T_{\mathrm{air}}$, with T_{sky} the sky temperature measured by a pyrometer, $P_6(\mathrm{ZA})$ a factor regarding the zenith angle (ZA) of the observation and H the humidity and T_{air} the air temperature at telescope level. The normalisation constants a, b and c are empirical and describe the influence of each addend. Data subruns with Cloudiness < 50 were accepted. Also the number of identified stars in the field of view of the observation is used as quality selection parameter. Typically, the number of identified stars is ≈ 20 (depending on the star field). Data subruns with a number of identified stars < 15 were discarded, pointing to a significantly reduced integral transmission of the atmosphere.

6.5 Stereo parameters

After the parametrisation of the individual telescope images, the two separate telescope data streams are merged into one single data file, containing the stereo events with the information of the two telescopes. Additionally, a set of stereo parameters is attributed to the combined stereo event, using the main axis and centroid position of both telescope images: *Impact* (reconstructed distance from each telescope to the shower axis in the plane perpendicular to the shower axis) and *MaxHeight* (reconstructed height of the shower maximum above the telescopes) [Car11]. Compared to the monoscopic observation, the *Impact* parameter significantly improves the energy reconstruction and the *MaxHeight* parameter increases the background rejection. Particularly for the rejection of muon induced showers at low distance above the telescope (< 4 km), which have a similar image distribution as low energy γ-ray events, the *MaxHeight* parameter is important and increases the sensitivity of the system at low energies.

For reconstructing the direction of the primary particle, the crossing point of the main axes of the shower images is combined with the DISP method [Les01]. While the crossing point of the axes is a pure geometrical result, the DISP parameter (distance from the shower image centre to the estimated source position) is obtained from a random forest (RF) classification method [Alb08b]. The corresponding DISP-RF is trained on Monte-Carlo (MC) datasets of simulated γ-ray events. The DISP method delivers one individual estimation of the DISP parameter for each telescope. The combination of the geometrical information from the axes crossing point plus the two estimations from the DISP method provides a unique source position estimation or rejects the event if the individual positions do not agree, which provides additional background rejection [Car11].

The angular distance between nominal and reconstructed source position of the event is called θ and is defined as

$$\theta = \sqrt{x_0^2 + y_0^2} \tag{6.15}$$

with x_0 and y_0 the coordinates of the reconstructed source position. This param-

eter is also shown in fig. 6.2. For convenience, the squared angular distance (θ^2) is used in the signal determination, since the θ^2 distribution is flat for background events[1] and shows a peak at $\theta^2 = 0$ for signal events from the nominal source position.

6.6 Separation between γ-ray and hadron induced showers

In MARS, the separation between γ-ray and hadron induced shower images is based on a random forest (RF) classification method [Alb08b]. This algorithm uses the image parameters from each telescope (*Size*, *Length*, *Width*, *Conc(n)*) as well as the stereo parameters (*Impact*, *MaxHeight*) and timing information to create one single parameter called *Hadronness*. Its value ranges from 0 to 1, for which 0 represents an ideal γ-like event and 1 represents an ideal hadron-like event. This parameter is used to separate γ- from hadron-like events by a dedicated *Hadronness*-cut (see sec. 6.9).

The RF classification is trained on MC datasets of simulated γ-ray events and real MAGIC data without a dedicated γ-ray source and therefore containing exclusively background events.

6.7 Energy reconstruction

The energy reconstruction is based on the direct proportionality of the event energy and the number of secondary particles at the maximum of the corresponding air shower. In MARS, an atmospheric model is used for computing the amount of light produced from an incident γ-ray of given energy for given zenith angle. MC simulated events are then used to fill look-up tables with the information of the simulated event energy, E_{true}, and the corresponding parameters *Size*, *Impact* and *MaxHeight*. The energy of a real event is then calculated individually for each telescope using these MC tables. The final energy estimation, E_{est}, is the weighted average value obtained from both telescopes.

The energy resolution can be calculated as the standard deviation of the $(E_{\mathrm{est}} - E_{\mathrm{true}})/E_{\mathrm{true}}$ distribution of MC simulated γ-ray events. In the medium energy range (from 300 GeV to 2 TeV), the energy resolution is as good as 16 %. For higher energies (above 2 TeV), it slightly worsens ($\lesssim 20$ %) due to the large fraction of truncated images, showers with high *Impact* parameters and worse statistics in the training sample. At low energies (below 300 GeV), the energy resolution also slightly worsens ($\lesssim 24$ %), here due to lower photon numbers, higher relative noise, and worse estimation of the arrival direction, which spoils the precision of the *Impact* parameter reconstruction [Ale11a].

[1] For a homogeneous distribution of N background events in a circle of radius θ around the nominal source position ($\mathrm{d}N = k_1\, 2\pi\, \theta \mathrm{d}\theta$) holds: $\mathrm{d}N/\mathrm{d}\theta^2 = k_2$, with k_1 and k_2 being constants.

6.8 Calculation of Spectra and Lightcurves

The spectrum (differential flux) is defined as:

$$\frac{\mathrm{d}F\,(E)}{\mathrm{d}E} = \frac{\mathrm{d}N_\gamma}{\mathrm{d}E\,\mathrm{d}A_{\mathrm{eff}}\,\mathrm{d}t_{\mathrm{obs}}} \tag{6.16}$$

with N_γ the number of excess events, A_{eff} the effective area and t_{obs} the effective observation time. N_γ is given by the direct measurement of γ-ray events, A_{eff} is obtained from MC simulation and t_{obs} from the arrival time distribution from all measured events (see below).

The effective area A_{eff} characterises the detection efficiency of the telescopes. It is calculated by MC simulated γ-ray events, the so-called test sample. In this sample, γ-rays of various energy are simulated homogeneously in a circular area of radius r. The simulated γ-rays undergo the same signal analysis chain and signal cuts as real data events. A_{eff} is then obtained from the ratio of triggered, cut surviving events $N_{\mathrm{MC\,signal}}$ to the total number of simulated events $N_{\mathrm{MC\,all}}$:

$$A_{\mathrm{eff}} = \pi r^2 \frac{N_{\mathrm{MC\,signal}}}{N_{\mathrm{MC\,all}}}\,. \tag{6.17}$$

A_{eff} depends on technical quantities (trigger efficiency, mirror reflectivity and field of view) and on observation-typical quantities (zenith angle), which enter the simulation. Fig. 6.4 shows typical values of the effective area as a function of estimated energy. Due to the little amount of Cherenkov light for low energy events and therefore a low trigger probability, A_{eff} shows a steep rise at low energies. This gives a limitation to the accuracy of flux calculations in that energy region: A small offset in the estimated energy can lead to a huge error in the value for A_{eff}.

The effective observation time t_{obs} is obtained by fitting an exponential function to the arrival time distribution. The arrival time Δt is defined as the time difference between two successive events. The distribution follows an exponential decrease of the following form:

$$\frac{\mathrm{d}N}{\mathrm{d}t} = k\,e^{-\,r\,t} \tag{6.18}$$

with N the number of events and k a constant. The fit parameter r is called signal rate. Fig. 6.5 shows a typical arrival time distribution. The effective observation time is then calculated from the exponential fit parameter r:

$$t_{\mathrm{obs}} = \frac{N_{\mathrm{total}}}{r} \tag{6.19}$$

with N_{total} the total number of events.

The integral flux is defined as:

$$F\,(E > E_0) = \int_{E_0}^{\infty} \frac{\mathrm{d}F\,(E)}{\mathrm{d}E}\mathrm{d}E = \int_{E_0}^{\infty} \frac{\mathrm{d}N_\gamma}{\mathrm{d}E\,\mathrm{d}A_{\mathrm{eff}}\,\mathrm{d}t_{\mathrm{obs}}}\mathrm{d}E \tag{6.20}$$

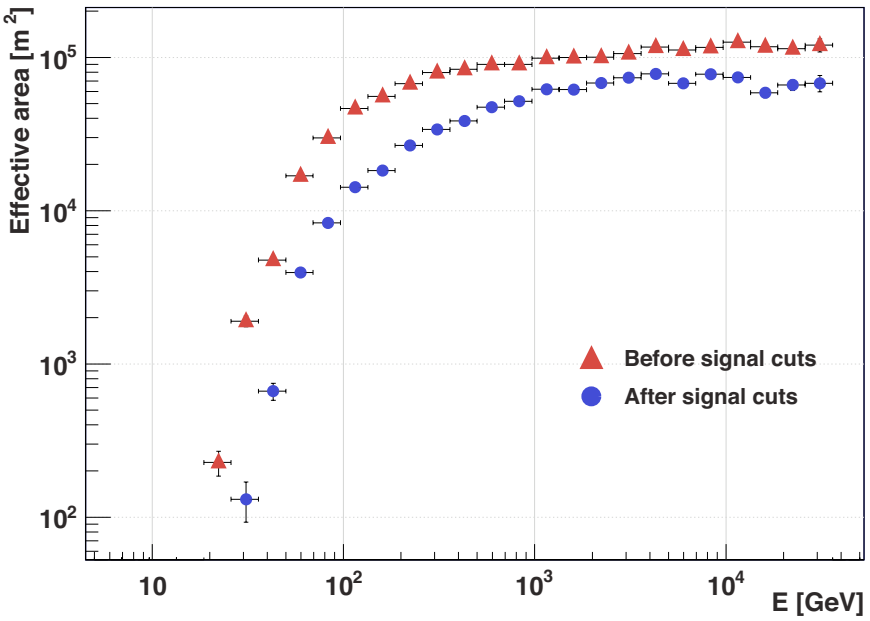

Figure 6.4: Typical values of the effective area A_{eff} as a function of estimated energy. A_{eff} is shown before and after applying signal separation cuts (see sec. 6.9) to the MC test sample. For low energies, the effective area shows huge differences between adjacent energy bins (steep rise). The shown sample was used for the analysis of Mrk 421 14/01/2010 data, average zenith angle of this sample is 18°.

with E_0 the energy above which the integral flux is calculated. The representation of $F(E > E_0)$ versus time is called *lightcurve*.

Since the integral flux is calculated as an integration of all energies above E_0, A_{eff} can not be represented in energy bins anymore (as done for the differential flux). For this reason, A_{eff} is calculated as an average effective area for events with an assumed power law spectrum with spectral index of -2.2. Therefore, the selection of E_0 becomes important: The systematic uncertainty of a lightcurve is dominated by the uncertainty of the events and A_{eff} at the lowest energies. To avoid huge errors in the integral flux, E_0 can not be set arbitrary low. To guarantee reliable results, $E_0 = 200$ GeV was chosen for this work.

6.9 Signal cuts

The cuts on the data sample used to discriminate signal from background are called signal cuts and refer to cuts in *Hadronness* and θ^2. The expression "tight cuts" describes *Hadronness*- and θ^2-cuts close to 0, i.e. close to the ideal values for γ-ray events from the aimed source. The expression "loose cuts" describes cuts far away from the ideal value 0. The selection of the signal cuts has a significant relevance: Too loose signal cuts result in a bad background discrimination and therefore a bad significance for a signal. If the signal cuts are too tight, the statistical significance

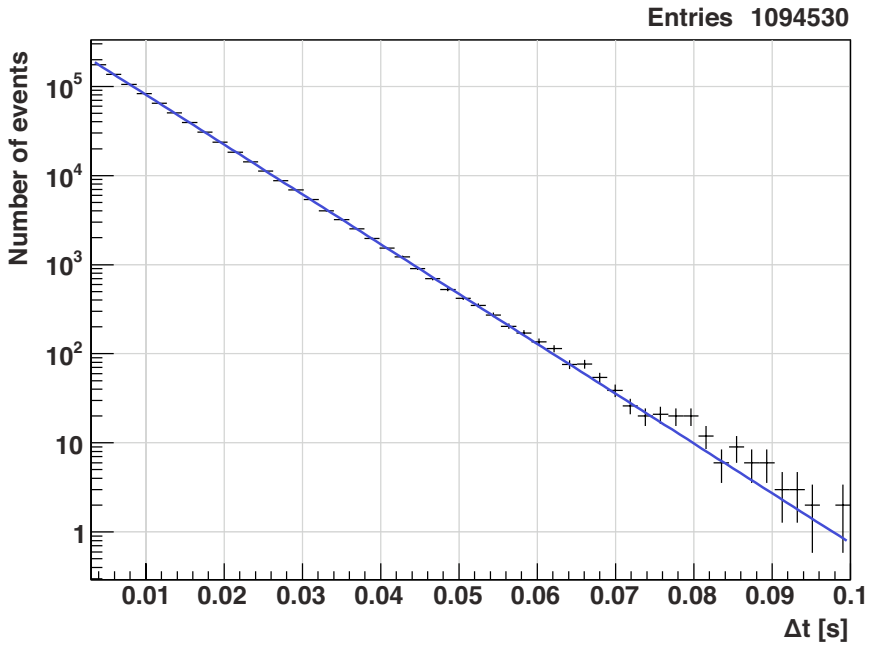

Figure 6.5: Typical arrival time distribution (logarithmic y-axis). The arrival time Δt is defined as the time difference between two successive events. From the exponential fit (blue line) the effective observation time t_{obs} is calculated using eq. 6.19. The shown arrival time distribution was obtained from Mrk 421 14/01/2010 data.

may be good, but the systematic error in A_{eff} may rise due to possible differences between the MC simulated γ-ray events (used to calculate A_{eff}, see sec. 6.8) and real data. Too tight signal cuts will identify only that events as γ-ray induced, which look most similar to the MC simulated events. So the dependence on the MC simulation rises with tightening the signal cuts. The way to find the right set of signal cuts is calibration on a well known source. For this work, the signal cuts were optimised on data of the Crab nebula (see chapter 8). This set of cuts was then applied to the Mrk 421 data.

In the next-to-last step of the MARS analysis chain, the signal cuts are applied to the data sample and the effective area A_{eff} and the effective observation time t_{obs} are calculated. With this information, a preliminary spectrum of the signal in bins of the estimated energy E_{est} and a lightcurve is calculated. To correct the estimated energy of the events for the detector response, a dedicated *unfolding* has to be applied. This procedure is described in the next section.

6.10 Unfolding

Measurements of physical quantities are often systematically distorted due to non-ideal detectors (i.e. biases, finite resolution). The process to correct the measurements for these distortions is called *unfolding*. In the case of the MAGIC telescopes,

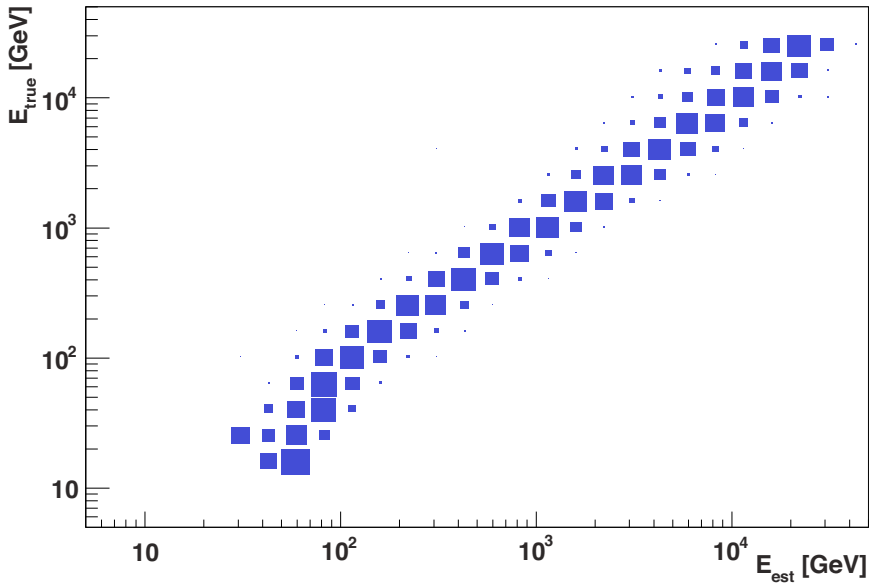

Figure 6.6: Typical migration matrix. The number of MC simulated events is plotted in the plane of estimated energy E_{est} (calculated energy after the standard analysis process) and true energy E_{true} (initial simulated energy). The migration matrix is is used in the unfolding process as quantity for the detector response. The shown migration matrix was derived for the analysis of Mrk 421 14/01/2010 data.

the distorted quantity is the estimated energy of each event. Here, the unfolding is needed to derive the correct distribution of events in true energy out of the distribution in estimated energy.

The measured distribution $Y(y)$ of events as a function of estimated energy is given by

$$Y(y) = \int M(x,y)\ S(x) \tag{6.21}$$

with $M(x,y)$ the detector response and $S(x)$ the true distribution as a function of true energy. In matrix notation this quotes:

$$Y = M \times S\,. \tag{6.22}$$

The goal of the unfolding process is to derive S from a given Y and M. M, called *migration matrix*, is obtained from MC simulations: Simulated events undergo the same analysis process as real events (see sections above). Then, these events are filled in a two-dimensional histogram with the basis of estimated energy (calculated within the analysis process) and true energy (the initial simulated energy). A typical migration matrix is shown in fig. 6.6.

For the unfolding process itself exist various approaches. The most obvious solution is to invert the matrix M, called *deconvolution*. This is technically correct, but often does not lead to useful results: Large correlations between adjacent bins of the migration matrix imply large fluctuations of their contents. Other

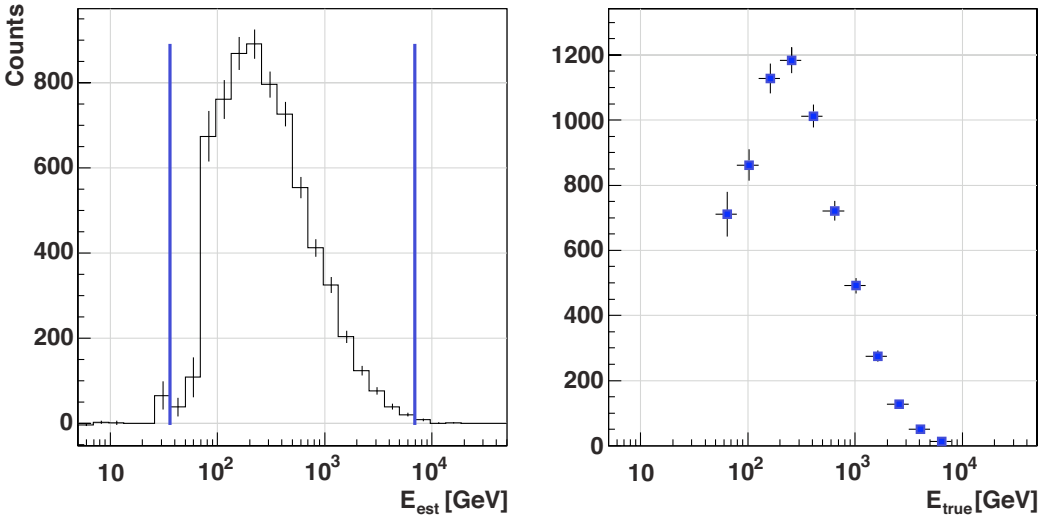

Figure 6.7: Typical quantities of the unfolding process: measured event distribution as a function of estimated energy E_{est} (left) and unfolded event distribution as a function of true energy E_{true} (right). The blue vertical lines represent the unfolding limits in E_{est}. The shown quantities were derived from the analysis of Mrk 421 14/01/2010 data.

approaches aim to avoid this effect. The most common approaches are methods with *regularisation*. Here two additional parameters are introduced: χ^2_0, describing the degree of agreement between $M \times S$ and Y, and Reg, describing the smoothness of S. The solution for S is then found by minimizing the expression

$$\chi^2 = \frac{w}{2} \times \chi^2_0 + Reg\,. \tag{6.23}$$

The fixed parameter w is called regularisation parameter and represents the influence of the regularisation. A large w leads to a suppressed regularisation, which results in a noisy unfolded distribution S, but which is perfectly fitting the measured distribution. A small w leads to an overemphasized regularisation: S is smooth, but shows larger deviations from the data. The used unfolding methods in this thesis vary in the determination of the regularisation parameter w and are following the methods by Bertero [Ber89], Schmelling [Sch94] and Tikhonov [Tik79]. Fig. 6.7 shows the measured distribution Y (left) and the unfolded distribution S (right) of events from Mrk 421 14/01/2010 data unfolded with the Tikhonov method. The blue vertical lines in the measured distribution represent the unfolding limits in E_{est} chosen for this particular analysis. For technical details of the implementation to MARS reference is made to [Alb07d].

6.11 Systematic uncertainties

The Earth's atmosphere, as a crucial part of an IACT detector, shows changing conditions, small deviations of the density profile from the one assumed in simu-

lations, as well as non-perfectly known atmospheric transmission. This introduces uncertainties in the absolute energy scale, which are estimated to be $\lesssim 10$ % [Ale11a]. Uncertainties in the amount of light focused by the mirrors are also estimated to produce a systematic error on the energy scale of about ≈ 8 %. Uncertainties in the conversion coefficient of photons to detectable photo electrons are thought to introduce additional systematic errors, as there are uncertainties in the light collection of the Winston cone (≈ 4 %), in the electron collection efficiency of the first PMT dynode (≈ 5 %), in the PMT quantum efficiency (≈ 4 %) and finally in the F-factor value of the PMT calibration (≈ 10 %, see sec. 5.5) [Ale11a].

A $\approx 6 - 8$ % systematic error on the energy scale and event rate can be introduced by the flatfielding procedure, which is performed to homogenise the camera response and is equalising the product of the quantum efficiency of the PMT for the wavelength of the calibration light pulser with the gain of the PMT-FADC chain. Non-linearities in the analogue signal chain and the small residual non-linearity of the DRS2 chip can produce a systematic uncertainty of about 0.04 in the index of power-law formed energy spectra. The deadtime of the read out (≈ 10 %, corrected in the analysis) leads to a negligible systematic error ($\lesssim 1$ %) on the effective observation time [Ale11a].

Also mispointing of one or both telescopes can influence the analysis. The typical mispointing of the individual MAGIC telescopes is $\lesssim 0.02°$ [Bre09]. One can conclude from MC simulations that the corresponding systematic error on the γ-ray efficiency is $\lesssim 4$ % [Ale11a].

Discrepancies between data and MC introduce a slight dependence of the reconstructed spectra on the applied signal cuts ($\lesssim 15$ % at energies below 300 GeV, $\lesssim 10$ % at energies above 300 GeV). Also the unfolding procedures (see sec. 6.10) are introducing systematic uncertainties in the indices of power law form spectra of the order of 0.1 [Alb07d].

Uncertainties introduced by the overlap of the non-circular trigger regions of the two telescopes are studied and discussed in detail in chapter 7.

In summary, the total systematic uncertainty in the absolute energy scale is found (by muon calibration and intertelescope cross-calibration) to be ≈ 17 % at energies below 300 GeV and ≈ 15 % at energies above 300 GeV respectively. The total systematic uncertainty in the slope of power law form energy spectra is estimated to be 0.15. At energies below 300 GeV, the total error on the flux normalisation (without the energy scale uncertainty) is estimated to be ≈ 19 %, at energies above 300 GeV it is estimated to be ≈ 11 % [Ale11a].

Chapter 7

Stereo trigger inhomogeneity

In 2009, regular data taking of MAGIC was switched from monoscopic to stereoscopic observation strategy. It was an important question, if the observed γ-rate is effected by the new trigger scheme. A detailed study on that question, particular in the Markarian (Mrk) 421 case, is presented in this chapter.

7.1 Appearance of a stereo trigger inhomogeneity

Each MAGIC telescope uses the signal information of a logical combination of camera pixels to trigger on air shower events (level-1 trigger, see sec. 5.3). In the monoscopic observation mode, the level-1 trigger was the last trigger level and lead to event recording. For the stereo system, a new trigger level was introduced: The stereo trigger is a coincidence trigger of the level-1 trigger of the single telescopes. Therefore, it is sensitive to events seen by both telescopes. In consequence, the stereo trigger probability rises for events that take place in an area between the two telescopes (see fig. 7.1). In the camera plane, the centre of gravity (CoG, see sec. 6.3) distribution of triggered events (primarily hadronic background events) becomes asymmetrical and indicates the area of increased trigger probability. This area, called *stereo spot*, is schematically shown in fig. 7.2 for the two MAGIC cameras and different observations (Zd-Az-positions). Additionally, the pointing of the telescopes in the wobble mode (see sec. 5.6) is shown. The CoG of γ-ray events from the source arrange in a ring shape structure around the intended source position. The overlay of this structure with the CoG of all triggered events varies with the source position (wobble 1 and 2) and Zd-Az-position (position of the stereo spot). This means that the same amount of γ-ray events from a source may have different trigger probabilities, depending on the geometrical conditions. This may lead to a deviation of the observed γ-rate and therefore to a misinterpretation of flux levels.

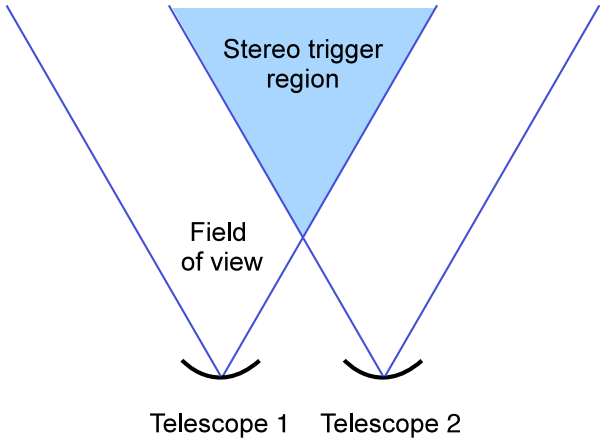

Figure 7.1: Scheme of the stereo trigger region (not to scale). The stereo trigger is a coincidence trigger of the single telescope trigger (level-1). In consequence it is sensitive to events seen by both telescopes, i.e. that are situated in an area between the two telescopes.

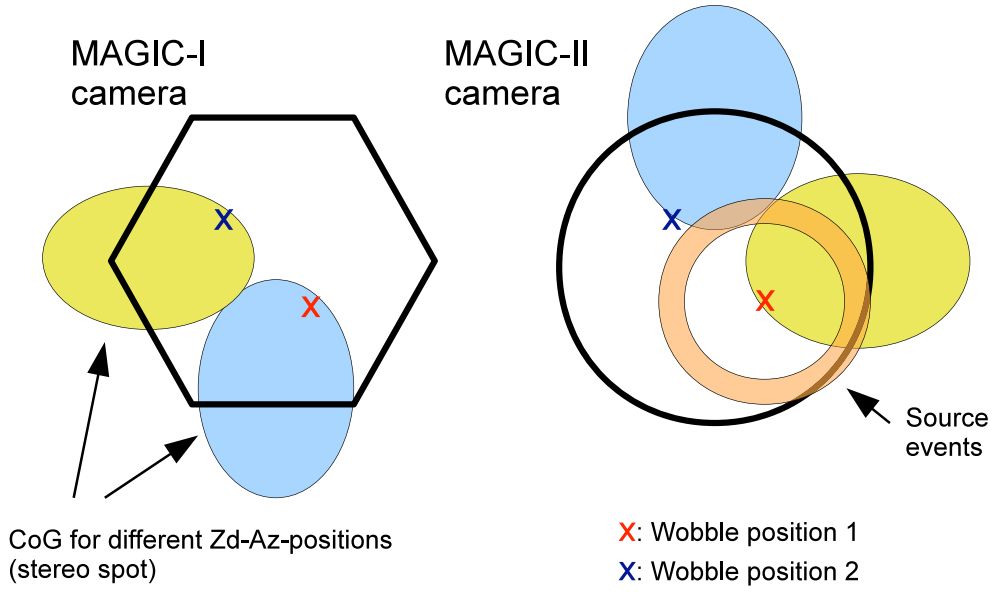

Figure 7.2: Scheme of the stereo trigger inhomogeneity (not to scale). Illustrated are the centre of gravity (CoG) distributions of all triggered events (primarily hadronic background), indicating the areas of increased trigger probability (*stereo spot*). Shown are the stereo spot areas for the two MAGIC cameras and different observations (Zd-Az-positions), corresponding areas are indicated by same colour. Additionally, the pointing of the telescopes in the wobble mode is shown. The CoG of γ-ray events from a source arrange in a ring-shaped structure around the intended source position. The overlay of this structure with the CoG of all triggered events varies with the source position (wobble 1 and 2) and Zd-Az-position (position of the stereo spot).

	Wobble 1	Wobble 2
$E_\gamma < 200$ GeV	2.6 ± 0.2	4.6 ± 0.4
$E_\gamma > 200$ GeV	4.5 ± 0.4	4.7 ± 0.3

Table 7.1: γ-rates (γ-ray events per minute) for Crab nebula observations on 13/11/2009 – 15/11/2009 (Zd-range $(6-30)^\circ$), broken down by wobble position and γ-ray energy below and above 200 GeV (signal cuts: *Hadronness* < 0.3 and $\theta^2 < 0.02$). For energies below 200 GeV, the γ-rates differ significantly for the two wobble positions.

7.2 Methodology of test

To study the effect of the trigger inhomogeneity, the following tests were performed: Firstly, possible γ-rate variations were studied on data with source signal. For this, datasets from the Crab nebula (see sec. 8) and Mrk 421 were broken down by wobble position and γ-ray energy. In this way, γ-rate variations can be associated to certain observation conditions. Secondly, the influence of the background positions (wobble positions) was studied on a dedicated dataset without source signal. In this way, the contribution of the background estimation can be separated from the contribution of the source signal.

7.3 Test on Crab nebula November 2009 data

Fig. 7.3 shows the CoG of all triggered events (E > 50 GeV, no *Hadronness*- and θ^2-cut) for Crab nebula observations on 13/11/2009 – 15/11/2009. The observations covered the entire Zd-range $(6-30)^\circ$ (the culmination of the Crab nebula is at 6°). The total effective observation time was 190 min, the wobble positions were $+035^\circ$ (wobble 1) and $+215^\circ$ (wobble 2) in camera coordinates. The corresponding stereo γ-rates (γ-ray events per minute) are listed in tab. 7.1. For γ-ray energies above 200 GeV, the γ-rates of the two wobble positions are similar. But for energies below 200 GeV, the rates differ significantly.

7.4 Test on Mrk 421 January 2010 data

Fig. 7.4 shows the CoG of all triggered events (E > 50 GeV, no *Hadronness*- and θ^2-cut) for a Mrk 421 observation on 14/01/2010. The observation covered the entire Zd-range $(8-30)^\circ$ (the culmination of Mrk 421 is at 8°). The total effective observation time was 156 min, the flux level was ≈ 2.7 Crab units (see sec. 9.3). The wobble positions were 0° (wobble 1) and $+180^\circ$ (wobble 2). The corresponding stereo γ-rates are listed in tab. 7.2. In contrast to the Crab observations presented above, the γ-rates do not differ for the two wobble positions. The differences between the rates below and above 200 GeV can be explained by the spectral behaviour of Mrk 421 for that particular flare activity (see sec. 9.5).

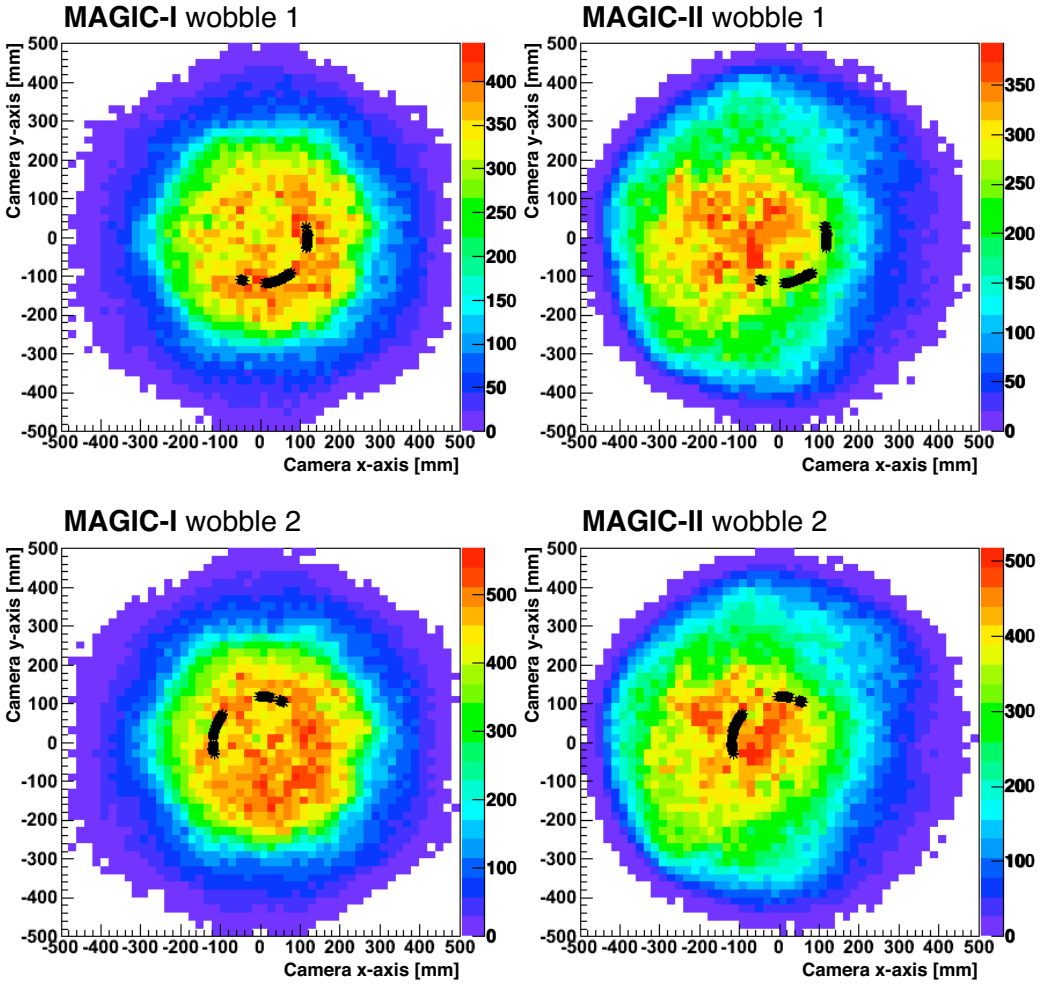

Figure 7.3: CoG distribution of all triggered events for Crab nebula observations on 13/11/2009 – 15/11/2009 (Zd-range $(6-30)^\circ$, 190 min total effective observation time, E $>$ 50 GeV, no *Hadronness*- and θ^2-cut). Additionally, the source positions during the observation are marked (black stars). For the MAGIC-II camera, wobble position 1 is more outlying the CoG spot (stereo spot) than wobble position 2. This might explain the reduced γ-rate in this position.

	Wobble 1	Wobble 2
$E_\gamma < 200$ GeV	7.4 ± 0.3	7.9 ± 0.3
$E_\gamma > 200$ GeV	11.3 ± 0.4	11.3 ± 0.5

Table 7.2: γ-rates for a Mrk 421 observation on 14/01/2010 (Zd-range $(8-30)^\circ$), broken down by wobble position and γ-ray energy below and above 200 GeV (signal cuts: *Hadronness* < 0.3 and $\theta^2 < 0.02$).

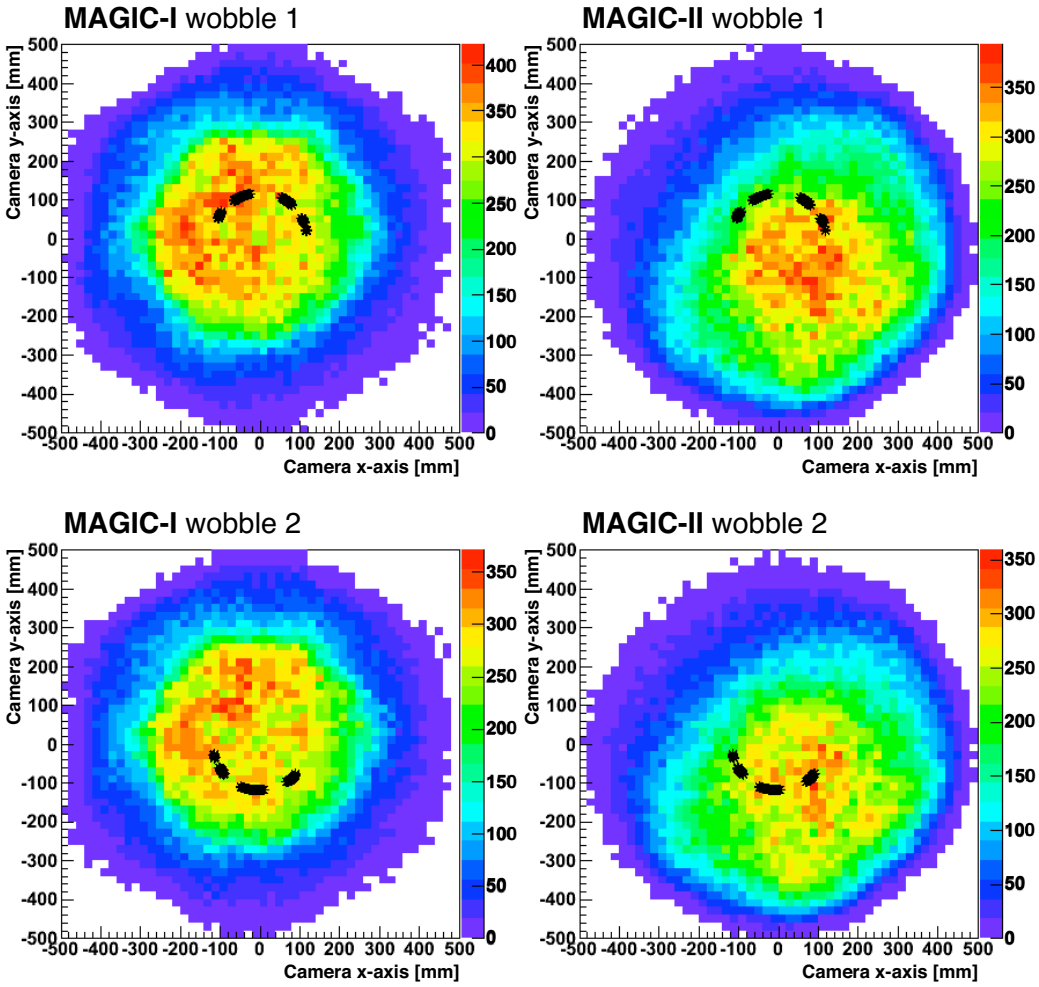

Figure 7.4: CoG distribution of all triggered events for a Mrk 421 observation on 14/01/2010 (Zd-range $(8-30)^\circ$, 156 min total effective observation time, E $>$ 50 GeV, no *Hadronness*- and θ^2-cut). Additionally, the source positions during the observation are marked (black stars). In contrast to the Crab observations, the γ-rates do not differ for the two wobble positions.

7.5 Comparison of tests

For the Crab nebula observations the γ-rates differ for energies below 200 GeV, while they do not differ for the Mrk 421 observations. The explanation for this behaviour is in the geometrical condition for the two observations: In the Crab case, the two wobble positions were situated in camera areas of different trigger sensitivity (see fig. 7.3). While the source was observed in wobble position 1, the corresponding background was taken in wobble position 2 and vice versa. Wobble position 1, situated at the edge of the stereo spot, has a reduced trigger probability, while wobble position 2, situated within the stereo spot, has an increased trigger probability. This leads to a reduced number of observed events in wobble position 1 in combination with an increased number of background events taken in wobble position 2. In total, both effects add up and decrease the γ-rate for wobble position 1. When the source was observed in wobble position 2 and the background was taken in wobble position 1, the geometrical condition had the opposite effect: An increased number of observed events in wobble position 2 and a decreased number of background events in wobble position 1. This increases the γ-rate in wobble position 2.

In the Mrk 421 case, both wobble positions were situated in camera regions of similar trigger sensitivity (see fig. 7.4). Here the number of source events and background events were taken in positions of comparable trigger probability and therefore the γ-rates do not differ.

The energy dependence of the trigger inhomogeneity effect is explained by the correlation of primary particle energy and image *Size*: High energy particles have large images in the camera, while low energy particles have small images. Therefore, the overlap of the images of the two telescopes in the stereo trigger region is larger in case of high energy particles, while it is smaller for low energy particles. The threshold at which this effect becomes critical is 200 GeV.

Since the path of a source in the night sky (Zd-Az-position) and the positions of the telescopes are constants, the presented study on the Crab nebula and Mrk 421 γ-rates is valid for all observations of that sources in the studied Zd-range from culmination to 30° and the corresponding Zd-Az-positions. For the Crab nebula, only equal amount of data taken in wobble 1 and wobble 2 guarantees a correct flux estimation below 200 GeV: In that case, the effects demonstrated above cancel out. For Mrk 421 even an unequal number of data taken in the two wobble positions does not lead to wrongly estimated fluxes. This is an important information on calculating differential spectra on short timescales as in this thesis.

7.6 Test on background calculation in different positions

To study the influence of one or more background positions to estimate the background flux for energies below 200 GeV, the following test was performed: A

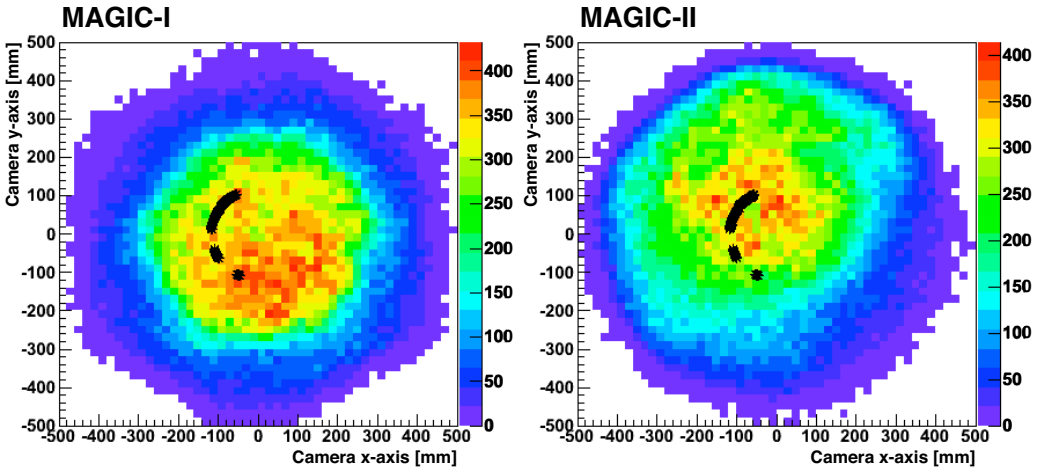

Figure 7.5: CoG distribution of all triggered events for Off dataset 17/11/2009 and 19/11/2009 (78 min total effective observation time, E > 50 GeV, no *Hadronness*- and θ^2-cut). The fake source, declared at +4° in declination from the camera centre, is marked by black stars.

Hadronness-cut	fake source / 1 background	fake source / 3 background	fake source / 1 background normalised	fake source / 3 background normalised
0.1	1.32	1.28	0.97	1.13
0.2	1.20	1.18	0.91	1.04
0.5	1.18	1.11	0.94	0.99
1	1.24	1.14	1.09	1.07

Table 7.3: Signal ratio of fake source and different background positions under varying *Hadronness*-cuts for events with E < 200 GeV.

dataset without a dedicated γ-source was chosen[1] and a "fake" source position was declared at +4° in declination from the camera centre (see fig. 7.5). The chosen dataset was taken on 17/11/2009 and 19/11/2009 and provides 1.3 h of data. In fig. 7.6, the θ^2 distribution of the fake source and 3 different background positions (90°, 180° and 270° with respect to the fake source position) under varying *Hadronness*-cuts is presented for events with energies below 200 GeV. The distributions are not congruent with each other, which is clearly demonstrating the presence of the trigger inhomogeneity. Collecting the events in the θ^2-range $0 - 0.04$ for each position holds the numbers listed in tab. 7.3. Shown is the ra-

[1]These datasets are called "Off"-data and are meant to be used for the analysis of so-called "On"-analysis data, where the source is located at the camera centre, i.e. where signal and background estimation are made from different datasets.

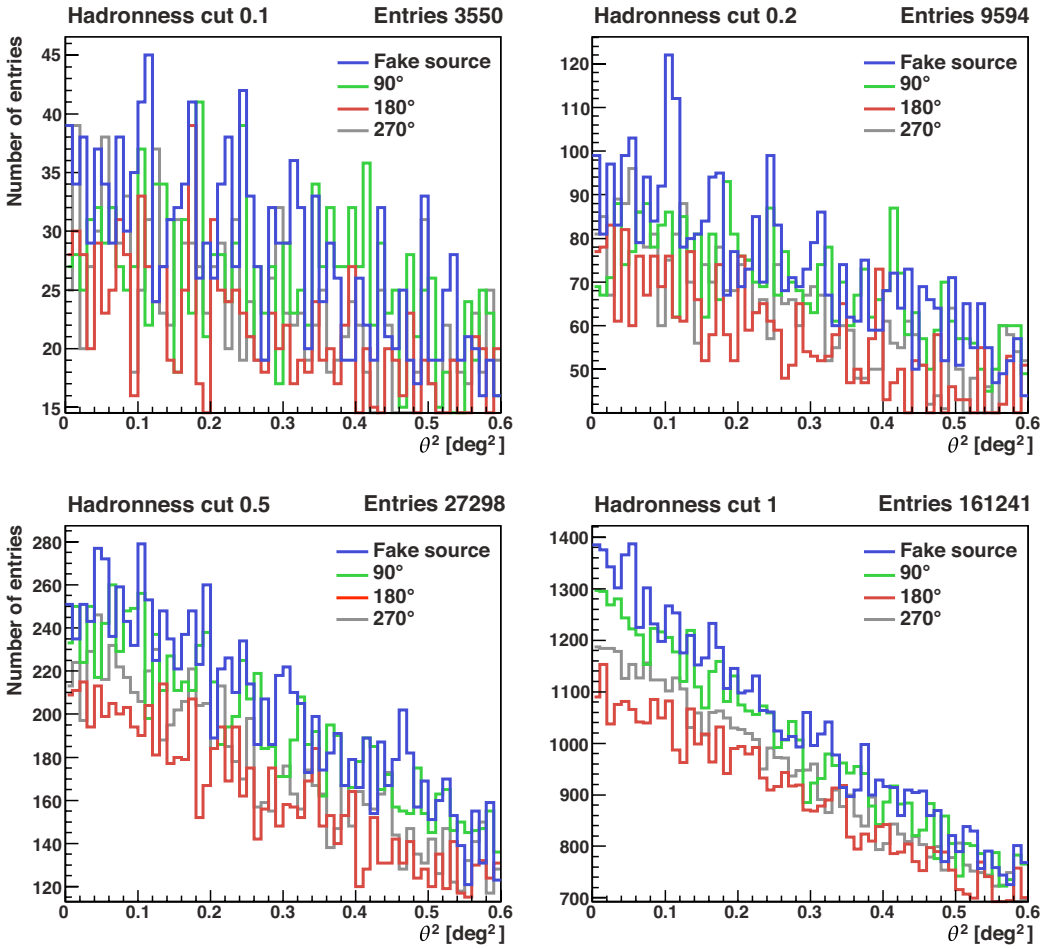

Figure 7.6: θ^2 distribution of the fake source and 3 different background positions (90°, 180° and 270° with respect to the fake source position) under varying *Hadronness*-cuts for events with E $<$ 200 GeV. The distributions are not congruent with each other, demonstrating the trigger inhomogeneity.

Hadronness-cut	σ fake source / 1 background normalised	σ fake source / 3 background normalised
0.1	-0.22	+1.19
0.2	+1.22	+0.59
0.5	+1.42	-0.14
1	4.27	4.30

Table 7.4: Fake detection risk for different background positions under varying *Hadronness*-cuts for events with E $<$ 200 GeV. A signal generated by the trigger inhomogeneity effect is called fake signal. The significance σ is calculated following eq. 17 in [Lia83]. In general, the threshold for a signal detection is 5 σ.

tio between the signal of the fake source and the antisource background position (fake source/1 background) and the ratio of the fake source and the 3 background positions (fake source/3 background) under varying *Hadronness* for events with an energy below 200 GeV. The effect of the trigger inhomogeneity results in an excessive increase of the fake source signal by up to 32 % for a *Hadronness*-cut of 0.1. This effect can be corrected by normalising the background distribution in the θ^2-range $0.1 - 0.5$ with respect to the fake source distribution, the resulting numbers are also listed in tab. 7.3. In this way, the effect can be reduced to max. 13 % for a *Hadronness*-cut of 0.1. This means that signal to background ratios at the order of 10 % might be produced by the trigger inhomogeneity effect.

The important question in this context is about the risk to generate a signal just by the trigger inhomogeneity effect. Such a signal (in absence of a real signal originated by a γ-ray source) is called fake signal, and the significance of a suchlike signal is called fake signal risk. Tab. 7.4 lists the fake signal risk for events with energies below 200 GeV of the above introduced dataset. The significance σ is calculated following eq. 17 in [Lia83]. Since the threshold for a signal detection generally is 5 σ, one can conclude that there is no fake detection risk for reasonable *Hadronness*-cuts well below 1.

7.7 Conclusion

From the above described studies the following conclusions can be drawn:

1. Depending on the Zd-Az-position of an observation, the γ-rates may differ significantly for two different wobble positions. This holds for events with energies E $<$ 200 GeV. Combining exactly the same amount of data from the two wobble positions provides a compensation for this effect. In the case of

Mrk 421, the geometrical condition of the observations prevents in general from the effect of trigger inhomogeneity.

2. The overall scale of the θ^2 distribution varies with different background positions up to $\approx$ 30 % for E $<$ 200 GeV. A correction by normalising with respect to the source distribution reduces this effect to $\approx$ 10 %.

3. There is no fake signal risk as long the signal to background ratio is well above 10 % and a reasonable *Hadronness*-cut well below 1 is applied. In other words: The systematic flux error for energies below 200 GeV is 10 % of the background rate.

Chapter 8

Reference analysis of the Crab nebula

In this chapter, the reference analysis of the Crab nebula – the "standard candle" for IACT – is presented. Such a reference analysis allows to test the analysis chain and to verify the applied signal cuts.

8.1 Crab nebula

The Crab nebula is a remnant of a supernova, which took place in the year 1054 at a distance of ≈ 2 kpc [Col99]. Its central object is a neutron star with a rotation frequency of ≈ 30 Hz (the Crab pulsar). The Crab nebula is one of the best studied non-thermal objects in the night sky, with observations ranging from radio band (10^{-5} eV) to γ-rays ($\approx 10^{14}$ eV) [Alb08a].

Particles accelerated in the pulsar are considered to build up a particle wind moving away from the acceleration region. This acceleration region might be located either near the polar caps of the pulsar (polar cap model, [Stu71, Rud75]) or in the outer regions of the magnetosphere (outer gap model, [Che86, Chi92]). On its way through the ambient medium, the particle wind sweeps up interstellar material until a critical mass is reached and a termination shock is formed. Here, the wind ram pressure balances the total pressure of the nebula. The wind particles are additionally accelerated in the shock and subsequently loose their energy by synchrotron emission [Alb08a]. This synchrotron radiation is dominating the spectrum of the Crab nebula in the radio to X-ray wavebands. The same population of accelerated particles (electrons and positrons) is considered to be responsible for the γ-ray emission by inverse Compton (IC) scattering of soft photons. In the synchrotron self-Compton model (SSC, see sec. 3.1.3), the synchrotron radiation serves as soft photon field for the upscattering. But also other photon fields are believed to contribute to the inverse Compton scattering, such as the cosmic microwave background or far-infrared excess[1] [Aha04b]. Additionally, it is believed that also

[1] The far-infrared excess describes the excess of infrared radiation compared to normal black-

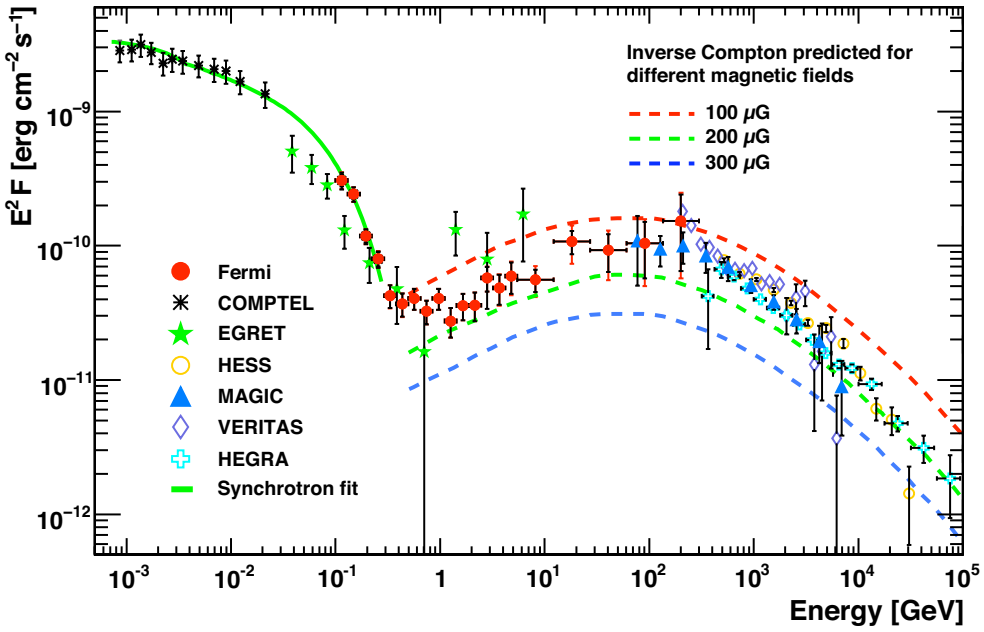

Figure 8.1: Spectral energy distribution (SED) of the Crab nebula from LE to VHE γ-rays. The MAGIC data are monoscopic data from [Alb08a]. The synchrotron component was fitted using the COMPTEL and Fermi LAT data (green line). Predictions of the inverse Compton spectra are overlaid for assuming a synchrotron self-Compton (SSC) model and three different values of the mean magnetic field: 100 μG (dashed red line), 200 μG (dashed green line) and 300 μG (dashed blue line) [Ato96]. From [Abd10b].

the hadronic component of the wind contributes to the VHE γ-ray emission at TeV energies and beyond due to decaying π^0 [Ato96, Bed97a, Bed03].

The Crab nebula, detected in 1989 as the first VHE γ-ray source [Wee89], shows a strong and stable emission of VHE γ-ray photons. Therefore, it became the reference source for all observations using the IACT technique. Fig. 8.1 shows the spectral energy distribution (SED) of the Crab nebula from LE to VHE γ-rays. Clearly, the two components of the considered synchrotron and inverse Compton emission can be seen. Assuming a SSC model (see sec. 3.1.3), the IC component can be modelled as a function of the mean magnetic field.

8.2 Data sample

The data for this reference analysis were taken in November 2009 and January 2010. After applying quality selections (see sec. 6.4), data from 7 nights with a total observation time of 452 min ($\approx$ 7.5 h) were analysed. The zenith angle ranged from 6° to 30°.

body radiation. It is mainly due to circumstellar dust, which is absorbing optical radiation, heating up and re-emitting in the infrared waveband.

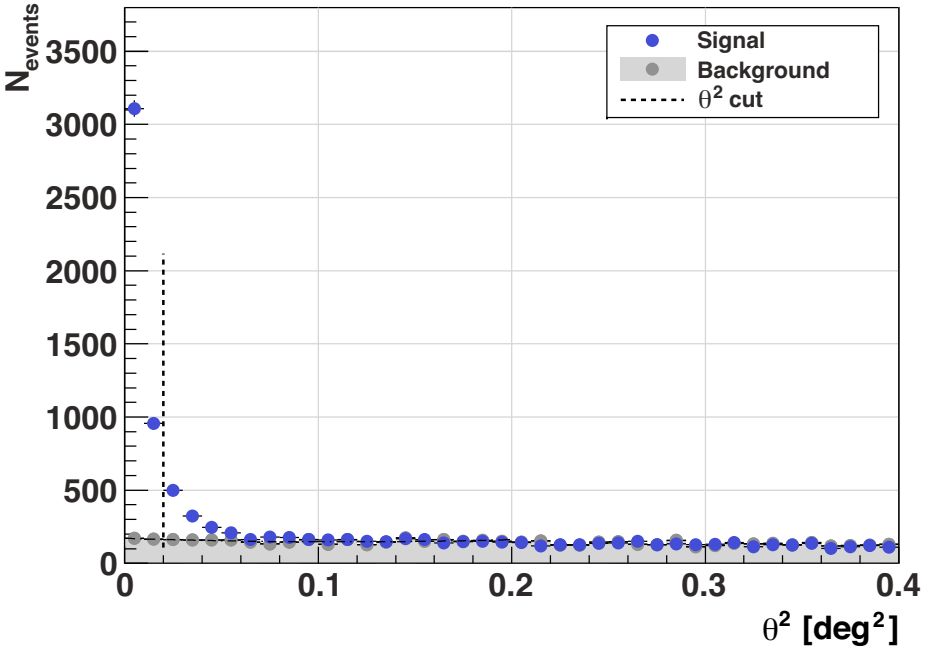

Figure 8.2: θ^2 distribution of signal- (blue points) and background-events (grey points) of the Crab nebula dataset 11/11/2009 – 11/01/2010 for event energies above 200 GeV. The total effective observation time is 452 min, the significance of the signal is 56.9 σ.

8.3 Results

8.3.1 Total signal

Fig. 8.2 shows the θ^2 distribution of signal- and background-events for energies above 200 GeV. The applied cuts are listed in app. B.1. In the signal region ($\theta^2 = 0 - 0.02$ deg^2) 4066 events are counted. With the fitted background events of (479 ± 21.9), this leads to an excess of (3587 ± 21.9) events and to a signal of significance 56.9 σ (according to eq. 17 from [Lia83]). The corresponding γ-rate is (7.94 ± 0.05) min^{-1}, the corresponding background rate is (1.05 ± 0.05) min^{-1}. The sensitivity is (0.95 ± 0.03) % of the Crab nebula flux in 50 hours at 5 σ level, i.e. a source emitting a flux of 0.95 % of the Crab nebula flux is detected with 5 σ significance after 50 hours of observation.

8.3.2 Flux stability

Fig. 8.3 shows the integrated flux above 200 GeV for each observation night. The applied cuts are listed in app. B.2. The mean value and its statistic error range are also shown ((2.36 ± 0.04) cm^{-2} s^{-1}). The reference value of the Crab nebula flux and its statistic error range are obtained from integrating the differential flux function from MAGIC-I [Alb08a] for energies above 200 GeV. The mean flux value from this analysis agrees with the reference value within error ranges. The

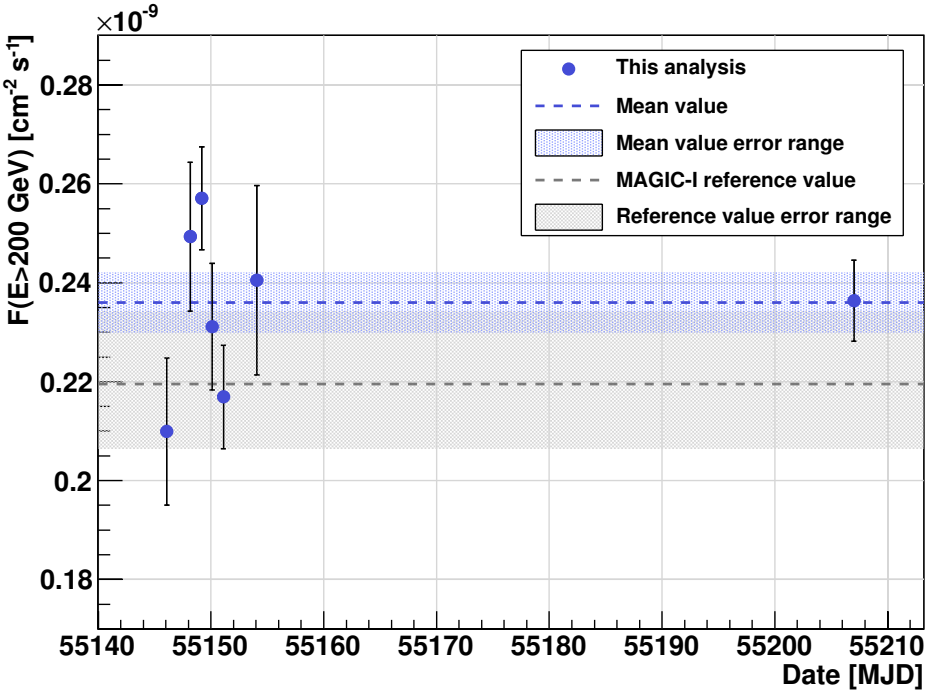

Figure 8.3: Integrated flux (lightcurve) for energies above 200 GeV of the Crab nebula dataset 11/11/2009 – 11/01/2010, total effective observation time 452 min. Shown are daily measurements of the Crab flux (blue points), the mean value and its statistic error range (blue dashed line and light-blue area). The reference Crab flux and its statistic error range (grey dashed line and light-grey area) are obtained from integrating the differential flux function from MAGIC-I [Alb08a] for energies above 200 GeV.

Date	N_{signal}	N_{bgd}	t_{obs} [min]	$F(E > 200\ \text{GeV})$ $[10^{-10}\text{cm}^{-2}\text{s}^{-1}]$	σ
11/11/2009	308	43 ± 6.6	35	2.10 ± 0.15	15.0
13/11/2009	394	46 ± 6.8	44	2.49 ± 0.15	17.8
14/11/2009	812	76 ± 8.7	82	2.57 ± 0.10	26.7
15/11/2009	513	75 ± 8.7	59	2.31 ± 0.13	19.1
16/11/2009	618	72 ± 8.5	78	2.12 ± 0.10	22.2
19/11/2009	227	27 ± 5.2	24	2.40 ± 0.19	13.4
11/01/2010	1194	140 ± 11.8	130	2.36 ± 0.08	30.9
Total	4066	479 ± 21.9	452	2.36 ± 0.04	56.9
MAGIC-I reference	-	-	-	$2.19^{+0.15}_{-0.13}$	-

Table 8.1: Integrated flux (lightcurve) values ($E > 200$ GeV) for each observation night of the Crab nebula dataset 11/11/2009 – 11/01/2010. N_{signal} and N_{bgd} denote the number of events in the signal and background region (fitted) respectively, t_{obs} denotes the observation time. The Crab reference flux and its statistic error range are obtained from integrating the differential flux function from MAGIC-I [Alb08a] for energies above 200 GeV.

dedicated numbers for each observation night are listed in tab. 8.1.

8.3.3 Spectral energy distribution (SED)

Fig. 8.4 shows the results of the differential flux analysis (spectral energy distribution, SED) in the energy range 50 GeV to 8 TeV for three different unfolding methods (see sec. 6.10): Bertero, Schmelling and Tikhonov method. The applied cuts are listed in app. B.2 and the corresponding values for each energy bin are listed in app. C.1. The shown SED can be fitted with a simple power law, a power law with exponential cutoff and a curved power law:

$$\text{Simple power law:} \qquad E^2\frac{\mathrm{d}F}{\mathrm{d}E} = E^2 f_0 \left(\frac{E}{r}\right)^{\alpha} \tag{8.1}$$

$$\text{Cutoff power law:} \qquad E^2\frac{\mathrm{d}F}{\mathrm{d}E} = E^2 f_0 \left(\frac{E}{r}\right)^{\alpha} e^{-E/E_0} \tag{8.2}$$

$$\text{Curved power law:} \qquad E^2\frac{\mathrm{d}F}{\mathrm{d}E} = E^2 f_0 \left(\frac{E}{r}\right)^{a+b\log_{10}(E/r)} . \tag{8.3}$$

The results of the fits are shown in tab. 8.2. The three unfolding methods agree within their error ranges and confirm consistency. For further analysis in this thesis, the Tikhonov method will be used. While the fits with a curved power law

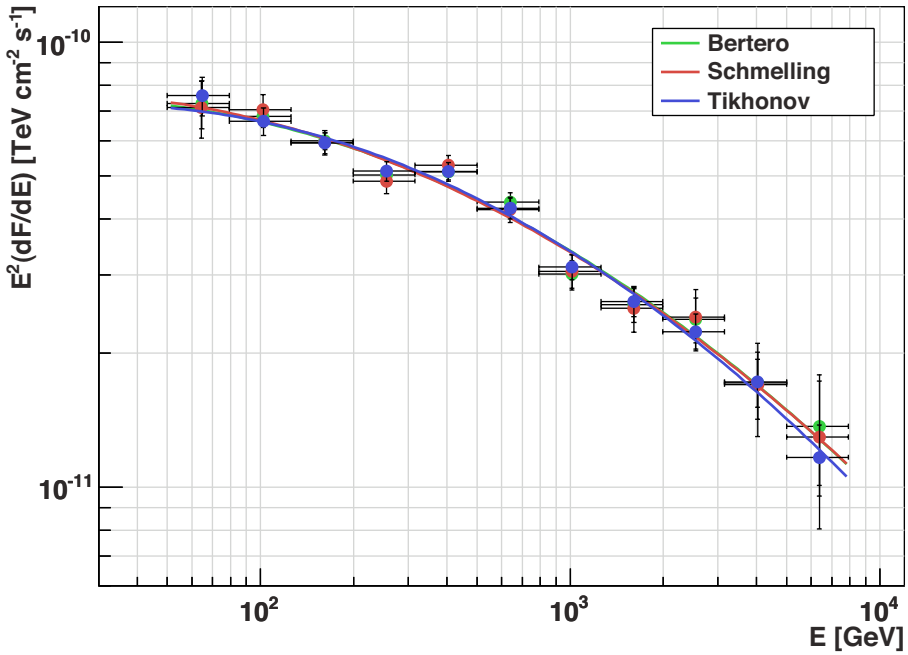

Figure 8.4: Spectral energy distribution (SED) of the Crab nebula dataset 11/11/2009 – 11/01/2010 in the energy range 50 GeV to 8 TeV. Shown are the results of three different unfolding methods: Bertero (green points), Schmelling (red points) and Tikhonov method (blue points). The three methods agree within error ranges for each data point. Additionally, a curved power law is fitted to the data (solid lines in corresponding colours, fit values see tab. 8.2).

and a power law with exponential cutoff result in acceptable values of χ^2/NDF (NDF = number degrees of freedom), the simple power law has much higher values of χ^2/NDF. Therefore, the curved and the cutoff power law are favoured for fitting the SED. Since the curved power law fit gives the best value of χ^2/NDF, it is used for further analysis of this datasample and additionally shown in fig. 8.4 for each unfolding method.

Fig. 8.5 shows the current analysis of the Crab nebula unfolded with the Tikhonov method and fitted with the curved power law in comparison with previous measurements of IACT: HEGRA [Aha04b], H.E.S.S. [Aha06] and MAGIC-I [Alb08a]. In the low energy region (50 GeV $< E <$ 600 GeV), the current analysis agrees well with the MAGIC-I measurement, while it follows the measurement of the H.E.S.S. telescopes in the high energy region (600 GeV $< E <$ 8 TeV). The resulting curvature seems to be smaller than measured with MAGIC-I, however the effective spectral slope is still within the statistical error (see tab. 8.2). This effect is also reported by other analyses of MAGIC stereoscopic observations of the Crab nebula [Car11, Zan11]. It is commonly accepted within the MAGIC collaboration that the improved sensitivity of the stereoscopic system is responsible for this effect.

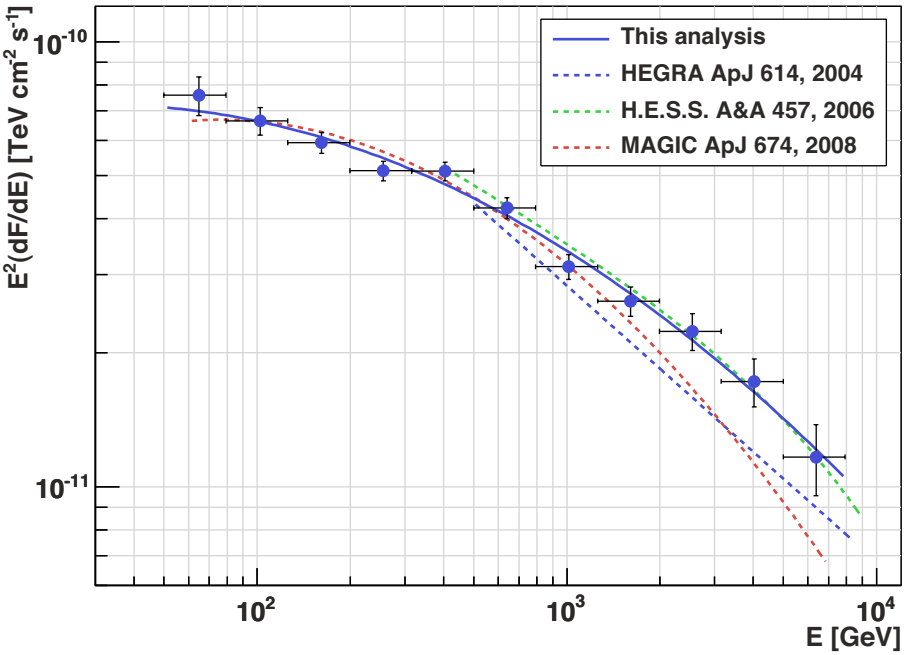

Figure 8.5: Crab nebula SED of the current analysis (blue points and blue solid line, unfolded with the Tikhonov method and fitted with a curved power law) in comparison with previous IACT measurements. The resulting curvature seems to be smaller than measured with MAGIC-I, which is also reported by other analyses of MAGIC stereoscopic observations of the Crab nebula [Car11, Zan11]. It is commonly accepted within the MAGIC collaboration that the improved sensitivity of the stereoscopic system is responsible for this effect.

8.4 Conclusion

The shown analysis of the Crab nebula gives results in good agreement with the reference values of previous measurements. Therefore, the integral (lightcurve) and differential (SED) flux analysis can be stated as confirmed and the used set of signal cuts (see app. B) can be applied to the analysis of Markarian (Mrk) 421. Additionally, the three unfolding methods Bertero, Schmelling and Tikhonov showed comparable results. The Tikhonov method is chosen to be applied to the further analysis.

Unfolding method	Simple power law $E^2\frac{\mathrm{d}F}{\mathrm{d}E} = E^2 f_0 \left(\frac{E}{r}\right)^{\alpha}$				
	f_0 [10^{-10} TeV^{-1} cm^{-2} s^{-1}]	r [GeV]	α	-	χ^2/NDF
Bertero	5.51 ± 0.09	300	-2.33 ± 0.02	-	23.87/9
Schmelling	5.48 ± 0.06	300	-2.33 ± 0.02	-	23.53/9
Tikhonov	5.41 ± 0.09	300	-2.35 ± 0.02	-	23.56/9
	Cutoff power law $E^2\frac{\mathrm{d}F}{\mathrm{d}E} = E^2 f_0 \left(\frac{E}{r}\right)^{\alpha} e^{-E/E_0}$				
	f_0 [10^{-10} TeV^{-1} cm^{-2} s^{-1}]	r [GeV]	α	E_0 [TeV]	χ^2/NDF
Bertero	5.88 ± 0.16	300	-2.24 ± 0.03	7.48 ± 2.72	13.74/8
Schmelling	5.87 ± 0.16	300	-2.24 ± 0.03	7.35 ± 2.65	13.34/8
Tikhonov	5.88 ± 0.17	300	-2.24 ± 0.03	7.07 ± 2.18	8.44/8
	Curved power law $E^2\frac{\mathrm{d}F}{\mathrm{d}E} = E^2 f_0 \left(\frac{E}{r}\right)^{a+b\log_{10}(E/r)}$				
	f_0 [10^{-10} TeV^{-1} cm^{-2} s^{-1}]	r [GeV]	a	b	χ^2/NDF
Bertero	5.77 ± 0.12	300	-2.28 ± 0.02	-0.13 ± 0.04	11.07/8
Schmelling	5.75 ± 0.11	300	-2.29 ± 0.02	-0.12 ± 0.04	11.47/8
Tikhonov	5.82 ± 0.14	300	-2.28 ± 0.02	-0.15 ± 0.04	6.69/8
MAGIC-I reference	6.0 ± 0.2	300	-2.31 ± 0.06	-0.26 ± 0.07	-

Table 8.2: SED fit results of the Crab nebula dataset 11/11/2009 – 11/01/2010 for three different unfolding methods (Bertero, Schmelling and Tikhonov) and simple power law, cutoff power law and curved power law fit. Additionally, the fit for the MAGIC-I measurement (curved power law, [Alb08a]) is shown.

Chapter 9

Analysis of MAGIC Mrk 421 observations January 2010

In this chapter, the analysis of the Markarian (Mrk) 421 dataset January 2010 is presented. These measurements mark the first stereoscopic observations of Mrk 421 with the MAGIC telescopes during high source activity and form the basis of this thesis.

9.1 Motivation: Markarian 421

Markarian[1] (Mrk) 421, located at RA 11:04:27 and DEC +38.21, is a high-frequency BL Lac (HBL) object and one of the brightest sources in the VHE γ-ray sky. It is detected and studied at basically all wavelengths of the electromagnetic spectrum. With a redshift of $z = 0.031$ (which corresponds to a distance of $\approx$ 500 million lightyears), it is the closest known and one of the best explored VHE γ-ray emitting blazars.

In 1992, Mrk 421 was the first extragalactic source detected in the VHE regime [Pun92]. The wide-range SED of Mrk 421 shows the characteristic two-component structure of blazars. The first component extends from radio to X-rays with a peak in the soft to medium X-ray range, the second component extends up to the GeV to TeV energies with a peak around 100 GeV [Fos08]. The currently most complete SED was measured during a multiwavelength campaign in 2009 [Abd11b] and is shown in fig. 9.1.

The first SED component is thought to arise from synchrotron radiation of high-energy electrons, while the origin of the second component is still uncer-

[1]The name *Markarian* originates from one of the first optical colour surveys on AGN, performed by Benjamin Markarian in 1981 [Mar81]. Because of their broadband continuum emission, AGN show different spectral shapes than ordinary stars or galaxies. Therefore, the ratios of the fluxes in different bands ("colour") distinguishes between AGN and other objects. In the Markarian survey, $\approx$ 1500 objects with characteristic UV emission were listed as AGN, the position in this catalogue specifying the name of the object.

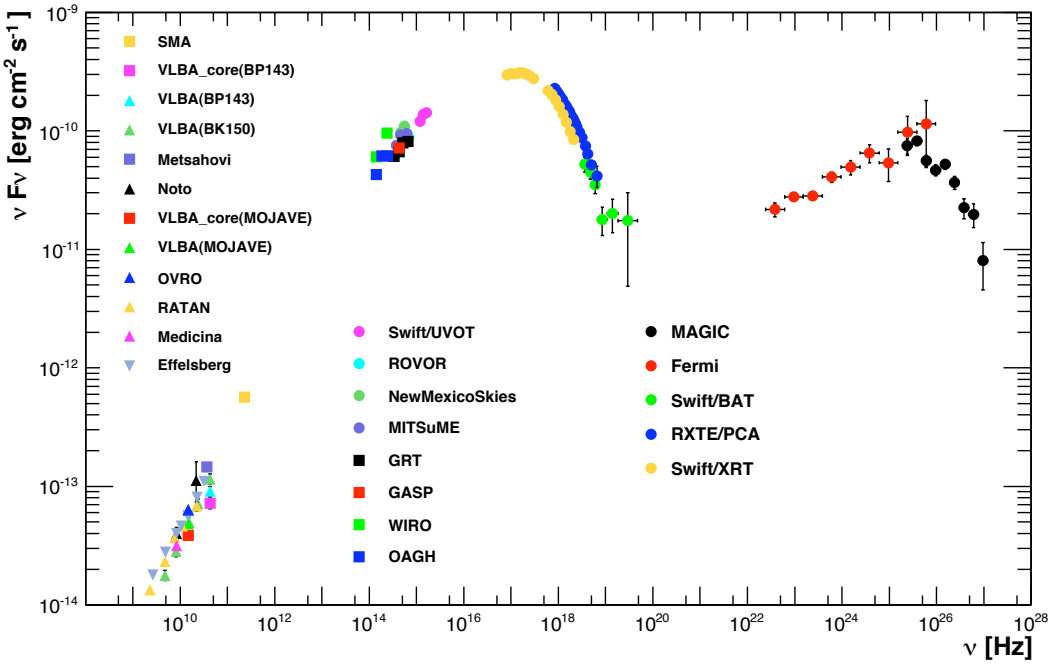

Figure 9.1: Averaged spectral energy distribution of Mrk 421 from a multifrequency campaign in 2009 (19/01/2009 – 01/06/2009), measured by the denoted instruments. The characteristic two component structure for blazars is clearly visible. This measurement marks the most complete SED ever collected for Mrk 421 or for any other BL Lac object. From [Abd11b].

tain. Possible scenarios include inverse Compton scattering of synchrotron (synchrotron self-Compton scenario (SSC), see sec. 3.1.3) or ambient photons (external Compton scenario (EC), see sec. 3.1.4) off a single electron population, accounting for the similarities in the spectral shape of the two SED components [Der92b, Fos08, Mar92, Mas97, Tav98, Sik94]. Alternative scenarios include hadronic components, in which high-energy protons produce the γ-ray emission either directly by synchrotron radiation (proton-synchrotron scenario) or indirectly by synchrotron radiation from secondary electrons produced in cascades induced by interactions of the high-energy protons with ambient photons (proton induced cascade scenario, PIC), see sec. 3.1.5 [Boe04, Mue03].

Additionally, flux variations by more than one order of magnitude [Fos08] and occasional flux doubling times as short as 15 min have been observed [Ale10]. Several groups reported variations in the hardness of the VHE γ-ray spectrum during flares and that the high-energy peak can move to higher energies in such phases [Aha05c, Fos08, Kre02]. Mutifrequency observations also showed hints for a correlation between the X-ray and γ-ray fluxes [Bla05, Fos08, Hor09, Kat03]. Since hadronic scenarios generally do not include intrinsic explanations for this correlated variability [Fos08], the leptonic scenarios, primarily the SSC scenario, are most favoured to explain the emission of Mrk 421. Some datasets require modifications of these simple models, for instance multiple SSC components or additional external seed photons, to successfully model the SED [Bla05, Fos08].

While the measurements in the radio, optical/UV and X-ray regime have already been performed with high sensitivity on short timescales in the past, the measurements in the γ-ray regime required averaging of particularly long time periods to achieve acceptable precision for spectral studies. For instance, the VHE γ-ray measurement by MAGIC for the SED shown in fig. 9.1 averages over 27.7 hours of effective observation time, spanned over ≈ 4.5 months [Abd11b]. With the beginning of scientific operation of the MAGIC stereoscopic system in late 2009, an improved quality in short time measurements also in the VHE γ-ray regime could be achieved. In the following sections, the first MAGIC stereoscopic observations of Markarian 421 during high source activity are analysed. The new sensitivity due to the stereoscopic observation mode makes this data set particularly valuable and important. It will allow unprecedented insight into emission mechanisms, since with this data set also the high energy SED component is sufficiently covered on short timescales.

9.2 Data sample and quality selections

In January 2010, Mrk 421 was observed on 16 nights from 08/01/2010 to 26/01/2010. These data were taken within the monitoring program of Mrk 421, which foresees nearly daily observations with short duration (typically $15-20$ min). These observations were extended up to ≈ 2 h on days with extraordinary high flux states (flares).

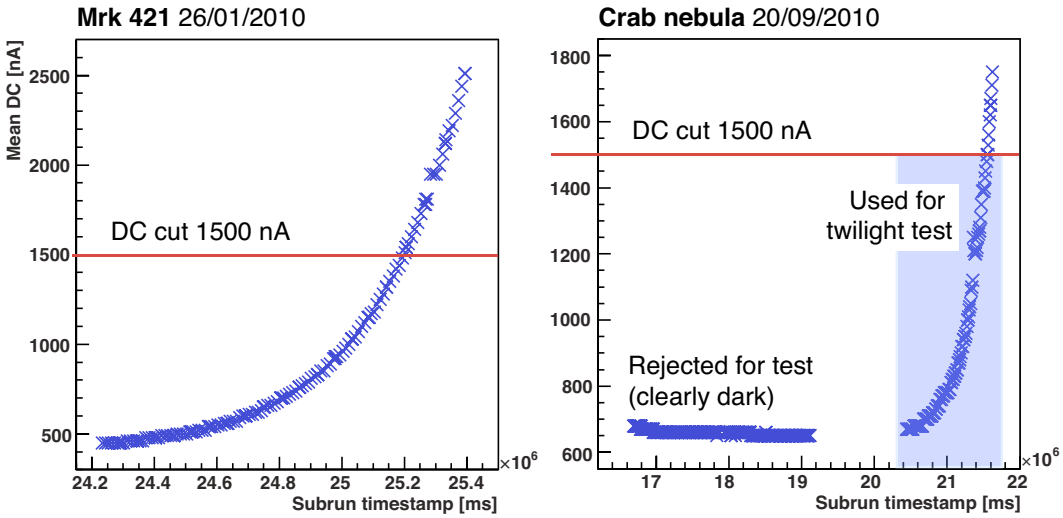

Figure 9.2: Application of direct current (DC) cut of 1500 nA exemplarily shown on 26/01/2010 data of Mrk 421 (left) and on 20/09/2010 data of the Crab nebula used for the twilight test. Shown is the mean DC value for each subrun of MAGIC-II. At the beginning of the two datasets, observation conditions were "dark night" with the typical mean DC value of $500-700$ nA for the night sky background (NSB). The transition from dark night to twilight by the rising sun can clearly be identified by the steep rise of the DC value at the end of the datasets.

For this thesis, also data taken during twilight condition were used. Present twilight (rising or setting sun) or moonlight leads to a general rise in the direct current (DC) of all camera photo multiplier tubes (PMT). This results in a decreased power of γ-ray event detection and allows a satisfactory operation of the telescope only during dark conditions. A cut in the mean DC value of all PMT was used to separate dark from bright observation conditions. In [Bri09] it is studied, up to which DC threshold an observation condition can be treated as dark and delivers sufficient results. The conclusion is that data with a mean DC value up to 2.5 times of the night sky background (NSB) value can be treated as dark. Since the NSB leads to a mean DC value of $\approx 500-700$ nA in the absence of twilight and moonlight, the threshold for separating dark from bright conditions in this thesis was set to 1500 nA. The cut was applied to the data by calculating the mean DC value for each subrun and subruns with a mean DC higher than 1500 nA were rejected.

Fig. 9.2 (left) shows exemplarily the application of the DC-cut to the dataset of Mrk 421 from 26/01/2010, a typical day of monitoring observation (20 min) during twilight. At the beginning of the dataset, observation conditions were "dark night" with the typical mean DC value of $500-700$ nA for the NSB. The transition from dark night to twilight by the rising sun can clearly be seen by the steep rise of the DC value at the end of the dataset.

In order to judge on the quality of these twilight monitoring data, a test on data

	Test sample	Reference value [Alb08a]
Integral flux E>200 GeV		
[ph cm^{-2} s^{-1}]	$(2.02 \pm 0.24) \cdot 10^{-10}$	$(2.11 + 0.14 - 0.13) \cdot 10^{-10}$
Differential flux fit	$f_0 \cdot (E/r)^{-\alpha}$	$f_0 \cdot (E/r)^{-\alpha}$
f_0 [ph cm^{-2} s^{-1} TeV^{-1}]	$(2.89 \pm 0.70) \cdot 10^{-11}$	$(2.88 \pm 0.10) \cdot 10^{-11}$
r [TeV]	1	1
α	2.51 ± 0.24	2.48 ± 0.03

Table 9.1: Results of the Crab nebula twilight test (20/09/2010). The total effective observation time is 16 min, the significance of the signal is 9.4 σ. Due to reduced statistics, a simple power law was chosen for fitting the differential flux (spectrum). The reference Crab flux and its statistic error range are obtained from integrating the corresponding differential flux function (simple power law) from MAGIC-I [Alb08a] for energies above 200 GeV. The results agree with the reference values and confirm the applicability of short twilight observations for monitoring purpose (typical duration $15 - 20$ min).

of the Crab nebula with the same conditions was performed (a detailed reference analysis of the Crab nebula including an introduction to the source is presented in chapter 8). Fig. 9.2 (right) shows the chosen test data from 20/09/2010. For the test, the DC-cut of 1500 nA was applied in addition to a time cut, which extracted only the subruns including the rising part of the mean DC value. In this way, it was possible to judge exactly on that part of the data, which was affected by twilight condition. 16 min of data remained for the test, which is of the same order as the typical monitoring data. The results for this dataset are given in tab. 9.1, the significance of the signal is 9.4 σ. Due to reduced statistics, a simple power law was chosen for fitting the differential flux (spectrum)[2]. The reference Crab flux and its statistic error range are obtained from integrating the corresponding differential flux function (simple power law) from MAGIC-I [Alb08a] for energies above 200 GeV. The results agree well with the reference values and allow to draw the following conclusion: Twilight data of the timescale $15 - 20$ min (monitoring timescale) in combination with a DC-cut of 1500 nA are applicable for reasonable results.

After applying the described DC selection in combination with the general quality selection discussed in sec. 6.4, data from all nights (08/01/2010 – 26/01/2010) were analysed, giving a total observation time of $\approx$ 12 h. The observation time before and after quality selection for each observation day and each telescope is listed in tab. 9.2. The mean $Rate_{100}$ values of the accepted data is also listed. The zenith angle of the accepted data ranges from 8° to 39°.

[2]For data samples with higher statistics, a curved power law is favoured, see chapter 8.

Date	MAGIC-I T_b [min]	MAGIC-I T_a [min]	MAGIC-II T_b [min]	MAGIC-II T_a [min]	MAGIC-I Mean $Rate_{100}$ [Hz]	MAGIC-II Mean $Rate_{100}$ [Hz]	ZA [°]
08/01/2010	185	37	185	133	62.9 ± 0.7	57.7 ± 0.3	20–30
11/01/2010	112	109	112	105	81.6 ± 0.5	74.8 ± 0.2	9–27
12/01/2010	19	19	19	19	81.4 ± 0.5	77.0 ± 0.2	16–20
13/01/2010	38	38	38	33	79.6 ± 0.7	77.1 ± 0.7	17–29
14/01/2010	163	161	159	157	84.9 ± 0.4	80.3 ± 0.3	8–29
15/01/2010	89	67	89	69	81.3 ± 1.0	76.3 ± 0.6	15–30
16/01/2010	30	18	30	19	81.3 ± 2.1	78.0 ± 1.3	18-31
18/01/2010	22	11	22	11	62.9 ± 3.1	59.8 ± 1.5	26–29
19/01/2010	38	25	38	22	61.4 ± 2.6	60.1 ± 1.4	25–34
20/01/2010	178	157	178	171	85.2 ± 0.5	92.5 ± 0.3	7–30
21/01/2010	33	27	33	29	80.5 ± 2.1	77.7 ± 1.1	21–35
22/01/2010	12	12	12	11	66.9 ± 1.7	67.8 ± 1.2	33-36
23/01/2010	30	20	31	20	80.8 ± 1.9	79.9 ± 1.2	18–23
24/01/2010	39	27	39	32	75.7 ± 1.3	73.7 ± 0.6	26–37
25/01/2010	120	113	110	106	80.3 ± 0.5	87.6 ± 0.5	16–38
26/01/2010	20	15	19	15	68.9 ± 1.5	66.1 ± 0.6	36–39

Table 9.2: Quality selection for Mrk 421 January 2010 data. The observation time before (T_b) and after quality cuts (T_a) is listed for each observation day and each telescope. Also the mean $Rate_{100}$ for each telescope and the zenith angle (ZA) range of the accepted data is listed.

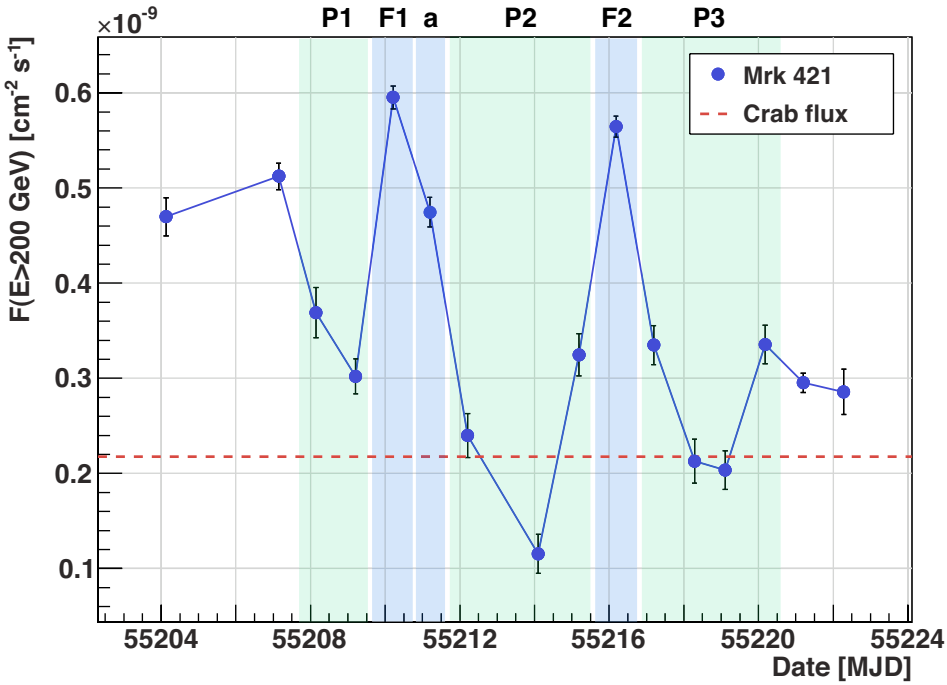

Figure 9.3: Integrated flux (lightcurve) for energies above 200 GeV of the Mrk 421 dataset 08/01/2010 – 26/01/2010. Shown are daily measurements of the Mrk 421 flux (blue points) and the Crab flux level (red dashed line, obtained from integrating the differential flux function from MAGIC-I [Alb08a] for energies above 200 GeV). To guide the eye, the daily measurements are connected with a line. Two distinct flares were observed on 14–15/01/2010 and 20/01/2010. These flares are denoted as analysis period F1 and F2 ("F" stands for flare), while the periods before, in between and after the flares are denoted as P1, P2 and P3 ("P" stands for pre-/post-flare).

9.3 Integral flux (lightcurve)

Fig. 9.3 shows the integrated flux above 200 GeV for each observation night. The applied cuts are listed in app. B.2. The dedicated numbers for each observation night are listed in tab. 9.3. Total effective observation time after dead time correction is 722 min.

Two distinct flares were observed on 14–15/01/2010 and 20/01/2010, reaching a flux level of 2.7 c.u.[3] and 2.6 c.u. respectively. The periods immediately before and after the flares show comparatively low flux levels ($\approx 0.5 - 1.5$ c.u.), which is making the flares prominent and good candidates for studying the flare production mechanisms. In the further analysis, the flares are denoted as analysis period F1 and F2 ("F" stands for flare), while the periods before, in between and after the flares are combining several days and are denoted as P1, P2 and P3 ("P" stands for

[3] A Crab unit (c.u.) is marking the flux state of the Crab nebula above 200 GeV ($2.19^{+0.15}_{-0.13}$ 10^{-10} cm^{-2} s^{-1})

Date	Period	N_{signal}	N_{bgd}	t_{obs} [min]	$F(E > 200$ GeV) $[10^{-10}\text{cm}^{-2}\text{s}^{-1}]$	c.u.	σ
08/01/2010	-	637	32 ± 5.7	33	4.70 ± 0.20	2.1	25.9
11/01/2010	-	1666	102 ± 10.1	89	5.12 ± 0.14	2.3	40.9
12/01/2010	P1	229	12 ± 3.5	17	3.69 ± 0.26	1.7	15.5
13/01/2010	P1	359	33 ± 5.7	29	3.02 ± 0.18	1.4	17.8
14/01/2010	F1	2935	161 ± 12.7	138	5.86 ± 0.12	2.7	55.0
15/01/2010	F1a	1106	68 ± 8.2	56	4.79 ± 0.16	2.2	33.3
16/01/2010	P2	164	22 ± 4.7	15	2.40 ± 0.23	1.1	11.1
18/01/2010	P2	55	10 ± 3.2	10	1.16 ± 0.21	0.5	5.9
19/01/2010	P2	262	18 ± 4.2	18	3.25 ± 0.22	1.5	16.0
20/01/2010	F2	3008	172 ± 13.1	137	5.60 ± 0.11	2.6	55.4
21/01/2010	P3	349	30 ± 5.5	24	3.35 ± 0.20	1.5	17.8
22/01/2010	P3	108	9 ± 3.0	10	2.13 ± 0.23	1.0	9.9
23/01/2010	P3	143	17 ± 4.1	17	2.03 ± 0.20	0.9	10.7
24/01/2010	P3	399	48 ± 6.9	24	3.35 ± 0.20	1.5	17.7
25/01/2010	-	1216	135 ± 11.6	91	2.95 ± 0.10	1.3	31.5
26/01/2010	-	226	34 ± 5.8	14	2.86 ± 0.24	1.3	12.6

Table 9.3: Integrated flux (lightcurve) values ($E > 200$ GeV) for each observation night of the Mrk 421 dataset 08/01/2010 – 26/01/2010. N_{signal} and N_{bgd} denote the number of events in the signal and background region (fitted), respectively, t_{obs} denotes the effective observation time after dead time correction and c.u. the flux in Crab units. Each observation night shows a significant detection ($\sigma > 5$). The affiliation with the analysis periods (flare (F) or pre-/post-flare (P)) is also listed.

pre-/post-flare). Since the F1 flare lasts two days (14/01/2010 and 15/01/2010) and each day having sufficient data for an individual analysis, the F1 flare is divided into two parts: The main flare on 14/01/2010 (F1, 138 min effective observation time) and the decreasing part of the flare on 15/01/2010 (F1a, 56 min). The flare on 20/01/2010 comprises an effective observation time of 137 min, the combined periods P1, P2 and P3 comprise 46 min (P1), 43 min (P2) and 75 min (P3).

9.4 Intranight variability

Fig. 9.4 shows the lightcurves for energies above 200 GeV of the extended observations on 14/01/2010 (F1), 15/01/2010 (F1a) and 20/01/2010 (F2) in a 10 min binning.

The data points were fitted with a constant function (mean value, see tab. 9.3). A χ^2-test of that function for each observation night resulted in $\chi^2/\mathrm{NDF} = 26.02/17$ for F1, $\chi^2/\mathrm{NDF} = 12.29/6$ for F1a and $\chi^2/\mathrm{NDF} = 23.02/15$ for F2, with NDF the degrees of freedom. The probability for the data points to be distributed uniformly around the mean value is 7.4 % for F1, 5.6 % for F1a and 8.4 % for F2. Thus, the constant function can not be rejected as fit and an intranight variability can not be claimed. Since variability is only seen between the observation days, a conservative estimation on the variability timescale is $t_{\mathrm{var}} = 1$ day.

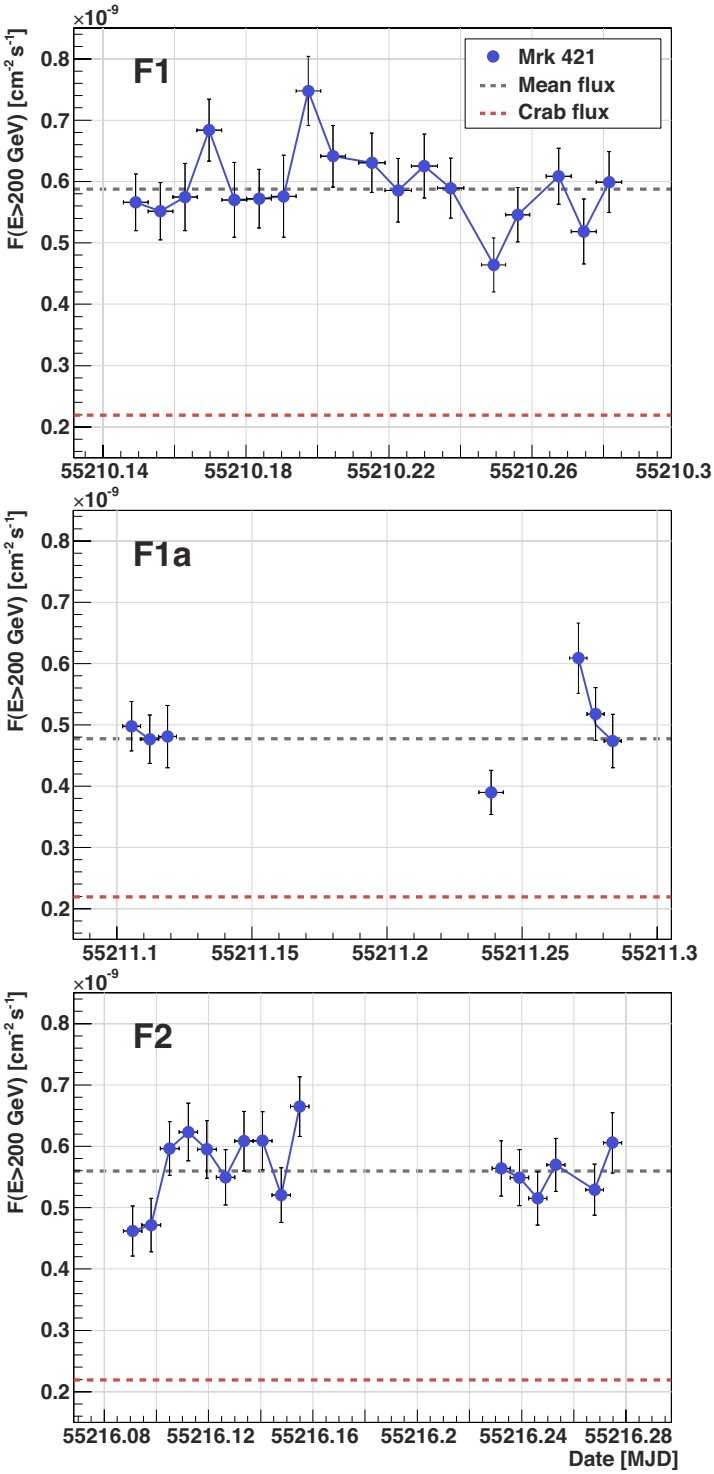

Figure 9.4: Intranight lightcurves for energies above 200 GeV of Mrk 421 14/01/2010 (F1), 15/01/2010 (F1a) and 20/01/2010 (F2) observations. Shown is the 10 min binned measurement of the Mrk 421 flux (blue points), the mean flux (grey dashed line) and the Crab flux level (red dashed line). To guide the eye, the measurements are connected with a line.

9.5 Spectral energy distribution (SED)

Figs. 9.5 and 9.6 show the results of the differential flux analysis (spectral energy distribution, SED) of the Mrk 421 flares F1 and F2 and their adjacent analysis periods (Tikhonov unfolding, see sec. 6.10 and 8.3.3). The SEDs of periods P1, F1, F1a, P2 and P3 range from 80 GeV to 5 TeV, the SED of period F2 extends to 8 TeV. The applied cuts are listed in app. B.2 and the corresponding values for each energy bin are listed in app. C.2.

The SEDs of the flare periods F1 and F1a contain a higher flux than the SEDs of analysis periods P1 and P2, corresponding to the results from the integral flux analysis. The time development of the SEDs can be followed via the colour coded points in fig. 9.5: First the pre-flare period P1, then the flare F1, then – one day later – the second flare measurement F1a and at the end the post-flare period P2.

The SED of flare period F2 contains a higher flux than the SEDs of analysis periods P2 and P3 (see fig. 9.6). The time development can also be followed: First the pre-flare period P2, then the flare F2 and at the end the post-flare period P3.

The shown data points can be fitted with a curved power law and a power law with exponential cutoff (see eq. 8.1). The corresponding fit values are listed in tab. 9.4. The goodness of the curved power law fit ($\chi^2/\mathrm{NDF} = 3.26/6 - 5.27/6$ and $\chi^2/\mathrm{NDF} = 2.95/7$, respectively) is slightly better than the goodness of the power law with cutoff fit ($\chi^2/\mathrm{NDF} = 3.63/6 - 7.29/6$ and $\chi^2/\mathrm{NDF} = 7.97/7$, respectively). Thus, the curved power law fit is shown in figs. 9.5 and 9.6 for each analysis period.

A simple power law fit of the form $E^2(\mathrm{d}F/\mathrm{d}E) = E^2\, f_0\, (E/r)^\alpha$ is excluded for flare F1 and flare F2 with high probability ($\chi^2/\mathrm{NDF} = 63.89/7$ (F1) and $\chi^2/\mathrm{NDF} = 115.78/8$ (F2)). This demonstrates that the VHE γ-ray spectra of the flares show a very clear curvature. Due to the low energy threshold and high sensitivity of the MAGIC stereoscopic system, the precision of this curvature measurement (parameter b in the curved power law fit) is improved by a factor of 3 compared to preceding works on comparable timescales (e.g. [Ale11b]). Also the other periods show comparatively high χ^2/NDF values for a simple power law fit (11.14/7 for P1, 15.81/7 for F1a, 6.74/7 for P2 and 14.81/7 for P3).

9.6 Apparent two-peak structure in periods P1, F1a and P2

The SEDs of the observation periods P1, F1a and P2 show a hint for a two-peak structure (see figs. 9.5 and 9.6). This three periods have in common that each of them is comprised of single, separated observations with small effective observation times of $\approx 10 - 20$ min (period F1a consists of two discontinuous observations taken on one day, see fig. 9.4). To reach an effective observation time of the order of 1 hour, these single observations had to be combined (an individual view of each single observation did not lead to satisfactory results). Spectral features of

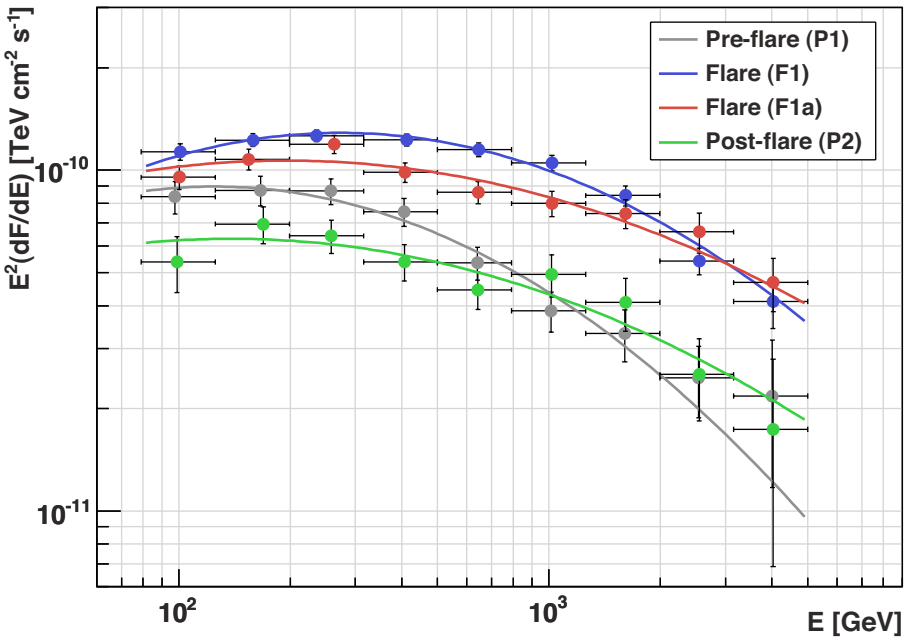

Figure 9.5: Spectral energy distribution (SED) of the Mrk 421 flare period F1 (blue points) and its adjacent analysis periods P1 (grey points), F1a (red points) and P2 (green points) (Tikhonov unfolding). A curved power law is fitted to the data (solid lines in corresponding colours, fit values see tab. 9.4).

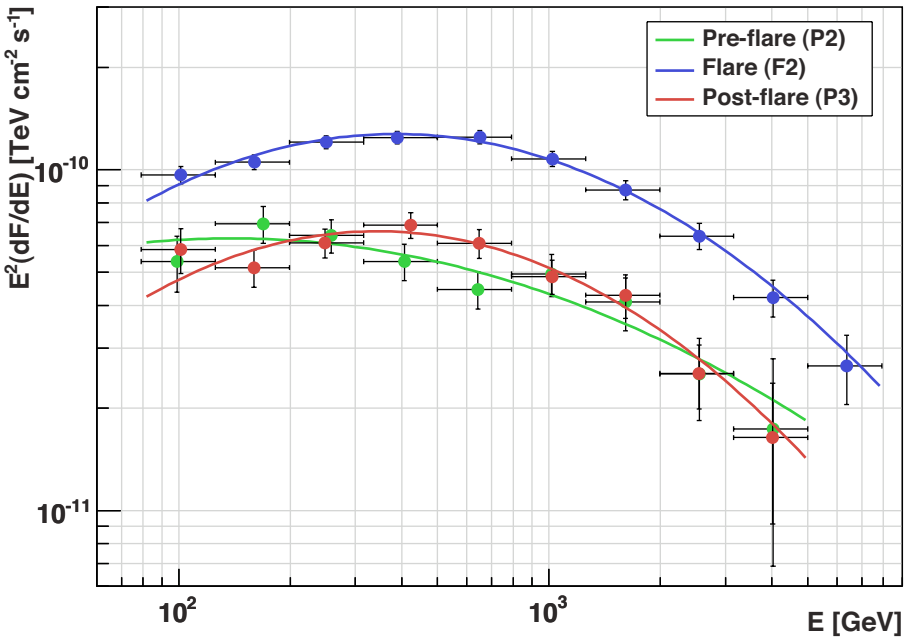

Figure 9.6: SED of the Mrk 421 flare period F2 (blue points) and its adjacent analysis periods P2 (green points) and P3 (red points) (Tikhonov unfolding). A curved power law is fitted to the data (solid lines in corresponding colours, fit values see tab. 9.4).

Period	Cutoff power law $E^2\frac{\mathrm{d}F}{\mathrm{d}E} = E^2 f_0 \left(\frac{E}{r}\right)^{\alpha} e^{-E/E_0}$				
	f_0 [10^{-10} TeV^{-1} cm^{-2} s^{-1}]	r [GeV]	α	E_0 [TeV]	χ^2/NDF
P1	9.58 ± 1.19	300	-2.14 ± 0.13	2.11 ± 1.21	6.39/6
F1	15.81 ± 0.57	300	-1.87 ± 0.05	2.16 ± 0.36	5.56/6
F1a	11.98 ± 0.54	300	-2.02 ± 0.06	4.69 ± 1.88	7.29/6
P2	6.98 ± 0.64	300	-2.06 ± 0.13	3.60 ± 2.52	3.93/6
F2	15.14 ± 0.51	300	-1.77 ± 0.05	2.13 ± 0.31	7.97/7
P3	8.42 ± 0.63	300	-1.76 ± 0.11	1.59 ± 0.43	3.63/6
	Curved power law $E^2\frac{\mathrm{d}F}{\mathrm{d}E} = E^2 f_0 \left(\frac{E}{r}\right)^{a+b\log_{10}(E/r)}$				
	f_0 [10^{-10} TeV^{-1} cm^{-2} s^{-1}]	r [GeV]	a	b	χ^2/NDF
P1	8.76 ± 0.49	300	-2.29 ± 0.06	-0.38 ± 0.15	3.26/6
F1	14.29 ± 0.29	300	-2.03 ± 0.03	-0.35 ± 0.05	4.57/6
F1a	11.66 ± 0.36	300	-2.08 ± 0.04	-0.21 ± 0.07	5.27/6
P2	6.60 ± 0.33	300	-2.15 ± 0.08	-0.22 ± 0.14	3.67/6
F2	13.99 ± 0.25	300	-1.91 ± 0.03	-0.43 ± 0.05	2.95/7
P3	7.31 ± 0.28	300	-1.94 ± 0.07	-0.50 ± 0.12	3.64/6

Table 9.4: SED fit results of the Mrk 421 analysis periods for cutoff power law and curved power law fit.

the single observations, introduced by source effects or statistical fluctuations, may therefore manifest as multi-peak structures in the SEDs, particularly if none of the single observations dominates the combined dataset.

The χ^2-test of the shown curved power law fit to the P1, F1a and P2 SEDs resulted in $\chi^2/\text{NDF} = 3.26/6$ for P1, $\chi^2/\text{NDF} = 5.27/6$ for F1a and $\chi^2/\text{NDF} = 3.67/6$ for P2 (see tab. 9.4). The probability for the data points to be distributed uniformly around the curved power law function is 77.6 % for P1, 51.0 % for F1a and 72.1 % for P2. Thus, the curved power law function can not be rejected as fit. The probability for the data points to be distributed uniformly around the cutoff power law fit is 38.1 % for P1 ($\chi^2/\text{NDF} = 6.39/6$), 29.5 % for F1a ($\chi^2/\text{NDF} = 7.29/6$) and 68.6 % for P2 ($\chi^2/\text{NDF} = 3.93/6$). Thus, the cut-off power law function can also not be rejected as fit, but it shows slightly worse probabilities than the curved power law function.

Observation period P3 does not show a two-peak structure in its SED. Although this period is also comprised of single, separated observations of small timescales, the single spectral features do not lead to a multi-peak feature in the combined SED. This might be due to the reduced source activity after the second flare, which might have resulted in a more constant spectral shape.

9.7 Extragalactic background light (EBL) correction

On their way from the source to the observer, VHE γ-rays can suffer significant absorption losses due to interaction with the extragalactic background light (EBL). This soft photon field consists of photons from starlight (optical and ultraviolet wavelengths) and reprocessed starlight (infrared wavelengths) [Ven09]. Here, VHE γ-ray photons suffer significant attenuation due to pair production. Since the EBL photon field is of low intensity, the EBL absorption feature scales with the distance of the source. Although Mrk 421 is located at small distance ($z = 0.031$), the EBL absorption has to be taken into account for a detailed interpretation of the spectral shape of this source.

To deduce from the presented results to the spectral shape at the γ-ray production site, a correction of the EBL absorption has to be applied. To compensate for the absorption, the Franceschini EBL model [Fra08] was used in this thesis. With this model, energy dependent attenuation factors corresponding to the redshift of Mrk 421 were calculated and applied to the data.

Fig. 9.7 exemplarily shows the effect of EBL correction on the F2 flare. Shown is the F2 SED without and with EBL correction. Since the pair production cross section rises with increasing γ-ray energy, the effect of the EBL correction rises with increasing energy.

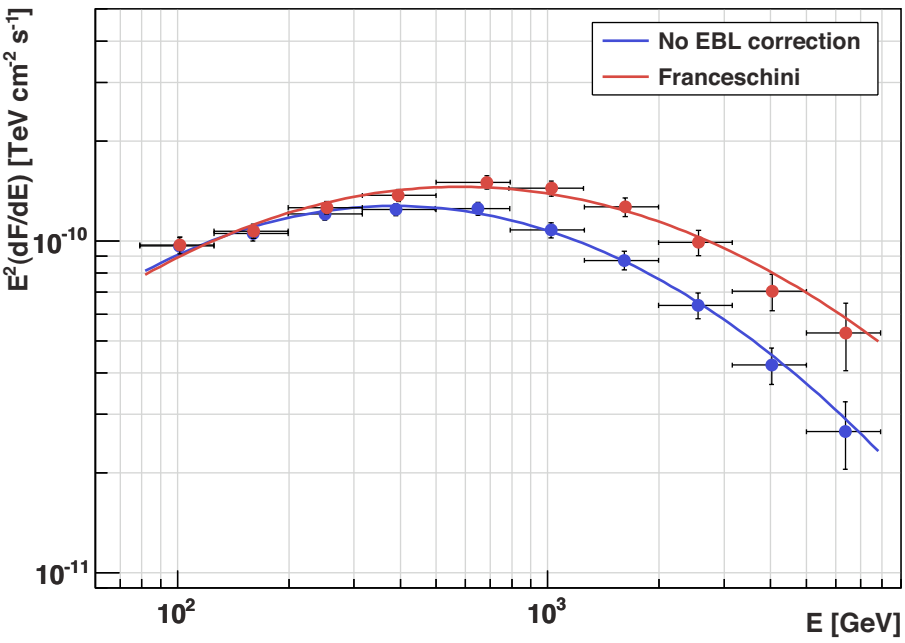

Figure 9.7: SED of the Mrk 421 F2 flare without (blue points) and with EBL correction calculated by the Franceschini model (red points). A curved power law is fitted to the data (solid lines in corresponding colours).

9.8 EBL corrected SEDs in comparison with historical data

Fig. 9.8 shows the SEDs of all analysis periods after EBL correction in comparison with historical data. The SED values of all analysis periods after EBL correction are listed in tab. C.4 and C.5. The corresponding values of a curved power law fit and a power law with cutoff fit are listed in tab. 9.5.

The results obtained in this work clearly extend to energies lower than previously measured (only the long-term (several month) averaged MAGIC SED from 2009 shows the same energy span as the SEDs from this work [Abd11b]). These data points from 80 to 300 GeV play an important role in model constraints, since the curvature of the SED is particularly prominent in this low energy region. The flux states from this work do not represent exceptionally high or low flux levels of the source. But all SEDs seem to be harder than historical SEDs with comparable flux levels. The Whipple high state measurement from 2000 – 2001 shows a comparable spectral shape to the ones from this work, although at an approximately six times higher (for the pre- and post-flare periods) and two times higher (for the flare periods) flux level, respectively. For a discussion of the spectral shape within a synchrotron self-Compton (SSC) emission model, please see the following chapters.

Particularly worthy of mention is the fact that the SEDs from this work are

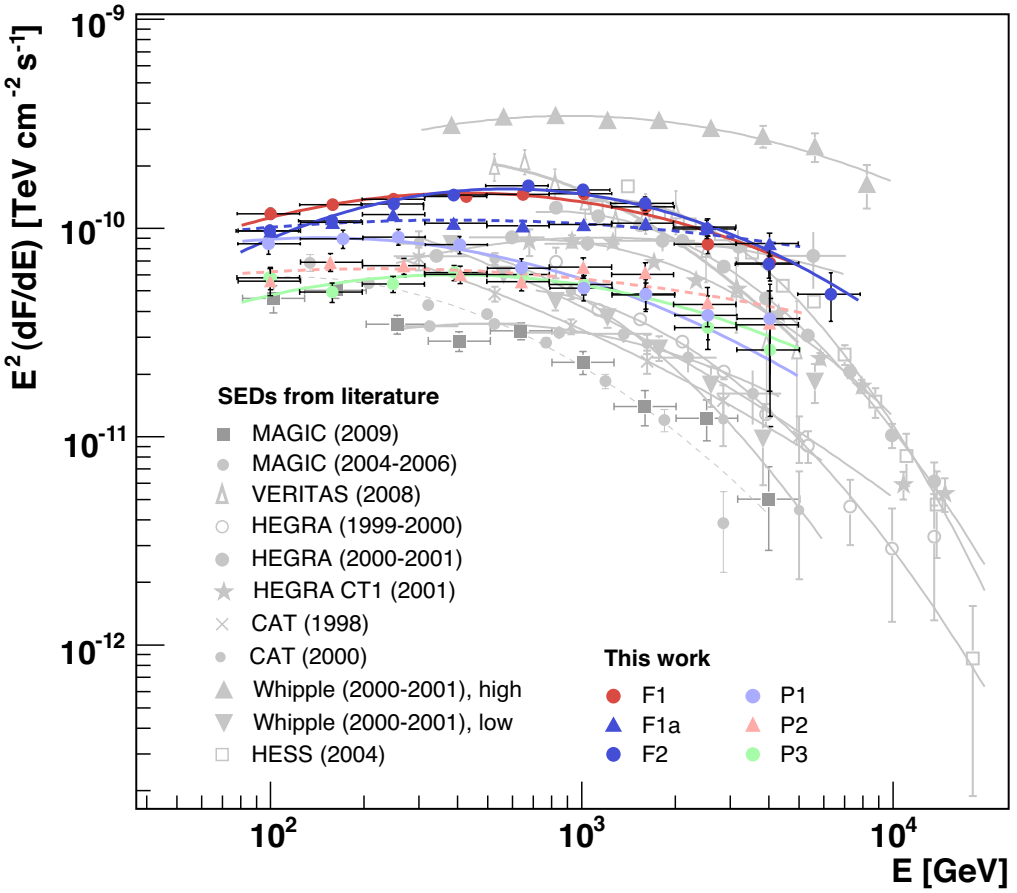

Figure 9.8: SEDs of all analysis periods after EBL correction in comparison with historical data [Abd11b, Alb07b, Ale10, Don09]. A curved power law is fitted to the data (solid lines in corresponding colours). Note that the historical data from [Alb07b] were EBL corrected using the model of [Pri05], those from [Ale10] and [Don09] were corrected using the model of [Kne08] and those from [Abd11b] and from this work were corrected using the model of [Fra08].

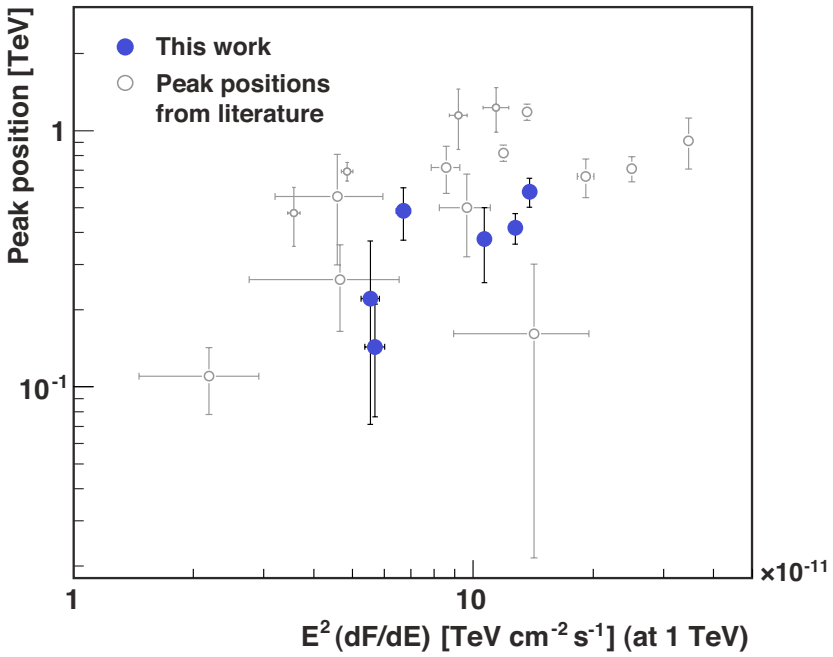

Figure 9.9: VHE γ-ray peak positions as a function of their spectral energy density at 1 TeV and in comparison with peak positions from literature [Alb07b, Ale10].

obtained from observation timescales of $1 - 2.5$ hours and show comparatively small errors. For instance, the MAGIC 2009 SED, obtained from monoscopic observations, includes averaged observations of several months. This demonstrates the improved sensitivity of the MAGIC stereo system, which makes high precision studies of emission variations on short timescales (as in this thesis) possible for the first time.

9.9 Peak position

The curved power law fits of the SEDs allow to locate a peak in the EBL corrected spectra at $E_{\mathrm{peak}} = r\, 10^{(2-a)/(2b)}$ [Ale10]. The results for each analysis period are listed in tab. 9.6 along with the energy density at the peak and at 1 TeV. Fig. 9.9 shows the peak positions as a function of their spectral energy density at 1 TeV and in comparison with historical data. The results from this work confirm the previously suggested correlation between flux level and peak position [Alb07b, Ale10]: For increasing fluxes, the peak shifts to higher energies.

Period	Cutoff power law $E^2\frac{\mathrm{d}F}{\mathrm{d}E} = E^2 f_0 \left(\frac{E}{r}\right)^{\alpha} e^{-E/E_0}$				
	f_0 [10^{-10} TeV^{-1} cm^{-2} s^{-1}]	r [GeV]	α	E_0 [TeV]	χ^2/NDF
P1	9.93 ± 1.14	300	-2.07 ± 0.13	3.01 ± 2.25	4.44/6
F1	16.72 ± 0.58	300	-1.78 ± 0.05	2.67 ± 0.51	5.22/6
F1a	12.87 ± 0.58	300	-1.92 ± 0.07	6.77 ± 4.02	7.43/6
P2	7.40 ± 0.65	300	-1.97 ± 0.13	5.19 ± 4.97	3.82/6
F2	16.21 ± 0.51	300	-1.67 ± 0.05	2.47 ± 0.40	5.45/7
P3	8.91 ± 0.64	300	-1.66 ± 0.11	1.82 ± 0.54	3.11/6
	Curved power law $E^2\frac{\mathrm{d}F}{\mathrm{d}E} = E^2 f_0 \left(\frac{E}{r}\right)^{a+b\log_{10}(E/r)}$				
	f_0 [10^{-10} TeV^{-1} cm^{-2} s^{-1}]	r [GeV]	a	b	χ^2/NDF
P1	9.37 ± 0.52	300	-2.18 ± 0.06	-0.28 ± 0.15	2.52/6
F1	15.36 ± 0.30	300	-1.92 ± 0.03	-0.28 ± 0.05	7.62/6
F1a	12.58 ± 0.38	300	-1.97 ± 0.04	-0.15 ± 0.07	4.64/6
P2	7.10 ± 0.35	300	-2.04 ± 0.08	-0.15 ± 0.14	3.87/6
F2	15.09 ± 0.27	300	-1.79 ± 0.03	-0.37 ± 0.05	5.61/7
P3	7.86 ± 0.30	300	-1.82 ± 0.07	-0.43 ± 0.12	4.05/6

Table 9.5: SED fit results of the Mrk 421 analysis periods for cutoff power law and curved power law fit after EBL correction.

Period	E_{peak} [GeV]	Energy density at peak [10^{-10} TeV cm^{-2} s^{-1}]	Energy density at 1 TeV [10^{-10} TeV cm^{-2} s^{-1}]
P1	143.1 ± 66.8	0.90 ± 0.25	0.569 ± 0.032
F1	416.8 ± 57.0	1.40 ± 0.16	1.276 ± 0.025
F1a	377.7 ± 122.8	1.14 ± 0.24	1.068 ± 0.032
P2	220.7 ± 149.5	0.64 ± 0.65	0.554 ± 0.029
F2	576.6 ± 74.1	1.45 ± 0.08	1.385 ± 0.025
P3	485.8 ± 112.1	0.74 ± 0.12	0.670 ± 0.027

Table 9.6: Peak positionsE_{peak} and corresponding spectral energy densities at the peak and at 1 TeV.

Chapter 10

January 2010 multiwavelength (MWL) SEDs and modelling

The data used in this thesis were taken as part of an extensive multiwavelength (MWL) campaign on Markarian (Mrk) 421. It aimed a regular and dense observation, covering all wavebands of the SED with several instruments over several months. The January 2010 flare observations are an extract of this campaign. In this chapter, firstly the instruments and wavebands offering simultaneous data with the particular MAGIC analysis periods are introduced. Secondly, the SEDs resulting from the MWL observations and their modelling within a one-zone synchrotron self-Compton (SSC) framework are presented.

10.1 MWL instruments

10.1.1 Radio waveband

Simultaneous radio data were taken by the single-dish telescopes of the University of Michigan Radio Astronomy Observatory (UMRAO, 26 m dish diameter, measured energy 8 and 14.5 GHz, simultaneous with observation periods F1a, P2 and P3 (as defined in sec. 9.3)), the Owens Valley Radio Observatory (OVRO, 40 m, 15 GHz, simultaneous with F1, P2 and P3) and Metsähovi (14 m, 37 GHz, simultaneous with P3). For these instruments, Mrk 421 is pointlike and unresolved. Consequently, these measurements denote the total flux density of the source integrated over the whole source extension, including blazar emission as well as the radio emission of the host galaxy. Therefore, the flux measurements of these instruments are treated as upper limits for the MWL blazar SEDs. Details of the particular observations used in this thesis are listed in app. D.1. For details of the data reduction please see [All85], [Ric10] and [Ter98].

10.1.2 Optical waveband

The coverage at optical frequencies was provided by the telescopes in the GASP-WESP program [Vil08, Vil09](Abastumani, Lulin, Roque de los Muchachos (KVA), St. Petersburg and Talmassons, R band, simultaneous observation at each observation period), the New Mexico Skies telescopes (V and R band, simultaneous with observation period P2) and the Bradford Robotic telescope (BRT, V band simultaneous with P2, R band simultaneous with F2). For calibration, the stars reported in [Vil98] were used and the Galactic extinction was corrected with the coefficients given in [Sch98]. The flux from the host galaxy was estimated using the flux values at the R band from [Nil07] and then subtracted from the measured flux [Abd11b]. Details of the particular observations used in this thesis are listed in app. D.1.

10.1.3 Swift/UVOT and -/XRT

The Ultraviolet/Optical Telescope (UVOT, [Rom05]) on board the Swift satellite performed observations during all the analysis periods defined in chapter 9. It cycled through each of three ultraviolet passbands (UVW1, UVM2, UVW2), covering an energy range of $1.05 - 1.93$ PHz. Photometric calibration was done as presented in [Poo08], the flux measurements were corrected for galactic extinction [Sch98, Fit99]. The X-ray Telescope (XRT, [Bur05]), on board the same satellite, also performed simultaneous observations with all the analysis periods of this thesis. It is covering an energy range of $0.3 - 9.6$ keV, details on the data extraction can be found in [Abd11b]. Details of the particular observations used in this thesis are listed in app. D.1.

10.2 Used synchrotron self-Compton (SSC) model

The simplest leptonic model typically used to describe the emission from blazars like Mrk 421 is the one-zone synchrotron self-Compton (SSC) scenario, see sec. 3.1.3. To model the Mrk 421 MWL SED from January 2010, the SSC model described in [Tak10] was applied: The electron injection spectrum is parametrised with two or three power law functions of the form

$$N_e^{\mathrm{inj}}(\gamma) = \begin{cases} q_e\, \gamma^{-s_1} & \text{for} \quad \gamma_{\mathrm{min}} < \gamma < \gamma_{\mathrm{br}} \\ q_e\, {\gamma_{\mathrm{br}}}^{s_2-s_1}\, e^{\frac{\gamma_{\mathrm{br}}}{\gamma_{\mathrm{max}}}}\, \gamma^{-s_2}\, e^{\frac{-\gamma}{\gamma_{\mathrm{max}}}} & \text{for} \quad \gamma_{\mathrm{br}} < \gamma < \gamma_{\mathrm{max}} \end{cases}$$

or

$$N_e^{\mathrm{inj}}(\gamma) = \begin{cases} q_e\, \gamma^{-s_1} & \text{for} \quad \gamma_{\mathrm{min}} < \gamma < \gamma_{\mathrm{br1}} \\ q_e\, {\gamma_{\mathrm{br1}}}^{s_2-s_1}\, \gamma^{-s_2} & \text{for} \quad \gamma_{\mathrm{br1}} < \gamma < \gamma_{\mathrm{br2}} \\ q_e\, {\gamma_{\mathrm{br1}}}^{s_2-s_1}\, {\gamma_{\mathrm{br2}}}^{s_3-s_2}\, e^{\frac{\gamma_{\mathrm{br2}}}{\gamma_{\mathrm{max}}}}\, \gamma^{-s_3}\, e^{\frac{-\gamma}{\gamma_{\mathrm{max}}}} & \text{for} \quad \gamma_{\mathrm{br2}} < \gamma < \gamma_{\mathrm{max}} \end{cases}$$

with all quantities measured in the comoving frame of the emission region. These injection spectra have one or two break values at the corresponding electron Lorentz

factors $\gamma_{\rm br}$ or $\gamma_{\rm br1}$ and $\gamma_{\rm br2}$, respectively, which are free parameters of the model. Broken injection spectra are motivated by radiative losses (cooling), which become significant above a certain electron Lorentz factor (break value $\gamma_{\rm br}$ and $\gamma_{\rm br2}$ in the corresponding models). Break value $\gamma_{\rm br1}$ in the double-broken spectrum is motivated by acceleration-intrinsic effects, leading to the broken shape. For meaning and interpretation of the break values, please see sec. 11.1.2. Depending on the demanded shape of the fit, the simple-broken or double-broken injection spectrum was chosen. The double-broken injection spectrum allows to fit two different slopes in the rising edge of the synchrotron emission below and above the corresponding break. This was required to include the optical/UV measurements into the model fit. The normalisation factor q_e, representing the number density of relativistic electrons, the electron Lorentz factors $\gamma_{\rm min}$ and $\gamma_{\rm max}$, representing the edges of the injection spectrum, and the spectral indices s_1 and s_2 or s_1, s_2 and s_3 are also free parameters of the model. Additional general parameters (corresponding to the assumptions discussed in sec. 3.1.3) are the size of the comoving emission region R, the homogeneous magnetic field in the comoving emission region of strength B and the beaming (Doppler) factor of the jet, given by $\delta = 1/[\Gamma(1 - \beta\cos\theta)]$, with Γ the bulk Lorentz factor of the emission region and θ the angle between the line of sight and the direction of the relativistic jet. The emission region can be constrained by the timescale of flux variations from a simple argument: Assuming a homogeneous one-zone emission region, flux variations of the timescale $t_{\rm var}$ can only occur in regions of sizes R, which are less or equal $t_{\rm var}$ times the speed of light c. Since the variations are measured in the observer frame, the beaming factor and redshift have to be taken into account. This holds:

$$R \leq \frac{\delta\, c\, t_{\rm var}}{1+z}\,. \tag{10.1}$$

The following approach was used for the modelling itself: First, the spectral slopes of the electron injection spectrum were adjusted according to the slopes of the synchrotron emission component of the SED. The slopes below and above the synchrotron peak therefore determine the slopes of the injection spectrum. Also the slopes of the inverse Compton (IC) component are determined in this way, since in the SSC scenario the IC emission is connected to the shape of the synchrotron spectrum (see sec. 3.1.3). Then, the break Lorentz factor(s) $\gamma_{\rm br}$, the magnetic field B, the beaming δ and electron number density q_e were adjusted according to the positions, distance and flux level of the synchrotron and IC peaks. Differences in the slope of the rising edge of the synchrotron and IC components were then balanced by adjusting the minimum Lorentz factor $\gamma_{\rm min}$.

From the model parameters, secondary information on the energetics of the emission can be calculated. Such are the electron energy density

$$U_e = m_e c^2 \int_{\gamma_{\rm min}}^{\gamma_{\rm max}} {\rm d}\gamma\, \gamma\, N_e^{\rm inj}(\gamma)\,, \tag{10.2}$$

the total electron energy

$$E_e = \frac{4\pi}{3} R^3 U_e \,, \tag{10.3}$$

and the energy density of the magnetic field

$$U_B = \frac{B^2}{8\pi} \,. \tag{10.4}$$

All three quantities are measured in the comoving frame.

For a detailed verification of the used code please see app. E.

10.3 MWL and model results

Figs. 10.1 – 10.6 show the MWL results containing MAGIC EBL corrected data (as presented in chapter 9) and simultaneous observations of the above mentioned instruments sorted by the specific MAGIC analysis periods (as defined in chapter 9). The values of the shown SEDs are listed in app. D.2. The two hump structure of blazar emission is clearly visible for each analysis period: The first peak, caused by synchrotron radiation in the synchrotron self-Compton (SSC) model, is clearly resolved in the X-ray regime by the Swift/XRT instrument and its rising edge in the optical/UV regime by the optical instruments and Swift/UVOT. The second peak, caused by inverse Compton (IC) scattering in the SSC model, is resolved by MAGIC (for the apparent two-peak structure in the MAGIC results of the observation periods P1, F1a and P2 please see sec. 9.6).

10.3.1 Two-break SSC model

First, the MWL SEDs were modelled with the one-zone SSC model with double-broken injection spectrum. Such an injection spectrum allows to fit two different slopes of the rising edge of the synchrotron emission below and above the corresponding break. This was required to include the optical/UV data into the model fit. Also [Abd11b] uses a double-broken injection spectrum to fit the SED of Mrk 421.

Each analysis period was modelled individually, the resulting model parameters are listed in tab. 10.1. The resulting values of U_e, E_e and U_B are also listed. The corresponding fits are shown in figs. 10.1 – 10.6.

An assumption for the model was an emission region of constant size, motivated by the concept of one region of stable dimension, in which environmental changes lead to the observed flux variations. This constant size was found to be $R = 2.51 \cdot 10^{16}$ cm ($\log_{10} R = 16.4$). Since no significant intranight variability was observed in the MAGIC datasets (see sec. 9.4), the variability timescale t_{var} was approximated to be of the order of 1 day ($t_{\mathrm{var}} = 8.64 \cdot 10^4$ s). According to eq. 10.1, the variability timescale gives an upper limit on the size of the emission region depending on the beaming factor δ. For the smallest found value of $\delta = 32$, this leads

to an upper limit of $R \leq 8.04 \cdot 10^{16}$ cm ($\log_{10} R \leq 16.91$). The size of the emission region used for the modelling fulfils this condition.

The found models describe satisfactorily the SED of each analysis period. Radio data were treated as upper limit, since these single dish measurements integrate over a region that is orders of magnitude larger than the blazar emission region. A slight weakening of the goodness of the fit had to be accepted in the low X-ray and low VHE γ-ray data points. This is due to the required match of the fit to the optical/UV data.

10.3.2 One-break SSC model

The two-break SSC model follows the MWL data points quite well, but also shows deviations in the low energy X-ray and VHE γ-ray range. Particularly in the analysis periods F1, F1a, P2 and F2, the curvature of the low energy X-ray data points suggests a steeper slope of the SED in this region than the slope required by matching the optical/UV data. In period P3, also the shape of the IC peak strongly suggests a different model shape than the one matching the optical/UV data. Under the assumption that most of the optical/UV emission is not correlated with the X-ray and VHE γ-ray emission, the SEDs were also fitted treating the optical/UV measurements as upper limits. In this case, a more simple, one-break SSC model was sufficient to fit the X-ray and VHE γ-ray data. Each analysis period was modelled individually, the resulting model parameters are listed in tab. 10.2. The resulting values of U_e, E_e and U_B are also listed. The corresponding fits are also shown in figs. 10.1 – 10.6. Radio data were again treated as upper limits.

Also in the one-break model, the emission region size was assumed to be constant ($R = 9 \cdot 10^{15}$ cm ($\log_{10} R = 15.954$)). The upper limit on the emission region size according to the approximated variability timescale of 1 day and following eq. 10.1 (see above) holds $R \leq 1.13 \cdot 10^{17}$ cm ($\log_{10} R \leq 17.05$) for the found beaming factor $\delta = 45$. As in the two-break model, the found emission region size fulfils this condition.

The inserts of figs. 10.1 – 10.6, representing a zoomed-in view of the MAGIC data range, clearly show that the difference between the two-break and the one-break model in the VHE γ-ray regime rises with decreasing flux level: While the difference is small for the flare periods F1 and F2, it increases over period F1a to periods P1, P2 and P3. Here, the position of the IC peak is located at lower energies in the two-break model than it is in the one-break model. This is a consequence of the different shapes of the synchrotron peak, which were required for including and excluding the optical/UV data in the two-break and one-break model, respectively.

10.4 Sequential view and implications

Fig. 10.7 shows the time development of the MWL SEDs of flare F1 and its adjacent periods F1a, P1 and P2 in a zoomed-in view of the optical/UV, X-ray and VHE

γ-ray regimes. The best matching models are also shown (one-break model). While the optical/UV measurements stay stable during the periods P1, F1, F1a and P2, the flux of the X-Ray and VHE γ-ray regime shows huge fluctuations: The X-ray and VHE γ-ray measurements rise from period P1 to period F1 (flare) and decrease afterwards in period F1a and P2. Additionally, the peak positions, nicely covered within these measurements, move to higher energies. A presented in sec. 9.9, the γ-ray peak shows a general correlation with the flux level: For increasing fluxes, the peak shifts to higher energies. Remarkably, the position of the X-ray peak does not seem to be connected to the flux state, since it clearly shifts to higher energy with each subsequent analysis period.

The time development of flare F2 and its adjacent periods P2 and P3 (see fig. 10.8) also shows a flux increase in the X-ray and VHE γ-ray regime for F2 with respect to P2 and a subsequent decrease in P3. The peak position in the γ-ray regime correlates with the flux level as stated in sec. 9.9, while the peak position in the X-ray range again subsequently shifts to higher energies from P2 over F2 to P3. Additionally and in contrast to F1, also the optical/UV measurements show a variation: Here the flux decreases steadily from P2 over F2 to P3. This strongly suggests that the flares in the X-ray and VHE γ-ray regime do not have connected emission in the optical/UV range.

Fig. 10.9 shows the development of the non-constant two-break model parameters as a function of the analysis period. The beaming factor δ, the magnetic field strength B and the spectral indices s_2 and s_3 seem to be correlated with the flare periods, whereas the other parameters show variations but no correlation with the flares. Fig. 10.10 shows the development of the energetic properties of the two-break model. Since the magnetic field strength B seems to be correlated with the flares, also the magnetic field density shows the same correlation. The electron density and total electron energy show a decrease through the periods P1 – P2 and a strong increase for flare F2.

Fig. 10.11 shows the development of the one-break model parameters as a function of the analysis period. The only parameter correlated with the flares seems to be q_e, which is increased for the flare periods (900 cm^{-3} for F1 and F1a, 1030 cm^{-3} for F2) and decreased for the non-flare periods (800 cm^{-3} for P1, 650 cm^{-3} for P2 and 700 cm^{-3} for P3). The parameters correlated with the flares in the two-break model (beaming δ, magnetic field strength B and the second spectral index s_2) are not correlated with the flares in the one-break model. δ is constant at a value of 45, B decreases or stays constant from P1 to F2 and increases again for P3. The spectral indices s_1 and s_2 (comparable to s_2 and s_3 in the two-break model, since both indices characterise the injection spectrum around the main break) also show no correlation.

Fig. 10.12 shows the development of the energetic properties in the one-break model. The change in electron density and total electron energy for the flare periods is obviously connected to the value change of q_e. The magnetic field density shows the same behaviour as the magnetic field itself.

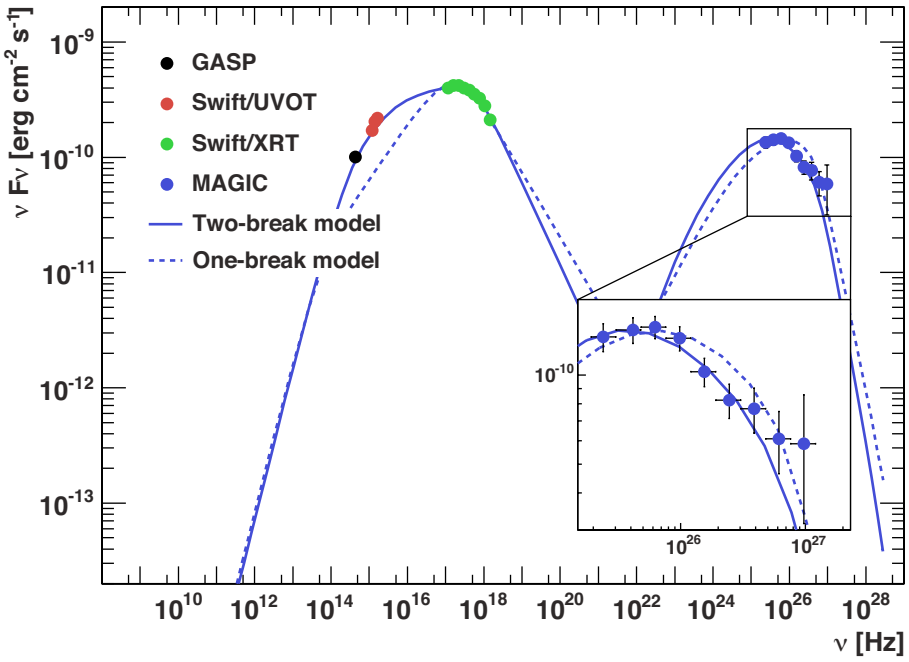

Figure 10.1: MWL SED for pre-flare period P1. Shown are the results of the dedicated instruments and the SSC model fits.

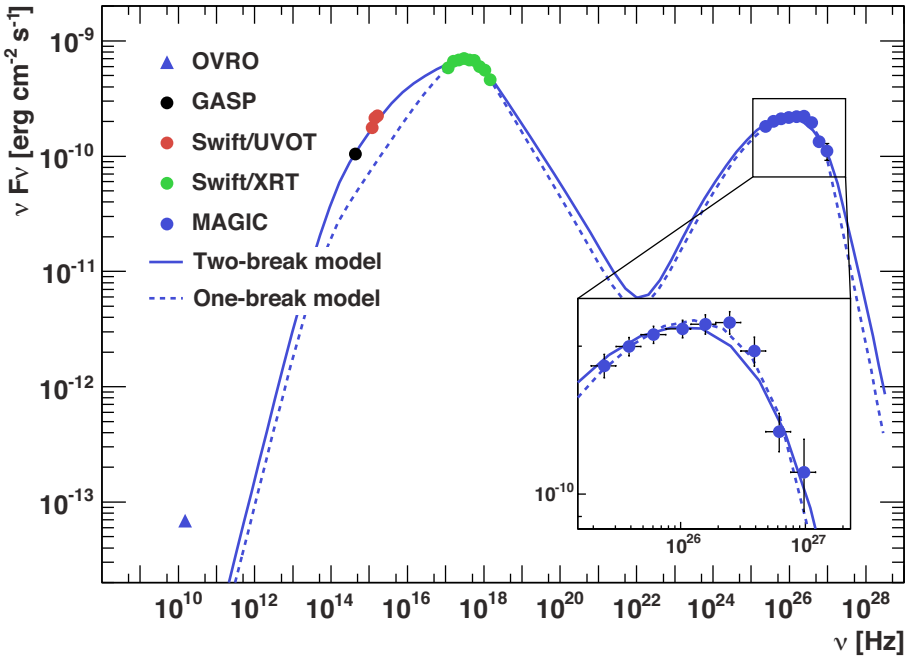

Figure 10.2: MWL SED for flare period F1. Shown are the results of the dedicated instruments and the SSC model fits.

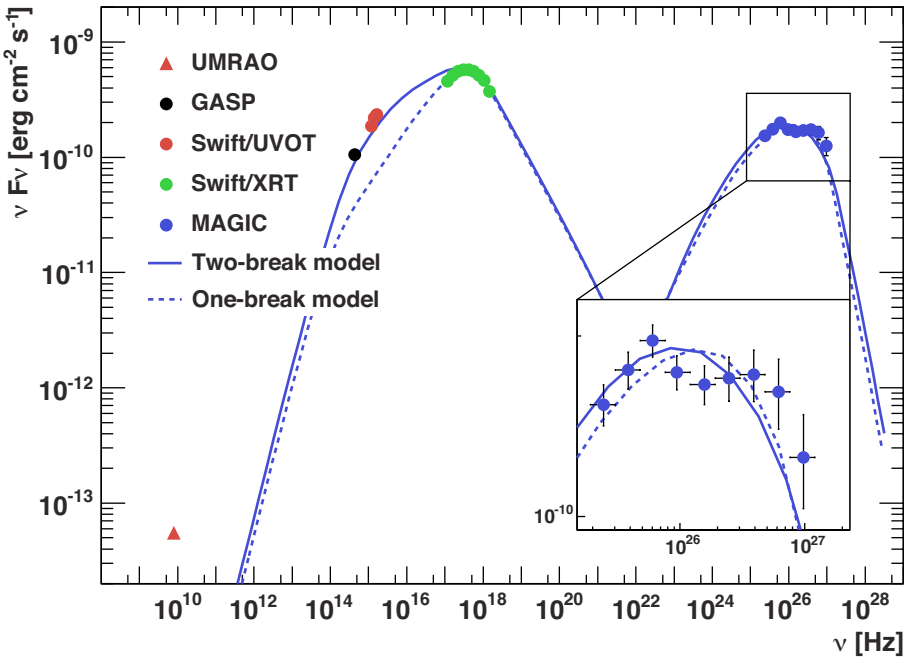

Figure 10.3: MWL SED for flare period F1a. Shown are the results of the dedicated instruments and the SSC model fits.

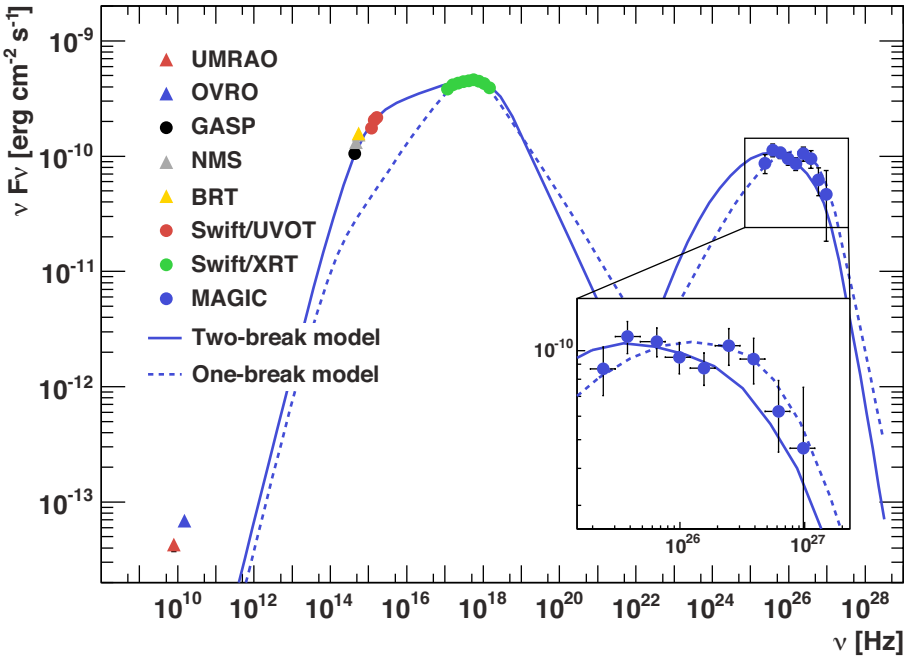

Figure 10.4: MWL SED for pre-/post-flare period P2. Shown are the results of the dedicated instruments and the SSC model fits.

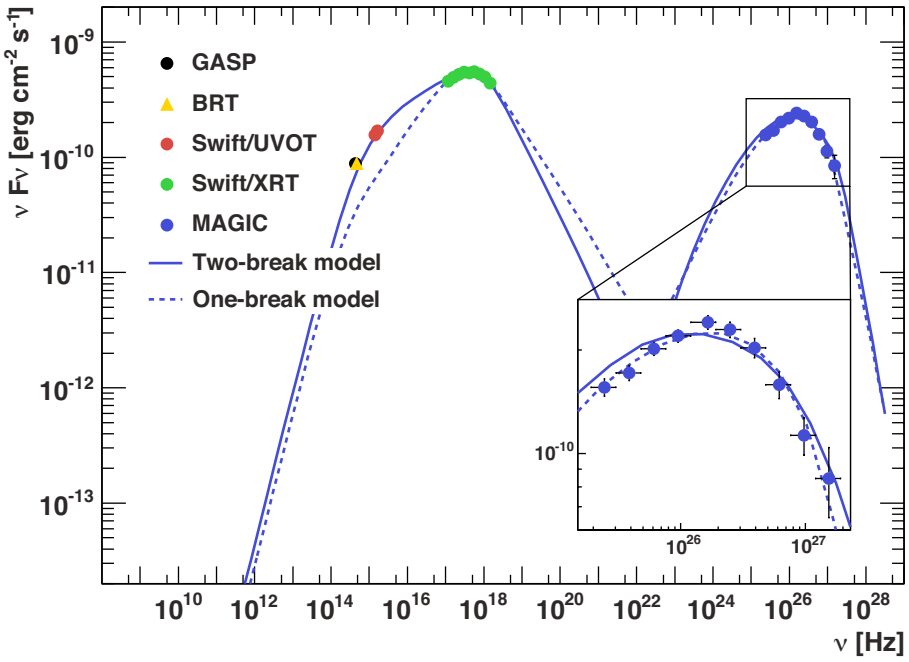

Figure 10.5: MWL SED for flare period F2. Shown are the results of the dedicated instruments and the SSC model fits.

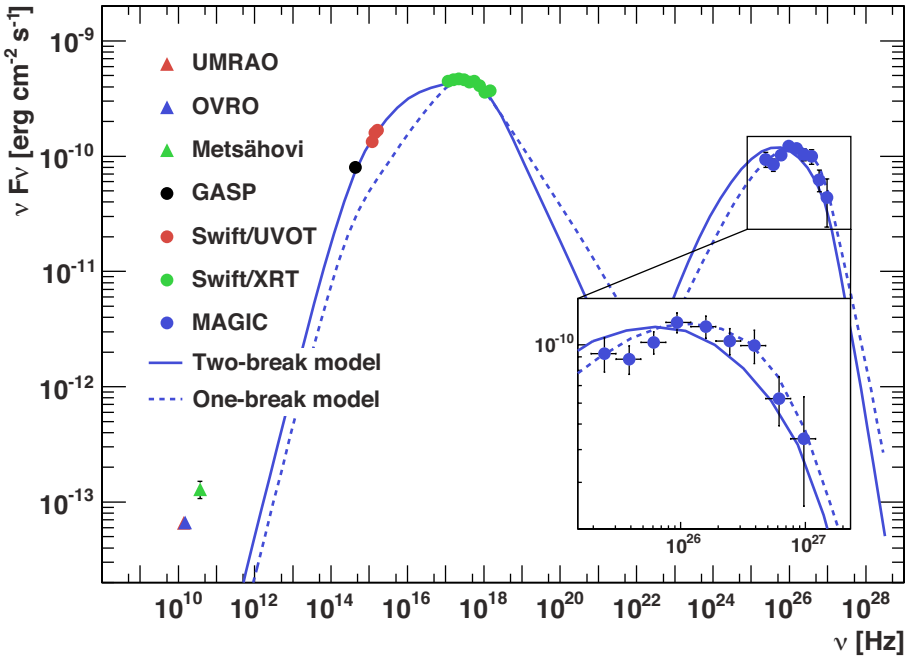

Figure 10.6: MWL SED for post-flare period P3. Shown are the results of the dedicated instruments and the SSC model fits.

Parameter	Symbol	P1	F1	F1a	P2	F2	P3
Emission region [$\log_{10}$ cm]	R	16.4	16.4	16.4	16.4	16.4	16.4
Beaming factor	δ	32	50	50	36	50	36
Magnetic field [mG]	B	40	18	17	40	13	34
Electron number density [cm^{-3}]	q_e	130	90	90	115	120	90
Minimum electron Lorentz factor [10^3]	$\gamma_{\rm min}$	7	5	8	8	12	8
Break 1 electron Lorentz factor [10^4]	$\gamma_{\rm br1}$	3	4	4	2	4	4
Break 2 electron Lorentz factor [10^5]	$\gamma_{\rm br2}$	3	3.7	3.8	5	5.5	4
Maximum electron Lorentz factor [10^8]	$\gamma_{\rm max}$	1	1	1	1	1	1
Low-energy electron spectral index	s_1	1.9	1.9	1.9	1.9	1.9	1.9
Medium-energy electron spectral index	s_2	2.75	2.55	2.55	2.75	2.55	2.75
High-energy electron spectral index	s_3	4.4	4.0	4.2	4.4	4.3	4.4
Electron density [10^{-4} erg cm^{-3}]	U_e	7.484	6.965	6.149	5.344	7.392	5.612
Total electron energy [10^{46} erg]	E_e	4.968	4.624	4.082	3.548	4.908	3.726
Magnetic field density [10^{-5} erg cm^{-3}]	U_B	6.366	1.289	1.150	6.366	0.672	4.599

Table 10.1: Parameter values of the Mrk 421 MWL SED one-zone SSC model with double-broken injection spectrum. Radio data were treated as upper limits for these model fits.

Parameter	Symbol	P1	F1	F1a	P2	F2	P3
Emission region [$\log_{10}$ cm]	R	15.954	15.954	15.954	15.954	15.954	15.954
Beaming factor	δ	45	45	45	45	45	45
Magnetic field [mG]	B	42	42	36	36	32	39
Electron number density [cm^{-3}]	q_e	800	900	900	650	1030	700
Minimum electron Lorentz factor [10^3]	γ_{min}	3	3	4	4	6	6
Break electron Lorentz factor [10^5]	γ_{br}	1.6	2.2	2.5	2.8	2.8	2.2
Maximum electron Lorentz factor [10^8]	γ_{max}	1	1	1	1	1	1
Low-energy electron spectral index	s_1	2.0	2.0	2.0	2.0	2.0	2.0
High-energy electron spectral index	s_2	4.1	4.1	4.2	4.0	4.0	4.0
Electron density [10^{-3} erg cm^{-3}]	U_e	2.904	3.500	3.368	2.516	3.645	2.339
Total electron energy [10^{46} erg]	E_e	0.885	1.067	1.027	0.767	1.111	0.713
Magnetic field density [10^{-5} erg cm^{-3}]	U_B	7.019	7.019	5.157	5.157	4.074	6.052

Table 10.2: Parameter values of the Mrk 421 MWL SED one-zone SSC model with simple-broken injection spectrum. Radio, optical and UV data were treated as upper limits for these model fits.

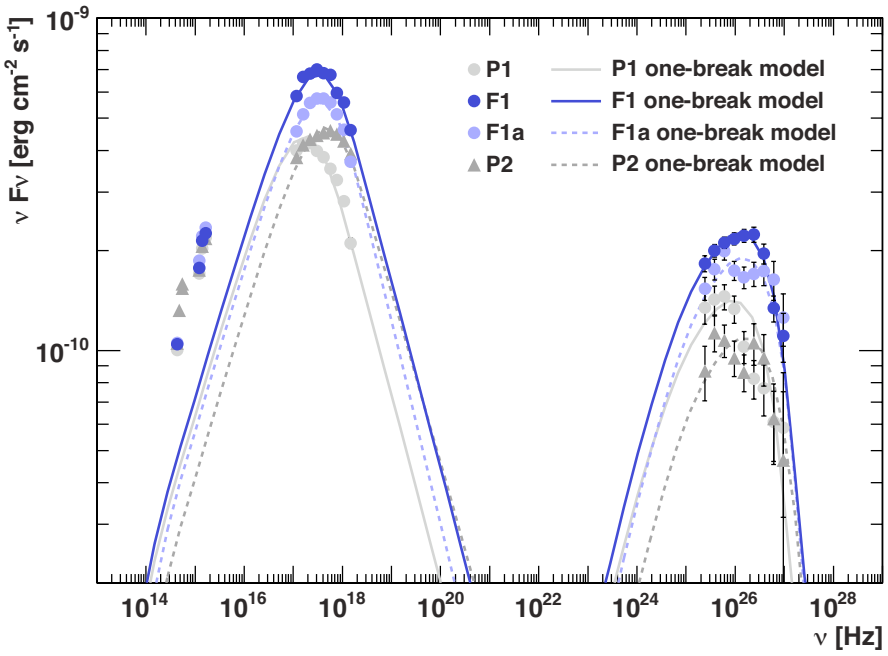

Figure 10.7: MWL SEDs (zoomed-in view of the optical/UV, X-ray and VHE γ-ray regimes) of analysis periods P1, F1, F1a and P2, depicting the time development of the F1 flare and adjacent periods. Shown are also the best matching SSC model fits for each period.

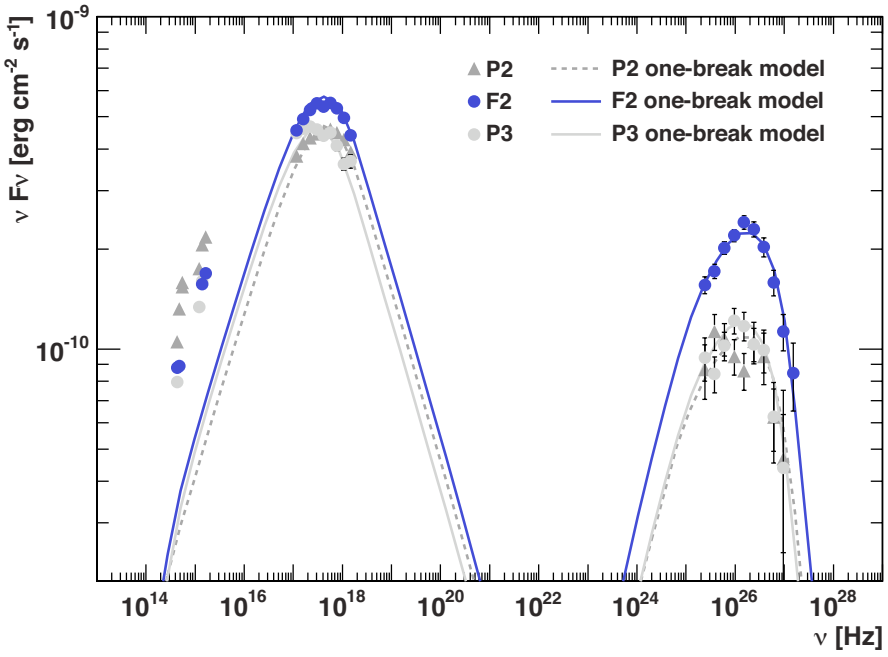

Figure 10.8: MWL SEDs (zoomed-in view of the optical/UV, X-ray and VHE γ-ray regimes) of analysis periods P1, F1, F1a and P2, depicting the time development of the F2 flare and adjacent periods. Shown are also the best matching SSC model fits for each period.

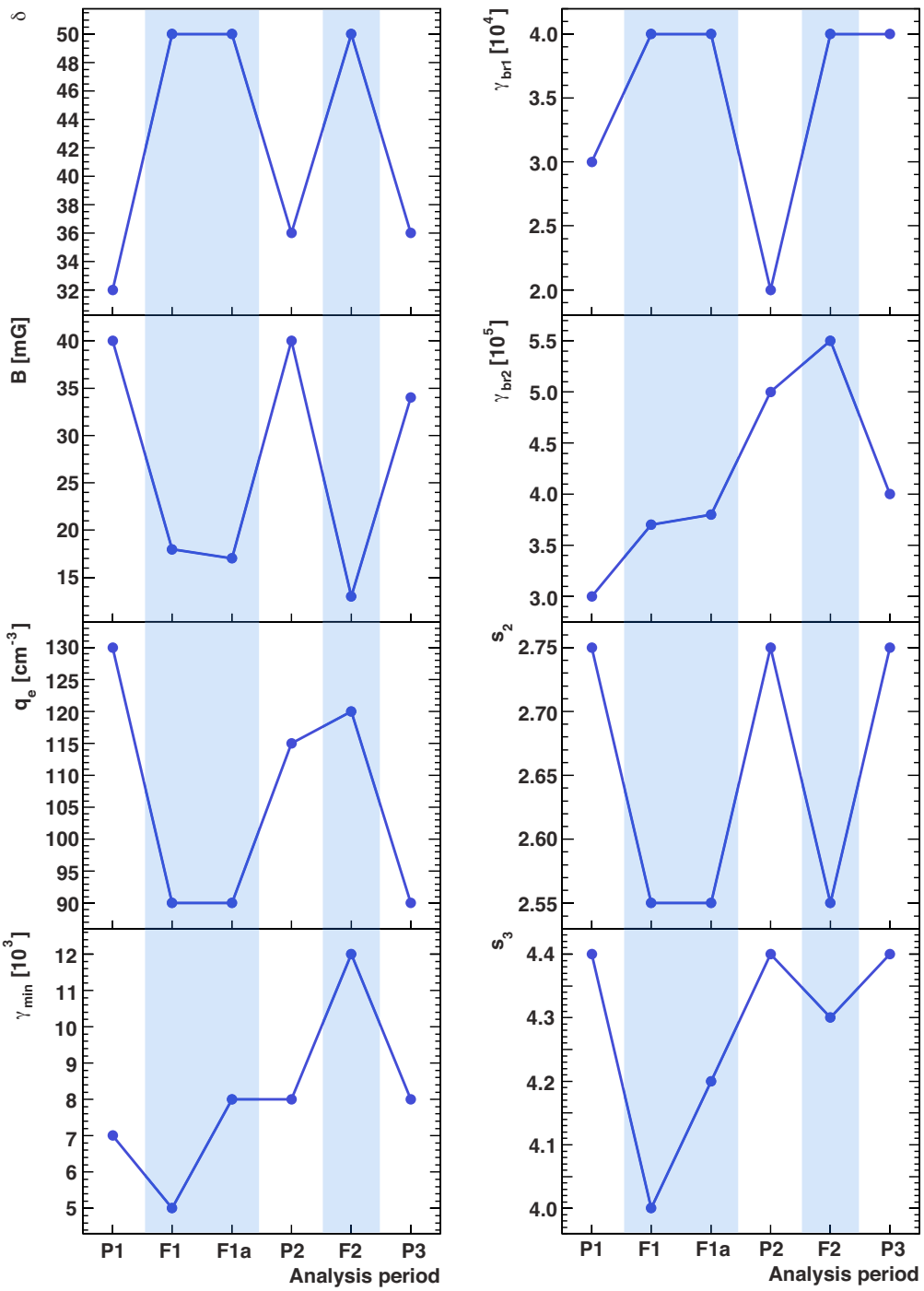

Figure 10.9: Development of model parameters for the one-zone SSC model with double-broken injection spectrum. Radio data were treated as upper limits for these model fits. The flare periods are marked with light-blue colour.

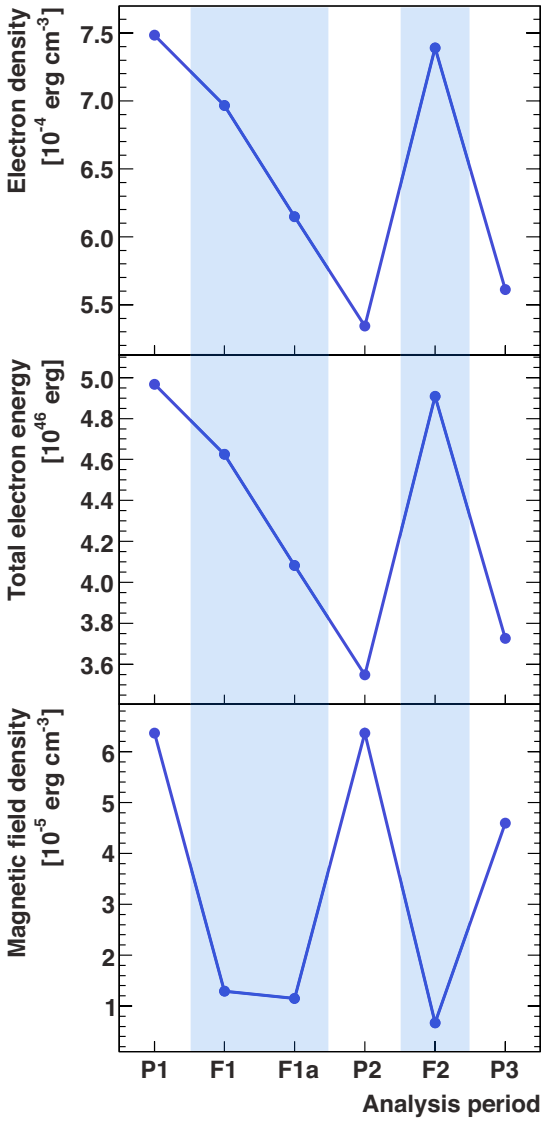

Figure 10.10: Development of energetic properties for the one-zone SSC model with double-broken injection spectrum. The flare periods are marked with light-blue colour.

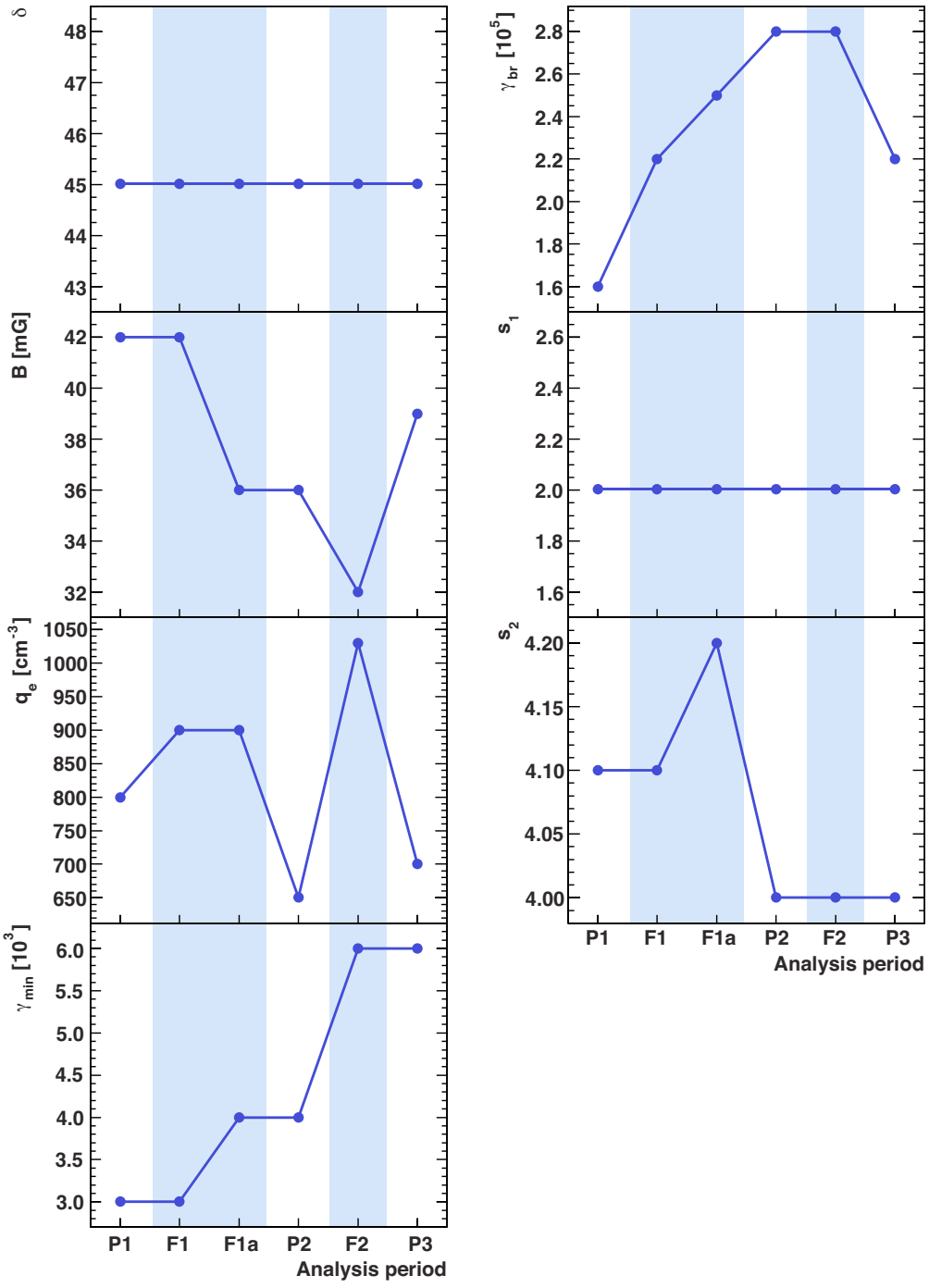

Figure 10.11: Development of model parameters for the one-zone SSC model with simple-broken injection spectrum. Radio, optical and UV data were treated as upper limits for these model fits. The flare periods are marked with light-blue colour.

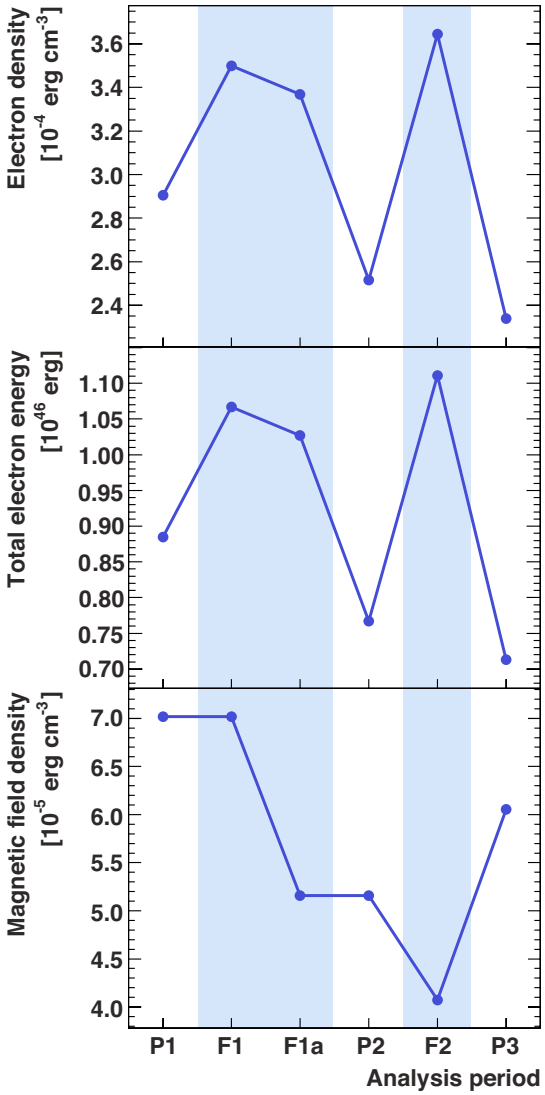

Figure 10.12: Development of energetic properties for the one-zone SSC model with simple-broken injection spectrum. The flare periods are marked with light-blue colour.

Chapter 11

Discussion

In the previous chapter, the MWL SEDs were fitted with two SSC models: One with a double-broken, the other with a simple-broken power law electron injection spectrum. For both models, the found parameter values of the injection spectrum q_e, γ_{br1}, γ_{br2}, γ_{min}, γ_{max}, s_1, s_2 and s_3 and of the general environment R, B and δ are within the range of SSC parameters in the literature for HBL in general [Cel08, Lef11, Tag08, Tav01, Tav09, Tav10] and for Markarian (Mrk) 421 in particular [Abd11b, Ale11b, Bed97b, Fos08, Ghi02, Kat06a, Kon03, Man11, Mar99, Tav98]. Since the double-broken injection spectrum was firstly used for Mrk 421 in [Abd11b], there is no large set of comparative parameter values on the additional break in the literature. But as the double-broken spectrum represents an injection spectrum with additional spectral shape information, one can compare the double-broken spectrum within the ranges of given simple-broken spectra. Here, the found values do not exceed the limits set by previous works. Other parameters range in the lower limits from literature values, as there are the magnetic field strength B in both of the models ($13-40$ mG two-break model, $32-42$ mG one-break model) and the electron number density q_e in the two-break model ($90-130$ cm^{-3}). The found size of the emission region R is an order of magnitude larger than in most of the previous models (due to the comparatively large variability timescale), but still within the range of all assumed emission region sizes so far for this source.

In the following sections, interpretation and physical consequences of the found parameter values are discussed.

11.1 Injection spectrum

11.1.1 Minimum electron Lorentz factor

In both models, the low energy slope of the γ-ray peak and therefore the small width of the peak requires a large and varying value of γ_{min} ($(5-12)\cdot 10^3$ in the two-break model, $(3-6)\cdot 10^3$ in the one-break model). Fig. 11.1 exemplarily shows the effect of γ_{min} variation for the F2 period (two-break model), for which the largest γ_{min} was required ($12\cdot 10^3$). A large γ_{min} parameter leads to a narrow

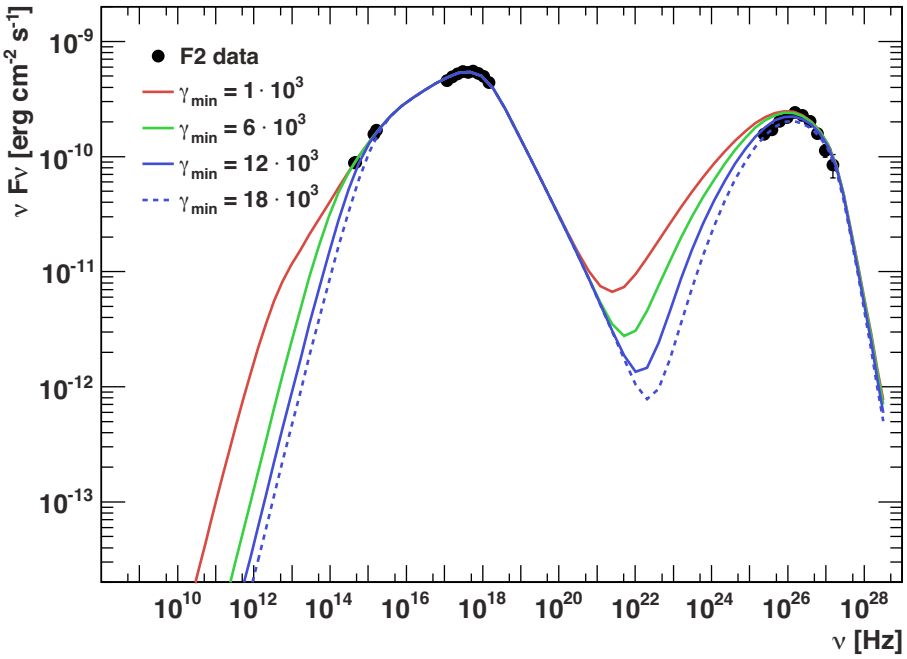

Figure 11.1: Effect of γ_{min} variation, exemplarily shown for the F2 period (two-break model). Other model parameters are fixed. A larger γ_{min} value bends the low energy edge of the IC component, producing a narrow IC peak without influencing the slope of the fit right below the synchrotron peak. But since the low energy edge of the synchrotron component gets truncated, the optical data points give an upper limit on the size of γ_{min}. Therefore, the best fit for the F2 two-break model uses $\gamma_{\mathrm{min}} = 12 \cdot 10^3$.

inverse Compton (IC) peak without influencing the slope of the fit right below the synchrotron peak (the low energy edge of the synchrotron gets truncated for large γ_{min}, but the slope below the peak does not change).

In the literature, large γ_{min} values up to 10^5 are used to model hard γ-ray spectra [Kat06a, Lef11, Tav09]. It is considered that the Fermi acceleration mechanism starts up at this energy and that the electrons are accelerated up to this energy by a pre-acceleration mechanism. If in addition the energy loss processes (*cooling* processes, see sec. 3.1.3) are inefficient for the low energy electrons (close to γ_{min}), the electron distribution will not develop a low energy tail below γ_{min} [Kat06a]. This is particularly true for flares, where the cooling timescale is large compared to the dynamic timescale (and this might point to an explanation, why the γ_{min} is larger for the flares studied in this work as for the ground state described in [Abd11b] ($4 \cdot 10^2$ and $8 \cdot 10^2$)). Also the comparatively small magnetic fields in both models ($B \approx 10 - 40$ mG) support the picture of inefficient cooling processes for the low energy electrons, since the synchrotron cooling timescale is proportional to $1/B^2$ (see eq. 3.17).

A conceivable pre-acceleration mechanism producing injection spectra truncated at such large γ_{min} values is magnetic reconnection [Tav09, Gia09]. Here,

magnetic energy is occasionally converted to kinetic energy (particle acceleration) by rearrangements of the magnetic topology (reconnection events). The acceleration of particles through this mechanism generally requires a highly magnetized jet with magnetic-to-kinetic energy ratios $\gg 1$ [Gia09]. For details on the application of magnetic reconnection to blazars please see [Gia09], for instance. Another possibility to produce truncated injection spectra is a process, in which electrons are efficiently accelerated at the shock front up to some maximal energy. Subsequently, the electrons escape and cool. The cooling processes might be compensated (re-heating, e.g. due to Fermi second order acceleration at magnetic turbulences [Kat06b]) and the Lorentz factor where re-heating and cooling balance might be identified with $\gamma_{\rm min}$ [Kat06a].

11.1.2 Spectrum shape and break values

For both model types, the break in the injection spectra at $\gamma_{\rm br} \approx 10^5$ is commonly interpreted as caused by cooling processes [Kin02, Kir98, Mar96, Zac10]. Following the time evolution of the electron distribution (eq. 3.9), these cooling processes are due to energy dependent synchrotron radiation and IC scattering. The break value at $\gamma_{\rm br} \approx 10^5$ marks the electron Lorentz factor, at which the cooling processes significantly effect the injection spectrum. In other words, this value separates those electrons which cool within the source ($\gamma > \gamma_{\rm br}$) from those which do not cool within the source ($\gamma < \gamma_{\rm br}$) [Kir98]. The resulting change in the spectral slope is found to be $\Delta s = 1.45 - 1.75$ for the double-broken and $\Delta s = 2.0 - 2.2$ for the simple-broken injection spectrum model.

The peak flux of the synchrotron peak dominates over the flux of the IC peak by a factor of $2 - 4$. In the SSC model, this flux ratio directly reflects the ratio of the corresponding cooling factors, i.e. the influences of the synchrotron and IC energy losses [Sch10]. Hence, a dominating synchrotron peak implies that the electrons mainly cool by synchrotron radiation.

The additional break at $\gamma_{br} \approx 10^4$ in the two-break model is commonly thought to be related to the acceleration process itself [Abd11a, Abd11b]. Below this break Lorentz factor, the acceleration process is effective and leads to a spectral slope of 1.9. Above the break, the slope is softer ($2.55 - 2.75$). The spectral slope resulting from first order Fermi acceleration is ≈ 2 (see sec. 3.2.1). Non linear effects, for instance strong shock modification, lead to values $s < 2$ [Ber99], whereas non-uniform magnetic fields with non-static field lines lead to disturbances in the stochastic transport of the particles and therefore to values $s > 2$ up to $s = 2.5$ [Kir96]. The found values of the spectral slope indicate such modifications. Additionally, the slope-separating break value is not necessarily pointing to a strict change in the acceleration process, but possibly is a first approximation of a curved injection spectrum. Such curved injection spectra might be caused by an overlap of the mentioned acceleration modifications, where the curved shape reflects a smooth transition of acceleration efficiency. Also episodic acceleration can cause curved electron spectra [Per05].

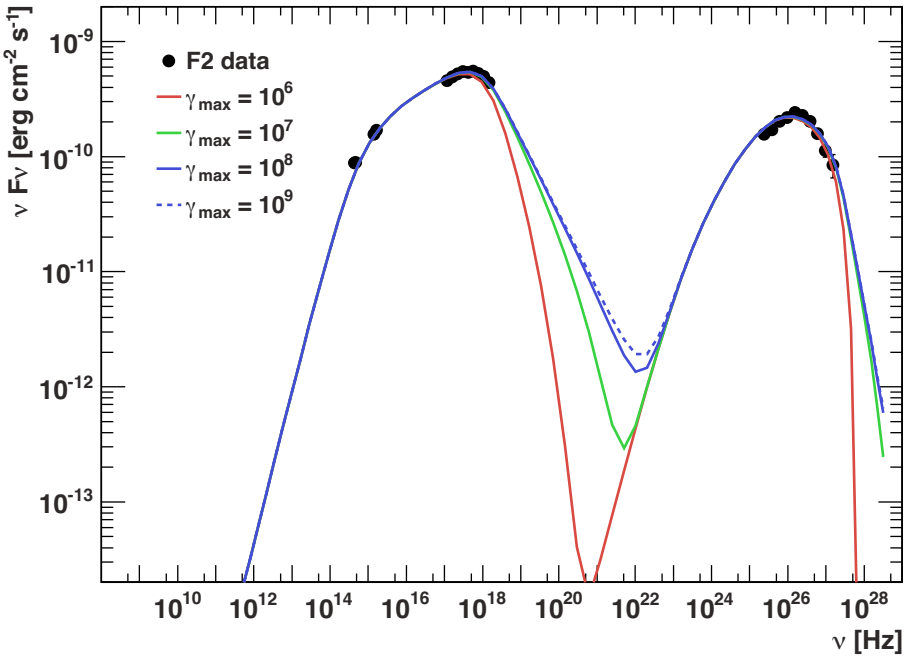

Figure 11.2: Effect of $\gamma_{\rm max}$ variation, exemplarily shown for the F2 period (two-break model). Other model parameters are fixed. The $\gamma_{\rm max}$ variation mainly influences the high energy part of the synchrotron component, which is not sufficiently covered by the observations. From the spectral slope right above the synchrotron peak one can conclude that the maximum Lorentz factor is of the order $\gamma_{\rm max} \gtrsim 10^7$.

11.1.3 Maximum achievable energy

In both models, the maximum electron Lorentz factor is set to $\gamma_{\rm max} = 10^8$. Fig. 11.2 exemplarily shows the effect of $\gamma_{\rm max}$ variation for the F2 period (two-break model). It is visible that the observations can not exactly constrain on this parameter, since the $\gamma_{\rm max}$ variation mainly influences the high energy part of the synchrotron component. But from the spectral slope right above the synchrotron peak one can conclude that the maximum Lorentz factor is of the order $\gamma_{\rm max} \gtrsim 10^7$. For the SED described in [Abd11b], observations in the high energy X-ray regime constrained $\gamma_{\rm max}$ to be $\gamma_{\rm max} = 10^8$. Since those observations mark the most complete SED measurement of Mrk 421 so far, $\gamma_{\rm max} = 10^8$ was also used in this work.

Maximum electron Lorentz factors of the order of 10^7 and 10^8 can only be reached in effective acceleration mechanisms as the first order Fermi acceleration (see sec. 3.2.4). Following eq. 3.18 for the maximum achievable energy in first order Fermi acceleration, one can compute the maximum electron energy $\gamma_{\rm max}^{\rm 1st}$ for a given magnetic field strength. Assuming a non-relativistic shock front ($u_s = 0.1\,c$, with u_s the shock velocity measured in the upstream frame [Rie06]) and using the found range of magnetic field strengths $B = 13 - 42$ mG results in a maximum electron Lorentz factor $\gamma_{\rm max}^{\rm 1st} = (2.4 - 4.4) \cdot 10^7$. This range is smaller than the assumed

value of $\gamma_{\max} = 10^8$, but fits to the lower limit of $\gamma_{\max} \gtrsim 10^7$ as discussed above. An acceleration mechanism with higher efficiency or a higher shock velocity u_s results in higher values of $\gamma_{\max}$ as calculated from eq. 3.18. For instance, doubling u_s to $u_s = 0.2\,c$ also doubles the maximum achievable energy to $\gamma_{\max}^{1\text{st}} = 8.8 \cdot 10^7$ (for the smallest magnetic field strength $B = 13$ mG), which is of the order of the assumed fit value.

11.2 Parameter development in two-break model

In the two-break model, four parameters were found to be correlated with the flares: The beaming factor δ, the magnetic field strength B and the second and third spectral index of the electron injection spectrum s_2 and s_3. A similar result is found on an analysis of Mrk 421 data in [Man11]: The MWL SED of nine observation periods from 2001 – 2008 were fitted with a one-zone SSC model with a simple-broken injection spectrum. Then, the found model parameters and their corresponding flux states were compared with one another. Those results suggest that the beaming factor and the electron spectrum break energy increase with source activity, whereas the magnetic field strength decreases. The other parameters turn out to be uncorrelated with source activity [Man11]. This is consistent with the correlation of δ and B with source activity found in this work. The increase of the break energy for high activity found in [Man11] can be interpreted as an increase of high energy electrons. The decrease with source activity of s_2 and s_3 found in this work (the electron injection spectrum gets harder below and above the second break) also reflects an increase of high energy electrons. In this way, the increase of the break energy in [Man11] and the decrease of s_2 and s_3 in this work are related to the same physical effect in the injection spectrum.

This consistency seems to represent a general feature of the blazar emission in Mrk 421. As [Man11] compares source activity over long time intervals (order of years), this work compares the activity changes on a day-to-day basis. Both analyses result in the same parameter correlations within the SSC framework. Although this result might be biased by the choice of the model, it consolidates the understanding of long- and short-term activities of Mrk 421.

11.2.1 Connection between B and δ

As discussed, the two-break model shows a correlation of the flare periods with the magnetic field strength B and the beaming (Doppler) factor δ. The magnetic field strength B is decreased during the flare states and increased for the pre- and post-flare states, while the beaming δ is increased for the flare states and decreased for the pre- and post-flare states. Both parameters can be connected in the framework of a emission region which is moving down the jet (see fig. 11.3): In a conical jet, the size of the emission region R scales with the distance to the black hole d as $R \propto d^{1/2}$ [Man11, Vla04, Kom07]. If the magnetic flux in the emission region is conserved, this consequently leads to $B \propto R^{-2} \propto d^{-1}$. In this scenario, also the

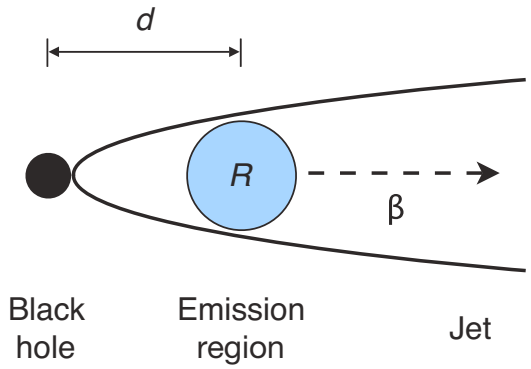

Figure 11.3: Sketch of a moving emission region in a conical jet (not to scale). The emission region is moving with relativistic velocity $\beta = v/c$. The distance to the black hole is denoted as d.

bulk Lorentz factor Γ scales as $\Gamma \propto d^{1/2}$ [Vla04, Kom07]. From this one finds $B \propto \Gamma^{-2}$. In the limit of $\delta \propto \Gamma$ (which is valid for small viewing angles θ), this results in $B \propto \delta^{-2}$ [Man11]. Under these assumptions, large beaming factors δ, occurring at large distances d from the black hole, call for small magnetic field strengths B. Small beaming factors, occurring near the black hole and therefore presumably closer to the formation of the emission region, call for large magnetic field strengths. In this way, a just formed emission region (a "young" region), close to the central black hole, results in a parameter set like the one used to model the non-flare periods. This view is supported by the fact that the change in the beaming parameter δ is roughly by a factor of 1.5 from non-flare to flare state, while the change in B is roughly by a factor of $0.4 \approx 1.5^{-2}$. This reflects the expected proportionality $B \propto \delta^{-2}$.

To the contrary, the emission region size R is found to be constant for all the observation periods ($\log_{10} R = 16.4$). In the framework discussed above, the emission region scales as $R \propto B^{-1/2}$ and therefore should show a correlation with the flare states (small R in the pre- and post-flare periods and larger R in the flare periods). A possible explanation is that the variation of R is not resolved in the current analysis and model accuracy since R is proportional to $B^{-1/2}$. A decrease of B by a factor of 2 (as found in the two-break model) increases R only by a factor of ≈ 1.4. In this case, a constant R holds as a first approximation.

The distance of the emission region to the black hole can be approximated by $d \approx R/\alpha$, with $\alpha \approx 1/\Gamma \approx 1/\delta$ the jet opening angle [Abd11b] (this approximation is valid for large distances compared to the gravitational radius of the black hole ($d \gg R_\mathrm{g}$)). For the Mrk 421 black hole mass of $(2-9) \cdot 10^8 M_\odot$ [Bar03, Wu02], the corresponding gravitational radius is $R_\mathrm{g} \approx (0.6 - 2.7) \cdot 10^{14}$ cm. This leads to distances $d \approx (3.0 - 13.4) \cdot 10^3 R_\mathrm{g}$ for the pre- and post-flare periods and of $d \approx (4.6 - 20.9) \cdot 10^3 R_\mathrm{g}$ for the flare periods. This supports the picture of moving emission regions down the jet.

11.2.2 Connection between B, s_2 and s_3

The two-break model also shows a correlation of the flare periods with the magnetic field strength B and the spectral indices s_2 and s_3. These values are decreased during the flare periods and increased in the pre- and post-flare periods. The decrease of s_2 and s_3 results in a harder electron injection spectrum below and above the second break, which means that the number of high energy electrons is increased. This suggests a higher efficiency of the acceleration mechanism. In the context of Fermi acceleration mechanisms, the acceleration efficiency can be connected to the maximum achievable energy. As discussed in sec. 3.2.4, the maximum achievable energy γ_{max} is proportional to the magnetic field strength B for first and second order Fermi acceleration (see eq. 3.18 and 3.19): $\gamma_{\mathrm{max}} \propto B^{-1/2}$ (in regions with smaller B, the electrons can be accelerated to higher energies, since the synchrotron losses are less effective). This means that a decreasing B results in an increasing γ_{max}. If one associates the injection spectrum slope to the efficiency of the mechanism and therefore to γ_{max}, one can motivate a connection between B and s_2 and s_3. In this way, the variations of s_2 and s_3 are explained as a result of the variations of B.

Contrary to this argumentation is the stability of γ_{max} through all observation periods ($\gamma_{\mathrm{max}} = 10^8$). But like in the case of R (see above), where the same proportionality to B is predicted, the variations of γ_{max} might not be resolved (increase only by factor of 1.4 for halved B). In this case, $\gamma_{\mathrm{max}} = 10^8$ also holds as a first approximation for all periods.

11.2.3 Scenario implications

In the framework of a moving emission region in a conical jet, the magnetic field B, the beaming δ and the hardness of the electron spectrum (spectral indices s_2 and s_3) are connected as described above. Fig. 11.4 shows the influence of these correlated parameter changes for the total SED shape (scenario a): In this scenario, the values of B, δ, s_2 and s_3 change as found for the two-break model, while the other parameters are kept constant. For parameters which also show variations during the observed periods in the two-break model, the mean values were taken ($\gamma_{\mathrm{min}} = 8 \cdot 10^3$, $\gamma_{\mathrm{br1}} = 3.5 \cdot 10^4$, $\gamma_{\mathrm{br2}} = 4.2 \cdot 10^4$ and $q_e = 106$). It is clearly visible that this scenario can not satisfactorily explain the observed flux changes. This is particularly seen in P2 and F2 period, where this scenario shows large deviations from the observed spectral shape in both the synchrotron and IC component. This implies that this scenario and the correlated variations of B, δ, s_2 and s_3 are not exclusively responsible for the flux variations.

Scenario b, also shown in fig. 11.4, includes scenario a and additional variations of the electron number density q_e (as found for the two-break model). These additional changes of q_e can be motivated by changing local plasma densities in jet regions overrun by the emission region. But also scenario b can not satisfactorily explain the observed spectral changes, as is again particularly seen in period P2.

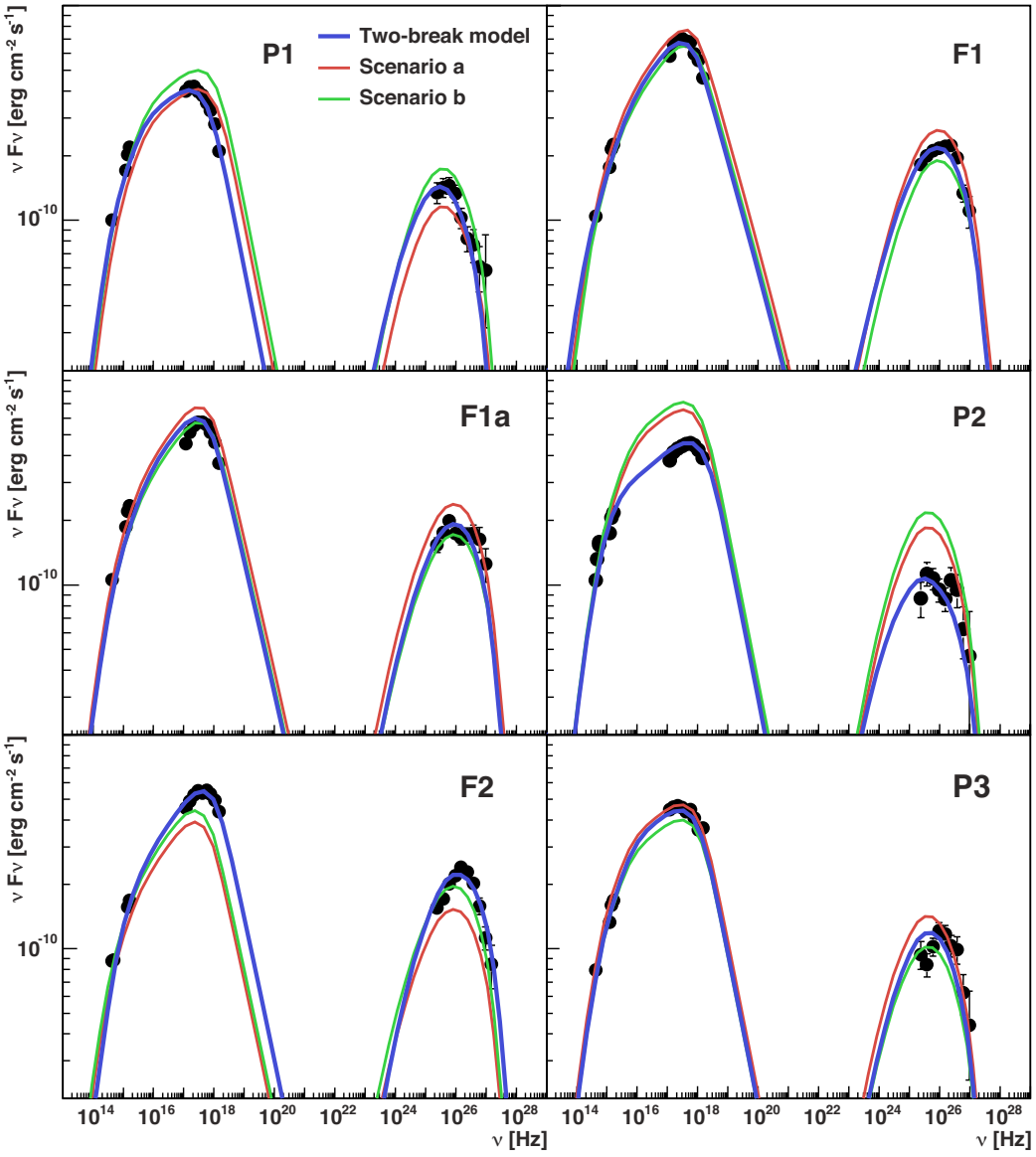

Figure 11.4: Scenario comparison two-break model (zoomed-in view of the optical/UV, X-ray and VHE γ-ray regimes). The best fitting two-break model is shown as blue line. Scenario a (red line): Correlated variation of B, δ, s_2 and s_3 as consequences of a moving emission region in a conical jet. Other model parameters are kept constant (mean value in case of non-constant parameters in the two-break model). Scenario b (green line): Scenario a plus variations of the electron number density q_e. Both scenarios can not satisfactorily explain the observed flux variations.

The failure of both scenarios in giving an explanation for the observed changes in the SED points to a high dynamic system of the flare emission. All parameters have to change in the way found for the two-break model. It is not a single parameter or a simple physics scenario, which is responsible for the main changes. Additional to B, δ, s_2, s_3 and q_e, also changes in the electron break Lorentz factors are required to entirely fit the observed data. This shows that the electron injection spectrum underlies various influences, which lead to these changes. While $\gamma_{\rm br1}$ is connected to the acceleration process itself, $\gamma_{\rm br2}$ is identified with the energy, at which the cooling processes significantly influence the electron spectrum. Therefore, changes in both values suggest variations both in the acceleration itself as in the influence of the cooling processes.

11.3 Parameter development in one-break model

To better match the X-ray and VHE γ-ray measurements, the MWL data were also fitted with a simple-broken injection spectrum. For these model fits, also the optical/UV measurements were treated as upper limits. This assumption can be motivated by the fact that the optical/UV emission does not show correlated emission to the flux variation in the X-ray and VHE γ-ray band. A possible way to explain this difference is the occurrence of an additional emission region, responsible for the flare emission in the X-ray and VHE γ-ray regime. In the one-break model fits, the optical/UV emission is a factor of 2 to 3 smaller than the measured emission. So, the additional region does contribute to the optical/UV emission, but does not dominate it as in the X-ray and VHE γ-ray regime.

The only parameter showing correlation to the flares is the electron number density q_e. Its value of $q_e = 900$ cm^{-3} and $q_e = 1030$ cm^{-3} during the flare periods F1, F1a and F2 is decreased to $q_e = 800$ cm^{-3}, $q_e = 650$ cm^{-3} and $q_e = 700$ cm^{-3} during the non-flare periods P1, P2 and P3. This can naturally explain the presence of the flares and the decreased flux before, in between and after: In the SSC model, the flux of the synchrotron peak is directly proportional to q_e ($F_{\rm sync} \propto q_e$), while the flux of the IC peak is proportional to q_e^2 ($F_{\rm IC} \propto q_e^2$). Fig. 11.5 shows the influence of the electron number density changes on the total SED shape (scenario c): In this scenario, only the q_e parameter changes as found for the one-break model, while the other parameters are kept constant. For parameters which also show variations during the observed periods in the one-break model, the mean values were taken ($B = 37.8$ mG, $\gamma_{\rm min} = 4.3{\cdot}10^3$, $\gamma_{\rm br} = 2.35{\cdot}10^5$ and $s_2 = 4.07$). Although deviations from the dataset are seen in period P1, this scenario can satisfactorily explain the overall spectral evolution for periods F1-P3. Small deviations, as in F2 period for instance, can be adjusted by the changes of the other parameters (fine tuning). For period P1, the additional change in the break Lorentz factor ($\gamma_{\rm br} = 1.6 \cdot 10^5$) and the magnetic field ($B = 42$ mG) adjust for the apparent deviation. Details of the spectral changes, for instance the observed hint for a shift of the SED peaks (see secs. 10.4 and 9.9), can not be explained in this scenario. However, the success

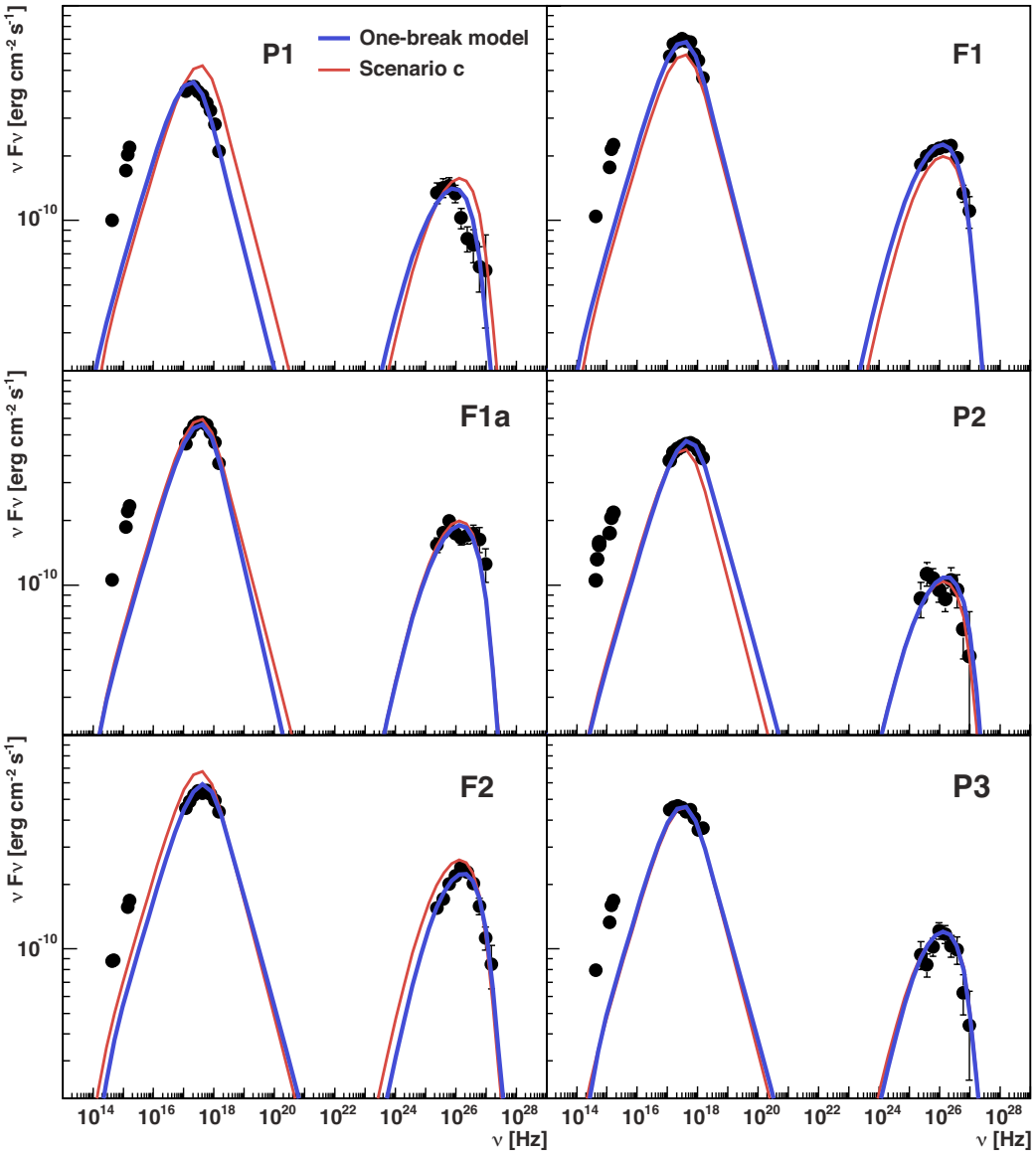

Figure 11.5: Scenario comparison one-break model (zoomed-in view of the optical/UV, X-ray and VHE γ-ray regimes). The best fitting one-break model is shown as blue line. Scenario c (red line): Correlated variation of the electron number density q_e. Other model parameters are kept constant (mean value in case of non-constant parameters in the one-break model). The changes of parameter q_e can satisfactorily explain the main flux variations.

of this scenario to explain the main spectral evolution supports the interpretation that the electron number density is responsible for the observed flux variations in the framework of an additional flare-emission environment.

A variation of q_e as found in the one-break model can be induced in an emission region, which is overrunning jet regions of variable local plasma density. In this picture, flares are expected to occur when the number of electrons injected into the acceleration process increases, i.e. when the emission region overruns a jet region with enhanced plasma density [Kir98]. Calculating the black hole distance of this region in the one-break model holds $d \approx (1.5 - 6.8) \cdot 10^3 R_{\rm g}$.

11.4 Energetics

In the two-break model, the electron energy density U_e dominates over the magnetic field energy density U_B by a factor of ≈ 10 for the pre- and post-flare states and by a factor of ≈ 50 for the first flare (F1, F1a) and by a factor of ≈ 110 for the second flare (F2). From this, one can conclude that the emission system is not in equilibrium state concerning the kinetic energy of the electrons and the magnetic field energy. This indicates that the emission timescale is smaller than the equilibrium timescale. This particularly holds for the short flare periods.

In the one-break model, U_e dominates over U_B by a factor of $\approx 39 - 65$ for periods P1 – P2 and P3, and by a factor of ≈ 90 for flare period F2. Also in this model the emission system is not in equilibrium state. Particularly for the short flare period F2, the ratio of U_e over U_B gives a large value (≈ 90).

The electron luminosity L_e (measured in the source (black hole system) frame) can be calculated from U_e by

$$L_e = U_e \, v \, A \, \Gamma^2 \tag{11.1}$$

with A the cross section of the emission region, v its velocity in the source frame and Γ the bulk Lorentz factor of the emission region. With $A = \pi R^2$, $v \approx c$ and $\Gamma \approx \delta$, this holds $L_e \approx (4.1 - 4.6) \cdot 10^{43}$ erg s^{-1} for the pre-/post-flare periods and $L_e \approx (1.0 - 1.1) \cdot 10^{44}$ erg s^{-1} for the flare periods in the two-break model. In the one-break model, the electron luminosity is $L_e \approx (3.6 - 4.5) \cdot 10^{43}$ erg s^{-1} for the pre-/post-flare periods and $L_e \approx (5.4 - 5.6) \cdot 10^{43}$ erg s^{-1} for the flare periods. In both models, L_e is increased for the flare states (by a factor of $\approx 2.3 - 2.7$ in the two-break model and by a factor of $\approx 1.2 - 1.6$ in the one-break model). Interestingly, the values of the pre-/post-flare states are of roughly same size in the two models, whereas the flare luminosities differ by a factor of $\approx 1.8 - 2.0$ between the models.

All found values are by factor of $2.3 \cdot 10^2 - 3.1 \cdot 10^3$ smaller than the Eddington luminosity of the Mrk 421 black hole ($(2 - 9) \cdot 10^8 M_\odot$), which is $L_{\rm Edd} \approx 2.5 \cdot 10^{46} - 1.1 \cdot 10^{47}$ erg s^{-1}.

In cases for which the emission timescale is known, the luminosity can also be calculated from the total electron energy E_e. For the flare periods, this character-

istic timescale can be approximated by the variability timescale t_{var}:

$$L_e = \frac{E_e\,\Gamma}{\frac{\delta}{\Gamma\,(1+z)}\,t_{\mathrm{var}}} = \frac{E_e\,\Gamma^2\,(1+z)}{\delta\,t_{\mathrm{var}}} \tag{11.2}$$

with z the cosmological redshift of the source. With $t_{\mathrm{var}} \approx 1$ day, $z = 0.031$ and $\Gamma \approx \delta$, this holds $L_e \approx (2.4 - 2.9) \cdot 10^{43}$ erg s^{-1} for the flare periods F1, F1a and F2 in the two-break model, and $L_e \approx (5.5 - 6.0) \cdot 10^{42}$ erg s^{-1} in the one-break model. These values are smaller than the values found by calculation from U_e (by a factor of $\approx 3.4 - 4.6$ in the two-break model and by a factor of $\approx 9.0 - 10.2$ in the one-break model), indicating that the real emission timescale is probably smaller than the approximated timescale of 1 day.

Chapter 12

Summary and outlook

This work is about the first stereoscopic observations of Markarian (Mrk) 421 with the MAGIC telescopes during high source activity. Mrk 421 is a constituent of the blazar subclass of Active Galactic Nuclei (AGN), for which one of the two relativistic particle jets perpendicular to the accretion plane points directly to the observer. Mrk 421 is the closest known ($z = 0.031$) and one of the best explored very high energy (VHE) γ-ray emitting blazars, making it a good candidate for studying the acceleration and emission processes in AGN jets.

The broadband spectral energy distribution (SED) of Mrk 421 shows the typical two-component structure of blazars: The first component extends from the radio to the X-ray waveband with a peak in the soft to medium X-ray range, the second component extends in the γ-ray waveband up to GeV and TeV energies with a peak around 100 GeV. Additionally, large and occasional flux variations (flares) up to one order of magnitude have been observed for this source on short and long timescales. Past observations also showed that the low- and high-energy peak can move to higher energies during such flares. While measurements in the radio, optical/UV and X-ray regime have already been performed with high sensitivity on short timescales in the past, measurements in the γ-ray regime required averaging of particularly long time periods to achieve acceptable precision for spectral studies. With the beginning of scientific operation of the MAGIC stereoscopic telescope system in late 2009, an improved quality in short time measurements in the VHE γ-ray regime could be achieved.

Before being able to use the MAGIC stereoscopic system for scientific operations, the second telescope, MAGIC-II, had to be commissioned. Therefore, an important part of this thesis was the installation and maintenance of the MAGIC-II camera control program. This included the development and implementation of safety routines, such as the automatic high voltage reduction of single or grouped overexposed camera pixels. An additional important result was the proof of operation condition stability, such as temperature ($(18 \pm 1)^\circ$ C) and humidity ($17 - 30$ % rel.) stability close by the pixels. Also studies on the influence of stereo trigger inhomogeneities were performed within this thesis, proving the reli-

ability of the Markarian 421 stereo data: It was found that in the case of Mrk 421 any amount of observation time taken at the two alternating camera source positions (wobble positions) delivers reliable results in the integral and differential flux analysis.

The MAGIC stereoscopic data on Mrk 421 in this thesis were taken in January 2010 within an extensive multiwavelength (MWL) campaign. The data collection comprised 16 observation nights with a total observation time of 722 min ($\approx$ 12 h). The zenith angle ranged from 8° to 39°. The integral flux analysis showed two distinct flares on 14–15/01/2010 and 20/01/2010, reaching a flux level of $(5.86 \pm 0.12) \cdot 10^{10}$ cm^{-2} s^{-1} (2.7 Crab units (c.u.)) and $(5.60 \pm 0.11) \cdot 10^{10}$ cm^{-2} s^{-1} (2.6 c.u.) above 200 GeV, respectively. The periods immediately before and after the flares showed comparatively low flux levels ($\approx (1.2 - 3.7) \cdot 10^{10}$ cm^{-2} s^{-1} ($0.5 - 1.5$ c.u.)). No significant intranight variability was detected for the flare states. The dataset was divided into 6 observations periods, comprising the first flare (F1, 14/01/2010, 138 min observation time), the decreasing part of the first flare (F1a, 15/01/2010, 56 min) and the second flare (F2, 20/01/2010, 137 min), and the periods before the first flare (pre-flare period P1, 12–13/01/2010, 46 min), between the two flares (post-/pre-flare period P2, 16–19/01/2010, 43 min) and after the second flare (post-flare period P3, 21–24/01/2010, 75 min).

The differential flux analysis of the MAGIC data resulted in SEDs for each observation period from 80 GeV to 5 TeV (P1, F1, F1a, P2, P3) and 80 GeV to 8 TeV (F2). Each SED was fitted with a curved power law function $E^2(\mathrm{d}F/\mathrm{d}E) = E^2 f_0 (E/r)^{a+b\log_{10}(E/r)}$ (a power law with exponential cutoff reached comparable fit quality, a straight power law function was excluded). The fit parameters for flare F1 were found to be $f_0 = (14.29 \pm 0.29) \cdot 10^{-10}$ TeV^{-1} cm^{-2} s^{-1}, $a = (-2.03 \pm 0.03)$ and $b = (-0.35 \pm 0.05)$ (the normalisation parameter was set to $r = 300$ GeV). The parameters for flare F2 were found to be $f_0 = (13.99 \pm 0.25) \cdot 10^{-10}$ TeV^{-1} cm^{-2} s^{-1}, $a = (-1.91 \pm 0.03)$ and $b = (-0.43 \pm 0.05)$ ($r = 300$ GeV). This demonstrates that the VHE γ-ray spectra of the flares possess a clear curvature. Due to the low energy threshold and high sensitivity of the MAGIC stereoscopic system, this is the first time that the spectral evolution in a broad VHE γ-ray range could be resolved on these short timescales.

Afterwards, the SEDs were corrected for the extragalactic background light (EBL) absorption with the model of Franceschini et al. 2008 [Fra08]. The position of the γ-ray peak after EBL correction was clearly resolved for the two flares: (416.8 ± 57.0) GeV for F1 and (576.6 ± 74.1) GeV for F2. The peak positions for the non-flare periods range from (143.1 ± 66.8) GeV (P1) to (485.8 ± 112.1) GeV (P3).

In order to improve the scientific interpretation of the MAGIC observations, these results were embedded into a MWL framework. Simultaneous observations were available for all observation periods from the GASP program (optical waveband), Swift/UVOT (optical/UV waveband) and Swift/XRT (X-ray wave-

band). Additional coverage was provided for some periods in the radio waveband (UMRAO, OVRO and Metsähovi) and the optical waveband (New Mexico Skies and BRT). With these MWL observations, a multifrequency SED for each observation period was produced. The typical two-peak structure of blazar emission was clearly resolved. The high-activity states found with MAGIC in the VHE γ-ray regime showed clear correlations with high emission activity in the X-ray regime, which suggests that both emissions are produced in the same region by (possibly) the same population of particles. Radio and optical/UV data did not show any correlated emission.

The multifrequency SEDs of each analysis period were described with two one-zone synchrotron self-Compton (SSC) models. SSC models are very successful in explaining the observed multifrequency spectra of blazars and have become the standard method for fitting the observational results. In these scenarios, the low-energy SED component is explained by synchrotron radiation of a certain population of relativistic electrons, accelerated in an emission region moving along the jet with relativistic bulk speed. The high-energy component is explained by inverse Compton scattering of the synchrotron photons off the same population of electrons. The measurements of MAGIC played an important role in the modelling process: As the only instrument covering the high-energy SED component in this analysis, the quality of the MAGIC results was crucial in imposing model constraints. With SEDs ranging from 80 GeV to 5 TeV and 8 TeV, respectively, obtained from hour-scale observations, these results constitute a substantial improvement compared to preceding works.

The first model aimed to explain the emission in the optical/UV, X-ray and VHE γ-ray regimes to originate from a common emission region. For this, a double-broken electron injection spectrum was required. The first break in the spectrum is connected to the acceleration efficiency, while the second break indicates the onset of significant energy losses (cooling). Radio data were treated as upper limits, since the radio flux is expected to arise from an extended region, which is larger than the modelled blazar emission region. In this model, four parameters appear to be correlated with the flares: The magnetic field strength of the emission region (B) and the spectral indices of the electron spectrum below and above the cooling break (s_2 and s_3) decrease with source activity while the beaming (Doppler) factor of the jet (δ) increases. The other parameters (electron number density, minimum electron Lorentz factor and Lorentz factors of the break values in the electron spectrum) show uncorrelated variations. The correlation between B, s_2, s_3 and δ can be explained as follows: In conical jets, emission regions are considered to be accelerated (δ increases) and to grow in size while moving down the jet. Because of magnetic flux conservation, the magnetic field strength B decreases and leads to harder electron spectra. In this view, the observed variations of B, s_2, s_3 and δ are manifestations of two moving emission regions. However, it was found that this scenario alone can not be responsible for the flare emission. To explain the observed flux variations, the variations of all the model parameters are required, pointing to an emission system of high dynamics.

The second model also used the optical/UV data as upper limits, since the first model had problems in connecting the low-energy X-ray shape with the optical/UV measurements. Under the assumption that the optical/UV emission is not dominantly produced in the flare-causing emission region, only the X-ray and VHE γ-ray data were included in the modelling. This is also motivated by the correlation between X-ray and VHE γ-ray emission and the lack of correlation with radio and optical/UV emission. For this model, a single-broken injection spectrum was sufficient, with cooling processes responsible for the break. Here, only the electron number density seems to be correlated with the source activity. Compared to the non-flare periods, its value is increased for the flares. It was found that these changes can satisfactorily explain the main flux variations in the X-ray and VHE γ-ray regime. In this framework, an increased electron number density is responsible for a raised flux level, which can be explained by an emission region overrunning a jet region with enhanced local plasma density, leading to an increased number of electrons injected into the acceleration process.

In both models, the electron energy density dominates over the magnetic field energy density. In the first model, the ratio is ≈ 10 for the pre- and post-flare states, ≈ 50 for flare period F1 and ≈ 110 for flare period F2. In the second model, the ratio is $\approx 39 - 65$ for periods P1 – P2 and P3, and ≈ 90 for flare F2. From this, one can conclude that the emission system is not in equilibrium state concerning the kinetic energy of the electrons and the magnetic field energy. This indicates that the emission timescale is smaller than the equilibrium timescale, particularly for the short flare periods.

The electron luminosity is found to be of the order of $10^{43} - 10^{44}$ erg s^{-1}, which is just a small fraction of the Eddington luminosity of Mrk 421 ($0.3 - 4$ ‰). The electron luminosity is increased for the flare states (by a factor of $\approx 2.3 - 2.7$ in the first model and by a factor of $\approx 1.2 - 1.6$ in the second model).

The results lead to the question whether and to what extent the apparent optical/UV emission is connected to the X-ray and VHE γ-ray flare emission. Although mechanisms like the SSC model predict a broadband SED including optical/UV emission, the dominant emission in that energy regime does not seem to be correlated with the activity in the X-ray and VHE γ-ray band in the case of the studied flares. This points to a kind of steady-state emission produced in a different region, either also by the SSC mechanism (with the corresponding X-ray and VHE γ-ray emission inferior to the observed flare emission) or other mechanisms producing radiation in the optical/UV band. Future research has to address this question, primarily with dedicated correlation studies of short-term flux variations.

A better knowledge of the emission system before and after a flare would also lead to a deeper understanding of flare evolution. Here, the VHE γ-ray measurements are in demand, since in this regime low-activity states are usually covered just by short, daily monitoring observations, while high-activity states trigger extended observations (like the MAGIC observations presented in this thesis). Obviously, it is not possible to know when a flare will happen and to schedule dedicated

pre-flare observations. Past observations showed that Mrk 421 can be inactive over long periods of time (e.g. during 2009), but when it gets active, it typically flares several times (as in the case of the flares studied in this thesis). Hence, there is a chance that a post-flare period also is a pre-flare period to a subsequent flare. As a consequence, flare observations should be followed by additional extended observations after the flare.

The next generation instrument for ground-based VHE γ-ray astronomy, the Cherenkov Telescope Array (CTA), will allow to intensify the study of short-term spectral variations in Mrk 421 and in blazars in general. With its design of an array of many tens of telescopes, the total accessible energy of CTA will range from a few tens of GeV to above 100 TeV. It also foresees to improve the sensitivity compared to current Cherenkov telescopes by a factor of $5 - 10$ (in the energy range 100 GeV $-$ 10 TeV). Therefore, on timescales comparable to the ones shown in this work, CTA will permit the precise characterisation of the SED over a large dynamic range. This will significantly improve the determination of the spectral shape, particularly for non-flare periods which are only covered by monitoring observations.

A reduction of the uncertainty of the VHE γ-ray spectra can also be achieved with an improved knowledge of the extragalactic background light (EBL). The corresponding absorption significantly influences the spectral shape for energies above 1 TeV, so that the spectra have to be corrected for that effect by using dedicated EBL models. While direct measurements of the EBL are affected by zodiacal light, it is possible to set limits on the EBL from deep galaxy surveys (lower limits) or VHE γ-ray observations of far extragalactic sources (upper limits). Future consolidation on the EBL models can narrow the range of the de-absorption calculations.

Additional measurements filling the gap between the X-ray and VHE γ-ray regime would allow to better constrain the blazar emission models. Including data from the X-ray satellites RXTE/PCA, MAXI, INTEGRAL and Swift/BAT would extend the covered X-ray range to higher energies and give valuable information on the falling edge of the synchrotron peak. In fact, RXTE/PCA and Swift/BAT are already included into currently ongoing MWL campaigns on Mrk 421. The sensitivity of RXTE/PCA allows to produce day-to-day SEDs in the energy range $\approx 3 - 32$ keV ($\approx 7 \cdot 10^{17} - 8 \cdot 10^{18}$ Hz) and hence this instrument can perform variability studies on short timescales as in this work. Swift/BAT will extend the covered energy range up to ≈ 200 keV ($\approx 5 \cdot 10^{19}$ Hz), but its sensitivity is not good enough to resolve the typical spectrum of the source on timescales of a few days. The Large Area Telescope (LAT) on board the Fermi Gamma-ray Space Telescope, covering a γ-ray range of $\approx$ 100 MeV $-$ 300 GeV ($\approx 2 \cdot 10^{22} - 7 \cdot 10^{25}$ Hz) and therefore observing the rising edge of the IC peak, is also included into ongoing MWL campaigns. But like Swift/BAT, this instrument can not resolve the typical spectrum of Mrk 421 on short timescales due to the low number of collected photons (detector size of ≈ 1 m^2). Consequently, improvements in future projects aiming at hard X-rays and γ-rays can be achieved by enlarging the effective area.

Appendix A

SED: Flux per logarithmic bandwidth

In most fields of astronomy, the property of light is measured as rate, at which energy arrives per unit area, called energy flux $F_\epsilon = \mathrm{d}^2E/\mathrm{d}A\,\mathrm{d}t$. The energy flux per unit frequency, called specific energy flux, is given by $F_\nu = \mathrm{d}F_\epsilon/\mathrm{d}\nu$ [Kro99]. It is convenient to analyse the energy per unit logarithmic frequency interval. These intervals are naturally representing the bands in the electromagnetic spectrum, since they are spanning over several decades, i.e. factor of 10, in frequency. The corresponding quantity, $\nu F_\nu \propto \mathrm{d}F_\epsilon/\mathrm{d}\log\nu$, is called energy flux per logarithmic bandwidth [Kro99]. The unit of νF_ν is:

$$[\nu F_\nu] = \frac{\mathrm{erg}}{\mathrm{cm}^2\,\mathrm{s}}\,. \tag{A.1}$$

The $\log(\nu F_\nu)$ versus $\log(\nu)$ representation is called spectral energy distribution (SED). It is the preferred format for examining where the energy is actually emitted as it reflects the amount of energy emitted in each equally spaced interval on the logarithmic frequency axis [Pet97]. In this representation it is easily visible, which band is most important in terms of energetics. A flat distribution corresponds to equal energy per bandwidth.

In HE and VHE γ-ray astronomy, where photon-counting devices prevail, the measured quantity is the rate, at which photons arrive per unit area [Kro99]. This quantity is also called flux and denoted as $F = \mathrm{d}^2N_\gamma/\mathrm{d}A\,\mathrm{d}t$. It equals to the energy flux F_ϵ divided by the energy carried by the photons:

$$F = \frac{F_\epsilon}{h\nu}\,. \tag{A.2}$$

For the specific flux at photon-counting experiments follows:

$$\frac{\mathrm{d}F}{\mathrm{d}E} = \frac{\mathrm{d}F_\epsilon}{h\nu\,\mathrm{d}E} = \frac{\mathrm{d}F_\epsilon}{h^2\nu\,\mathrm{d}\nu} = \frac{F_\nu}{h^2\nu}\,. \tag{A.3}$$

For the flux per logarithmic bandwidth follows:

$$E^2 \frac{\mathrm{d}F}{\mathrm{d}E} = h^2\nu^2 \frac{\mathrm{d}F}{\mathrm{d}E} = h^2\nu^2 \frac{F_\nu}{h^2\nu} = \nu F_\nu \,. \tag{A.4}$$

Therefore, the specific flux of photon-counting devices has to be multiplied by E^2 in order to express νF_ν and to achieve a comparable representation with other fields of astronomy.

Appendix B

Applied signal cuts

B.1 Applied cuts for total signal analysis $E > 200$ GeV (θ^2-plot)

The cuts used for the total signal analysis are listed in tab. B.1. They result in the same signal excess above $E > 200$ GeV as the integrated flux analysis (lightcurve).

Hadronness	θ^2 [deg^2]	*Size* [phe]	E_{est} [GeV]	*Leakage(2)*
0.4165	0.02	50	200	0.2

Table B.1: Applied cuts for total signal analysis (θ^2-plot).

B.2 Applied cuts for integrated (lightcurve) and differential (SED) flux analysis

For the integrated (lightcurve) and differential (SED) flux analysis, the range in estimated energy (E_{est}) from 5 GeV to 50 TeV is divided into 28 log-equidistant ranges. For each energy range, dedicated cuts in *Hadronness* are defined. This cuts are listed in tab. B.2. For the lightcurve, a common θ^2-cut of $\theta^2 = 0.02$ deg^2 is used, whereas for the SED also dedicated θ^2-cuts for each energy bin are used. This cuts are also listed in B.2.

To achieve a lightcurve above a certain energy, a cut in estimated energy representing the energy threshold E_0 has to be applied. In this thesis, lightcurves are produced above $E_0 = 200$ GeV.

Additional cuts used in the lightcurve and SED analysis are *Size* > 50 and *Leakage(2)* < 0.2.

Bin number	1	2	3	4	5	6	7	8	9	10
Hadronness	0.99	0.99	0.99	0.99	0.99	0.99	0.99	0.9	0.9	0.85
θ^2 [deg^2]	0.1	0.1	0.1	0.1	0.1	0.1	0.05	0.04	0.03	0.02
Bin number	11	12	13	14	15	16	17	18	19	20
Hadronness	0.75	0.75	0.7	0.6	0.6	0.5	0.4	0.4	0.4	0.4
θ^2 [deg^2]	0.02	0.02	0.02	0.02	0.02	0.02	0.02	0.02	0.02	0.02
Bin number	21	22	23	24	25	26	27	28		
Hadronness	0.4	0.4	0.5	0.6	0.6	0.6	0.6	0.6		
θ^2 [deg^2]	0.02	0.02	0.02	0.02	0.02	0.02	0.02	0.02		

Table B.2: Applied cuts for integrated (lightcurve) and differential (SED) flux analysis. The θ^2-cut is only applied to the SED analysis. For the lightcurve, a common cut of $\theta^2 = 0.02$ deg^2 is used.

Appendix C

MAGIC SED values

C.1 Crab nebula

Tab. C.1 lists the SED values of fig. 8.4 for each energy bin.

Energy bin [GeV]	$E^2 \frac{\mathrm{d}F}{\mathrm{d}E}$ [10^{-11} TeV^{-1} cm^{-2} s^{-1}]		
	Bertero method	Schmelling method	Tikhonov method
$64.59^{+14.65}_{-14.59}$	7.28 ± 0.90	7.13 ± 1.04	7.58 ± 0.75
$102.00^{+23.59}_{-22.76}$	6.80 ± 0.38	7.05 ± 0.56	6.64 ± 0.48
$161.37^{+37.68}_{-35.77}$	6.00 ± 0.26	5.95 ± 0.38	5.93 ± 0.32
$255.40^{+60.08}_{-56.35}$	5.03 ± 0.22	4.87 ± 0.31	5.13 ± 0.26
$404.42^{+95.58}_{-88.94}$	5.11 ± 0.21	5.29 ± 0.28	5.12 ± 0.25
$640.37^{+152.07}_{-140.37}$	4.37 ± 0.22	4.20 ± 0.28	4.23 ± 0.23
$1014.00^{+241.95}_{-221.55}$	3.01 ± 0.21	3.05 ± 0.28	3.12 ± 0.20
$1605.61^{+384.93}_{-349.67}$	2.57 ± 0.22	2.52 ± 0.30	2.61 ± 0.20
$2543.56^{+611.23}_{-553.02}$	2.38 ± 0.28	2.41 ± 0.37	2.23 ± 0.21
$4029.42^{+970.58}_{-874.63}$	1.72 ± 0.29	1.70 ± 0.40	1.72 ± 0.21
$6380.35^{+1544.12}_{-1380.35}$	1.37 ± 0.36	1.30 ± 0.49	1.17 ± 0.21

Table C.1: SED values of the Crab nebula dataset 11/11/2009 – 11/01/2010 from 50 GeV to 8 TeV.

C.2 Mrk 421

Tab. C.2 lists the SED values of fig. 9.5, tab. C.3 lists the SED values of fig. 9.6

Energy bin [GeV]	$E^2 \frac{dF}{dE}$ [10^{-11} TeV^{-1} cm^{-2} s^{-1}]			
	P1	F1	F1a	P2
$97.74^{+27.86}_{-18.49}$	8.36 ± 0.91	11.32 ± 0.63	9.54 ± 0.76	5.38 ± 1.01
$166.14^{+32.91}_{-40.55}$	8.73 ± 0.87	12.26 ± 0.53	10.77 ± 0.77	6.95 ± 0.86
$257.62^{+57.86}_{-58.56}$	8.69 ± 0.76	12.63 ± 0.51	11.92 ± 0.74	6.41 ± 0.72
$405.89^{+94.11}_{-90.42}$	7.55 ± 0.71	12.28 ± 0.51	9.85 ± 0.64	5.38 ± 0.66
$640.96^{+151.49}_{-140.96}$	5.35 ± 0.59	11.49 ± 0.52	8.62 ± 0.64	4.46 ± 0.56
$1013.53^{+242.41}_{-221.09}$	3.87 ± 0.51	10.51 ± 0.55	7.99 ± 0.68	4.95 ± 0.70
$1602.67^{+387.86}_{-346.73}$	3.32 ± 0.58	8.43 ± 0.57	7.46 ± 0.73	4.09 ± 0.72
$2535.41^{+619.38}_{-544.87}$	2.46 ± 0.58	5.42 ± 0.49	6.59 ± 0.88	2.52 ± 0.68
$4010.97^{+989.03}_{-856.18}$	2.18 ± 1.00	4.12 ± 0.69	4.68 ± 0.83	1.74 ± 1.05

Table C.2: SED values Mrk 421 analysis periods P1, F1, F1a and P2.

for each energy bin. The corresponding SED values after application of the EBL correction (Franceschini model) are listed in tab. C.4 resp. C.5.

Energy bin [GeV]	$E^2 \frac{\mathrm{d}F}{\mathrm{d}E}$ [10^{-11} TeV^{-1} cm^{-2} s^{-1}]		
	P2	F2	P3
$101.31^{+24.29}_{-22.06}$	5.38 ± 1.01	9.66 ± 0.56	5.84 ± 0.87
$159.83^{+39.23}_{-34.23}$	6.95 ± 0.86	10.52 ± 0.52	5.17 ± 0.64
$250.16^{+65.31}_{-51.11}$	6.41 ± 0.72	12.05 ± 0.52	6.11 ± 0.60
$389.01^{+110.99}_{-73.53}$	5.38 ± 0.66	12.42 ± 0.52	6.89 ± 0.61
$650.61^{+141.84}_{-150.61}$	4.46 ± 0.56	12.48 ± 0.57	6.09 ± 0.60
$1021.41^{+234.53}_{-228.97}$	4.95 ± 0.70	10.78 ± 0.56	4.87 ± 0.56
$1611.49^{+379.05}_{-355.54}$	4.09 ± 0.72	8.74 ± 0.57	4.29 ± 0.63
$2547.05^{+607.74}_{-556.51}$	2.52 ± 0.68	6.39 ± 0.56	2.53 ± 0.54
$4025.73^{+974.27}_{-870.94}$	1.74 ± 1.05	4.22 ± 0.53	1.64 ± 0.73
$6368.65^{+1555.82}_{-1368.65}$	–	2.66 ± 0.61	–

Table C.3: SED values Mrk 421 analyis periods P2, F2 and P3.

Energy bin [GeV]	$E^2 \frac{\mathrm{d}F}{\mathrm{d}E}$ [10^{-11} TeV^{-1} cm^{-2} s^{-1}]			
	P1	F1	F1a	P2
$99.27^{+26.33}_{-20.02}$	8.40 ± 0.92	11.38 ± 0.63	9.59 ± 0.76	5.41 ± 1.01
$171.87^{+27.18}_{-46.28}$	8.87 ± 0.89	12.46 ± 0.54	10.95 ± 0.78	7.06 ± 0.88
$258.66^{+56.82}_{-59.61}$	9.06 ± 0.79	13.17 ± 0.53	12.43 ± 0.77	6.69 ± 0.76
$406.82^{+93.18}_{-91.34}$	8.32 ± 0.78	13.54 ± 0.56	10.86 ± 0.71	5.93 ± 0.73
$642.42^{+150.03}_{-142.42}$	6.41 ± 0.71	13.83 ± 0.63	10.36 ± 0.77	5.37 ± 0.68
$1015.85^{+240.09}_{-223.41}$	5.14 ± 0.68	13.94 ± 0.74	10.61 ± 0.90	6.58 ± 0.94
$1607.08^{+383.46}_{-351.14}$	4.81 ± 0.84	12.20 ± 0.83	10.84 ± 1.07	5.93 ± 1.05
$2542.39^{+612.40}_{-551.85}$	3.80 ± 0.91	8.36 ± 0.76	10.21 ± 1.37	3.89 ± 1.06
$4023.88^{+976.12}_{-869.10}$	3.66 ± 1.70	6.91 ± 1.16	7.83 ± 1.40	2.92 ± 1.77

Table C.4: SED values Mrk 421 analysis periods P1, F1, F1a and P2 after EBL correction (Franceschini model).

Energy bin [GeV]	$E^2 \frac{\mathrm{d}F}{\mathrm{d}E}$ [10^{-11} TeV^{-1} cm^{-2} s^{-1}]		
	P2	F2	P3
$101.54^{+24.06}_{-22.29}$	5.41 ± 1.01	9.72 ± 0.57	5.87 ± 0.87
$160.41^{+38.64}_{-34.82}$	7.06 ± 0.88	10.70 ± 0.53	5.25 ± 0.65
$252.96^{+62.52}_{-53.90}$	6.69 ± 0.76	12.58 ± 0.54	6.38 ± 0.62
$395.38^{+104.62}_{-79.90}$	5.93 ± 0.73	13.71 ± 0.58	7.60 ± 0.67
$684.83^{+107.62}_{-184.83}$	5.37 ± 0.68	15.01 ± 0.68	7.32 ± 0.72
$1029.76^{+226.19}_{-237.31}$	6.58 ± 0.94	14.30 ± 0.75	6.45 ± 0.75
$1618.83^{+371.70}_{-362.89}$	5.93 ± 1.05	12.65 ± 0.82	6.20 ± 0.91
$2555.20^{+599.59}_{-564.66}$	3.89 ± 1.06	9.89 ± 0.87	3.90 ± 0.83
$4038.64^{+961.36}_{-883.86}$	2.92 ± 1.77	7.05 ± 0.88	2.74 ± 1.22
$6386.20^{+1538.27}_{-1386.20}$	–	5.28 ± 1.22	–

Table C.5: SED values Mrk 421 analyis periods P2, F2 and P3 after EBL correction (Franceschini model).

Appendix D

MWL observations

D.1 Used MWL observations

The following tables list details of the MWL observations used in this thesis, sorted by instrument, and their affiliation to the analysis periods.

Date	Period	MJD start	MJD end	Instrument	Band
14/01/2010	F1	55210.00	55210.02	OVRO	–
15/01/2010	F1a	55211.87883	–	UMRAO	8 GHz
17/01/2010	P2	55213.00	55210.02	OVRO	–
17/01/2010	P2	55213.80092	–	UMRAO	8 GHz
18/01/2010	P2	55214.86583	–	UMRAO	8 GHz
21/01/2010	P3	55217.82408	–	UMRAO	14 GHz
24/01/2010	P3	55220.00	55210.02	OVRO	–
24/01/2010	P3	55220.45139	–	Metsähovi	–

Table D.1: MWL coverage by radio instruments (OVRO: Owens Valley Radio Observatory, UMRAO: University of Michigan Radio Astronomy Observatory).

Date	Period	MJD	Instrument	Band
12/01/2010	P1	55208.79284	Roque (KVA 35 cm)	R
14/01/2010	F1	55210.77229	Roque (KVA 35 cm)	R
15/01/2010	F1a	55211.70107	Roque (KVA 35 cm)	R
16/01/2010	P2	55212.49132	Talmassons	R
16/01/2010	P2	55212.74050	Roque (KVA 35 cm)	R
17/01/2010	P2	55213.21097	Lulin (SLT)	R
17/01/2010	P2	55213.76895	Roque (KVA 35 cm)	R
18/01/2010	P2	55214.08552	Lulin (SLT)	R
18/01/2010	P2	55214.74537	Roque (KVA 35 cm)	R
19/01/2010	P2	55215.34936	Lulin (SLT)	R
19/01/2010	P2	55215.46215	Talmassons	R
20/01/2010	F2	55216.33353	Lulin (SLT)	R
20/01/2010	F2	55216.47030	St.Petersburg	R
20/01/2010	F2	55216.75673	Roque (KVA 35 cm)	R
21/01/2010	P3	55217.48368	Talmassons	R
21/01/2010	P3	55217.55619	Abastumani (70 cm)	R
21/01/2010	P3	55217.55691	Abastumani (70 cm)	R
21/01/2010	P3	55217.55763	Abastumani (70 cm)	R
21/01/2010	P3	55217.55833	Abastumani (70 cm)	R
21/01/2010	P3	55217.55905	Abastumani (70 cm)	R
21/01/2010	P3	55217.55977	Abastumani (70 cm)	R
21/01/2010	P3	55217.56049	Abastumani (70 cm)	R
21/01/2010	P3	55217.56119	Abastumani (70 cm)	R
21/01/2010	P3	55217.76109	Roque (KVA 35 cm)	R
22/01/2010	P3	55218.45380	St.Petersburg	R
22/01/2010	P3	55218.76487	Roque (KVA 35 cm)	R
23/01/2010	P3	55219.77443	Roque (KVA 35 cm)	R
24/01/2010	P3	55220.14046	Lulin (SLT)	R
24/01/2010	P3	55220.35938	Talmassons	R
24/01/2010	P3	55220.74092	Roque (KVA 35 cm)	R

Table D.2: MWL coverage by optical instruments within the GASP program.

Date	Period	MJD start	MJD end	Duration [s]	Instrument	Band
16/01/2010	P2	55212.69800	55212.70008	180	BRT	*V*
16/01/2010	P2	55212.74477	54212.74824	300	NMS	*V*
16/01/2010	P2	55212.74946	55212.75293	300	NMS	*R*
20/01/2010	P3	55216.69346	55216.69554	180	BRT	*R*

Table D.3: MWL coverage by other optical instruments (BRT: Bradford Robotic Telscope, NMS: New Mexico Skies).

Date	Period	MJD start	MJD end	Duration [s]
12/01/2010	P1	55208.3752202900	55208.3776945245	210.402
12/01/2010	P1	55208.4321164484	55208.4341277856	171.039
13/01/2010	P1	55209.3586133076	55209.3606241343	170.995
13/01/2010	P1	55209.3773788505	55209.3798529572	210.391
14/01/2010	F1	55210.3665918516	55210.3716122137	426.918
15/01/2010	F1a	55211.3681281111	55211.3719912940	328.515
15/01/2010	F1a	55211.8530695377	55211.8569325921	328.504
16/01/2010	P2	55212.3757279762	55212.3802855685	387.565
16/01/2010	P2	55212.7074891657	55212.7111208352	308.827
17/01/2010	P2	55213.3085687095	55213.3126634042	348.202
17/01/2010	P2	55213.3752337215	55213.3793277778	348.147
18/01/2010	P2	55214.3131991662	55214.3172932227	348.147
18/01/2010	P2	55214.3802246660	55214.3852451553	426.929
19/01/2010	P2	55215.2667455521	55215.2703770935	308.816
19/01/2010	P2	55215.3328029856	55215.3366659120	328.493
20/01/2010	F2	55216.3315204308	55216.3347821660	277.369
24/01/2010	P3	55220.2824205759	55220.2867466551	367.878

Table D.4: MWL coverage by Swift/UVOT UVM2.

Date	Period	MJD start	MJD end	Duration [s]
12/01/2010	P1	55208.3777502000	55208.3799210292	184.601
12/01/2010	P1	55208.4341811627	55208.4354766368	110.164
13/01/2010	P1	55209.3606789157	55209.3625589817	159.876
13/01/2010	P1	55209.3799097819	55209.3820043769	178.119
14/01/2010	F1	55210.3716742741	55210.3764472894	405.884
15/01/2010	F1a	55211.3720497785	55211.3757548738	315.071
15/01/2010	F1a	55211.8569909493	55211.8604764069	296.394
16/01/2010	P2	55212.3803448192	55212.3847804618	377.195
16/01/2010	P2	55212.7111808521	55212.7146416648	294.298
17/01/2010	P2	55213.3127222718	55213.3167263023	340.492
17/01/2010	P2	55213.3793879225	55213.3833916977	340.470
18/01/2010	P2	55214.3173511965	55214.3201971537	242.013
18/01/2010	P2	55214.3853068324	55214.3896418507	368.638
19/01/2010	P2	55215.2704374937	55215.2729763419	215.897
19/01/2010	P2	55215.3367259292	55215.3403374225	307.112
20/01/2010	P3	55220.2868083322	55220.2910305949	359.050

Table D.5: MWL coverage by Swift/UVOT UVW1.

Date	Period	MJD start	MJD end	Duration [s]
12/01/2010	P1	55208.3726879539	55208.3751621887	210.402
12/01/2010	P1	55208.4300489250	55208.4320611563	171.115
13/01/2010	P1	55209.3565471889	55209.3585583984	171.028
13/01/2010	P1	55209.3748460035	55209.3773202380	210.402
14/01/2010	F1	55210.3615107060	55210.3665311961	426.929
15/01/2010	F1a	55211.3642064435	55211.3680693711	328.493
15/01/2010	F1a	55211.8491471051	55211.8530100317	328.493
16/01/2010	P2	55212.3711098562	55212.3756673208	387.554
16/01/2010	P2	55212.7037985005	55212.7074295315	308.773
17/01/2010	P2	55213.3044142535	55213.3085086924	348.180
17/01/2010	P2	55213.3710786268	55213.3751733215	348.202
18/01/2010	P2	55214.3090351329	55214.3131309769	348.299
18/01/2010	P2	55214.3751417333	55214.3801622227	426.929
19/01/2010	P2	55215.2630561644	55215.2666878336	308.827
19/01/2010	P2	55215.3288819574	55215.3327450118	328.504
20/01/2010	F2	55216.3266696486	55216.3314586262	407.242
24/01/2010	P3	55220.2780348623	55220.2823606866	367.856

Table D.6: MWL coverage by Swift/UVOT UVW2.

Date	Period	Observation ID	MJD
13/01/2010	P1	30352177	55209.35648161673
14/01/2010	F1	30352178	55210.36144451955
15/01/2010	F1a	30352179	55211.36412958008
15/01/2010	F1a	30352180	55211.84908098097
16/01/2010	P2	30352181	55212.37104412485
16/01/2010	P2	30352182	55212.70373558896
17/01/2010	P2	30352183	55213.30434490852
18/01/2010	P2	30352184	55214.30895612342
19/01/2010	P2	30352185	55215.26299062934
19/01/2010	P2	30352186	55215.32881201524
20/01/2010	F2	30352187	55216.32660420105
24/01/2010	P3	30352188	55220.27796297974

Table D.7: MWL coverage by Swift/XRT.

D.2 MWL SED values

Frequency [Hz]	νF_ν [erg cm^{-2} s^{-1}]	Instrument
$4.339585 \cdot 10^{14}$	$(1.00179 \pm 0.02002) \cdot 10^{-10}$	GASP
$1.200322 \cdot 10^{15}$	$(1.706307 \pm 0.017381) \cdot 10^{-10}$	Swift/UVOT
$1.385656 \cdot 10^{15}$	$(2.030495 \pm 0.020897) \cdot 10^{-10}$	Swift/UVOT
$1.628061 \cdot 10^{15}$	$(2.185828 \pm 0.021302) \cdot 10^{-10}$	Swift/UVOT
$1.161883 \cdot 10^{17}$	$(3.99501 \pm 0.05476) \cdot 10^{-10}$	Swift/XRT
$1.595901 \cdot 10^{17}$	$(4.19724 \pm 0.05488) \cdot 10^{-10}$	Swift/XRT
$2.192048 \cdot 10^{17}$	$(4.21130 \pm 0.04793) \cdot 10^{-10}$	Swift/XRT
$3.010890 \cdot 10^{17}$	$(3.98428 \pm 0.04527) \cdot 10^{-10}$	Swift/XRT
$4.135607 \cdot 10^{17}$	$(3.81669 \pm 0.05426) \cdot 10^{-10}$	Swift/XRT
$5.680458 \cdot 10^{17}$	$(3.52384 \pm 0.06824) \cdot 10^{-10}$	Swift/XRT
$7.802386 \cdot 10^{17}$	$(3.25726 \pm 0.07767) \cdot 10^{-10}$	Swift/XRT
$1.071695 \cdot 10^{18}$	$(2.81109 \pm 0.08240) \cdot 10^{-10}$	Swift/XRT
$1.472024 \cdot 10^{18}$	$(2.10502 \pm 0.07348) \cdot 10^{-10}$	Swift/XRT
$2.412270 \cdot 10^{25}$	$(1.34618 \pm 0.14734) \cdot 10^{-10}$	MAGIC
$3.823193 \cdot 10^{25}$	$(1.42172 \pm 0.14241) \cdot 10^{-10}$	MAGIC
$6.059363 \cdot 10^{25}$	$(1.45231 \pm 0.12623) \cdot 10^{-10}$	MAGIC
$9.603433 \cdot 10^{25}$	$(1.33250 \pm 0.12561) \cdot 10^{-10}$	MAGIC
$1.522041 \cdot 10^{26}$	$(1.02684 \pm 0.11348) \cdot 10^{-10}$	MAGIC
$2.412270 \cdot 10^{26}$	$(8.22822 \pm 1.09650) \cdot 10^{-11}$	MAGIC
$3.823193 \cdot 10^{26}$	$(7.70190 \pm 1.34248) \cdot 10^{-11}$	MAGIC
$6.059363 \cdot 10^{26}$	$(6.08909 \pm 1.45182) \cdot 10^{-11}$	MAGIC
$9.603433 \cdot 10^{26}$	$(5.86510 \pm 2.71696) \cdot 10^{-11}$	MAGIC

Table D.8: MWL SED values Mrk 421 analysis period P1.

Frequency [Hz]	νF_ν [erg cm^{-2} s^{-1}]	Instrument
$1.499967 \cdot 10^{10}$	$(6.870 \pm 0.315) \cdot 10^{-14}$	OVRO
$4.339585 \cdot 10^{14}$	$(1.04470 \pm 0.01936) \cdot 10^{-10}$	GASP
$1.200322 \cdot 10^{15}$	$(1.77283 \pm 0.03340) \cdot 10^{-10}$	Swift/UVOT
$1.385656 \cdot 10^{15}$	$(2.14401 \pm 0.04172) \cdot 10^{-10}$	Swift/UVOT
$1.628061 \cdot 10^{15}$	$(2.25394 \pm 0.04151) \cdot 10^{-10}$	Swift/UVOT
$1.161883 \cdot 10^{17}$	$(5.83357 \pm 0.06248) \cdot 10^{-10}$	Swift/XRT
$1.595901 \cdot 10^{17}$	$(6.65054 \pm 0.06491) \cdot 10^{-10}$	Swift/XRT
$2.192048 \cdot 10^{17}$	$(6.82681 \pm 0.05756) \cdot 10^{-10}$	Swift/XRT
$3.010890 \cdot 10^{17}$	$(7.01573 \pm 0.05698) \cdot 10^{-10}$	Swift/XRT
$4.135607 \cdot 10^{17}$	$(6.83726 \pm 0.06870) \cdot 10^{-10}$	Swift/XRT
$5.680458 \cdot 10^{17}$	$(6.76508 \pm 0.08901) \cdot 10^{-10}$	Swift/XRT
$7.802386 \cdot 10^{17}$	$(5.96038 \pm 0.09401) \cdot 10^{-10}$	Swift/XRT
$1.071695 \cdot 10^{18}$	$(5.56885 \pm 0.11013) \cdot 10^{-10}$	Swift/XRT
$1.472024 \cdot 10^{18}$	$(4.60731 \pm 0.09993) \cdot 10^{-10}$	Swift/XRT
$2.412270 \cdot 10^{25}$	$(1.82395 \pm 0.10097) \cdot 10^{-10}$	MAGIC
$3.823193 \cdot 10^{25}$	$(1.99656 \pm 0.08648) \cdot 10^{-10}$	MAGIC
$6.059363 \cdot 10^{25}$	$(2.11083 \pm 0.08522) \cdot 10^{-10}$	MAGIC
$9.603433 \cdot 10^{25}$	$(2.16888 \pm 0.08955) \cdot 10^{-10}$	MAGIC
$1.522041 \cdot 10^{26}$	$(2.21582 \pm 0.10033) \cdot 10^{-10}$	MAGIC
$2.412270 \cdot 10^{26}$	$(2.23423 \pm 0.11796) \cdot 10^{-10}$	MAGIC
$3.823193 \cdot 10^{26}$	$(1.95447 \pm 0.13330) \cdot 10^{-10}$	MAGIC
$6.059363 \cdot 10^{26}$	$(1.33936 \pm 0.12105) \cdot 10^{-10}$	MAGIC
$9.603433 \cdot 10^{26}$	$(1.10733 \pm 0.18559) \cdot 10^{-10}$	MAGIC

Table D.9: MWL SED values Mrk 421 analysis period F1.

Frequency [Hz]	νF_ν [erg cm^{-2} s^{-1}]	Instrument
$8.000000 \cdot 10^{9}$	$(5.52 \pm 0.24) \cdot 10^{-14}$	UMRAO
$4.339585 \cdot 10^{14}$	$(1.05500 \pm 0.02081) \cdot 10^{-10}$	GASP
$1.200322 \cdot 10^{15}$	$(1.867120 \pm 0.025270) \cdot 10^{-10}$	Swift/UVOT
$1.385656 \cdot 10^{15}$	$(2.205945 \pm 0.030728) \cdot 10^{-10}$	Swift/UVOT
$1.628061 \cdot 10^{15}$	$(2.345400 \pm 0.031008) \cdot 10^{-10}$	Swift/UVOT
$1.161883 \cdot 10^{17}$	$(4.55759 \pm 0.06359) \cdot 10^{-10}$	Swift/XRT
$1.595901 \cdot 10^{17}$	$(5.14281 \pm 0.06594) \cdot 10^{-10}$	Swift/XRT
$2.192048 \cdot 10^{17}$	$(5.55991 \pm 0.05985) \cdot 10^{-10}$	Swift/XRT
$3.010890 \cdot 10^{17}$	$(5.72120 \pm 0.05855) \cdot 10^{-10}$	Swift/XRT
$4.135607 \cdot 10^{17}$	$(5.72166 \pm 0.07105) \cdot 10^{-10}$	Swift/XRT
$5.680458 \cdot 10^{17}$	$(5.58347 \pm 0.09155) \cdot 10^{-10}$	Swift/XRT
$7.802386 \cdot 10^{17}$	$(5.14833 \pm 0.01016) \cdot 10^{-10}$	Swift/XRT
$1.071695 \cdot 10^{18}$	$(4.62302 \pm 0.11736) \cdot 10^{-10}$	Swift/XRT
$1.472024 \cdot 10^{18}$	$(3.69904 \pm 0.10411) \cdot 10^{-10}$	Swift/XRT
$2.412270 \cdot 10^{25}$	$(1.53662 \pm 0.12156) \cdot 10^{-10}$	MAGIC
$3.823193 \cdot 10^{25}$	$(1.75514 \pm 0.12466) \cdot 10^{-10}$	MAGIC
$6.059363 \cdot 10^{25}$	$(1.99197 \pm 0.12278) \cdot 10^{-10}$	MAGIC
$9.603433 \cdot 10^{25}$	$(1.73925 \pm 0.11376) \cdot 10^{-10}$	MAGIC
$1.522041 \cdot 10^{26}$	$(1.66013 \pm 0.12394) \cdot 10^{-10}$	MAGIC
$2.412270 \cdot 10^{26}$	$(1.70056 \pm 0.14434) \cdot 10^{-10}$	MAGIC
$3.823193 \cdot 10^{26}$	$(1.73622 \pm 0.17106) \cdot 10^{-10}$	MAGIC
$6.059363 \cdot 10^{26}$	$(1.63640 \pm 0.21934) \cdot 10^{-10}$	MAGIC
$9.603433 \cdot 10^{26}$	$(1.25442 \pm 0.22409) \cdot 10^{-10}$	MAGIC

Table D.10: MWL SED values Mrk 421 analysis period F1a.

Frequency [Hz]	νF_ν [erg cm^{-2} s^{-1}]	Instrument
$8.000000 \cdot 10^{9}$	$(4.28 \pm 0.56) \cdot 10^{-14}$	UMRAO
$1.499967 \cdot 10^{10}$	$(6.915 \pm 0.165) \cdot 10^{-14}$	OVRO
$4.339585 \cdot 10^{14}$	$(1.050586 \pm 0.004883) \cdot 10^{-10}$	GASP
$4.713597 \cdot 10^{14}$	$(1.319810 \pm 0.016099) \cdot 10^{-10}$	NMS
$5.462307 \cdot 10^{14}$	$(1.540770 \pm 0.049595) \cdot 10^{-10}$	NMS
$5.462307 \cdot 10^{14}$	$(1.583720 \pm 0.005450) \cdot 10^{-10}$	BRT
$1.200322 \cdot 10^{15}$	$(1.746473 \pm 0.012655) \cdot 10^{-10}$	Swift/UVOT
$1.385656 \cdot 10^{15}$	$(2.061233 \pm 0.015343) \cdot 10^{-10}$	Swift/UVOT
$1.628061 \cdot 10^{15}$	$(2.175363 \pm 0.015317) \cdot 10^{-10}$	Swift/UVOT
$1.161883 \cdot 10^{17}$	$(3.812682 \pm 0.032078) \cdot 10^{-10}$	Swift/XRT
$1.595901 \cdot 10^{17}$	$(4.152032 \pm 0.031862) \cdot 10^{-10}$	Swift/XRT
$2.192048 \cdot 10^{17}$	$(4.323898 \pm 0.028828) \cdot 10^{-10}$	Swift/XRT
$3.010890 \cdot 10^{17}$	$(4.434682 \pm 0.028672) \cdot 10^{-10}$	Swift/XRT
$4.135607 \cdot 10^{17}$	$(4.517620 \pm 0.035613) \cdot 10^{-10}$	Swift/XRT
$5.680458 \cdot 10^{17}$	$(4.584234 \pm 0.046965) \cdot 10^{-10}$	Swift/XRT
$7.802386 \cdot 10^{17}$	$(4.485420 \pm 0.052874) \cdot 10^{-10}$	Swift/XRT
$1.071695 \cdot 10^{18}$	$(4.266612 \pm 0.062070) \cdot 10^{-10}$	Swift/XRT
$1.472024 \cdot 10^{18}$	$(3.912088 \pm 0.057697) \cdot 10^{-10}$	Swift/XRT
$2.412270 \cdot 10^{25}$	$(8.67189 \pm 1.62409) \cdot 10^{-11}$	MAGIC
$3.823193 \cdot 10^{25}$	$(1.13113 \pm 0.14038) \cdot 10^{-10}$	MAGIC
$6.059363 \cdot 10^{25}$	$(1.07238 \pm 0.12105) \cdot 10^{-10}$	MAGIC
$9.603433 \cdot 10^{25}$	$(9.49747 \pm 1.16263) \cdot 10^{-11}$	MAGIC
$1.522041 \cdot 10^{26}$	$(8.60679 \pm 1.08399) \cdot 10^{-11}$	MAGIC
$2.412270 \cdot 10^{26}$	$(1.05351 \pm 0.15014) \cdot 10^{-10}$	MAGIC
$3.823193 \cdot 10^{26}$	$(9.49514 \pm 1.67471) \cdot 10^{-11}$	MAGIC
$6.059363 \cdot 10^{26}$	$(6.23180 \pm 1.69622) \cdot 10^{-11}$	MAGIC
$9.603433 \cdot 10^{26}$	$(4.67613 \pm 2.84237) \cdot 10^{-11}$	MAGIC

Table D.11: MWL SED values Mrk 421 analysis period P2.

Frequency [Hz]	νF_ν [erg cm^{-2} s^{-1}]	Instrument
$4.339585 \cdot 10^{14}$	$(8.783797 \pm 0.205416) \cdot 10^{-11}$	GASP
$4.713597 \cdot 10^{14}$	$(8.87656 \pm 0.02340) \cdot 10^{-11}$	BRT
$1.385656 \cdot 10^{15}$	$(1.56831 \pm 0.03156) \cdot 10^{-10}$	Swift/UVOT
$1.628061 \cdot 10^{15}$	$(1.68826 \pm 0.03133) \cdot 10^{-10}$	Swift/UVOT
$1.161883 \cdot 10^{17}$	$(4.54217 \pm 0.07605) \cdot 10^{-10}$	Swift/XRT
$1.595901 \cdot 10^{17}$	$(4.91281 \pm 0.07606) \cdot 10^{-10}$	Swift/XRT
$2.192048 \cdot 10^{17}$	$(5.23439 \pm 0.06905) \cdot 10^{-10}$	Swift/XRT
$3.010890 \cdot 10^{17}$	$(5.49048 \pm 0.06933) \cdot 10^{-10}$	Swift/XRT
$4.135607 \cdot 10^{17}$	$(5.36135 \pm 0.08425) \cdot 10^{-10}$	Swift/XRT
$5.680458 \cdot 10^{17}$	$(5.51300 \pm 0.11176) \cdot 10^{-10}$	Swift/XRT
$7.802386 \cdot 10^{17}$	$(5.30422 \pm 0.12863) \cdot 10^{-10}$	Swift/XRT
$1.071695 \cdot 10^{18}$	$(4.95880 \pm 0.14164) \cdot 10^{-10}$	Swift/XRT
$1.472024 \cdot 10^{18}$	$(4.39345 \pm 0.13436) \cdot 10^{-10}$	Swift/XRT
$2.412270 \cdot 10^{25}$	$(1.55666 \pm 0.09084) \cdot 10^{-10}$	MAGIC
$3.823193 \cdot 10^{25}$	$(1.71447 \pm 0.08544) \cdot 10^{-10}$	MAGIC
$6.059363 \cdot 10^{25}$	$(2.01554 \pm 0.08695) \cdot 10^{-10}$	MAGIC
$9.603433 \cdot 10^{25}$	$(2.19646 \pm 0.09214) \cdot 10^{-10}$	MAGIC
$1.522041 \cdot 10^{26}$	$(2.40549 \pm 0.10921) \cdot 10^{-10}$	MAGIC
$2.412270 \cdot 10^{26}$	$(2.29123 \pm 0.11955) \cdot 10^{-10}$	MAGIC
$3.823193 \cdot 10^{26}$	$(2.02733 \pm 0.13213) \cdot 10^{-10}$	MAGIC
$6.059363 \cdot 10^{26}$	$(1.58384 \pm 0.14004) \cdot 10^{-10}$	MAGIC
$9.603433 \cdot 10^{26}$	$(1.12897 \pm 0.14109) \cdot 10^{-10}$	MAGIC
$1.522041 \cdot 10^{27}$	$(8.45910 \pm 1.95127) \cdot 10^{-11}$	MAGIC

Table D.12: MWL SED values Mrk 421 analysis period F2.

Frequency [Hz]	νF_ν [erg cm^{-2} s^{-1}]	Instrument
$1.400000 \cdot 10^{10}$	$(6.58 \pm 0.28) \cdot 10^{-14}$	UMRAO
$1.499967 \cdot 10^{10}$	$(6.66 \pm 0.10) \cdot 10^{-14}$	OVRO
$3.700000 \cdot 10^{10}$	$(1.295 \pm 0.222) \cdot 10^{-13}$	Metsähovi
$4.339585 \cdot 10^{14}$	$(7.960455 \pm 0.041491) \cdot 10^{-11}$	GASP
$1.385656 \cdot 10^{15}$	$(1.59811 \pm 0.03159) \cdot 10^{-10}$	Swift/UVOT
$1.200322 \cdot 10^{15}$	$(1.33634 \pm 0.02543) \cdot 10^{-10}$	Swift/UVOT
$1.628061 \cdot 10^{15}$	$(1.68353 \pm 0.03136) \cdot 10^{-10}$	Swift/UVOT
$1.161883 \cdot 10^{17}$	$(4.47008 \pm 0.10078) \cdot 10^{-10}$	Swift/XRT
$1.595901 \cdot 10^{17}$	$(4.60026 \pm 0.09700) \cdot 10^{-10}$	Swift/XRT
$2.192048 \cdot 10^{17}$	$(4.67212 \pm 0.08581) \cdot 10^{-10}$	Swift/XRT
$3.010890 \cdot 10^{17}$	$(4.57233 \pm 0.08308) \cdot 10^{-10}$	Swift/XRT
$4.135607 \cdot 10^{17}$	$(4.38115 \pm 0.09949) \cdot 10^{-10}$	Swift/XRT
$5.680458 \cdot 10^{17}$	$(4.48370 \pm 0.13407) \cdot 10^{-10}$	Swift/XRT
$7.802386 \cdot 10^{17}$	$(4.09296 \pm 0.14104) \cdot 10^{-10}$	Swift/XRT
$1.071695 \cdot 10^{18}$	$(3.59966 \pm 0.15351) \cdot 10^{-10}$	Swift/XRT
$1.472024 \cdot 10^{18}$	$(3.66979 \pm 0.17182) \cdot 10^{-10}$	Swift/XRT
$2.412270 \cdot 10^{25}$	$(9.40372 \pm 1.40078) \cdot 10^{-11}$	MAGIC
$3.823193 \cdot 10^{25}$	$(8.41788 \pm 1.04639) \cdot 10^{-11}$	MAGIC
$6.059363 \cdot 10^{25}$	$(1.02213 \pm 0.09963) \cdot 10^{-10}$	MAGIC
$9.603433 \cdot 10^{25}$	$(1.21741 \pm 0.10709) \cdot 10^{-10}$	MAGIC
$1.522041 \cdot 10^{26}$	$(1.17310 \pm 0.11480) \cdot 10^{-10}$	MAGIC
$2.412270 \cdot 10^{26}$	$(1.03418 \pm 0.11953) \cdot 10^{-10}$	MAGIC
$3.823193 \cdot 10^{26}$	$(9.93270 \pm 1.45217) \cdot 10^{-11}$	MAGIC
$6.059363 \cdot 10^{26}$	$(6.24742 \pm 1.33218) \cdot 10^{-11}$	MAGIC
$9.603433 \cdot 10^{26}$	$(4.39478 \pm 1.95903) \cdot 10^{-11}$	MAGIC

Table D.13: MWL SED values Mrk 421 analysis period P3.

Appendix E

Verification of SSC code

To verify the applicability of the SSC code described in sec. 10.2, the dataset of fig. 9.1 from [Abd11b] is modelled with the same input parameters as used in [Abd11b]. Two different variability timescales were assumed: $t_{\mathrm{var}} = 1$ hour, leading to an emission region of size $R = 5.3 \cdot 10^{15}$ cm ($\log_{10} R = 15.724$, model 1) and $t_{\mathrm{var}} = 1$ day, leading to an emission region of size $R = 5.2 \cdot 10^{16}$ cm ($\log_{10} R = 16.716$, model 2). In both cases, the double-broken injection spectrum is used. The result is shown in fig. E.1. The corresponding model values are listed in tab. E.1. The corresponding values for the electron density, the total electron energy and the magnetic field density are also listed. The models and data are in good agreement, proving the applicability of the used SSC code. It is worth mentioning, that the radio data ($10^9 - 10^{11}$ Hz) are treated as upper limit, since this single dish measurements integrate over a region that is orders of magnitude larger than the blazar emission region. For details on the interpretation of the shown result please see [Abd11b].

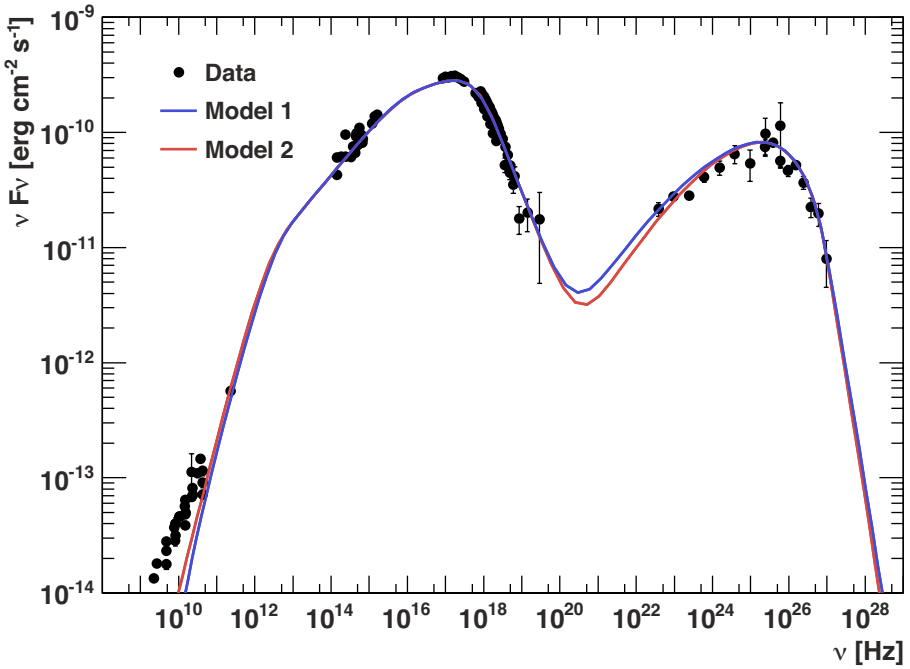

Figure E.1: SSC model for the Mrk 421 data of [Abd11b], model parameters see tab. E.1.

Parameter	Symbol	Model 1	Model 2
Emission region [$\log_{10}$ cm]	R	15.724	16.716
Beaming factor	δ	50	21
Magnetic field [mG]	B	82	38
Electron number density [cm^{-3}]	q_e	11000	900
Minimum electron Lorentz factor [10^2]	γ_{min}	4	8
Break 1 electron Lorentz factor [10^4]	γ_{br1}	2.2	5
Break 2 electron Lorentz factor [10^5]	γ_{br2}	1.7	3.9
Maximum electron Lorentz factor [10^8]	γ_{max}	1	1
Low-energy electron spectral index	s_1	2.2	2.2
Medium-energy electron spectral index	s_2	2.7	2.7
High-energy electron spectral index	s_3	4.7	4.7
Electron density [erg cm^{-3}]	U_e	$8.872 \cdot 10^{-3}$	$6.404 \cdot 10^{-4}$
Total electron energy [erg]	E_e	$5.522 \cdot 10^{45}$	$3.772 \cdot 10^{47}$
Magnetic field density [erg cm^{-3}]	U_B	$2.675 \cdot 10^{-4}$	$5.745 \cdot 10^{-5}$

Table E.1: Parameter values of the one-zone SSC model to the Mrk 421 SED shown in fig. E.1.

List of Figures

List of Tables

Bibliography

[Abd09] A. A. Abdo *et al.* [Fermi LAT Collaboration], *Fermi Large Area Telescope Bright Gamma-ray Source List*, Astrophys. J. Suppl. **183** (2009) 46

[Abd10a] A. A. Abdo *et al.* [Fermi LAT Collaboration], *Fermi Large Area Telescope First Source Catalog*, Astrophys. J. Suppl. **188** (2010) 405

[Abd10b] A. A. Abdo *et al.* [Fermi LAT Collaboration, Fermi Pulsar Timing Consortium], *Fermi Large Area Telescope Observations of the Crab Pulsar and Nebula*, Astrophys. J. **708** (2010) 1254

[Abd10c] A. A. Abdo *et al.*, *The Spectral Energy Distribution of Fermi bright blazars*, Astrophys. J. **716** (2010) 30

[Abd11a] A. A. Abdo *et al.* [Fermi LAT and MAGIC and VERITAS Collaborations], *Insights Into the High-Energy Gamma-ray Emission of Markarian 501 from Extensive Multifrequency Observations in the Fermi Era*, Astrophys. J. **727** (2011) 129

[Abd11b] A. A. Abdo *et al.* [Fermi LAT and MAGIC Collaborations], *Fermi-LAT Observations of Markarian 421: the Missing Piece of its Spectral Energy Distribution*, Astrophys. J. **736** (2011) 131

[Aha00] F. A. Aharonian, *TeV gamma rays from BL Lac objects due to synchrotron radiation of extremely high energy protons*, New Astron. **5** (2000) 377

[Aha01] F. Aharonian *et al.*, *Evidence for TeV gamma ray emission from Cassiopeia A*, Astron. Astrophys. **370** (2001) 112

[Aha02] F. Aharonian *et al.* [HEGRA Collaboration], *Variations of the TeV energy spectrum at different flux levels of Mkn 421 observed with the HEGRA system of Cherenkov telescopes*, Astron. Astrophys. **393** (2002) 89

[Aha04a] F. Aharonian, *Very High Energy Cosmic Gamma Radiation*, River Edge, USA: World Scientific (2004) 495 p.

[Aha04b] F. Aharonian *et al.* [HEGRA Collaboration], *The Crab nebula and pulsar between 500-GeV and 80-TeV. Observations with the HEGRA stereoscopic air Cherenkov telescopes*, Astrophys. J. **614** (2004) 897

[Aha05a] F. Aharonian *et al.* [H.E.S.S. Collaboration], *Discovery of very high energy gamma-rays associated with an x-ray binary*, Science **309** (2005) 746

[Aha05b] F. Aharonian *et al.* [H.E.S.S. Collaboration], *Discovery of the binary pulsar PSR B1259-63 in very-high-energy gamma rays around periastron with H.E.S.S.*, Astron. Astrophys. **442** (2005) 1

[Aha05c] F. Aharonian *et al.* [H.E.S.S. Collaboration], *Observations of Mkn 421 in 2004 with H.E.S.S. at large zenith angles*, Astron. Astrophys. **437** (2005) 95

[Aha06] F. Aharonian *et al.* [H.E.S.S. Collaboration], *Observations of the Crab Nebula with H.E.S.S*, Astron. Astrophys. **457** (2006) 899

[Aha07] F. Aharonian *et al.* [H.E.S.S. Collaboration], *An Exceptional VHE Gamma-Ray Flare of PKS 2155-304*, Astrophys. J. **664** (2007) L71

[Alb06] J. Albert *et al.* [MAGIC Collaboration], *Variable Very High Energy Gamma-ray Emission from the Microquasar LS I +61 303*, Science **312** (2006) 1771

[Alb07a] J. Albert *et al.* [MAGIC Collaboration], *Observation of VHE gamma-rays from Cassiopeia A with the MAGIC telescope*, Astron. Astrophys. **474** (2007) 937

[Alb07b] J. Albert *et al.* [MAGIC Collaboration], *Observations of Mkn 421 with the MAGIC telescope*, Astrophys. J. **663** (2007) 125

[Alb07c] J. Albert *et al.* [MAGIC Collaboration], *Very High Energy Gamma-ray Radiation from the Stellar-mass Black Hole Cygnus X-1*, Astrophys. J. **665** (2007) L51

[Alb07d] J. Albert *et al.* [MAGIC Collaboration], *Unfolding of differential energy spectra in the MAGIC experiment*, Nucl. Instrum. Meth. A **583** (2007) 494

[Alb07e] J. Albert *et al.* [MAGIC Collaboration], *Variable VHE gamma-ray emission from Markarian 501*, Astrophys. J. **669** (2007) 862

[Alb08a] J. Albert *et al.* [MAGIC Collaboration], *VHE Gamma-Ray Observation of the Crab Nebula and Pulsar with MAGIC*, Astrophys. J. **674** (2008) 1037

[Alb08b] J. Albert *et al.* [MAGIC Collaboration], *Implementation of the Random Forest Method for the Imaging Atmospheric Cherenkov Telescope MAGIC*, Nucl. Instrum. Meth. A **588** (2008) 424

[Ale10] J. Aleksić *et al.* [MAGIC Collaboration], *MAGIC TeV Gamma-Ray Observations of Markarian 421 during Multiwavelength Campaigns in 2006*, Astron. Astrophys. **519** (2010) A32

[Ale11a] J. Aleksić *et al.* [MAGIC Collaboration], *Performance of the MAGIC stereo system obtained with Crab Nebula data*, to be published in Astrop. Phys. (2011)

[Ale11b] J. Aleksić *et al.* [MAGIC Collaboration], *Mrk 421 active state in 2008: the MAGIC view, simultaneous multi-wavelength observations and SSC model constrained*, to be published in Astron. Astrophys. (2011)

[Alf42] H. Alvén, *Existence of Electromagnetic-Hydrodynamic Waves*, Nature **150** (1942) 405

[Ali08] E. Aliu *et al.* [MAGIC Collaboration], *Observation of pulsed gamma-rays above 25 GeV from the Crab pulsar with MAGIC*, Science **322** (2008) 1221

[All85] H. D. Aller, M. F. Aller, G. E. Latimer and P. E. Hodge, *Spectra and linear polarizations of extragalactic variable sources at centimeter wavelengths*, Astrophys. J. Suppl. **59** (1985) 513

[Ant93] R. Antonucci, *Unified models for active galactic nuclei and quasars*, Ann. Rev. Astron. Astrophys. **31** (1993) 473

[Ato96] A. M. Atoyan and F. A. Aharonian, *On the mechanisms of gamma radiation in the Crab Nebula*, Mon. Not. Roy. Astron. Soc. **278** (1996) 525

[Bar98] J. A. Barrio *et al.*, *The MAGIC Telescope - Design study for the construction of a 17 m Cherenkov telescope for Gamma-Astronomy above 10 GeV*, MPI-PhE/98-5 (1998)

[Bar03] A. J. Barth, L. C. Ho and W. L. W. Sargent, *The Black hole masses and host galaxies of BL Lac objects*, Astrophys. J. **583** (2003) 134

[Bed97a] W. Bednarek and R. J. Protheroe, *Gamma-rays and neutrinos from the Crab Nebula produced by pulsar accelerated nuclei*, Phys. Rev. Lett. **79** (1997) 2616

[Bed97b] W. Bednarek and R. J. Protheroe, *Testing the homogeneous synchrotron self-Compton model for gamma-ray production in MRK 421*, Mon. Not. Roy. Astron. Soc. **292** (1997) 646

[Bed03] W. Bednarek and M. Bartosik, *Gamma-rays from the pulsar wind nebulae*, Astron. Astrophys. **405** (2003) 689

[Ber81] E. G. Berezhko and G. F. Krymskii, *A Kinetic Analysis of the Charged Particle Acceleration Process in Collisionless Plasma Shear Flows*, Sov. Astr. Lett. **7** (1981) 352

[Ber99] E. G. Berezhko and D. C. Ellison, *A Simple Model of Nonlinear Diffusive Shock Acceleration*, Astrophys. J. **526** (1999) 385

[Ber89] M. Bertero, *Linear inverse and ill-posed problems*, Adv. Electr. Phys. **75** (1989) 1

[Ber04] L. Bergström and A. Goobar, *Cosmology and Particle Astrophysics*, Chichester, UK: Praxis Pub. (2004) 364 p.

[Bil07] A. Biland *et al.*, *The Active Mirror Control of the MAGIC Telescope*, Proc. 30$^{\text{th}}$ ICRC, Merida (2007)

[Bla78] R. D. Blandford and M. J. Rees, *Some comments on radiation mechanisms in Lacertids*, Proc. Pittsb. Conf. BL Lac Obj. (1978) 328

[Bla90] R. D. Blandford, *Physical processes in active galactic nuclei*, in *Active Galactic Nuclei*, Berlin, Germany: Springer (1990) 161

[Bla95] R. D. Blandford and A. Levinson, *Pair cascades in extragalactic jets. 1: Gamma rays*, Astrophys. J. **441** (1995) 79

[Bla05] M. Blazejowski *et al.*, *A Multiwavelength View of the TeV Blazar Markarian 421: Correlated Variability, Flaring, and Spectral Evolution*, Astrophys. J. **630** (2005) 130

[Blu09] J. Bluemer, R. Engel and J. R. Hoerandel, *Cosmic Rays from the Knee to the Highest Energies*, Prog. Part. Nucl. Phys. **63** (2009) 293

[Boe98] M. Böttcher and C. D. Dermer, *On Compton Scattering Scenarios for Blazer Flares*, Astrophys. J. **501** (1998) L51

[Boe04] M. Böttcher and A. Reimer, *Modeling the Multiwavelength Spectra and Variability of BL Lacertae in 2000*, Astrophys. J. **609** (2004) 576

[Boe10] M. Böttcher, *Models for the Spectral Energy Distributions and Variability of Blazars*, Fermi Meets Jansky Conf. Proc. (2010) 41

[Bor09] D. Borla Tridon *et al. Performance of the Camera of the MAGIC II Telescope*, Proc. 31$^{\text{st}}$ ICRC, Lodz (2009)

[Bre09] T. Bretz, D. Dorner, R. M. Wagner and P. Sawallisch, *The drive system of the Major Atmospheric Gamma-ray Imaging Cherenkov Telescope*, Astropart. Phys. **31** (2009) 92

[Bri09] D. Britzger, *Studies of the Influence of Moonlight on Observations with the MAGIC Telescope*, Diploma thesis, LMU University Munich, Munich (2009)

[Bru97] R. Brun and F. Rademakers, *ROOT – An object oriented data analysis framework*, Nucl. Instrum. Meth. A **389** (1997) 81

[Bur05] D. N. Burrows *et al.*, *The Swift X-ray Telescope*, Space Sci. Rev. **120** (2005) 165

[Car11] E. Carmona *et al.*, *Performance of the MAGIC Stereo System*, Proc. 32nd ICRC, Beijing (2011)

[Cel08] A. Celotti and G. Ghisellini, *The power of blazar jets*, Mon. Not. Roy. Astron. Soc. **385** (2008) 283

[Che86] K. S. Cheng, C. Ho and M. A. Rudermann, *Energetic Radiation from Rapidly Spinning Pulsars. II. Vela and Crab*, Astrophys. J. **300** (1986) 522

[Chi92] J. Chiang and R. W. Romani, *Gamma radiation from pulsar magnetospheric gaps*, Astrophys. J. **400** (1992) 629

[Col99] G. W. Collins, W. P. Claspy and J. C. Martin, *A Reinterpretation of Historical References to the Supernova of A.D. 1054*, Publ. Astr. Soc. Pac. **111** (1999) 871

[Dar97] A. Dar and A. Laor, *Hadronic Production of TeV Gamma-Ray Flares from Blazars*, Astrophys. J. **478** (1997) L5

[Dau97] A. Daum *et al.*, *First results on the performance of the HEGRA IACT array*, Astrop. Phys. **8** (1997) 1

[Der92a] C. D. Dermer and R. Schlickeiser, *Quasars, blazars, and gamma rays*, Science **257** (1992) 1642

[Der92b] C. D. Dermer, R. Schlickeiser and A. Mastichiadis, *High-energy gamma radiation from extragalactic radio sources*, Astron. Astrophys. **256** (1992) L27

[Der93] C. D. Dermer and R. Schlickeiser, *Model for the High-Energy Emission from Blazars*, Astrophys. J. **416** (1993) 458

[Die04] M. E. Dieckmann, B. Eliasson and P. K. Shukla *Self-consistent Studies of Electron Acceleration to Ultrarelativistic Energies by Upper Hybrid Waves*, Astrophys. J. **617** (2004) 1361

[Don09] I. Donnarumma *et al.*, *The June 2008 Flare of Markarian 421 from Optical to TeV Energies* Astrophys. J. **691** (2009) L13

[Dor08] M. Doro *et al.*, *The reflective surface of the MAGIC telescope*, Nucl. Instrum. Meth. A **595** (2008) 200

[Dru83] L. O. Drury, *An introduction to the theory of diffusive shock acceleration of energetic particles in tenuous plasmas*, Rept. Prog. Phys. **46** (1983) 973

[Fer49] E. Fermi, *On the Origin of the Cosmic Radiation*, Phys. Rev. **75** (1949) 1169

[Fit99] E. L. Fitzpatrick, *Correcting for the effects of interstellar extinction*, Publ. Astron. Soc. Pac. **111** (1999) 63

[Fom94] V. P. Fomin *et al.*, *New methods of atmospheric Cherenkov imaging for gamma-ray astronomy. I. The false source method.*, Astrop. Phys. **2** (1994) 137

[Fos98] G. Fossati, L. Maraschi, A. Celotti, A. Comastri and G. Ghisellini, *A Unifying view of the spectral energy distributions of blazars*, Mon. Not. Roy. Astron. Soc. **299** (1998) 433

[Fos08] G. Fossati *et al.*, *Multiwavelength Observations of Markarian 421 in 2001 March: An Unprecedented View on the X-Ray/TeV Correlated Variability*, Astrophys. J. **677** (2008) 906

[Fra08] A. Franceschini, G. Rodighiero and M. Vaccari, *Extragalactic optical-infrared background radiation, its time evolution and the cosmic photon-photon opacity*, Astron. Astrophys. **487** (2008) 837

[Gai90] T. K. Gaisser, *Cosmic rays and particle physics*, Cambridge and New York: Cambridge Univ. Pr. (1990) 292 p.

[Gau05] M. Gaug, H. Bartko, J.Cortina and J. Rico, *Calibration of the MAGIC Telescope*, Proc. 29$^{\text{th}}$ ICRC, Pune **5** (2005) 375

[Geb04] J. Gebauer *et al. Evaluation of a New High QE Photomultiplier for Air Cherenkov Telescopes*, Nucl. Instrum. Meth. A **518** (2004) 615

[Ghi96] G. Ghisellini and P. Madau, *On the origin of the gamma-ray emission in blazars*, Mon. Not. Roy. Astron. Soc. **280** (1996) 67

[Ghi02] G. Ghisellini, A. Celotti and L. Costamante, *Low power BL lacertae objects and the Blazar sequence: Clues on the particle acceleration process*, Astron. Astrophys. **386** (2002) 833

[Gia09] D. Giannios, D. A. Uzdensky and M. C. Begelman, *Fast TeV variability in blazars: jet in a jet*, Mon. Not. Roy. Astron. Soc. **395** (2009) L29

[Goe07] F. Goebel *et al.*, *Upgrade of the MAGIC telescope with a Multiplexer Fiber-Optic 2GSamples/s FADC Data Acquisition system*, Proc. 30$^{\text{th}}$ ICRC, Merida (2007)

[Han11] W. Hanlon, *Cosmic ray spectrum*, http://www.physics.utah.edu/∼whanlon/spectrum.html (2011)

[Har99] R. C. Hartmann *et al.*, *The Third EGRET Catalog of High-Energy Gamma-Ray Sources*, Astrophys. J. Suppl. **123** (1999) 79

[Hes12] V. F. Hess, *Über die Beobachtungen der durchdringenden Strahlung bei sieben Freiballonfahrten*, Phys. Zeitschr. **13** (1912) 1084

[Hil85] A. M. Hillas, *Cherenkov light images of EAS produced by primary gamma*, Proc. 19$^{\text{th}}$ ICRC, La Jolla, Vol.3 (1985) 445

[Hil96] A. M. Hillas, *Differences between gamma-ray and hadronic showers*, Space Sci. Rev. **75** (1996) 17

[Hor09] D. Horan *et al.*, *Multiwavelength Observations of Markarian 421 in 2005 - 2006*, Astrophys. J. **695** (2009) 596

[Ino96] S. Inoue and F. Takahara, *Electron Acceleration and Gamma-Ray Emission from Blazars*, Astrophys. J. **463** (1996) 555

[Jak06] P. Jakobsson *et al.*, *A mean redshift of 2.8 for swift gamma-ray bursts*, Astron. Astrophys. **447** (2006) 897

[Jes01] S. Jester, H.-J. Röser, K. Meisenheimer, R. Perley and R. Conway, *HST optical spectral index map of the jet of 3C 273*, Astron. Astrophys. **373** (2001) 447

[Jes05] S. Jester, H.-J. Röser, K. Meisenheimer and R. Perley , *The radio-ultraviolet spectral energy distribution of the jet in 3C 273*, Astron. Astrophys. **431** (2004) 477

[Jok90] J. R. Jokipii and G. Morfill, *Particle acceleration in step function shear flows - A microscopic analysis*, Astrophys. J. **356** (1990) 255

[Jon74] T. W. Jones, S. L. O'Dell and W. A. Stein, *Physics of Compact Nonthermal Sources. Theory of Radiation Processes*, Astrophys. J. **188** (1974) 353

[Kat03] K. Katarzynski, H. Sol and A. Kus, *The multifrequency variability of Mrk 421*, Astron. Astrophys. **410** (2003) 101

[Kat06a] K. Katarzynski, G. Ghisellini, F. Tavecchio, J. Gracia and L. Maraschi, *Hard TeV spectra of blazars and the constraints to the IR intergalactic background*," Mon. Not. Roy. Astron. Soc. Lett. **368** (2006) L52

[Kat06b] K. Katarzynski, G. Ghisellini, A. Mastichiadis, F. Tavecchio and L. Maraschi, *Stochastic particle acceleration and synchrotron self-compton radiation in TeV blazars*, Astron. Astrophys. **453** (2006) 47

[Kaz92] D. Kazanas and A. Mastichiadis, *The origin of TeV electrons in blazars*, Astropart. Phys. **11** (1999) 41

[Kin02] M. Kino, F. Takahara and M. Kusunose, *Energetics of TeV Blazars and physical constraints on their emission regions*, Astrophys. J. **564** (2002) 97

[Kir92] J. G. Kirk and A. Mastichiadis, *X-ray flares from runaway pair production in active galactic nuclei*, Nature **360** (1992) 135

[Kir96] J. G. Kirk, P. Duffy and Y. A. Gallant, *Stochastic particle acceleration at shocks in the presence of braided magnetic fields*, Astron. Astrophys. **314** (1996) 1010

[Kir98] J. G. Kirk, F. M. Rieger and A. Mastichiadis, *Particle acceleration and synchrotron emission in blazar jets*, Astron. Astrophys. **333** (1998) 452

[Kne08] T. M. Kneiske and H. Dole, *A strict lower-limit EBL: Applications on gamma-ray absorption*, AIP Conf. Proc. **1085** (2009) 620

[Kom07] S. S. Komissarov, M. V. Barkov, N. Vlahakis and A. Konigl, *Magnetic acceleration of relativistic AGN jets*, Mon. Not. Roy. Astron. Soc. **380** (2007) 51

[Kon03] A. K. Konopelko, A. Mastichiadis, J. G. Kirk, O. C. de Jager and F. W. Stecker, *Modeling the TeV gamma-ray spectra of two low redshift AGNs: Mkn 501 and Mkn 421*, Astrophys. J. **597** (2003) 851-859

[Kre02] F. Krennrich *et al.*, *Discovery of spectral variability of Markarian 421 at TeV energies*, Astrophys. J. **575** (2002) L9

[Kro99] J. H. Krolik, *Active galactic nuclei : from the central black hole to the galactic environment*, Princeton, USA: Univ. Pr. (1999) 598 p. (Princeton Series in Astrophysics)

[Lef11] E. Lefa, F. M. Rieger and F. Aharonian, *Formation of hard very-high energy spectra of blazars in leptonic models*, Astrophys. J. **740** (2011) 64

[Les01] R. W. Lessard, J. H. Buckley, V. Connaughton and S. Le Bohec, *A new analysis method for reconstructing the arrival direction of TeV gamma rays using a single imaging atmospheric Cherenkov telescope*, Astropart. Phys. **15** (2001) 1

[Lia83] T. P. Li and Y. Q. Ma, *Analysis methods for results in gamma-ray astronomy*, Astrophys. J. **272** (1983) 317

[Lom11] S. Lombardi *et al.*, *Advanced stereoscopic gamma-ray shower analysis with the MAGIC telescopes*, Proc. 32$^{\text{nd}}$ ICRC, Beijing (2011)

[Lon11] M. S. Longair, *High Energy Astrophysics*, Cambridge, UK: Univ. Pr. (2011) 861 p.

[Man11] N. Mankuzhiyil *et al.*, *The environment and distribution of emitting electrons as a function of source activity in Markarian 421* Astrophys. J. **733** (2011) 14

[Man91] K. Mannheim, P. L. Biermann and W. M. Kruells, *A novel mechanism for nonthermal X-ray emission*, Astron. Astrophys. **251** (1991) 723

[Man93] K. Mannheim, *The proton blazar*, Astron. Astrophys. **269** (1993) 67

[Mar92] L. Maraschi, G. Ghisellini and A. Celotti, *A jet model for the gamma-ray emitting blazar 3C 279*, Astrophys. J. **397** (1992) L5

[Mar99] L. Maraschi *et al.*, *Simultaneous X-Ray and TEV Observations of a Rapid Flare from Markarian 421*, Astrophys. J. **526** (1999) L81

[Mar81] B. Markarian, V. Lipovetsky, D. Stepanian, *Galaxies with ultraviolet continuum. XV*, Astrophysics **17** (1982) 321

[Mar85] A. P. Marscher and W. K. Gear, *Models for high-frequency radio outbursts in extragalactic sources, with application to the early 1983 millimeter-to-infrared flare of 3C 273*, Astrophys. J. **298** (1985) 114

[Mar96] A. P. Marscher and J. P. Travis, *Synchrotron self-Compton interpretation of multiwaveband observations of gamma-ray bright blazars*, Astron. Astrophys. Suppl. **120** (1996) 537

[Mas97] A. Mastichiadis and J. G. Kirk, *Variability in the synchrotron self-Compton model of blazar emission*, Astron. Astrophys. **320** (1997) 19

[McC01] K. G. McClements *et al.*, *Surfatron and Stochastic Acceleration of Electrons at Supernova Remnant Shocks*, Phys. Rev. Lett. **87** (2001) 25

[Mik10] M. S. Mikhailova, E. Y. Bannikova and V M. Kontorovich, *Determining the Inclination of the Kiloparsec-Scale Jet of the Quasar 3C 273 Based on Competition of Mechanisms for the Knot X-ray Emission*, Astron. Rep. **54** (2010) 481

[Mim04] P. Mimica, M. A. Aloy, E. Muller and W. Brinkmann, *Synthetic X-ray light curves of BL Lacs from relativistic hydrodynamic simulations*, Astron. Astrophys. **418** (2004) 947

[Mon95] C. von Montigny *et al.*, *High-energy gamma-ray emission from active galaxies: EGRET observations and their implications*, Astrophys. J. **440** (1995) 525

[Mor09] A. Moralejo *et al.*, *Mars, the MAGIC Analysis and Reconstruction Software*, Proc. 31st ICRC, Lodz (2009)

[Mue00] A. Muecke and R. J. Protheroe, *Modeling the April 1997 flare of Mkn 501*, AIP Conf. Proc. **515** (2000) 149

[Mue03] A. Muecke, R. J. Protheroe, R. Engel, J. P. Rachen and T. Stanev, *BL Lac objects in the synchrotron proton blazar model*, Astropart. Phys. **18** (2003) 593

[Muk97] R. Mukherjee *et al.*, *EGRET Observations of High-energy Gamma-Ray Emission from Blazars: an Update*, Astrophys. J. **490** (1997) 116

[Muk99] R. Mukherjee *et al.*, *Broadband Spectral Analysis of PKS 0528+134: A Report on Six Years of EGRET Observations*, Astrophys. J. **527** (1999) 132

[Mur00] H. Muraishi *et al.* [CANGAROO Collaboration], *Evidence for TeV gamma-ray emission from the shell type SNR RX J1713.7-3946*, Astron. Astrophys. **354** (2000) L57

[Nak10] K. Nakamura *et al.* [Particle Data Group], *Review of particle physics*, J. Phys. G **37** (2010) 075021

[Nil07] K. Nilsson, M. Pasanen, L. O. Takalo, E. Lindfors, A. Berdyugin, S. Ciprini and J. Pforr, *Host galaxy subtraction of TeV candidate BL Lacertae objects*, Astron. Astrophys. **475** (2007) 199

[Ost00] A. Ostankov, D. Paneque, M. Martinez, E. Lorenz and R. Mirzoyan, *A study of the new hemispherical 6-dynodes PMT from electron tubes*, Nucl. Instrum. Meth. A **442** (2000) 117

[Pad95] P. Padovani and P. Giommi, *A sample-oriented catalogue of BL Lacertae objects*, Mon. Not. Roy. Astron. Soc. **277** (1995) 1477

[Per05] A. S. Perlman *et al.*, *Intrinsic Curvature in the X-Ray Spectra of BL Lacertae Objects*, Astrophys. J. **625** (2005) 727

[Pet97] B. M. Peterson, *An Introduction to Active Galactic Nuclei*, Cambridge, UK: Univ. Pr. (1997) 238 p.

[Poo08] T. S. Poole *et al.*, *Photometric Calibration of the Swift Ultraviolet/Optical Telescope*, Mon. Not. Roy. Astron. Soc. **383** (2008) 627

[Pri05] J. R. Primack, J. S. Bullock and R. S. Somerville, *Observational gamma-ray cosmology*, AIP Conf. Proc. **745** (2005) 23

[Pun92] M. Punch *et al.* [Whipple Collaboration], *Detection of TeV photons from the active galaxy Markarian 421*, Nature **358** (1992) 477

[Rac00] J. P. Rachen, *Hadronic blazar models and correlated X-ray/TeV flares*, AIP Conf. Proc. **515** (2000) 41

[Ram86] P. V. Ramana Murthy and A. W. Wolfendale, *Gamma-ray astronomy*, Cambridge, UK: Univ. Pr. (1986) 248 p. (Cambridge Astrophysics Series)

[Ree92] M. J. Rees and P. Meszaros, *Relativistic fireballs - Energy conversion and time-scales*, Mon. Not. Roy. Astron. Soc. **258** (1992) 41

[Ree94] M. J. Rees and P. Meszaros, *Unsteady outflow models for cosmological gamma-ray bursts*, Astrophys. J. **430** (1994) L93

[Ric10] J. L. Richards *et al.*, *15 GHz Monitoring of Gamma-ray Blazars with the OVRO 40 Meter Telescope in Support of Fermi*, AIP Conf. Proc. **1248** (2010) 503

[Rie04] F. M. Rieger and P. Duffy, *Shear acceleration in relativistic astrophysical jets*, Astrophys. J. **617** (2004) 155

[Rie06] F. M. Rieger, V. Bosch-Ramon and P. Duffy, *Fermi acceleration in astrophysical jets*, Astrophys. Space Sci. **309** (2007) 119

[Rit04] S. Ritt, *The DRS2 Chip: a 4.5 GHz Waveform Digitizing Chip for the MEG Experiment*, Proc. IEEE/NSS, Rome (2004)

[Rom05] P. W. A. Roming *et al.*, *The Swift Ultra-Violet/Optical Telescope*, Space Sci. Rev. **120** (2005) 95

[Rud75] M. A. Rudermann and P. G. Sutherland, *Theory of pulsars - Polar caps, sparks, and coherent microwave radiation*, Astrophys. J. **196** (1975) 51

[Sch79] P. A. G. Scheuer and A. C. S. Readhead, *Superluminally expanding radio sources and the radio-quiet QSOs*, Nature **277** (1979) 182

[Sch98] D. J. Schlegel, D. P. Finkbeiner and M. Davis, *Maps of dust IR emission for use in estimation of reddening and CMBR foregrounds*, Astrophys. J. **500** (1998) 525

[Sch96a] R. Schlickeiser, *Gamma-Rays from Active Galactic Nuclei: Emission Processes and Particle Acceleration*, Space Sci. Rev. **75** (1996) 299

[Sch96b] R. Schlickeiser, *Models of high-energy emission from active galactic nuclei*, Astron. Astrophys. Suppl. **120** (1996) 481

[Sch10] R. Schlickeiser, M. Böttcher and U. Menzler, *Combined synchrotron and nonlinear synchrotron-self-Compton cooling of relativistic electrons*, Astron. Astrophys. **519** (2010) A9

[Sch94] M. Schmelling, *The method of reduced cross-entropy: A general approach to unfold probability distributions*, Nucl. Instrum. Meth. A **340** (1994) 400

[Sch11] F. Schmidt, *CORSIKA Shower Images*, http://www.ast.leeds.ac.uk/∼fs/showerimages.html (2011)

[Sch02] T. Schweizer, E. Lorenz, M. Martinez, A. Ostankov and D. Paneque, *The optical calibration of the MAGIC telescope camera*, IEEE Trans. Nucl. Sci. **49** (2002) 2497

[Sik94] M. Sikora, M. C. Begelman and M. J. Rees, *Comptonization of diffuse ambient radiation by a relativistic jet: The source of gamma rays from blazars?*, Astrophys. J. **421** (1994) 153

[Spa01] M. Spada, G. Ghisellini, D. Lazzati and A. Celotti, *Internal shocks in the jets of radio-loud quasars*, Mon. Not. Roy. Astron. Soc. **325** (2001) 1559

[Sta04] L. Stawarz, *On the Jet Activity in 3C 273*, Astrophys. J. **613** (2004) 119

[Stu71] P. A. Sturrock, *A Model of Pulsars*, Astrophys. J. **164** (1971) 529

[Tag08] G. Tagliaferri *et al. Simultaneous multiwavelength observations of the blazar 1ES1959+650 at a low TeV flux* Astrophys. J. **679** (2008) 1029

[Tak10] H. Takami, *Gamma-rays as a diagnostic of the origin of core radiation in low-luminosity active galactic nuclei*, accepted for publication in Mon. Not. Roy. Astron. Soc., [arXiv:1012.5403 [astro-ph.HE]].

[Tav98] F. Tavecchio, L. Maraschi and G. Ghisellini, *Constraints on the physical parameters of TeV blazars*, Astrophys. J. **509** (1998) 608

[Tav01] F. Tavecchio *et al.*, *Theoretical Implications from the Spectral Evolution of Markarian 501 Observed with BeppoSAX*, Astrophys. J. **554** (2001) 725

[Tav09] F. Tavecchio, G. Ghisellini, G. Ghirlanda and A. Franceschini, *The hard TeV spectrum of 1ES 0229+200: new clues from Swift*, Mon. Not. Roy. Astron. Soc. Lett. **399** (2009) L59

[Tav10] F. Tavecchio *et al.*, *TeV BL Lac objects at the dawn of the Fermi era*, Mon. Not. Roy. Astron. Soc. **401** (2010) 1570

[Ter98] H. Teräsranta *et al.*, *Fifteen years monitoring of extragalactic radio sources at 22, 37 and 87 GHz*, Astron. Astrophys. Suppl. **132** (1998) 305

[Tes09] D. Tescaro *et al.*, *The readout system of the MAGIC-II Cherenkov Telescope*, Proc. 31$^{\text{st}}$ ICRC, Lodz (2009)

[Tik79] A. N. Tikhonov and V. J. Arsenin, *Methods of solution of Ill-posed problems*, Washington, USA: Winston & Sons (1979) 258 p.

[Tlu07] M. Tluczykont, M. Shayduk, O. Kalekin and E. Bernardini, *Long-term gamma-ray lightcurves and high state probabilities of Active Galactic Nuclei*, J. Phys. Conf. S. **60** (2007) 318

[Ulr97] M. H. Ulrich, L. Maraschi and C. M. Urry, *Variability of active galactic nuclei*, Ann. Rev. Astron. Astrophys. **35** (1997) 445

[Urr95] C. M. Urry and P. Padovani, *Unified schemes for radio-loud active galactic nuclei*, Publ. Astron. Soc. Pac. **107** (1995) 803

[Ven09] T. M. Venters, V. Pavlidou and L. C. Reyes, *The extragalactic background light absorption feature in the Blazar component of the extralactic gamma-ray background*, Astrophys. J. **703** (2009) 1939

[Vil98] Villata, M.; Raiteri, C. M.; Lanteri, L.; Sobrito, G.; Cavallone, M. M. Villata, C. M. Raiteri, L. M. Lanteri, G. Sobrito and M. Cavallone, *BVR photometry of comparison stars in selected blazar fields. I. Photometric sequences for 10 BL Lacertae objects*, Astron. Astrophys. Suppl. **130** (1998) 305

[Vil08] M. Villata, C. M. Raiteri, V. M. Larionov, O. M. Kurtanidze, K. Nilsson, M. F. Aller, M. Tornikoski and A. Volvach, *Multifrequency monitoring of the blazar 0716+714 during the GASP-WEBT-AGILE campaign of 2007*, Astron. Astrophys. **481** (2008) L79

[Vil09] M. Villata, C. M. Raiteri, M. A. Gurwell, V. M. Larionov, O. M. Kurtanidze, M. F. Aller, A. Lahteenmaki, W. P. Chen *et al.*, *The GASP-WEBT monitoring of 3C 454.3 during the 2008 optical-to-radio and gamma-ray outburst*, Astron. Astrophys. **504** (2009) L9

[Vir05] J. J. P. Virtanen and R. Vainio, *Stochastic Acceleration in Relativistic Parallel Shocks*, Astrophys. J. **621** (2005) 313

[Vla04] N. Vlahakis and A. Konigl, *Magnetic driving of relativistic outflows in active galactic nuclei. 1. Interpretation of parsec - scale accelerations,* Astrophys. J. **605** (2004) 656

[Wag06] R. M. Wagner, *Measurement of Very High Energy Gamma-Ray Emission from Four Blazars Using the MAGIC Telescope and a Comparative Blazar Study*, PhD thesis, Technical University Munich, Munich (2006)

[Wag11] R. M. Wagner, *VHE γ-ray Sky Map and Source Catalog*, http://www.mpp.mpg.de/∼rwagner/sources/ (2011)

[Web87] G. M. Webb, *Hydrodynamical constraints on cosmic-ray acceleration in relativistic shocks*, Astrophys. J. **319** (1987) 215

[Wee89] T. C. Weekes *et al.*, *Observation of TeV gamma rays from the Crab nebula using the atmospheric Cherenkov imaging technique*, Astrophys. J. **342** (1989) 379

[Wee03] T. C. Weekes, *Very High Energy Gamma-Ray Astronomy*, Bristol, UK: IOP (2003) 221 p.

[Win70] R. Winston, *Light Collection within the Framework of Geometric Optics*, J. Opt. Soc. Amer. **60** (1970) 245

[Wu02] X.-B. Wu, F. K. Liu and T. Z. Zhang, *Supermassive black hole masses of AGNs with elliptical hosts*, Astron. Astrophys. **389** (2002) 742

[Zan11] R. Zanin *et al.*, *MAGIC measurement of the Crab Nebula spectrum over three decades in energy*, Proc. 32$^{\text{nd}}$ ICRC, Beijing (2011)

[Zac10] M. Zacharias and R. Schlickeiser, *Blazar synchrotron emission of instantaneously power-law injected electrons under linear synchrotron, non-linear SSC, and combined synchrotron-SSC cooling*, Astron. Astrophys. **524** (2010) A31

Acknowledgement

I thank Prof. Dr. Siegfried Bethke, Prof. Dr. Masahiro Teshima, Dr. Razmik Mirzoyan and Dr. Robert-Marcus Wagner for giving me the possibility of writing a PhD thesis in this exciting field of research and for their supervision throughout the last three years.

Further, I am very thankful to Dr. David Paneque, who organised the multi-wavelength campaign from which this thesis profited a lot. In this context, I also thank the analysers of the other participating experiments for sharing their results.

My thanks also go to Dr. Hajime Takami, who provided me with the synchrotron self-Compton code with which I modelled my results and who introduced me to the subtleties of acceleration and radiation mechanisms in blazar jets.

I thank all members of the MPI Munich group and of the MAGIC collaboration for the fruitful cooperation and the open-minded atmosphere. I particularly want to thank Ulisses Barres de Almeida, Daniela Borla Tridon, Francesco Borracci, Emiliano Carmona, Pierre Colin, Christian Fruck, Dennis Häfner, Tobias Jogler, Hanna Kellermann, Max Knötig, Julian Krause, Hiroko Miyamoto, Daisuke Nakajima, Nina Nowak, David Paneque, Takayuki Saito, Thomas Schweizer, Julian Sitarek, Shang-Yu Sun, Hajime Takami, Takeshi Toyama and Robert-Marcus Wagner for many enriching discussions and the vital life in and outside the institute. I would like to accent my additional thanks to Daniela Borla Tridon, Tobias Jogler and Julian Krause for sharing ideas and work on scripts and programming issues.

My thanks also go to my proofreaders Malika Damian, Christoph Göllnitz, Susan Komansky, David Paneque, Hajime Takami and Robert-Marcus Wagner. Their comments and suggestions helped a lot to improve this work.